Colloidal Self-Assembly of Novel Materials Displaying Structural Colour

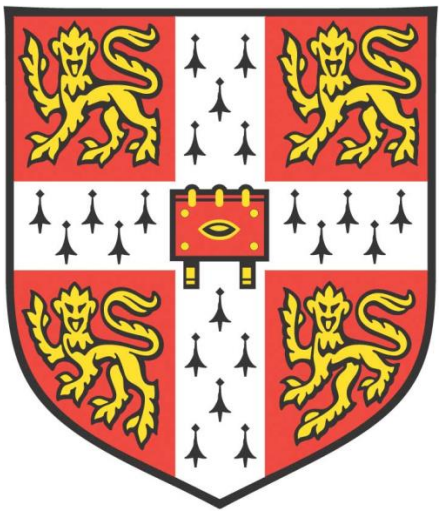

Thomas James O'Neill

St Catharine's College

Department of Physics

University of Cambridge

This dissertation is submitted for the degree of Doctor of Philosophy

May 2019

DECLARATION

This dissertation is the result of my own work and includes nothing which is the outcome of work done in collaboration except as declared in the Preface and specified in the text.

It is not substantially the same as any that I have submitted, or is being currently submitted for a degree or diploma or other qualification at the University of Cambridge or any other University or similar institution except as declared in the Preface and specified in the text. I further state that no substantial part of my dissertation has already been submitted or is being concurrently submitted for any such degree diploma or other qualification at the University of Cambridge or any other University or similar institution except as declared in the Preface and specified in the text.

In accordance with the Department of Physics guidelines, this thesis does not exceed 60,000 words.

Signed:_____

Date:_____

Thomas James O'Neill

Cambridge

ABSTRACT

Self-assembly of colloids is a powerful technique for the synthesis of novel materials. While top-down manufacturing methods can also produce structures patterned on the mesoscale, they are frequently limited in resolution, slow to employ or restricted to two-dimensional systems; in contrast, self-assembly theoretically offers full control over the three-dimensional microstructure of a material and can be tuned by varying initial conditions and external forces. Self-assembly is particularly attractive because of its prevalence in the natural world; most naturally occurring nanostructures with interesting properties are produced through self-assembly processes that can then be mimicked in synthetic systems.

One such class of materials exhibits structural colour, where light is differentially scattered or reflected based not on absorption but on the physical arrangement of the material on the nanoscale. Structurally produced colours tend to be brighter and more vivid than pigment-based ones and do not fade over time. As such they have numerous potential applications not only as a source of colouration but also in next-generation non-backlit displays and optoelectronic systems.

This thesis discusses the synthesis, functionalisation and self-assembly of colloids into novel functional materials, particularly those that mimic naturally occurring structural colour based on disordered and ordered systems. The functionalisation of colloids with DNA introduces a specific, tuneable and thermally reversible attractive potential between particles, making it an excellent system to explore self-assembly. DNA-coated polystyrene particles were used to investigate gel formation through a spinodal decomposition mechanism and how the resulting gel structure reproducibly depends upon suspension properties. Subsequently, the tendency of such gels to produce structural colour was investigated using both polystyrene and silica DNA-coated colloidal systems, in comparison with similar natural materials. Finally, soft solution-phase photonic crystals were assembled using highly charged colloids of a low refractive index. This system was found to exhibit isotropic structural colour tuneable throughout the visible range, coupled with high transparency.

"*It's still magic even if you know how it's done*"

– Terry Pratchett, *A Hat Full of Sky*

ACKNOWLEDGEMENTS

I would like to thank my supervisors Erika Eiser and Silvia Vignolini for all their guidance and mentorship over the past four years. It has been an absolute pleasure to be able to discuss science with and learn from them and work as part of their groups. Thanks also to the NanoDTC and all those who work so hard to run it for the opportunity to study for a PhD at all.

To the other members of the Eiser group, past and present: it has been a privilege working with you all over the past four years. In particular, Darshana, Zhongyang and Yang: thank you for making the Eiser group such a welcoming place and for all your help getting started. Alessio, Zach, Iliya, Talha and most of all Myk: you are what made this PhD amazing. It's been such a pleasure working with you, thanks for your friendship and always being there to laugh with, bounce ideas off and vent to.

To all the friends who have kept me sane (ish!) throughout the PhD, I am forever grateful. Thanks for all the good times, the climbing and the food. You know who you are.

Finally, I'd like to thank those closest to me. To my parents, thank you for your unwavering love and support, even while moving as far away as physically possible! To my brother, thank you for never failing to respond to "The beacons are lit!". And to Helena, I have no idea who, what and where I'd be without you. Thank you for everything. I love you.

CONTENTS

LIST OF TABLES

List of Figures

List of Abbreviations and Acronyms

APS	Ammonium persulfate
BCC	Body-centred cubic
DBCO	Dibenzylcyclooctyne
DCM	Dichloromethane
DLS	Dynamic light scattering
DMF	Dimethyl formamide
DMSO	Dimethyl sulfoxide
DNA	Deoxyribonucleic acid
DNACC	DNA-coated colloid
dsDNA	Double-stranded DNA
EDC	1-ethyl-3-(3-dimethylaminopropyl)carbodiimide
EDTA	Ethylenediaminetetraacetic acid
FCC	Face-centred cubic
FITC	Fluorescein isothiocyanate
FL	Fluorinated latex
FTIR	Fourier-transform infra-red
HCP	Hexagonal close packed
HFBMA	Heptafluorobutyl methacrylate
KPS	Potassium persulfate
MES	2-(N-morpholino)ethanesulfonic acid
MsCl	Mesyl chloride
NHS	N-hydroxy succinimide
NP	Nanoparticle
OD	Oil droplet
PB	Phosphate Buffer

PDI	Polydispersity index
PEG	Poly(ethylene glycol)
PLL	Poly(L-lysine)
PBA	Poly(butyl acrylate)
PMMA	Poly(methyl methacrylate)
PPO	Poly(propylene oxide)
PS	Polystyrene
PVP	Poly(vinyl pyrrolidone)
SAXS	Small-angle X-ray scattering
SDS	Sodium dodecyl sulfate
SEM	Scanning electron microscopy
Si	Silica
SPAAC	Strain-promoted azide-alkyne cycloaddition
ssDNA	Single-stranded DNA
SVBS	Sodium 4-vinylbenzenesulfonate
TE	Tris-EDTA buffer
TEA	Triethylamine
TEM	Transmission electron microscopy
THF	Tetrahydrofuran
TsCl	Tosyl chloride
UV-Vis	Ultraviolet-visible

List of Appendices

PREFACE

Contributions by other authors:

Chapter 2.2: The silica carbodiimide functionalisation protocol was developed by Zachary Ruff as part of his PhD.

Chapter 3.2: The surfactant-free emulsion polymerisation of polystyrene method developed here was based on syntheses developed by Dr Yang Lan.

Chapter 3.3: Development of the synthesis and functionalisation of fluorinated latex colloids was done in collaboration with Mykolas Zupkauskas.

Chapter 4.4: The functionalisation and gelation of silica colloids was done in collaboration with Zachary Ruff.

Chapter 5.2: Reflectivity measurements were carried out in collaboration with Dr Talha Erdem.

Chapter 5.3: Fitting of the colloid size distribution to the experimental form factor was done using code written by Alessio Caciagli.

Chapter 5.4: Simulations were carried out by Dr Talha Erdem.

Chapter 6.1: The emulsion droplet syntheses were developed by Alessio Caciagli and Mykolas Zupkauskas as part of their PhDs.

Chapter 6.3: Synthesis of colloidosomes was done in collaboration with David Brossault in the Alex Routh group.

Related Publications:

- Z. Ruff, P. Cloetens, T. O'Neill, C. Grey and E. Eiser, "Thermally Reversible Nanoparticle Gels with Tuneable Porosity Showing Structural Colour", *Phys. Chem. Chem. Phys.*, 2017, 20 (1), 467-477
- Z. Xing, A. Caciagli, T. Cao, I. Stoev, M. Zupkauskas, T. O'Neill, T. Wenzel, R. Lamboll, D. Liu and E. Eiser, "Microrheology of DNA Hydrogels", *PNAS*, 2018, 115 (32), 8137-8142
- A. Caciagli, M. Zupkauskas, A. Levin, T. Knowles, C. Mugemana, N. Bruns, T. O'Neill, W. Frith and E. Eiser, "DNA-Coated Functional Oil Droplets", *Langmuir*, 2018, 34 (34), 10073-10080

- P. Xu, Y. Lan, L. Dai, T. O'Neill, I. Stoev, T. Cao and E. Eiser, "Discotic Liquid Crystals of Cucurbit[7]uril (CB[7])-Functionalised Laponite Clays", *Mol Phys.*, 2018, 116 (21-22), 1-9
- T. O'Neill[1], T. Erdem[1], M. Zupkauskas, A. Caciagli, P. Xu, Y. Lan, P. Boesecke and E. Eiser, "Tuneable Colloidal Photonic Crystals", 2019. (Manuscript accepted for publication in *Mater. Horiz.*). http://arxiv.org/abs/1808.0626

  [1] – these authors contributed equally.
- T. Erdem, Y. Lan, P. Xu, Y. Altintas, T. O'Neill, A. Caciagli, C. Ducati, E. Mutlugun, O. Scherman and E. Eiser, "Transparent Films Made of Highly Scattering Particles", 2019. (Manuscript submitted to *Langmuir*)

Manuscripts in Preparation:

- T. O'Neill, Z. Ruff, M. Zupkauskas, Y. Lan and E. Eiser, "Scaling Laws in the Structure of DNA-Mediated Mesoporous Colloidal Gels".
- T. O'Neill[1], A. Caciagli[1], M. Zupkauskas, D. E. P. Pinto, D. Joshi and E. Eiser, "Crystallisation and Phase Separation of Colloids at a Two-Dimensional Interface".

  [1] – these authors contributed equally.

1 Introduction: Colloids, DNA and Structural Colour

Colloids are broadly defined as particles with sizes between 1 nm and 10 μm dispersed in a continuous medium[1]; both particles and media can be solids, liquids or gases and still be considered a colloidal dispersion. Particle motion on these length-scales is typically dominated by thermal (stochastic) forces and not by gravity. Consequently, they do not sediment – this property is often used as an alternative definition[2]. Single colloidal particles are too large to be described well by atomic and molecular considerations and too small for bulk properties to dominate their behaviour; however, they frequently exhibit emergent phenomena due to this intermediate size. Colloids are ubiquitous in everyday life: they are present in the vast majority of foods and domestic formulations[3,4], as well as playing pivotal roles in everything from cellular biology to atmospheric chemistry. As such, a full understanding of colloidal behaviour and interactions is vital across academia and industry.

This chapter details the physics that underpins colloidal interactions, the structure and behaviour of DNA and the way grafting DNA to the surface of a colloid modifies typical colloidal behaviour. It establishes the state-of-the-art in colloidal self-assembly with a particular emphasis on how DNA and DNA-coated colloids can be used to synthesise novel micro- and nanostructures with emergent properties. Finally, it concludes with a discussion of structural colour, its physical origin and its occurrence in both natural and

synthetic self-assembled systems, giving context for the subsequent discussion of DNA-mediated self-assembly as a promising new route for the synthesis of biomimetic materials that exhibit structural colour.

1.1 Colloidal Interactions

1.1.1 Colloid-Medium Interactions

Colloidal suspensions are best described by statistical mechanics and are subject to thermal motion due to collisions with the molecules in the medium. Hence their spatial distribution can be described by a barometric height distribution of the form

$$n(h) = n_0 e^{\frac{-mgh}{k_B T}} \tag{1.1}$$

where $n(h)$ is the number density at height h of particles with mass m and n_0 is the number density at height 0. g is the gravitational acceleration, k_B is the Boltzmann constant and T is the temperature. For a suspension to be well-mixed and uniform, its barometric height must be larger than the size of the system. This is true when the thermal forces of the system are greater than the gravitational forces on the particles

$$k_B T \geq \Delta\rho V g h \tag{1.2}$$

where $\Delta\rho$ is the difference in density between the particles and the medium, V is the volume of a single particle and h is the height of the system[2,5]. From this, we can see that the cut-off above which a colloidal suspension will no longer be uniform will depend on the temperature, the density difference between the solvent and the particle material and the size of the latter.

The continuous collisions with the molecules of the medium cause the suspended colloids to exhibit stochastic Brownian motion in n dimensions according to

$$< \Delta x^2 > = 2nD\Delta t \tag{1.3}$$

where Δx is the particle's displacement at time Δt and D is the particles' diffusion constant[5]. For the systems considered here, spherical particles dispersed in a viscous medium, the diffusion constant is related to the particle radius R by the Stokes-Einstein equation[6,7]

$$D = \frac{k_B T}{6\pi\eta R} \tag{1.4}$$

where η is the dynamic viscosity of the medium. This result allows meaningful analysis of data about how a particle is diffusing in a medium[8]; if the viscosity and temperature of the medium are known then the particle size can be determined[9] (for example in Dynamic Light Scattering), if the particle size is known then information about the visco-elastic properties of the medium can be determined[10] (for example in micro-rheology).

1.1.1 Colloid-Colloid Interactions

For denser suspensions, the interactions between colloids become increasingly important to the behaviour and stability of the system. As colloids behave as a pseudo-atomic system, the interactions between them define the phase diagram and can lead to crystalline, glassy, liquid or gaseous colloidal states.

At very short separations, colloidal interactions are exclusively repulsive due to hard-sphere repulsion[2], modelled as

$$V_{hard}(r) = \begin{cases} \infty & r < 2R \\ 0 & r \geq 2R \end{cases} \tag{1.5}$$

where r is the centre-to-centre separation of two particles of radius R. Intuitively, this is because two solid objects cannot occupy the same volume and arises physically from the Pauli Exclusion Principle. It has been shown that in the absence of any attractive forces, hard spheres will still crystallise due to entropic effects at high volume fractions[11].

Systems exhibiting purely hard-sphere interactions are rare for colloidal dispersions, however, due to the difficulty in suppressing other forces, most notably van der Waals or London dispersion interactions[2,12]. These arise quantum-mechanically from fluctuations in the dipole moments of atoms and molecules; classically, if one molecule develops an instantaneous dipole due to the random shifts in its electron cloud, that dipole can then induce and interact with dipoles on nearby molecules. As such, all atoms and molecules experience attractive van der Waals forces with those around them.

While van der Waals forces are long-range, they only exceed thermal forces over length-scales shorter than a few nanometres. Pairwise interactions have the form

$$v(r) = -Cr^{-6} \tag{1.6}$$

where C is the interatomic pair-potential coefficient and depends on the polarisabilities of the atoms or molecules constituting the particles[12]. To calculate the attractive force between two larger particles, some approximations are usually made, namely that molecular dipoles do not interact, dispersion interactions are pair-wise additive and they

are not subject to retardation effects. This expression can then be integrated over the volumes of the relevant particles to obtain a total potential. For like spheres, this potential is

$$V_{disp}(r) = -\frac{A}{6}\left(\frac{2R^2}{r^2-4R^2} - \frac{2R^2}{r^2} + ln\left(\frac{r^2-4R^2}{r^2}\right)\right) \quad (1.7)$$

where A is the Hamaker constant, which depends on the polarisabilities of the particles and the medium, and r is now the separation between particle surfaces[12,13]. Finally, the Derjaguin approximation can be applied, in which the particle radii are far larger than both their closest approach distance, r, and the distance over which the interaction decays. This simplifies the interaction potential to

$$V(r) = -\frac{A}{12}\frac{R}{r} \quad (1.8)$$

It is interesting to note that while pairwise van der Waals forces are always attractive, the overall interaction will become effectively repulsive if the refractive index of the medium lies between the refractive indices of two particles of different materials, as the colloids are more strongly attracted to the solvent than to each other[13,14].

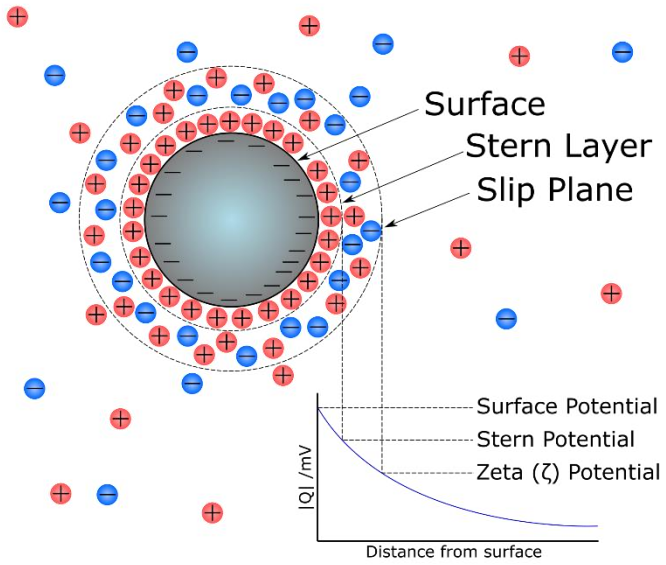

Figure 1.1: Ion coordination around a charged particle.

As a consequence of the attractive nature of van der Waals interactions, colloidal suspensions are normally inherently unstable and will aggregate in the absence of additional, repulsive terms in the inter-colloid potential, leading to large clusters of particles in hard contact that sediment out of suspension[2,13-15]. One such stabilising

mechanism is electrostatic repulsion; if dispersed in a polar medium most colloids will develop a surface charge due to either dissociation of functional groups at the surface or preferential adsorption of ions from solution. Basic Coulomb theory states that like colloids with a total charge Q per particle in a medium with dielectric constant ε will experience a repulsive force given by

$$v(r) = \frac{Q^2}{4\pi\varepsilon r} \tag{1.9}$$

However, in a solution of electrolyte, ions will be attracted to the charged colloids and screen the electrostatic potential. Close to the surface, co-ions will form a tightly bound Stern layer, while further from the surface both positive and negative ions form a loosely bound diffuse layer[16-18], as shown in Figure 1.1. The thickness of this diffuse layer is also known as the Debye screening length. The electrostatic potential decays exponentially with distance from the surface and both Stern and diffuse layers are carried with the particle as it moves. The slip plane is the plane at which solvent and ions are no longer carried with the particle as it diffuses; the radius at the slip plane is the hydrodynamic radius, and the potential at this radius is the zeta (ζ) potential[17]. The electrostatic potential between colloids in solution then becomes

$$V_{elec}(r) = \left(\frac{Qe^{\kappa R}}{1+\kappa R}\right)^2 \frac{e^{-\kappa R}}{4\pi\varepsilon r} \tag{1.10}$$

where κ is the decay constant. In the limit of small potentials, also known as the Debye-Hückel approximation, this is given by

$$\lambda_D = \frac{1}{\kappa} = \sqrt{\frac{\varepsilon k_B T}{\sum_i p_i q_i^2}} \tag{1.11}$$

where λ_D is the Debye screening length and p_i and q_i are the concentration and charge of ionic species i, respectively[15,19]. From this we can see that the electrostatic repulsion between colloids can be tuned by varying the ionic strength of the solution.

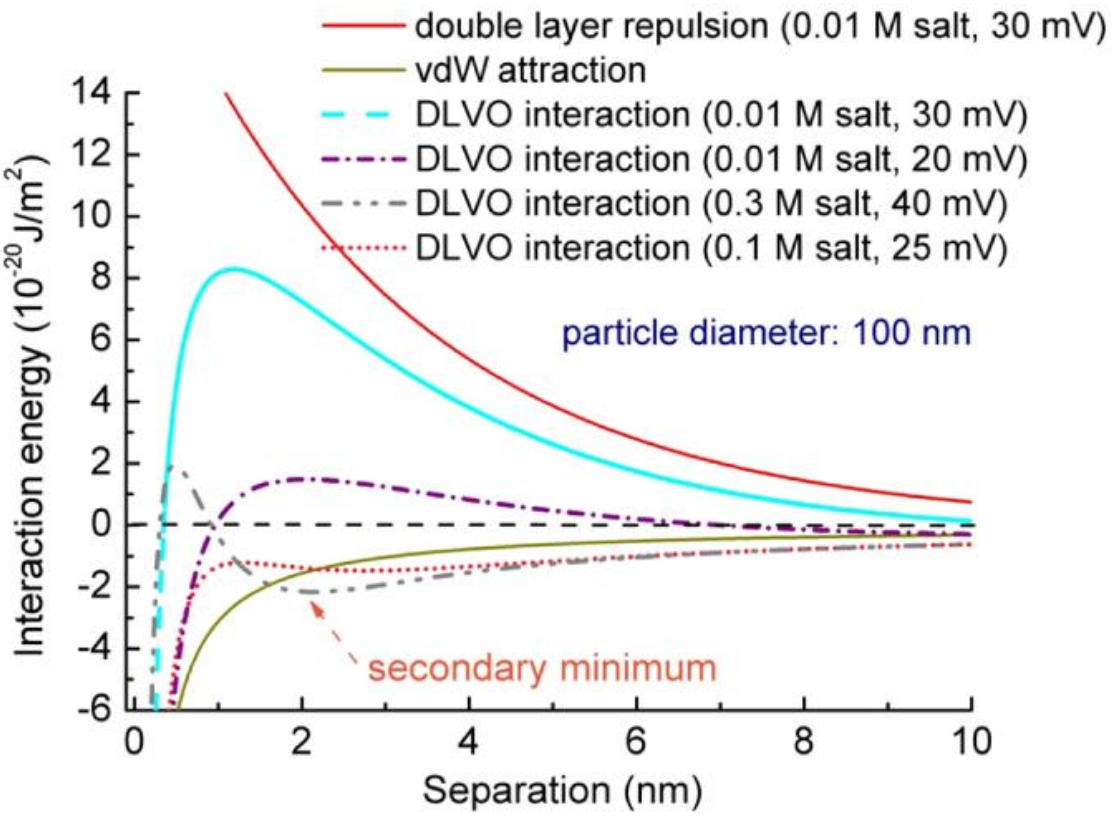

Figure 1.2: DLVO potentials at different ionic strengths. Taken from [19].

DLVO theory, so named because it was developed independently by Derjaguin & Landau[16] et al. and Verwey & Overbeek[18] et al., combines these two potentials to give a relatively complete description of inter-particle interactions in colloidal suspensions[16,18]

$$V_{DLVO}(r) = \left(\frac{Qe^{\kappa R}}{1+\kappa R}\right)^2 \frac{e^{-\kappa R}}{4\pi\varepsilon r} - \frac{A}{6}\left(\frac{2R^2}{r^2-4R^2} + \frac{2R^2}{r^2} + ln\frac{r^2-4R^2}{r^2}\right) \qquad (1.12)$$

The precise form of this potential depends on the concentration of ions in solution, as sketched in Figure 1.2, but has several consistent characteristics. At very short separations and moderate ionic strengths, the potential is dominated by dispersion forces and exhibits a primary minimum that corresponds to hard contact and irreversible aggregation. At low salt concentrations, there is an energy barrier at moderate separations arising from electrostatic repulsion. As the salt concentration increases, the height of this barrier decreases due to the reduced Debye screening length and a secondary minimum appears, sometimes known as the flocculation minimum (although this term is also applied to irreversible aggregation). Particles will often loosely associate in this energy well but can be resuspended easily through agitation or heating[20]. Finally, at larger salt concentrations,

the electrostatic repulsion is effectively screened by the dispersion medium and the energy barrier disappears entirely, resulting in spontaneous aggregation.

Steric stabilisation is an alternative method to stabilise colloidal suspensions that does not require the use of charged particles. If polymers are grafted to the colloids in good solvent conditions, such that they form a stretched brush, then they will generate an additional repulsive force when the colloids are close enough that the polymers start to interact. The origin of this force is the loss of entropy experienced by the polymer chains at short separations[2,21]. As the polymer brushes start to overlap, the local concentration of polymer in the overlap volume increases and so the number of available polymer conformations goes down. This potential can be described by de Gennes scaling theory[21], and has the form

$$V_{steric}(r) = \begin{cases} \sigma^{\frac{3}{2}}\left(\left\{\frac{2R_g}{r}\right\}^{\frac{9}{4}} - \left\{\frac{r}{2R_g}\right\}^{\frac{3}{4}}\right) & r < 2R_g \\ 0 & r \geq 2R_g \end{cases} \qquad (1.13)$$

where σ is the grafting density and R_g is the radius of gyration of the polymer. The first term is entropic in origin as described above, while the second term corresponds to the elastic energy stored in the compressed polymer chains.

There are several requirements for such stabilisation to be effective. First, the polymers must be non-interacting, otherwise they may have the opposite effect and tether colloids together. Second, they must be long enough that their radius of gyration, R_g, is sufficiently large that the repulsive steric forces are larger than the attractive dispersion forces when the grafted polymers begin to overlap. Finally, the polymer chains must be well solvated by the dispersion medium. The requirement for this is that polymer-solvent interactions are energetically preferable to polymer-polymer interactions, more commonly referred to as good solvent conditions. If this condition is not met, polymers will not form a random coil, but instead collapse on to the surface of the colloids and hence will not contribute any stabilising term.

Additionally, if the polymers are not grafted to the surface but are instead free in solution, they can introduce attractive depletion forces between particles instead. Depletion forces may be generated whenever there are macromolecular species dissolved in the dispersion medium. These species are often polymers or other, smaller colloids.

The origin of these forces is entropic: Figure 1.3 shows a suspension of colloids (red) with excluded volumes (light red). As two particles come closer together, their excluded volumes overlap, preventing smaller species (green) from accessing the space between colloids. This sets up an osmotic potential that draws the solvent out from the overlap region and hence pulls the colloids together. Equivalently, once the colloids have aggregated, the smaller species have a larger total volume to explore and correspondingly higher entropy[22]. This entropy gain is large enough to offset the loss of entropy on aggregation of the larger colloids.

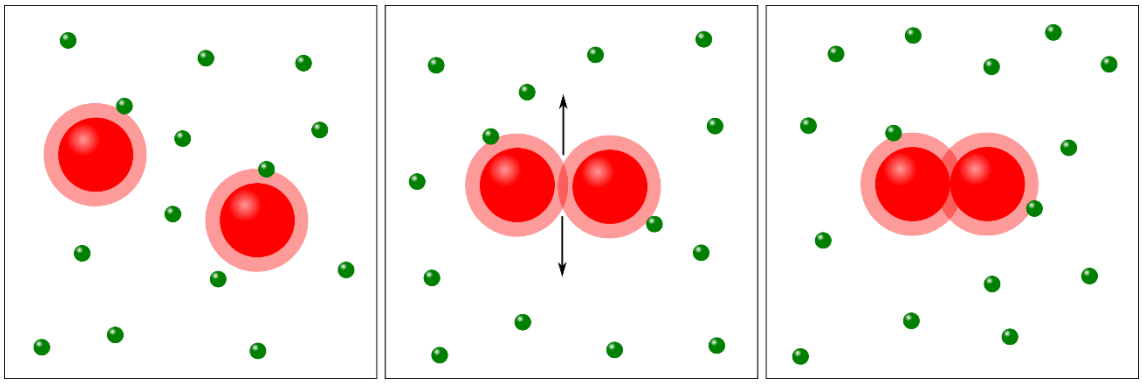

Figure 1.3: Depletion forces between colloids. Colloids (red) exclude a volume of a similar size to the depletant (green). When these excluded volumes overlap, depletant cannot enter. Osmotic pressure drives solvent from the inter-particle volume, leading to aggregation.

1.2 DNA Functionalised Colloids

Colloidal particles are often functionalised in various ways to stabilise colloidal suspensions or to introduce new behaviours[23-30]. Surface functionalisation of colloids with DNA has several advantages when designing self-assembling systems. First, DNA is a negatively charged polymer, so surface grafted DNA both electrostatically and sterically stabilises a colloidal suspension against aggregation. Second, the use of DNA allows for the exploitation of the highly sequence specific Watson-Crick base pairing; colloids coated with complementary DNA strands will have an additional strong short-range attraction to each other due to the hybridisation of the DNA into a double helix[31,32].

1.2.1 Structure of DNA

DNA is best known for its role as the material that stores genetic information in living things, however, it can also be very useful as a structural material for self-assembly due to its complex and well-defined secondary structure. DNA is a biological polymer comprised of a sugar-phosphate backbone and functional side groups called nucleotide bases, which can hydrogen bond to one another[33]. The ribose-phosphate backbone is directional, with the terminal phosphate group termed the 5' end and the terminal ribose hydroxyl group termed the 3' end. The four bases of DNA are adenine, cytosine, guanine and thymine (A, C, G and T), and they form stable pairs of cytosine-guanine and adenine-thymine via hydrogen bonds provided the DNA backbones are antiparallel, as shown in Figure 1.4. Other pairings are possible but are less energetically favourable due to disruption to the overall helical structure[34].

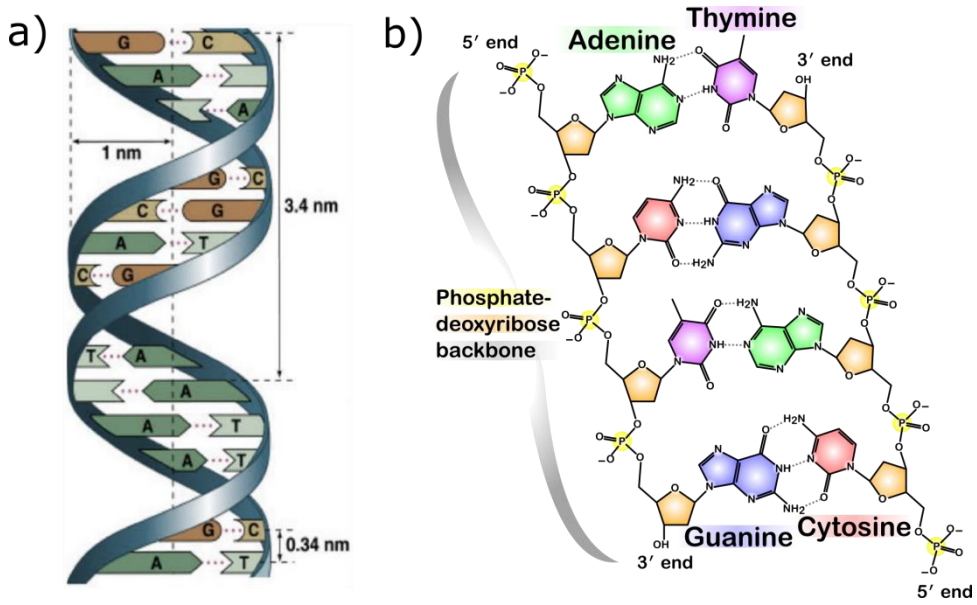

Figure 1.4: The Structure of DNA. a) The DNA double helix. Taken from [36]. b) Chemical structure of the backbone and nucleotide bases of DNA, highlighting hydrogen bonding. Taken from [37].

This interaction between bases gives double-stranded DNA (dsDNA) its unique secondary structure. While single-stranded DNA (ssDNA) adopts a typical random coil configuration in water with a persistence length of ~1 nm[38], two pieces of ssDNA with complementary sequences can form a complete hydrogen bond network by adopting a double helical configuration in a process called DNA hybridisation[33]. This interaction is further strengthened by the stacking energy between neighbouring base pairs. The hydrophilic sugar-phosphate backbone is at the exterior of the twisted dsDNA strand and

each phosphate group can dissociate depending on pH, giving DNA its negative charge. Consequently, the secondary structure is much more rigid than the free strands, resulting in a persistence length varying between 35 nm and 50 nm, depending on the ionic strength of the solution[35]. DNA strands are termed complementary if, when the backbones are antiparallel, each base aligns with its corresponding partner on the other strand, as noted above.

DNA hybridisation is a thermally reversible process; each base pair contributes 1-3k_BT to the free energy of hybridisation[39,40], so even short strands will be bound at room temperature while longer strands can easily have binding strengths comparable to covalent bonds, which can be upwards of 100 k_BT in strength. To an excellent approximation, the binding energies of DNA strands can be predicted using the SantaLucia rules[40]. DNA binding is mediated by both the formation of hydrogen bonds between opposite bases and π-π stacking interactions between adjacent base pairs. The SantaLucia model calculates binding energies from tabulated values of enthalpy and entropy of binding for all ten possible base pair nearest neighbours, plus an initiation contribution from the first base pair that lacks the π-π term but contains information about all other sequence-independent effects. While partial hybridisation is possible without exactly complementary sequences, the resulting structure is considerably less stable due to additional strain exerted on the sugar-phosphate backbone[34]. The sticky ends used in this work are typically 7-10 base pairs in length, resulting in strands that are bound at room temperature but can be melted by heating to moderate temperatures without destroying the DNA[2].

The melt temperature of DNA is defined as the temperature at which half of the possible base pairs are bound. It depends on the binding free energy, ΔG°, according to[40]

$$T_m = \frac{\Delta H°}{\Delta S° + Rln([DNA])} = \frac{\Delta G°}{Rln([DNA])} \qquad (1.14)$$

where R is the gas constant and [DNA] is the concentration of DNA. Despite the high cooperativity of DNA, the melt region of free DNA in solution can be as broad as 20 °C. However, if DNA is grafted to the surface of colloids, there are many strands in the binding region, shifting T_m to higher temperatures and making the melt transition much sharper, as shown in Figure 1.6. T_m also depends on the ionic strength. At very low ionic strengths, hybridisation becomes impossible, as the strong Coulomb repulsion between

the ssDNA backbones prevents proper hydrogen bonding and π-stacking. DNA is typically employed in ionic strengths of between 50 mM and 500 mM NaCl.

This dependence of the melt temperature of a strand on the precise sequence of bases present, the overall concentration of DNA and the ionic strength of the medium[41-43] is what makes DNA such an attractive material for self-assembly, alongside its thermal reversibility and specificity[44].

1.2.2 DNA-Coated Colloids

When DNA (or any polymer) is end-grafted to a surface, it limits the volume accessible by the polymer. The conformational space accessible is then determined by the grafting density. At low grafting densities, the polymer is in the "mushroom" regime – effectively adopting a random coil at the surface – while at high grafting densities, neighbouring chains begin to repel one another both sterically and electrostatically and extend out from the surface in the "brush" regime[21], as shown in Figure 1.5.

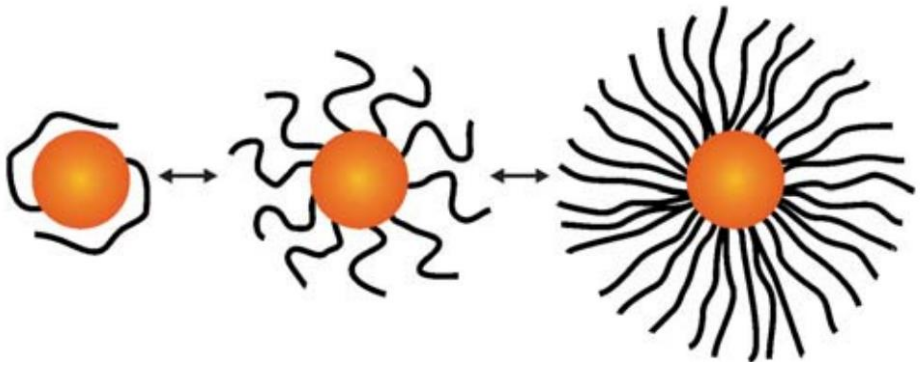

Figure 1.5: Configuration of polymers grafted to a spherical particle at different grafting densities. On the left, polymers adopt a random coil in the mushroom regime; on the right, polymers are stretched out linearly in the brush regime. Taken from [44].

DNA on particles also exhibits slightly different hybridisation characteristics to free strands. These largely arise from the fact that when DNA-coated colloids (DNACCs) are in close contact, many strands may hybridise simultaneously because they are held in the same binding volume, thus incurring an additional statistical term in the binding dynamics. The probability that a single strand of dsDNA is unbound at temperature T is[45]

$$P(T) = \left(1 + e^{\frac{\Delta G°(T)}{k_B T}}\right)^{-1} \qquad (1.15)$$

where $\Delta G°(T)$ is the free energy change of hybridisation. For DNA on particles, if N strands are in the inter-particle volume and close enough to bind, this becomes

$$P_N(T) = \left(1 + e^{\frac{\Delta G°(T)}{k_B T}}\right)^{-N} \quad (1.16)$$

under the assumption of distinct binding pairs. From this expression it is clear that as N increases, the melt transition of the DNA-coated colloids becomes sharper, as shown in Figure 1.6a, and that T_m increases logarithmically. In addition, for longer DNA strands and a correspondingly higher $\Delta G(T)$, T_m increases linearly, as shown in Figure 1.6b. Absorbance at 260 nm is frequently used to measure DNA hybridisation as ssDNA absorbs ~35% more strongly than dsDNA at this wavelength[46], when normalised against absorbance at 280 nm.

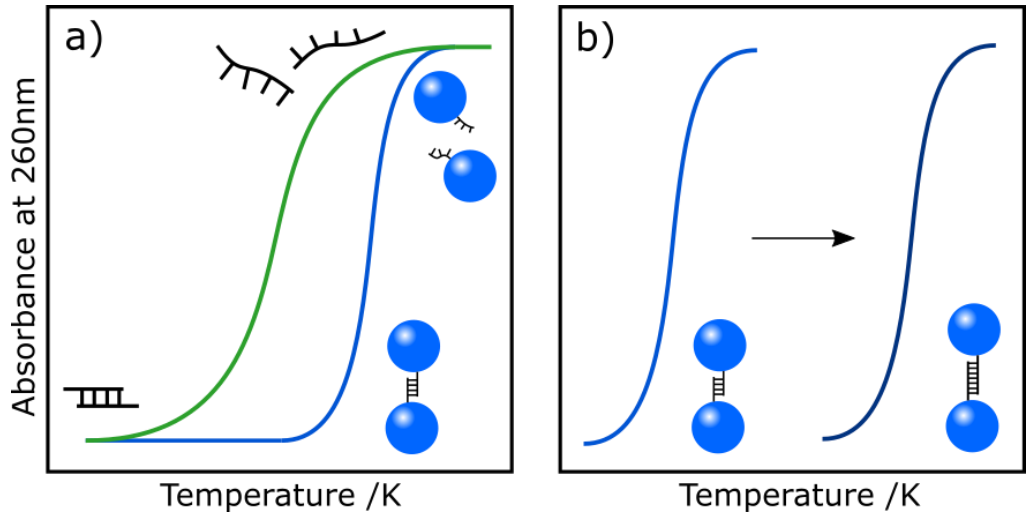

Figure 1.6: Schematic DNA melt curves. a) Comparison of free and grafted DNA. b) Melt temperature change with DNA length.

Experimental DNA sequences used to bind colloids together will often be less than ten base pairs, or 3.4 nm, long, which is too short to allow the ssDNA to explore a large enough volume to achieve effective inter-colloid binding[45,47]. To solve this, the short DNA "sticky end", the sequence intended to hybridise with the complementary strand, is connected to the surface via a long spacer. The polymeric spacer can be an alkyl chain, an inert (non-complementary) ssDNA strand or a more rigid sequence of dsDNA. These three different scenarios are visualised in Figure 1.7.

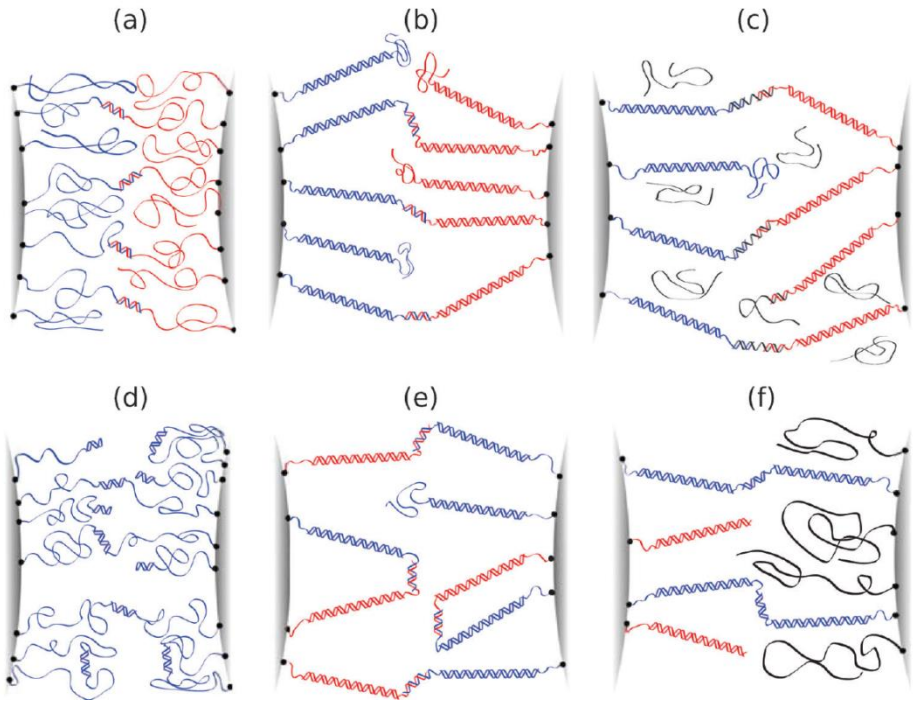

Figure 1.7: Common DNA grafting morphologies. a) and d) show an inert ssDNA spacer, b), c), e) and f) show a more rigid dsDNA spacer. Taken from [48].

The models above assume a system of two species of particles, each coated exclusively with DNA complementary to the other. In reality other systems are often employed for simplicity or tuneability[48]. Common grafting morphologies are shown in Figure 1.7: a) and b) both show the case described above of two distinct colloids coated with complementary DNA; c) demonstrates how binding can be mediated by a linker ssDNA strand in solution that is complementary to both grafted strands. d) shows colloids coated with palindromic DNA sequences (palindromic DNA is self-complementary, not necessarily reversible), while e) shows all colloids coated with both strands. In both cases, intra-colloidal binding will compete with inter-colloidal binding, though this will be less significant for e) due to the use of more rigid dsDNA spacers. f) shows the use of inert dsDNA or other polymers to reduce DNA grafting density, which avoids the unpredictability and quench-dependence of using intra-colloid binding to reduce effective grafting density.

Grafting ssDNA to colloidal particles changes both the behaviour of the particles and the DNA. DNA-coated colloids are electrostatically and sterically stabilised against free aggregation, but will also experience a strong, short-range attraction to particles or surfaces coated with complementary DNA[45,48]. The specificity of this attractive force nominally allows for the design of arbitrarily complex systems with any number of

distinct attractive potentials, allowing control of all nearest-neighbour interactions[49-51], but is practically subject to some limitations[52].

Ideally, each specific interaction to be introduced would have its own unique sequence of dsDNA, however, there are a finite number of valid sequences, as if a strand becomes too long, its melt temperature becomes too high to be workable. In addition, some sequences should be avoided due to their tendency to misfold into other secondary structures, for example GGGG sequences can form G-quadruplexes[53]. Even in the simple case of the assembly of like spheres, particles can have up to twelve nearest neighbours, requiring twelve distinct grafted ssDNA sequences, which might lead to the grafting density of any particular strand being too low to yield a successful binding interaction. Nevertheless, DNA-coated colloids remain one of the most robust and versatile systems for the self-assembly of microstructures, due to the strength, thermal reversibility, specificity, stability and tuneability of the DNA hybridisation interaction.

1.3 Self-Assembly

Self-assembly is a powerful bottom-up technique for creating materials with novel micro-structures on length-scales that conventional top-down approaches cannot achieve[54-60]. The underlying principle of self-assembly is the design of building blocks, which can be molecular or macromolecular species, such that they arrange themselves spontaneously in a well-defined and reproducible manner. This assembly is driven by the underlying molecular interactions, for example the hydrophobic-hydrophilic interaction in surfactants, and external conditions such as temperature.

All biological systems can be considered to be self-assembled, from individual molecules such as lipid membranes, proteins and DNA to cells and tissues. While synthetic self-assembly methods are normally vastly inferior to naturally observed ones both in scale and complexity, mimicry of how natural materials are formed can often produce novel and interesting structures[55].

1.3.1 DNA-Mediated Self-Assembly

The concept of using DNA to control self-assembly was first introduced in 1982 with the design of DNA junctions that could bind to one another to create lattices[61], a precursor to modern DNA origami techniques. It has since been extensively shown experimentally and theoretically that with careful enough control of DNA sequences, one or more DNA strands can be designed that will fold into any two- or three-dimensional structure[62].

While this level of control is nominally the gold standard for self-assembly, DNA origami does suffer from the high financial and time costs of synthesising long specific DNA sequences, as well as long annealing times for larger systems. Alternative methods have had great success employing shorter DNA sequences that can be produced in large volumes using polymerase chain reaction[63] (PCR) to form smaller DNA building blocks or to functionalise other particles such as colloids.

The use of DNA to mediate colloidal assembly was first reported by two groups in 1996 in the same issue of Nature, where Mirkin[31] and Alivisatos[32] described a process utilising the well understood reaction of thiols with gold to attach short DNA sequences to the surface of gold nanoparticles. They each demonstrated thermally reversible aggregation of DNA-coated nanoparticles into amorphous aggregates and small clusters.

Several groups subsequently built upon these works, developing new surface functionalisation techniques and exploring the phase behaviour of DNA-coated nanoparticles and colloids[64-70] (DNACCs). Depending on the properties of the DNACCs and the temperature during aggregation, it was found that DNACCs can form amorphous aggregates, colloidal crystals or intermediate phases with short-range order such as spinodal gels, as shown in Figure 1.8.

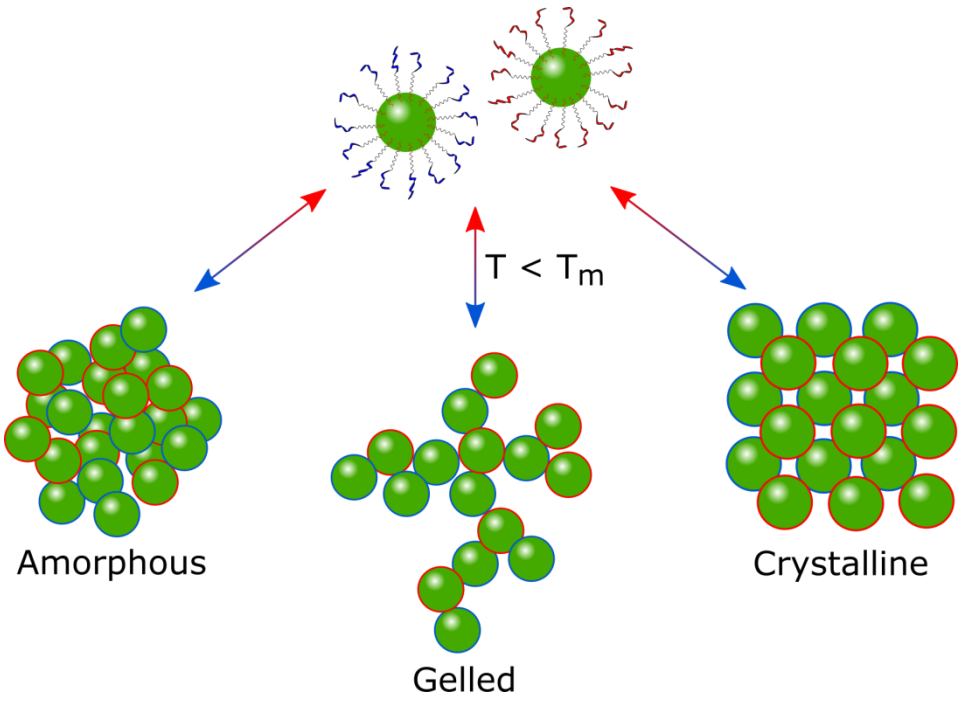

Figure 1.8: Different morphologies adopted by complementary DNA-coated colloids on assembly.

Much of this initial interest was driven by the desire to synthesise novel photonic crystals[66,69]; while the crystallisation of colloids is not particularly difficult, it has been shown that spherical colloids aggregating purely under DLVO-type forces exclusively form face-centred cubic (FCC) and body-centred cubic (BCC) crystals of limited photonic activity[66]. It was theorised, and then later shown computationally, that DNACCs could assemble into far more diverse crystal structures, such as square or diamond lattices[71]. However, crystalline phases of DNACCs proved difficult to realise experimentally because of the narrow DNA melt region; BCC +and FCC crystals of nanoparticles were only reported in 2008[66,69]. This is attributed to the kinetics of such systems: because the DNA binding is strong and the phase transition is sharp, particles are unable to rearrange once bound. It is therefore very easy for the system to become trapped in metastable free energy minima that dramatically slow down equilibration, preventing it from ever reaching the thermodynamically favourable crystalline state[45,64]. Several methods have been attempted to overcome this, for example by reducing the interaction strength by binding inert polymers to the surface, as in Figure 1.7f, but success in DNA-mediated crystallisation has still been largely limited to DNA-coated nanoparticles, as they bind with fewer strands of dsDNA, meaning the DNA hybridisation interaction is both weaker and less sharp[72]. They are also more mobile than larger particles, allowing them to rearrange to find the global thermodynamic minimum.

Synthesis of colloidal crystals of micron-sized DNACCs has proven far harder to realise experimentally, due to this difficulty in annealing the system after aggregation starts, and hence most reported assemblies of such colloids are non-crystalline. Two notable exceptions to this are Crocker et al.[73] and Pine et al.[72]. In 2005, Crocker et al.[73] demonstrated the self-assembly of micron-sized polystyrene spheres that had been allowed to sediment to the bottom of a sample chamber into plate-like crystals. They estimated that even in this quasi-two-dimensional environment, conditions are only appropriate for crystal formation over temperature ranges of 0.5 °C around the melt temperature. More recently, Pine et al.[72,74] showed that with sufficiently high DNA grafting densities, particles can roll over each other if the system is only a little below the melt temperature and so rearrange even while remaining strongly bound. This prevents the full kinetic arrest of the suspension and allows it to anneal toward the thermodynamic minimum. Unfortunately, despite these improvements, all but the simplest crystal lattices remain elusive.

However, interest has more recently turned toward the amorphous and gelled phases that were previously discarded as unwanted by-products. Such structures are interesting for a variety of applications and have the advantage over colloidal crystals that they form much more rapidly once the attraction is switched on[57,75-77].

A schematic phase diagram for a suspension of DNA-coated colloids is shown in Figure 1.9. The binodal line (solid black) is an equilibrium phase boundary that separates the gas and two-phase regions and gives the equilibrium compositions for a given temperature. The spinodal line (dashed black) does not represent an equilibrium phase, but instead denotes the point at which the homogenous suspension becomes unstable and the system will phase separate spontaneously via a spinodal decomposition mechanism[57,80,81], in which any instantaneous density fluctuations propagate through the system driven by the attractive force between colloids.

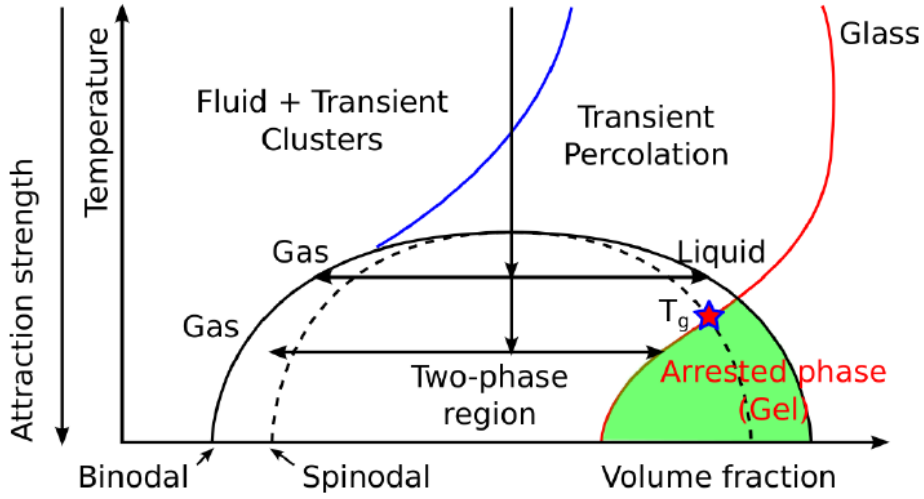

Figure 1.9: Phase diagram of a suspension of attractive colloids. Taken from [78].

Behaviour in the gas phase is dominated by volume fraction; at low volume fractions, colloids are broadly isolated but will associate in short-lived clusters. Above a certain threshold (blue line), there will be sufficient clusters to begin to percolate the full volume; these transient percolating clusters become longer lived at higher volume fractions, until eventually the system can be described as arrested (red line). The percolation and dynamic arrest lines are kinetic transitions. As such, their position is not fixed but is instead defined by the length of time it takes for a colloid to diffuse a fixed distance from its original position, normally one colloid diameter. As the interaction strength tends to zero, the dynamic arrest line tends to volume fractions of 0.64 (for spheres) and the arrested phase becomes a glass.

When a suspension is quenched into the two-phase region, it will phase separate into a colloid-sparse gas phase and a colloid-rich aggregate phase. If the final quench temperature T is above the gel point, where the arrest line meets the spinodal line, here denoted T_g, then the phase separation will go to completion, with compositions given by the binodal line. However, if $T < T_g$ then demixing becomes arbitrarily slow when the composition of the colloid-rich phase meets the dynamic arrest line; this prevents the system from achieving equilibrium compositions over experimental timescales and instead results in a gel with no long-range order. A gel is defined as a space-spanning network of material that does not flow and is able to support a mechanical stress[78,80]. In the context of the above discussion, colloidal crystal formation can occur either when quenching is slow enough that the system spends a significant time in the region between the binodal and spinodal lines or when small enough particles are used that the dynamic arrest line is shifted to higher volume fractions and so extends less far into the two-phase region.

Our group has previously demonstrated the use of micron-sized DNA-coated polystyrene colloids to form macroscopic percolating colloidal gels that have a well-defined structure reproducible over many melt-quench cycles[45,57,77]. Precise control over the morphology of these structures can be achieved by varying the parameters of the initial colloidal suspension and the conditions of the quench, but further modifications post-aggregation are difficult to realise for the reasons discussed above. However, by exploiting the specificity of DNA, more complex morphologies can be accessed through the introduction of multiple independent attractive potentials with different phase transition temperatures.

Varrato et al.[57] explored the behaviour of a system of two distinct colloids, G (green) and R (red), coated with DNA in such a way that intra-species interactions (G-G and R-R) were attractive, but inter-species (G-R) remained repulsive, see Figure 1.10. The DNA sequences for G and R were chosen to have nearly identical melt temperatures. In addition, because the DNA grafting density was not high enough to reliably prevent non-specific aggregation, short inert PEG chains were also grafted to the colloid surfaces to sterically stabilise the suspension, as discussed generally in Figure 1.7f. It was shown that when a suspension of both species of colloids was quenched into the two-phase region, the colloidal species segregated into two distinct, interpenetrating gel networks each spanning the entire sample volume, termed a bigel.

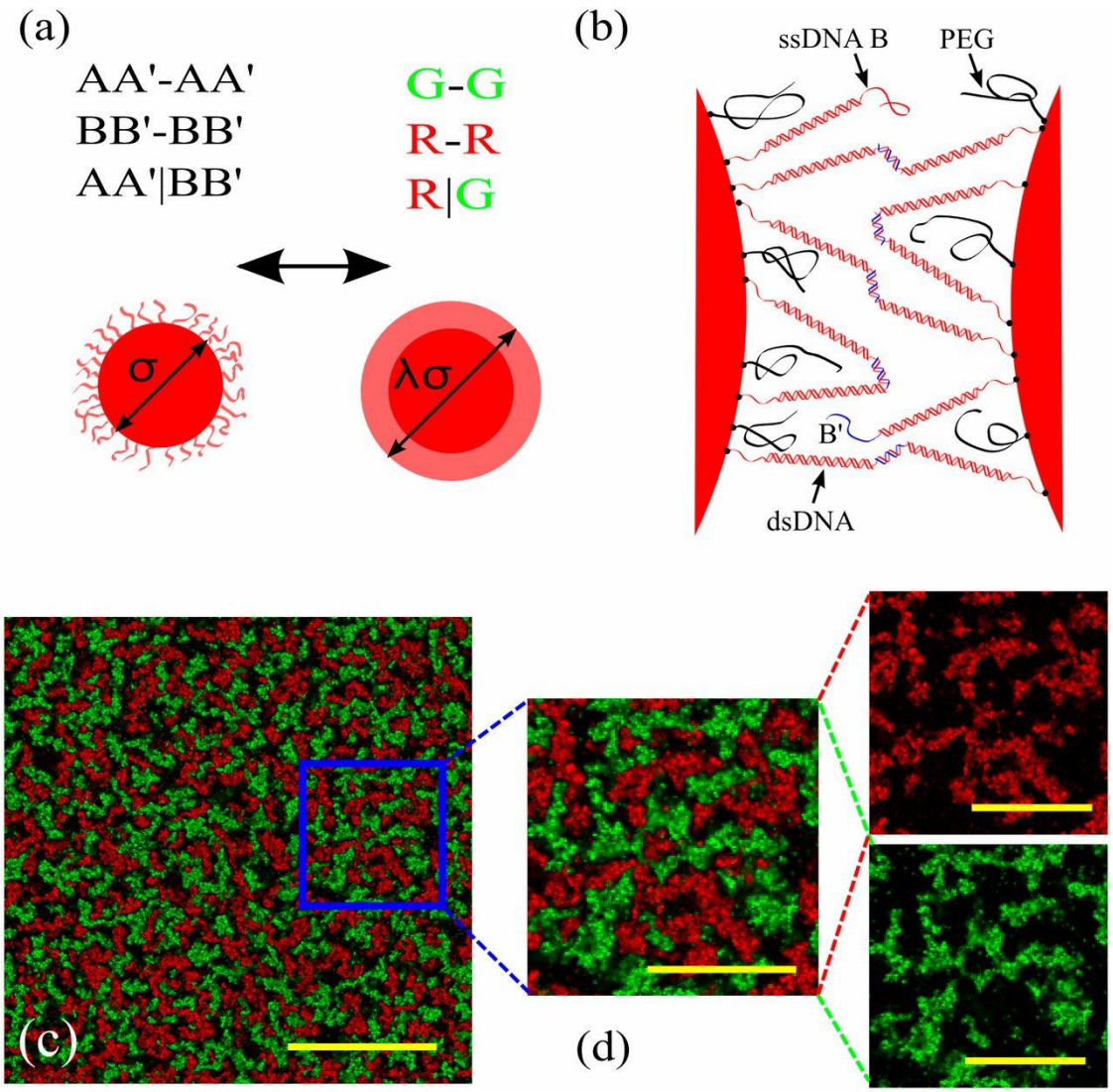

Figure 1.10: Structure and characterisation of bigels. a) Description of colloid-colloid interactions. b) Cartoon of colloid binding. c) Confocal micrograph of a bigel. Scale bar is 50 µm. d) Zoomed section of c), separating colloid species. Scale bar is 25 µm. Taken from [57].

Bigels are harder and have a higher yield stress than their single-component equivalents, due to the greater tendency of single gels to collapse under an imposed strain[79]. Bigels also show promise as scaffolds for high surface area junctions[81], for example in solar cells, in an analogous way to the double gyroid structures achieved by the self-assembly of block copolymers[82]. The phase space of bigel formation has since been well explored away from the ideal case of equal melt temperatures and symmetrical volume fractions[79]. It was found that except at very high volume fractions, gel morphology for each bigel component is independent of the concentration of the other component. The percolation threshold, the volume fraction, φ, above which a gel will span the full three-dimensional

volume of the sample, was similarly shown to be independent, and was estimated by simulation to be φ = 5-10% by volume.

Other protocols on the assembly of DNACCs have been reported in the literature, including the synthesis of core-shell gels[83] and the imposition of external fields during quenching. However, perhaps greatest control over the structure of the gel arises from the choice of particles used, which has led to great interest in the design of novel colloidal units.

1.3.2 Patchy Particles

The properties of a self-assembled phase depend strongly on the size, shape and functionality of the particles used to create it; in particular, the design of "patchy" particles, in which the spherical symmetry of colloids synthesised using standard recipes is broken by the introduction of specific binding sites, has been shown both theoretically and experimentally to lead to novel structures[23-26,84-87].

Success has been demonstrated by a number of groups in introducing surface anisotropy by trapping colloids at an interface and then activating specific surface regions. Granick et al.[84] trapped colloids at a planar oil-water interface and then functionalised only the colloidal surface in the aqueous phase, while Sacanna et al.[87] used emulsion droplets to assemble clusters of well-defined valency that they then fused in a continuous matrix. Both approaches led to spherical colloids retaining near-isotropic interactions but with differential surface functionality. More common is the use of shape anisotropy to induce specific binding; Kraft et al.[23] used divalent or trivalent particles with differential roughness to assemble colloidal micelles; the smoother region of the colloid has a larger excluded volume, and so is subject to greater depletion forces than the rough side. Sacanna et al. have shown the synthesis of dimpled spherical and aspherical particles via the seeding of an oil-based polymer[25,86,87]. The dimples on these particles act as preferential binding sites for other colloids aggregating under DLVO-type forces due to the increased dispersion interaction strength when colloids bind to the concave cavities.

However, while all these methods show the successful introduction of discrete binding sites to a mesoscopic object, they are not able to create distinct selective binding sites on an individual building block. The specificity of DNA has been proposed as a potential solution to this problem. Grünwald and Geissler[88] computationally demonstrated the synthesis of colloidal "metaparticles", well-defined clusters of colloids formed through DNA-mediated attraction to a central "glue particle", as shown in Figure 1.11a.

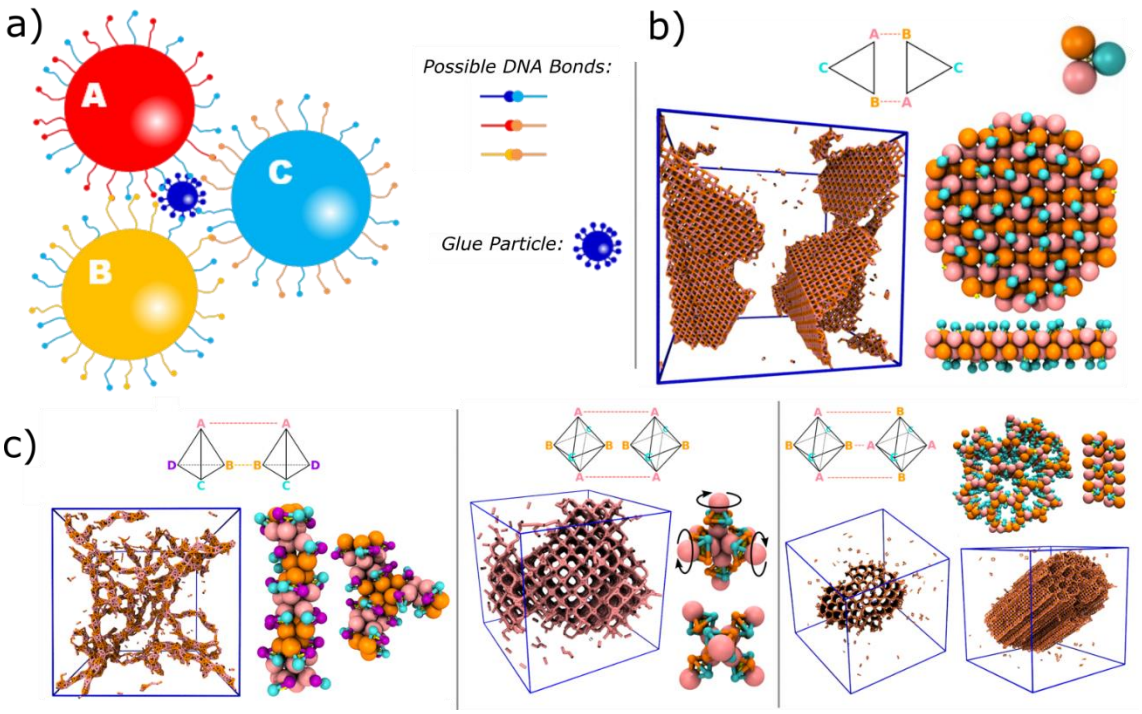

Figure 1.11: Hierarchical self-assembly of DNA-coated colloids into metaparticles and then superstructures. a) Cartoon showing attractive DNA interactions in a trivalent metaparticle. Image courtesy of Erika Eiser. b) Simulation snapshot of self-assembly of the same trivalent metaparticles, showing the binding rules. c) Simulation snapshots of the phases formed by higher-order metaparticles under specific binding rules. Modified from [88].

Metaparticles were assembled from a set of distinct corona particles (coloured) and a smaller "glue" particle (dark blue). DNA interactions were chosen such that all corona particles had a strong attraction to the glue particle, weak attractions to corona particles of a different type and repulsive interactions with corona particles of the same type. The valency of the resulting metaparticles was selected through the size ratio of corona and glue particles.

Once these metaparticles had formed, further assembly was initiated by the introduction of new strong attractive interactions between specific corona particles. Example binding rules are shown schematically in Figure 1.11b&c. An experimental equivalent to introduce these new interactions would be the introduction of bivalent linker DNA strands corresponding to the desired corona pairing. Depending on the binding rules chosen, these metaparticles were shown to assemble into a wide range of one-, two- or three-dimensional structures.

As a part of this PhD thesis, we attempted to recreate the computational results described in [88] in an experimental system but had little success. It was ultimately deemed that our control over the DNA interaction strength was too crude, both in terms of ssDNA sequence design and experimental temperature control, and the experiment was ultimately abandoned.

1.4 Structural Colour

Structural colour arises when a material preferentially scatters or reflects specific wavelengths of visible light due to the physical arrangement of the material on the nanoscale, in contrast to the more common mechanism of colour production, in which a chromophore differentially absorbs wavelengths of visible light. Hence structural colour is an emergent property: materials that would not be coloured on the molecular level or in the bulk can still give rise to structural colour if assembled in an appropriate way. A crucial difference between colour generated due to absorbing molecules (chromophores) and due to the specific interaction of light with a material with periodic refractive index variation is the brilliance of the observed colours. Chromophores typically absorb in a broad band, while structural materials scatter in very narrow wavelength regions, giving rise to much "purer" colours. Additionally, as the interaction is primarily electromagnetic instead of electronic, structurally coloured materials do not experience photobleaching, making them more attractive for most applications, including as optoelectronic components or in optical computing.

1.4.1 Physical Mechanism

Visible light is scattered when it interacts with a material which has spatial refractive index variation over similar length-scales to the wavelength of the light; a trivial example of such a material would be a dispersion of colloids with diameters on the order of hundreds of nanometres. The scattering of light by a spherical particle is described by Mie scattering theory, a general solution of Maxwell's equations[89,90]. However, the term Mie scattering is also more broadly used to describe situations where the scattering particles are similar in size to the wavelength of the incident radiation. For cases where the particles are much smaller than the wavelength of light

$$\frac{2\pi r}{\lambda} \ll 1 \qquad (1.17)$$

the Rayleigh scattering approximation is used. The scattering power in this regime is broadly angle-independent but shows a strong f^4 dependence[89], where f is frequency, meaning shorter wavelengths are scattered much more strongly. Two other limits are commonly employed but are not pertinent here: particles much larger than the wavelength of light are described by classical geometric optics and particles with very low refractive indices are described by Rayleigh-Gans-Debye theory[89].

Structural colour from a material can be divided into two broad mechanistic archetypes, coherent scattering and incoherent scattering[89,90], as shown in Figure 1.12. Incoherent scattering arises when the individual scatterers in a material are spatially uncorrelated, and so scatter light with random phases relative to one another. The net scattering character of the material is therefore determined only by the scattering character of the individual particles. Because shorter wavelengths are scattered much more strongly than long, to the human eye incoherently scattering materials are exclusively blue. For example, gases and aerosols scatter sunlight as it travels through our atmosphere, giving rise to the blue colour of the sky.

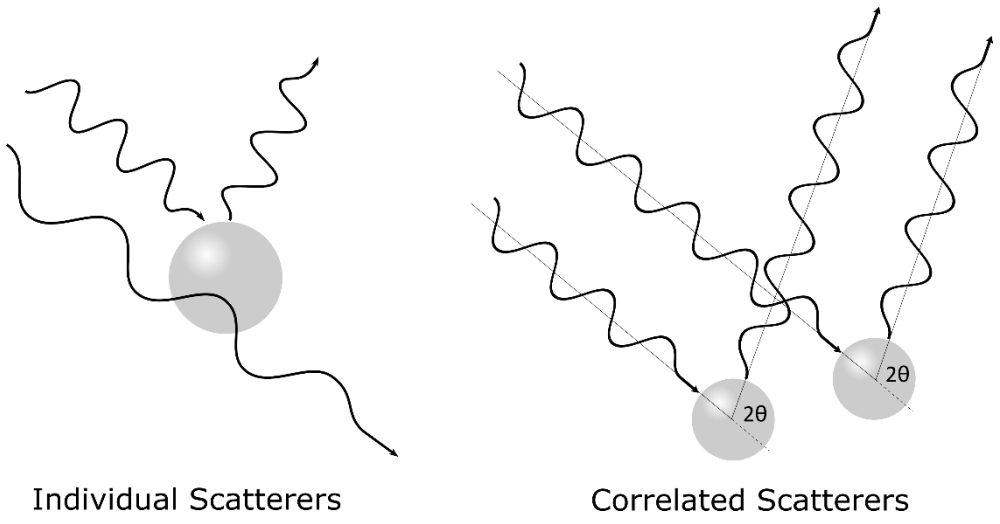

Figure 1.12: Key features of incoherent and coherent scattering.

While for incoherent scattering the spatial relationship between scatterers is random, coherent scattering arises when scatterers are spatially correlated on length-scales comparable with the wavelength of light. This means that scattered waves have non-random phases and allows for the constructive or destructive interference of light of distinct wavelengths. Coherently scattered light therefore generally has a narrow wavelength range which can theoretically be tuned throughout the visible spectrum by varying the inter-scatterer distance; however, because coherent scattering is always

convoluted with the f^4 scattering power of the individual particles, it is very common for coherently scattered light of longer wavelengths to be swamped out by the simultaneous isotropic scattering of shorter wavelengths[91]. Several methods to avoid this issue are employed in natural and synthetic materials and will be discussed below.

While incoherent scatterers are inherently disordered in terms of scatterer distribution, it was long assumed that coherently scattering materials must be crystalline, in order to impart a constant path difference to scattered light. However, another class of coherently scattering material exists, in which scatterers are arranged with short-range order but long-range disorder[92-94]. Coherent scatterers can be then be divided into photonic crystals that do have long-range order and photonic glasses that do not. Photonic crystals are well characterised in the literature and the photonic band gaps that arise from different lattice types have been tabulated[95,96]. They may be periodic in one, two or three dimensions and are also highly iridescent, i.e., the colour of light observed is strongly viewing-angle dependent. Bragg theory can be used to determine which wavelengths will be scattered with high intensities under which geometries. This reliable behaviour has led to their proposed and actualised use in a wide range of technological applications from fibre optics to consumer product packaging[97-100].

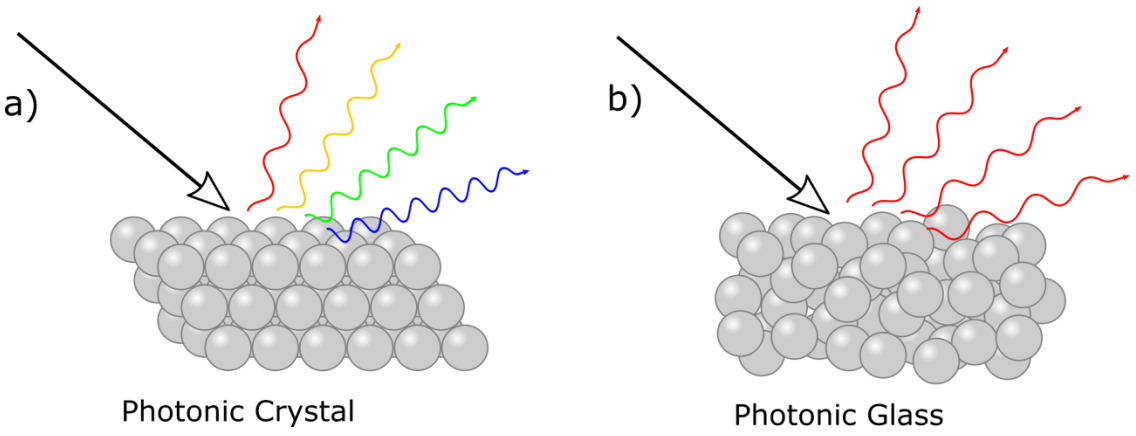

Figure 1.13: Angle dependence of structural colour from ordered and quasi-ordered coherent scatterers when illuminated with white light. a) Iridescence in scattering from a photonic crystal. b) Isotropic scattering from a photonic glass.

While photonic crystals are at this point ubiquitous, perhaps more interesting are the class of coherent scatterers that do not have long-range order. These materials are often called quasi-ordered and have short-range correlations between scatterers but no long-range ones. An analogous consideration is that nearest-neighbour scatterers have well-defined displacements but random orientations. As a result, they scatter light isotropically,

without the angle dependence typical of coherent scatterers, as shown in Figure 1.13, making them very attractive for use in industrial applications as substitutes for pigments and as sources of colour in reflection for non-backlit displays[101,102].

1.4.2 Natural Materials

Many of the brightest and most vivid colours in nature are produced through structural colouration, with examples found among almost any taxonomic class, including mammals, reptiles, birds, insects and plants[103-111]. It was recently even shown that some bird-like dinosaurs had structural colouration after coherently scattering nanostructures were found preserved in fossils[104,105]. These structural colours are produced by a huge range of different materials, including incoherent scatterers, photonic crystals, quasi-ordered phases and thin films. Examples exist of both inorganic and organic materials; precious opals are coloured due to photonic crystals consisting of square arrays of silica spheres, while peacock feathers rely on a two-dimensional photonic crystal of melanin rods in a keratin matrix[103].

Interestingly, despite the huge range of viable structures for the production of structural colour, natural examples are dominated by three distinct morphologies[112], shown in Figure 1.14 for three different bird species and discussed below. More interestingly still, these morphologies appear to have evolved independently more than fifty times[109-111]. Figure 1.14a shows a laminar array of plate-like melanosomes (melanin-containing lipid vesicles) from the green back feathers of the superb sunbird (*Nectarinia coccinigastra*). These layered structures set up an alternating refractive index contrast and effectively form a one-dimensional photonic crystal in a similar fashion to thin-film reflectors and quarter-wave stacks. This type of layering gives rise to iridescent colour of the kind also seen on oily surfaces and soap bubbles. Figure 1.14b shows a crystalline hexagonal array of aligned collagen fibres from the green facial feathers of the velvet asity (*Philepitta castanea*), which effectively acts as a two-dimensional Bragg scatterer. While this morphology is common, the packing of the collagen fibres is very rarely actually crystalline, instead normally showing quasi-ordered characteristics. This means that the scattered colour is no longer iridescent, although the two-dimensional nature of the structure means that it is not entirely without viewing-angle dependence. Finally, Figure 1.14c shows a quasi-ordered nanostructure composed of air vacuoles trapped in a β-keratin matrix from the blue feather barbs of the rose-faced lovebird (*Agapornis roseicollis*).

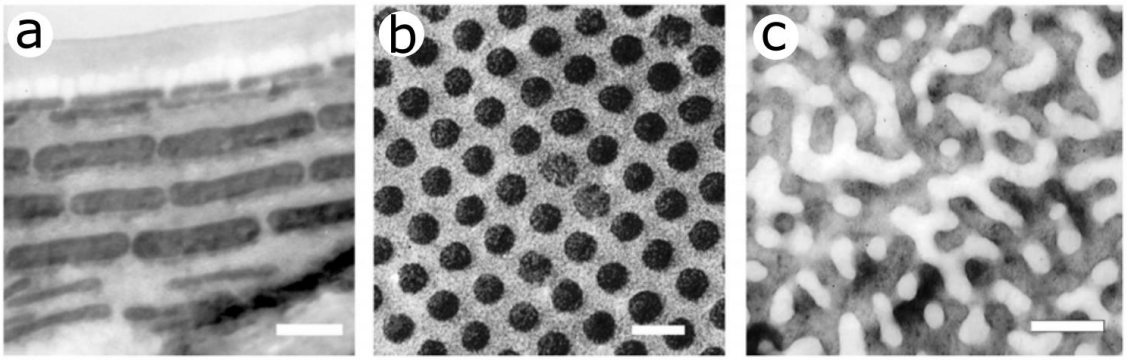

Figure 1.14: Electron micrographs of the three main classes of natural coherently scattering nanostructures. Scale bars are 200nm. Taken from [112].

This third morphology is perhaps the most interesting, as it is isotropic in all directions and gives rise to uniform, non-iridescent structural colour. Such nanostructures can be subdivided further into those with spherical or tubular air vacuoles; spherical vacuoles cause the material to behave in a very similar manner to synthetic photonic glasses made from spherical colloids[73], as in Figure 1.17 below, while the tubular vacuoles give rise to a tortuous keratin matrix very reminiscent of percolating gels. Both structures are produced through the arrested phase-separation of β-keratin protein strands from the cellular cytoplasm. A nucleation and growth mechanism has been proposed for the photonic glass of spherical air vacuoles, relying on a fast nucleation and slow growth step to give monodisperse bubbles[113,114], while the bicontinuous gel of tubular air vacuoles has been attributed to a spinodal decomposition mechanism[114,115]. These keratin-air gels exhibit non-iridescent coherent structural colour over a very large range of gel densities and volume fractions, as shown in Figure 1.15.

As discussed above, the intensity, $I(q)$, of scattered light from a material can be calculated from the convolution of the form and structure factors

$$I(q) \propto F(q) \times S(q) \qquad (1.18)$$

where the form factor, $F(q)$, is the scattering cross-section of the individual scatterer and the structure factor, $S(q)$, is the scattering character of the array, be it crystalline, quasi-ordered or amorphous. For incoherently scattering arrays, the structure factor is effectively one, and so only the form factor remains. It should also be noted that the above model assumes one scattering event per wave; if multiple scattering occurs, chromatic information will quickly be lost into a background of multiply scattered light that appears

white. Therefore, effective coherent scatterers must solve the suppression of both multiple scattering and the form factor.

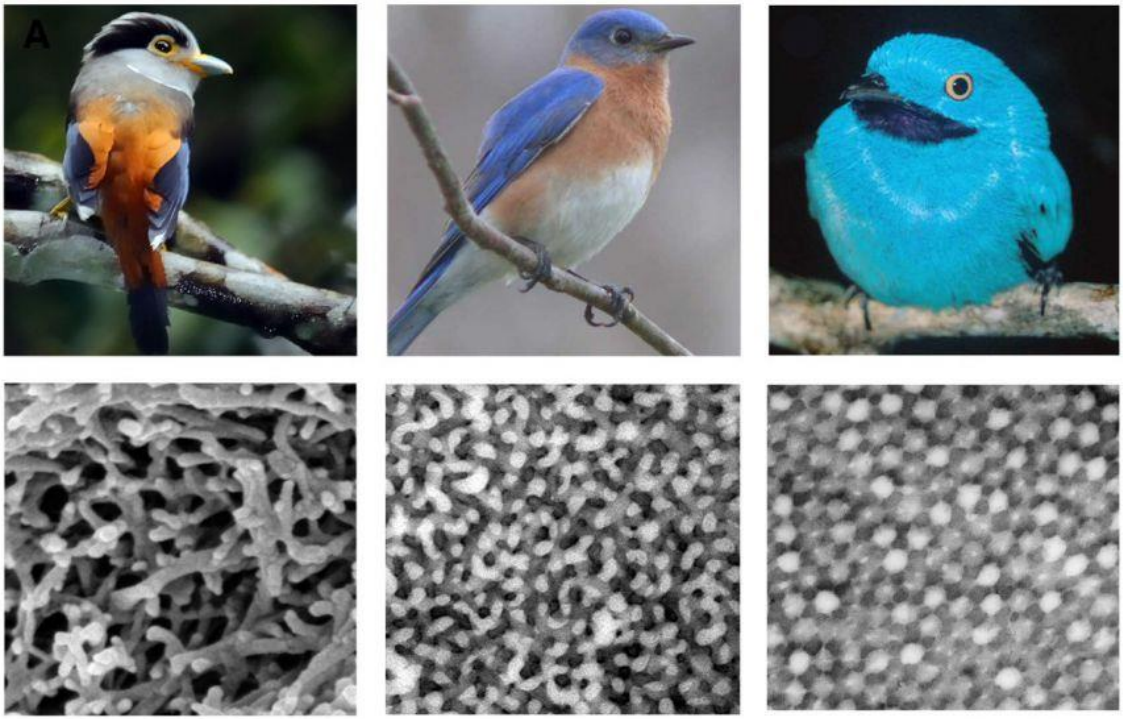

Figure 1.15: SEM micrographs of keratin-air quasi-ordered nanostructures responsible for the blue colour in the feathers of three birds; the female silver-breasted broadbill (left), the male eastern bluebird (centre) and the male plum-throated cotinga (right). Taken from [114].

Suppression of multiple scattering is normally done through the introduction of a contrast material, most commonly melanin in biological systems[110,111]. This contrast agent serves to absorb light, resulting in only light scattered from close to the surface escaping the material. The effects of this are perhaps most striking in the feathers of the Eurasian jay, which show distinctive black-blue-white banding due to a concentration gradient of melanin, as shown in Figure 1.16. Where there is too much melanin, no colour is reflected; too little and white light dominates due to multiple scattering. However, when the concentration is just right the colour is a vivid blue due to coherent scattering.

Controlling the form factor is more challenging. The simplest method is to use smaller scatterers: if particles are small enough then the form factor peak falls in the UV and the coherently scattered light will dominate the visible spectrum. However, in many photonic glasses and quasi-ordered systems the inter-particle distance is directly set by the particle size, resulting in a co-dependence of the form and structure factors. For blue structural

colours, this is not a problem, as the form factor peaks in the UV, but red structural colours inevitably become purple as the red coherent component overlaps with the blue incoherent component. In order to produce true full-spectrum structural colours, the particle separation must be tuneable independently of the particle size.

Figure 1.16: Image of a Eurasian jay feather showing distinctive black-blue-white banding.

The keratin-air quasi-ordered gel shown in Figure 1.14c is an excellent example of a viable system, as the air vacuoles act as scatterers and their separation can be tuned by varying the thickness of the keratin gel arms. Theoretically, such gels are a perfect candidate for vivid, full-spectrum structural colour. However, naturally occurring materials based on this morphology are uniformly blue and green, with some yellows. It is not clear whether this absence of red structural colour is a fundamental limit or merely an evolutionary quirk; blue pigments bleach faster than red, creating a greater evolutionary imperative for the development of blue structural colour[101,108,113].

It has been shown that these keratin-air gels are formed through the arrested spinodal decomposition of a keratin suspension in the extra-cellular matrix of the feather[113]. This similarity with the formation mechanism of arrested phases of DNA-coated colloids leads us to suggest that DNA-coated colloidal gels are an excellent candidate for the synthesis of full-spectrum biomimetic structural colour. This is discussed further in Chapter 4.

1.4.3 Synthetic Materials

Many synthetic materials exhibiting structural colour have been reported in the literature. The majority of these are Bragg scatterers, including colloidal crystals, thin-film interfaces and quarter-wave stacks, but there have also been several notable examples of non-iridescent colour in recent years. Synthetic photonic glasses were first reported in 2007 by García et al.[93], who used both direct assembly and vertical deposition of highly monodisperse polystyrene and polymethyl methacrylate microspheres to create photonic

glasses, see Figure 1.17. These pseudo-random assemblies of spherical particles are perhaps the simplest example of quasi-ordered phases with photonic activity.

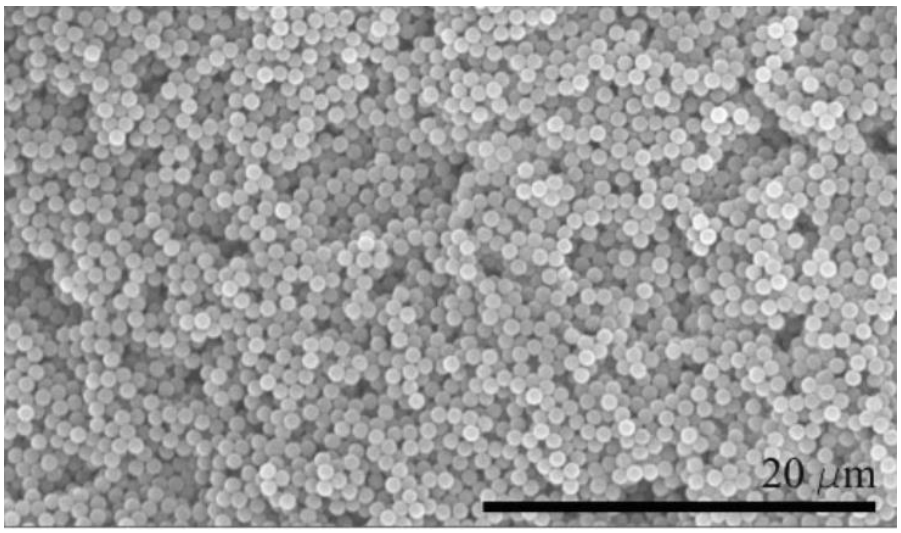

Figure 1.17: SEM micrograph of a photonic glass of 780 nm polystyrene spheres. Structure was assembled through the flocculation and sedimentation of a previously stable colloidal suspension by increasing the ionic strength. Taken from [93].

This work was then built upon by Takeoka et al.[92,116] who demonstrated the assembly of soft and hard spheres into both photonic crystals and photonic glasses with tuneable colour. However, both approaches relied on colloids in hard contact, and so were unable to sufficiently suppress incoherent scattering to obtain pure red colours.

Finally, success has been demonstrated in recent years by Manoharan et al.[101] through the use of core-shell colloids with a strongly scattering core and a weakly scattering shell. This allowed the suppression of incoherent scattering by keeping the strongly scattering core small, while controlling the inter-scatterer distance through the overall particle diameter. These colloids were self-assembled into photonic glasses first by centrifugation and then later by confinement inside microfluidic droplets; the curvature of the droplet walls helps to suppress crystallisation and encourage quasi-order. These microcapsules display intense non-iridescent structural colour tuneable across the whole visible spectrum, as shown in Figure 1.18. However, there is still a clear blue edge visible in the reflectance spectrum and the micrographs of the red microcapsules, indicating that further efforts to remove the effects of the form factor are needed.

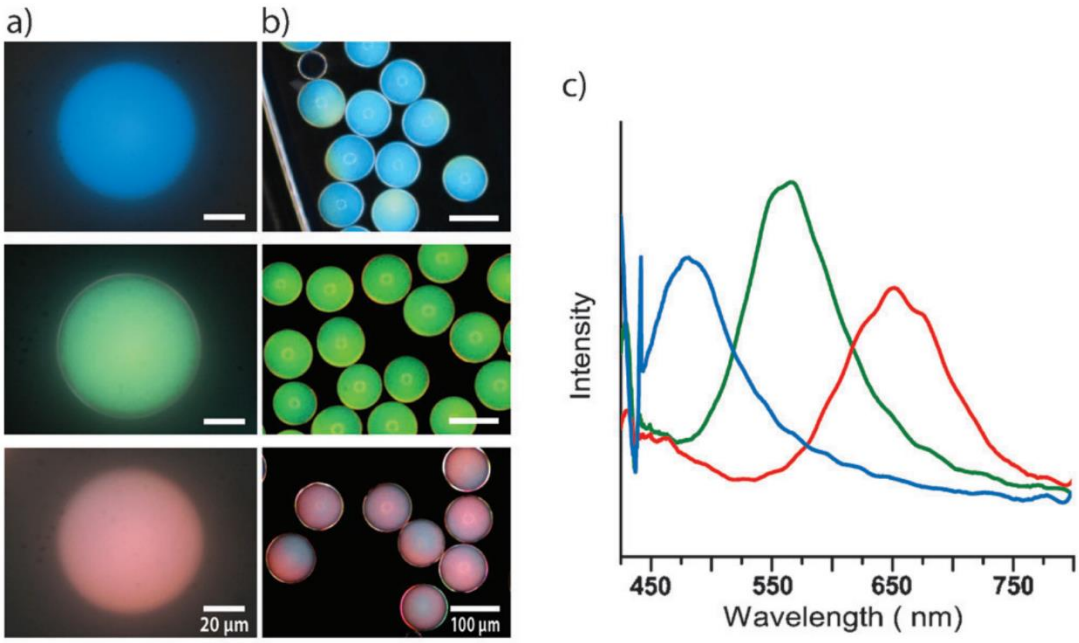

Figure 1.18: Non-iridescent structural colour produced by microcapsules of core-shell colloids. a) Bright and b) dark field reflectance optical micrographs. c) Reflectance spectra. Taken from [101].

1.5 Conclusions

This chapter presented the dominant forces and interactions that govern the behaviour of colloidal suspensions. DNA was presented as a structural material, where its information properties allow it to be used to introduce a number of specific interactions and mediate self-assembly of a broad range of structures. The state-of-the-art of both DNA-mediated colloidal self-assembly and the incidence of structural colour in assembled materials was presented as context for the work reported in this thesis. Subsequent chapters will discuss the synthesis, functionalisation, assembly and characterisation of both DNA-coated and other colloidal species.

2 METHODS

2.1 Colloidal Synthesis

The colloids used initially in this work were purchased commercially pre-functionalised. However, it was found that these colloids did not provide enough control over particle size, were very expensive and had poor coating densities. As a result, we chose to synthesise and functionalise colloids within the group. This allowed for much finer control over particle size, morphology, surface functionality and coating density. Representative synthetic protocols are given here for each type of colloid used in this thesis and are discussed in greater detail in Chapter 3. Unless stated otherwise, all chemicals were purchased from Sigma-Aldrich and used without further purification.

2.1.1 Polystyrene

Polystyrene (PS) colloids were synthesised by two different methods depending on the desired particle size. Colloids smaller than 500 nm were synthesised via a surfactant-free emulsion polymerisation, while colloids larger than 500 nm were synthesised via a dispersion polymerisation.

2.1.1.1 Surfactant-Free Emulsion Polymerisation

Sodium 4-vinylbenzenesulfonate (SVBS; charged monomer) and potassium persulfate (KPS; initiator) were dissolved in a round-bottomed flask of deionised water (MilliQ). The flask was sealed and degassed, either by cycling vacuum and nitrogen five times or by bubbling with nitrogen for 30 minutes, and then immersed in an oil bath and heated to 70 °C with vigorous stirring (1000 rpm). Styrene was injected immediately, with the dye where applicable, and the polymerisation reaction allowed to proceed at 70 °C for 24

hours, before being quenched on ice. The synthesised colloids were washed by centrifugation a minimum of three times using deionised water. Reagent quantities for specific reactions are given in *Table 3.1* in Chapter 3.2.1.

2.1.1.2 Dispersion Polymerisation

2.2 ml of styrene (686 mM) and 11 mg of polyvinylpyrrolidone (PVP; surfactant; 7 μM) were dissolved in 25 ml of ethanol and charged into a round-bottomed flask, along with SVBS where relevant. Separately, 3 ml of initiator solution containing 13 mM ammonium persulfate (APS; initiator) in deionised water was prepared in a vial. Both solutions were sealed and degassed by bubbling with nitrogen for 30 minutes. The flask was then immersed in an oil bath at 70 °C with vigorous stirring (900 rpm) and the initiator solution injected immediately through the seal. The reaction proceeded for 18 hours before being quenched on ice. 1.2 μm polystyrene colloids were collected and washed by centrifugation a minimum of three times using deionised water. Reagent quantities for other reactions are given alongside the discussion in Chapter 3.2.2.

2.1.2 Fluorinated Latex

Fluorinated latex (FL) particles were synthesised via an emulsion polymerisation. A flask was charged with 124 ml deionised water and 3.25 g 2,2,3,3,4,4,4-heptafluorobutyl methacrylate (HFBMA, Alfa Aesar; 98 mM) and sodium dodecyl sulfate (SDS; surfactant) added. The mixture was then degassed by cycling vacuum and nitrogen five times and the mixture emulsified by stirring at room temperature for one hour. A solution of 68 g KPS in 1 ml deionised water was injected and the mixture heated to 70 °C to initiate the reaction, before being allowed to react with stirring for 12 hours. The reaction was finally quenched on ice and the resulting particles washed by dialysis in deionised water. Reagent quantities given here yielded particles 200 nm in diameter. Further protocols are given as part of the discussion in Chapter 3.3.1.

2.1.3 Silica

The silica colloids used in this thesis were a mixture of purchased and synthesised, depending on the size required and their commercial availability. Synthesised particles were made using a modified Stöber sol-gel process[117]. 0.5 ml of 35% aqueous ammonium hydroxide was added to a mixture of 42.5 ml of absolute ethanol (ThermoFisher Scientific) and 4.5 ml deionised water and stirred for 30 minutes in a flask. 1 ml of tetraethyl orthosilicate (TEOS) was added and allowed to react at room temperature for

24 hours with continued stirring. The resulting silica nanoparticles, here with a diameter of 100 nm, were washed by centrifugation three times with deionised water.

2.2 Surface Functionalisation

All particles used in this thesis were surface functionalised to one degree or another, from the incorporation of charged functional groups to stabilise the suspension to the grafting of DNA to mediate specific binding. For DNA-mediated colloidal aggregation, we used commercially available polystyrene colloids, surface-functionalised with streptavidin and fluorescently labelled. These colloids readily bound with biotin-terminated DNA strands. However, because these commercial colloids gave variable DNA coatings that did not consistently prevent non-specific binding, we switched to in-house synthesis of colloids, and a swelling-deswelling method was developed based on one reported by Suk Oh et al.[74], in which particles were densely grafted with inert azide-terminated polyethylene glycol (PEG) chains. Alkyne-terminated DNA strands were then attached to these grafted polymers via a strain-promoted azide-alkyne cycloaddition. Silica particles were functionalised through a carbodiimide-catalysed acid-amine condensation reaction.

2.2.1 Biotin-Streptavidin

Streptavidin is a large natural protein with an extremely high affinity for the molecule biotin (also known as vitamin B_7). The biotin-streptavidin bond is one of the strongest non-covalent bonds that exist in nature, and its high tolerance for temperature, pH and organic solvents has led to its extensive use in bionanotechnology as a reliable lock-and-key tool for linking mesoscopic objects. We purchased polystyrene colloids surface functionalised with streptavidin from Microparticles GmbH and DNA oligomers terminated with biotin from Integrated DNA Technologies (IDT). Typical ssDNA sequences are:

A [Biotin]-5'-TTTTT-[S]-TTTTT-ATC CCG GCC-3'

A' [Biotin]-5'-TTTTT-[S]-TTTTT-GGC CGG GAT-3'

S 5'-GAG GAG GAA AGA GAG AAA GAA GGA GAG GAG AAG GGA GAA AAG AGA GAG GGA AAG AGG GAA-3'

S' 5'-TTC CCT CTT TCC CTC TCT CTT TTC TCC CTT CTC CTC TCC CTC TTT CTC TCT TTC CTC CTC-3'

Primes are used to denote strands with complementary ssDNA oligomers. In this case, S and S' are fully complementary to one another, while only the sticky ends of A and A' are complementary, as shown in Figure 2.1. The double stranded spacer S-S' was necessary due to the low coating density of streptavidin on the particle surface; using more rigid dsDNA spacers provides greater steric stabilisation than very flexible ssDNA spacers[57].

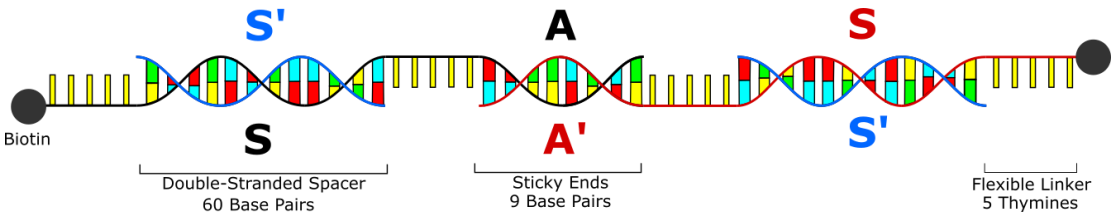

Figure 2.1: Diagram of DNA-binding for biotinylated DNA with a double-stranded DNA spacer. Terminal biotin molecules bind to streptavidin on the colloids' surface.

DNA was first prepared by mixing a 2x excess of S' ssDNA with either A or A' ssDNA. The mixture was heated to 80 ºC for two hours, before being cooled slowly to room temperature over ten hours, ensuring complete formation of the double-stranded spacer. These DNA constructs were then mixed with colloids in a 5x excess in 10 mM tris-EDTA (TE) buffer with 50 mM NaCl and allowed to bind while on a shaker for six hours. Due to the negative charges on both the particles and the DNA backbone, incremental salting was found to be necessary to achieve good coverage, as initial salt concentrations that were too high led to particle aggregation due to non-specific DLVO-type interactions. Salt was increased to 100, 200, 300 and 500 mM over 24 hours. Finally, the particles were washed by centrifugation with 10 mM TE with 75 mM NaCl and stored at 5% w/w at 4 ºC.

2.2.2 PEG Chain Grafting

Ultimately, the surface coating of streptavidin on the Microparticles GmbH colloids was found to be too low to give reliable behaviour and the switch was made to in-house synthesis of colloids with denser DNA coatings. To avoid prohibitive DNA costs, a protocol was developed using an inert poly(ethylene glycol) polymer instead of DNA as a spacer between the particle and the DNA sticky end. A hydroxyl-terminated polystyrene-*b*-poly(ethylene glycol) block copolymer (PS-*b*-PEG) was either purchased or synthesised, and end-functionalised with an azide. This polymer was then grafted to the surface of the colloids via a swelling-deswelling mechanism, before DNA was attached to the free azide end via a strain-promoted azide-alkyne cycloaddition.

2.2.2.1 Diblock Copolymer Azide Functionalisation

Replacement of the terminal hydroxyl group on the PEG block with an azide group was achieved through the activation of the hydroxyl with mesyl or tosyl chloride, followed by nucleophilic substitution, as shown in Figure 2.2. 100 mg of PS-*b*-PEG diblock (M_W=1300-*b*-5600, Polymer Source) was dissolved in 2 ml dichloromethane (DCM) and 42 µl of triethylamine (TEA) added to the solution. The flask was then cooled to 0 ºC and 23.5 µl of mesyl chloride (MsCl) or an equivalent molarity of tosyl chloride (TsCl) was injected. The reaction was allowed to continue overnight while the mixture warmed to room temperature. The solvent was then evaporated under reduced pressure using a rotary evaporator and the activated polymer washed by dissolving it in 2 ml methanol (MeOH) containing 3% hydrochloric acid (HCl) and precipitating with 30 ml of diethyl ether at -18 ºC for 30 minutes. Washing was repeated twice with 3% HCl in MeOH and three times with MeOH, and the polymer dried under vacuum.

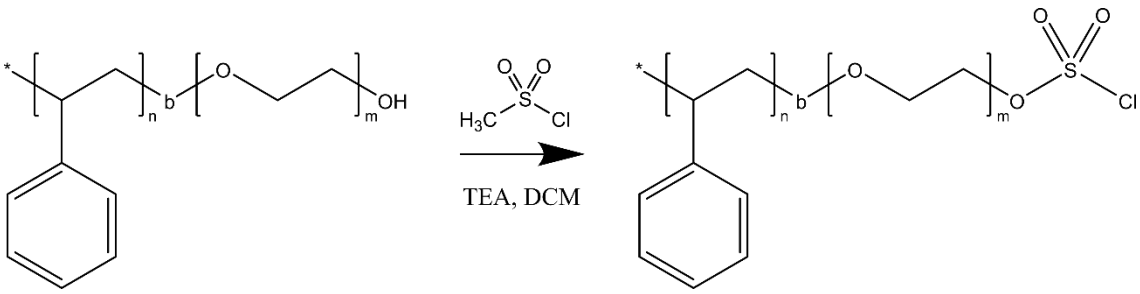

Figure 2.2: Mesylation of PS-b-PEG copolymer via nucleophilic attack on a sulfonyl chloride.

The activated polymer was then dissolved in 2 ml dimethyl formamide (DMF) containing 10 mg of sodium azide and stirred at 70 ºC for 24 hours, before being dried and washed with MeOH and ether four times as above. PS-*b*-PEG-N_3 was collected as a white crystalline powder in yields of up to 95%. The reaction scheme is shown in Figure 2.3.

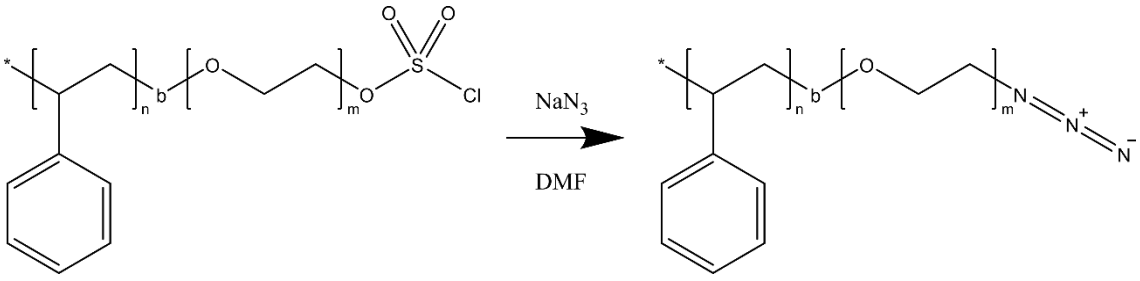

Figure 2.3: Azide-functionalisation of PS-b-PEG-Ms via an S_N2 reaction.

2.2.2.2 Surface Grafting of Diblock Copolymer

The PS-*b*-PEG-N_3 diblock acts as a surfactant. The PEG block is well solvated in water at temperatures between 0 and 90 °C while the PS block is hydrophobic at all temperatures. When mixed with a suspension of polystyrene colloids, the PS block will adsorb to the particle surface, while the PEG block stretches out into the medium. When THF is then added to such a solution, it preferentially solvates the particle polymer matrix, thereby lowering its glass transition temperature (T_g (PS) ≈ 108 °C); this causes the particles to swell, allowing the hydrophobic block to diffuse into the colloid's polymer matrix. Once dense grafting is achieved, the particles are deswelled through the dilution and evaporation of the THF. The diblock copolymers are permanently grafted to the surface by the entanglement of the hydrophobic block with the particle matrix. No significant changes to the surface morphology or sphericity of the particles were observed due to this process. Only a small increase in the particle hydrodynamic radius was measured, due to the additional grafted polymer layer.

To accomplish this, 100 µl of 200 nm diameter PS colloids (5% w/w) were mixed with 100 µl of PS-*b*-PEG-N_3 solution (10 mg ml^{-1}) and 200 µl of THF and the mixture shaken for 30 minutes. Deionised water was added to bring the THF volume fraction below 10% and the mixture heated to 60 ºC for 30 minutes to evaporate the THF. Finally, the PEG-grafted colloids were washed three times by centrifugation with deionised water. This procedure is discussed in more detail for other copolymers and particles in Chapter 3.

2.2.3 DNA Coupling

DNA was coupled to the azide-terminated surface-grafted polymers through a strain-promoted azide-alkyne cycloaddition. This reaction first gained prominence as one of the earliest "click" chemical reactions, a set of simple and effective small-molecule reactions used in bionanotechnology[118]. The requirement for a click reaction is that it proceeds in water, is tolerant of a range of pH's and temperatures, produces minimal by-products and is both rapid and high-yielding. Copper(I) catalysed azide-alkyne cycloadditions are perhaps the gold standard of click chemistry[119], but Cu(I) damages DNA[120], so an alternative method of catalysis was needed. The strained alkyne in dibenzylcyclooctyne also incites a rapid reaction with azides, but on the order of minutes not seconds. Amide-terminated DNA was purchased from IDT and reacted with dibenzylcyclooctyne-sulfo-N-hydroxysuccinimidyl ester (DBCO-sulfo-NHS), as shown in Figure 2.4. The NHS

group is a good leaving group, making NHS esters excellent acid analogues for the formation of amide bonds.

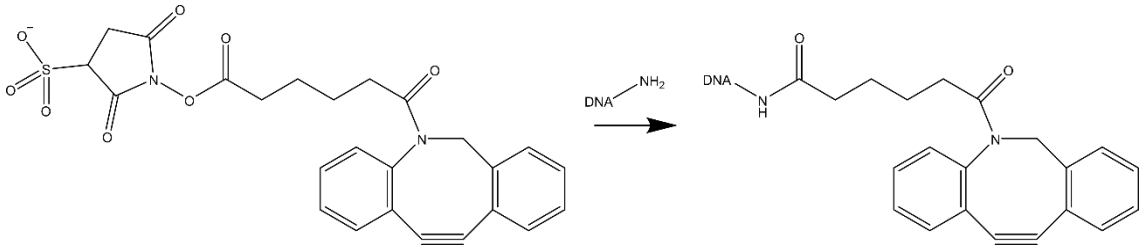

Figure 2.4: Conjugation of DNA with DBCO via a nucleophilic attack on a reactive NHS-ester.

The DBCO-functionalised DNA was then purified and reacted with the azide-functionalised particles to give DNA-coated colloids, as shown in Figure 2.5. Typical DNA sequences used were:

α [amine]-5'-TTT TTT TTT TTT TTT-GGT GCT GCG-3'

α' [amine]-5'-TTT TTT TTT TTT TTT-CGC AGC ACC-3'

50 µL of aminated DNA dissolved in 10 mM phosphate buffer (PB) was mixed with 50 µl of PB containing 200 mM NaCl and 12 µl of DBCO-sulfo-NHS dissolved in dimethyl sulfoxide (DMSO, 25 mM) and reacted for 24 hours, before being purified using Illustra Nap-5 gel filtration columns (GE Healthcare) and eluted with PB. Dissolved DBCO-DNA was collected at 50 mM and either used immediately or stored frozen.

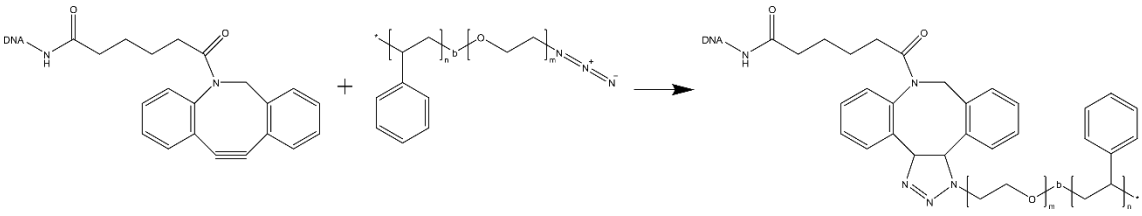

Figure 2.5: Coupling of DBCO-DNA and azide-terminated PS-b-PEG polymers via a strain-promoted azide-alkyne cycloaddition.

100 µl of PEG-coated colloids were mixed with 500 µl of DBCO-DNA and 400 µl of PB and reacted at 65 ºC with vigorous shaking for 24 hours. Where required, incremental salting was used to bring the concentration of NaCl up to 500 mM; while such incremental salting was not as necessary for PEG-stabilised colloids as when binding DNA directly to negatively-charged particles, it was found that salting did slightly increase DNA

binding density. DNA-coated colloids were washed by centrifugation three times with PB and once with PB with 62.5 mM NaCl before being resuspended and refrigerated.

2.2.4 Carbodiimide Chemistry

Silica particles were functionalised through amide chemistry as it was easy to either synthesise or purchase silica colloids surface-functionalised with carboxylic acid groups. While carboxylic acids and amines will react with one another, this reaction is slow in the absence of a catalyst due to the tendency of the acid to protonate the amine, reducing the reactivity of both. Here, carboxylic acids were activated by reaction with a carbodiimide, transforming them into reactive acylisourea intermediates, which were then stabilised against hydrolysis by reaction with sulfo-N-hydroxysuccinimide (sulfo-NHS, ThermoFisher Scientific)[164], as shown in Figure 2.6. A large excess of DNA is used to ensure that the hydrolysis reaction is not competitive; this is also why the carbodiimide is dissolved in DMSO and added last. 2-(N-morpholino)ethanesulfonic acid (MES) buffer was used for this reaction, as the acylisourea is most stable between pH's of 4.0 and 6.0.

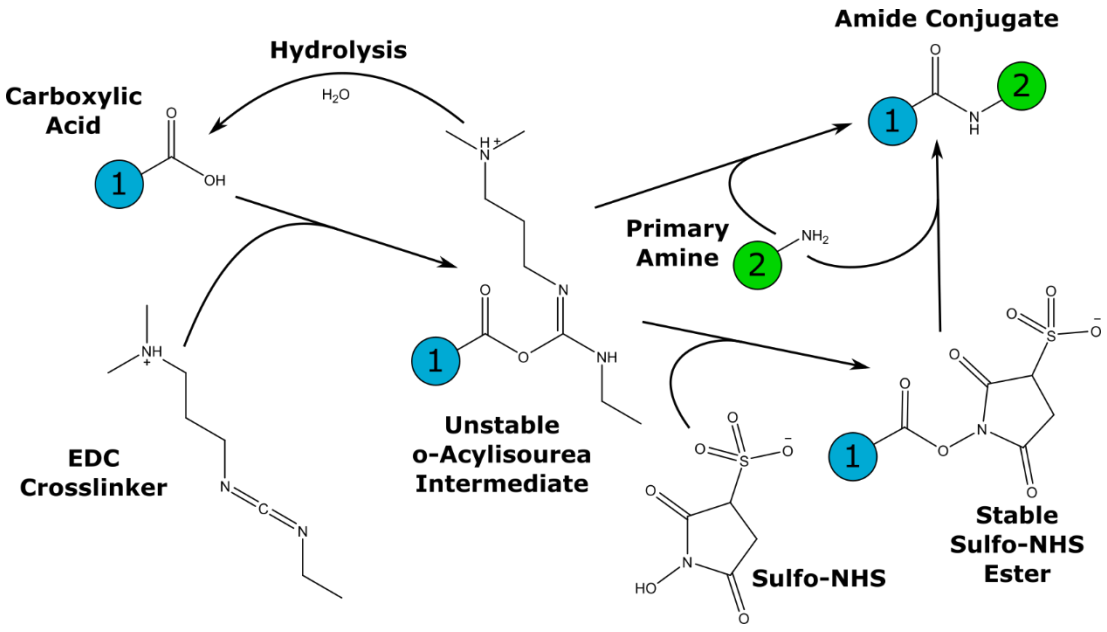

Figure 2.6: Reaction scheme for the EDC and NHS catalysed condensation of an amine and a carboxylic acid.

100 nm silica nanoparticles were suspended in 100 mM MES buffer to a concentration of 0.5% w/v, and the suspension sonicated for 30 minutes to break up aggregates. 50 nanomoles of amine-functionalised DNA was added to the particles along with 12.5 mg 1-ethyl-3-(3-dimethylaminopropyl)carbodiimide (EDC, Pierce) dissolved in DMSO and 12.5 mg NHS in 250 µl of buffer. The reaction mixture was vortexed immediately on

addition and then placed on the rollers overnight. The DNA-coated silica nanoparticles were then washed three times by centrifugation in PB and stored at 4 ºC. NHS and EDC are both ionic species, so no incremental salting is needed to achieve good DNA coverage.

2.3 Microscopy and Characterisation

2.3.1 Dynamic Light Scattering

Dynamic light scattering is a non-invasive technique that can give information about the hydrodynamic radius by measuring their diffusivity, D. The sample is illuminated by a laser and the resulting scattering pattern collected by a photomultiplier at a fixed angle. As particles diffuse within the sample, the scattering pattern changes, which can be tracked through the second order autocorrelation function of the scattered light intensity

$$g^2(q,\tau) = \frac{\langle I(t)I(t+\tau)\rangle}{\langle I(t)\rangle^2} \tag{2.1}$$

where q is the wavevector corresponding to the scattering angle θ under which the measurement is done and has the form

$$\mathrm{q} = \frac{4\pi}{\lambda}\sin\theta \tag{2.2}$$

$I(q,t)$ is the scattered intensity at time t. It can be shown that the second order intensity autocorrelation function decays exponentially with decay rate Γ, where

$$\Gamma = q^2 D \tag{2.3}$$

Hence the particle diffusivity can be determined, and the particle radius extrapolated from the Stoke-Einstein equation (Equation 1.4). If multiple species are present in the sample, the autocorrelation function becomes a linear sum of the component exponentials.

DLS was also used to measure the polydispersity index (PDI) of a particle size distribution. PDI is defined as the normalised second cumulant of the fit to the intensity autocorrelation function, the first cumulant being the average particle size, $\bar{z}$. For Gaussian distributions, the PDI is equal to

$$Đ = \left(\frac{\sigma}{\bar{z}}\right)^2 \tag{2.4}$$

where Đ is the dispersity, or PDI, and σ is the standard deviation in particle size. In this thesis, a Malvern ZSP Zetasizer was used for all dynamic light scattering and zeta

potential measurements. Data was analysed using either the Malvern software's built-in cumulant method or the CONTIN algorithm, which gives more accurate results for a polydisperse suspension.

2.3.2 Zeta Potential

A similar light scattering technique can be used to extract the electrophoretic mobility, μ_e, via analysis of the Doppler shift when a suspension of charged particles is subjected to an alternating electric field and illuminated in a similar way to that in dynamic light scattering. This is then related to the zeta potential via the Smoluchowski equation[121]

$$\mu_e = \frac{v}{E} = \frac{\varepsilon_r \varepsilon_0 \zeta}{\eta} \qquad (2.5)$$

where η is the viscosity of the medium, ε_0 is the permittivity of free space and ε_r is the dielectric constant of the medium. The zeta potential gives the potential at the slip plane, the radius at which the layer of associated ions no longer moves with the particle, see Figure 1.1, and as such is a good measure of the electrostatic stability of a colloidal suspension.

2.3.3 Optical Microscopy

Brightfield, reflection and epifluorescence optical microscopy were carried out using a Nikon Ti Eclipse inverted microscope equipped with a CMOS sensor CCD camera (Point Grey Grasshopper3). A variety of objectives were used, including a Nikon Plan Apo Lambda 40x NA 0.95 and a Plan Fluor E 40x 0.75, and reflectance and epifluorescence imaging modes were achieved using 50%, GFP, TXR and CY3 filter blocks to separate incident and emitted light. This microscope was equipped with a custom-built Peltier stage so that temperature could be controlled during imaging.

2.3.4 Confocal Microscopy

Confocal microscopy is a variant of optical microscopy in which the reflected light beam is passed through a pinhole in the back focal plane to remove all light from planes not perfectly at the focus position, though in reality, the finite size of the pinhole results in a resolution in the *z*-direction of around 500 nm. The Abbe diffraction limit also sets the maximum resolution in the *xy*-plane to

$$d = \frac{\lambda}{2.NA} \qquad (2.6)$$

where NA is the numerical aperture of the lens used. In this work, the maximum achievable resolution in the *xy*-plane was around 200 nm. This resolution is often larger than the individual particles under consideration in this work, so optical and confocal microscopy can give information about the microstructure of our systems but other techniques, such as SAXS or x-ray tomography, must be used to determine the nanostructure. Confocal experiments were performed using a Leica TCS SP5 inverted scanning microscope equipped with a 63x NA 1.2 oil immersion objective. Excitation was done using a HeNe (594, 633 nm) or argon laser and the sample scanned though a range in *z* to build up a *z*-stack of two-dimensional image slices that were then used to reconstruct the three-dimensional sample.

2.3.5 Spectroscopy

2.3.5.1 UV-Vis

UV-Vis spectroscopy was primarily used to quantify DNA concentrations and hybridisation dynamics. ssDNA absorbs 37% more strongly than dsDNA at 260 nm[45], and so the hybridised fraction can be tracked using UV-Vis absorption measurements. Tracking of hybridisation kinetics was done using a Cary 300 Bio spectrometer with built-in temperature control, while DNA concentration measurements were done using a Nanodrop 2000 UV-Vis.

2.3.5.2 FTIR

Fourier-transform infra-red spectroscopy (FTIR) is a powerful technique for characterising the functional groups present in a sample. It was used in this thesis to characterise the functional groups present in the di- and tri-block copolymers and the surface groups of the colloids themselves. A Cary 600 series ATR-FTIR spectrometer was used, which has several advantages over a conventional IR spectrometer. In an attenuated total reflectance setup, a solid sample is loaded onto a crystal waveguide, which is illuminated with IR radiation. The waveguide traps the reflecting IR beam and the sample absorbs radiation due to the evanescent waves that penetrate shallowly into the sample. This means that samples do not need to be dissolved, and very small sample sizes can be used.

2.3.6 Electron Microscopy

Scanning electron microscopy involves the tight collimation of an electron beam that is then scanned over a sample to create a raster image. Interaction with the high energy

electrons evicts secondary electrons from the material, which are collected and counted by a charged detector coupled with a photomultiplier tube. The count rate is used as the intensity for each pixel. An alternative method, transmission electron microscopy (TEM), involves the detection of electrons that pass completely through the sample. Synthesised particles were characterised by electron microscopy using a Hitachi S-5500 electron microscope in both scanning (SEM) and scanning transmission (STEM) modes.

2.3.7 Reflectivity

Reflectivity measurements were done using a reflection probe bundle coupled with LED light sources (Thorlabs MCWHF2 and M490F3) and a spectrometer (Thorlabs CCS 100). Illumination and collection were both done normal to the sample, and reference measurements were done using a Thorlabs BB1-E02 dielectric mirror.

2.3.8 Fluorescence Assay

Fluorescence assays are a widespread method for the quantification of surface and bulk functionality for a variety of systems, including colloidal suspensions[65,74]. While many variants exist, the basic principle is the same: a fluorescent dye is bound to the functional site of interest and the system washed. By then measuring the fluorescent response of either the bound or residual dye, the number of available functional sites can be estimated. Here the residual dye was measured due to the strong scattering of the colloidal particles. Quantification of the fluorescent response can be done by referencing tabulated extinction coefficients and intensities, but this method can easily introduce systematic errors due to unavoidable additional effects like photobleaching. As a result, in this work, all fluorescent assays were compared with a series of reference solutions that were processed in the same way as the sample and measured immediately beforehand.

For assays measuring the number of free azide sites on polymers and particles, DBCO-Cy5 (646/661 nm) and DBCO-Cy3 (553/563 nm) dyes were used. The DBCO couples the dye to the azide-terminated polymer through the same mechanism described for DNA. For quantification of DNA coverage, complementary DNA strands functionalised with a Cy5 fluorophore were used. Typically, 2.5 µl of colloids at 5% w/w were reacted with 5 µl of dye at 165 µM in 1 ml of TE buffer, in parallel with a control solution without colloids for 24 hours. The particles were then pelleted by centrifugation and the supernatant removed, diluted 10x and the fluorescence spectrum measured. This was compared to a calibration series made by diluting the control sample.

2.3.9 X-ray Scattering

Small-angle x-ray scattering (SAXS) is used to characterise the length-scales present in a system in the range of a few Angstroms to several hundred nanometres. As the length-scales of interest in a sample are often many times larger than the wavelength of the x-rays used, the scattering angles are very small, necessitating very long sample-to-detector distances[122]. As the scattering power of a material for x-rays is proportional to the electron density contrast with the background medium, contrast in SAXS experiments is strongly correlated with material density. In organic or biological systems, in which this electron density contrast is low, sufficient experimental contrast is only achieved at high fluxes. For this reason, most SAXS experiments are done at synchrotrons, in which very intense coherent x-ray beams are generated by accelerating high-energy electrons through magnetic fields.

The typical components of a synchrotron are a central ring that houses the electron beam, which may be fed or topped up from a smaller ring, a number of Bending Magnets or Insertion Devices on the primary ring that stimulate x-ray emission and beamlines that emanate out tangentially from these points. These beamlines contain the focussing and beam-shaping optics that guide the x-ray beam to the sample.

Once the sample has been illuminated, the scattering must be measured. Because x-rays have such small wavelengths, no optics exist that can reconstruct the image from the scattered beams, so instead only the scattered intensities can be measured[122]. As the phases are lost, a three-dimensional holographic reconstruction is impossible. The unscattered light is blocked by a beamstop to protect the detector, as only a very small fraction of the beam is scattered. Practically, this sets a lower limit on the scattering angle that can be measured and hence an upper limit on the feature size. In order to measure smaller angles and larger features, the sample-to-detector distance must be increased to allow shallowly scattered light to propagate sufficiently away from the unscattered beam. Many detector types exist, including solid-state or scintillation plates, but the raw data always has the form of a two-dimensional array of intensities.

To extract meaningful results from the raw data, several different measurements are needed. A dark image is recorded before every exposure without the beam, to measure the residual response of the detector, and subtracted from all subsequent exposures. A blank image of the sample holder is needed to subtract the scattering contribution of the holder and solvent from the sample. Most importantly, a form factor image is needed.

Similar to static scattering of visible light as discussed in Chapter 1.4, the scattered x-ray intensities measured have the form

$$I(q) \propto P(q) \times S(q) \times R(q) \qquad (2.7)$$

where P(q) is the form factor of the individual scatterers, here the colloids, S(q) is the structure factor describing the spatial distribution of the colloids and R(q) is the instrument resolution. This separation of P(q) and S(q) is only valid when the location and structure of the colloids are independent. By measuring the scattering from a very dilute suspension of colloids, the form factor can be measured as S(q) tends to 1. The structure factor of any sample can then be calculated by dividing the scattered intensities by the form factor intensities as shown in Figure 2.7. Before this step, it is common to radially average the scattered intensities to convert the two-dimensional array into a linear trace of $I(q)$ against the scattering vector, q.

Figure 2.7 also shows the q^{-4} envelope of $I(q)$ predicted for monodisperse spherical colloids by Porod's law. For a sample illuminated by a point collimated beam, scattering curves will follow a linear slope of q^{-4} provided all background contributions have been appropriately subtracted.

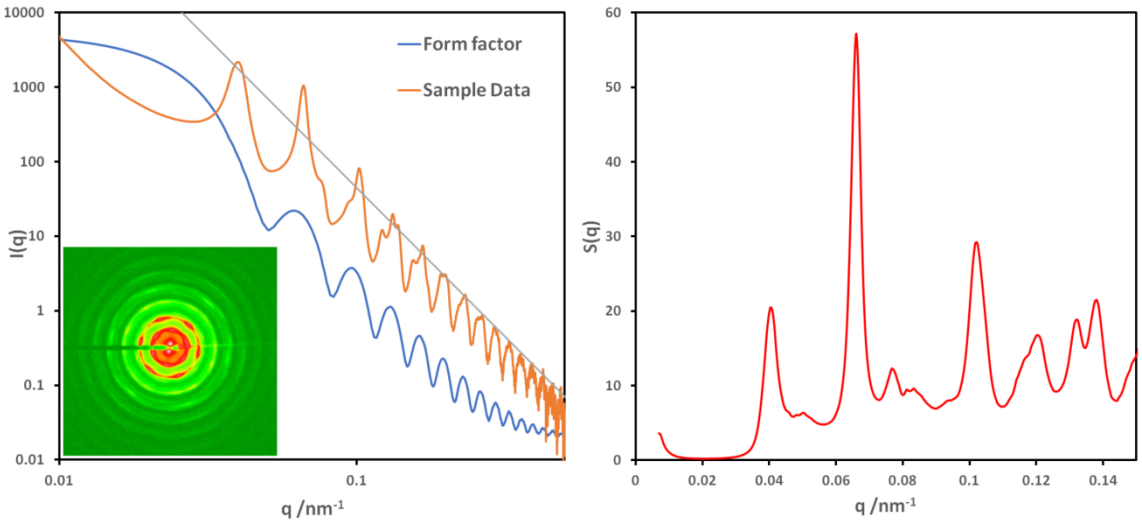

Figure 2.7: Plots showing the extraction of the structure factor (S(q), red) from the scattered intensities (I(q), orange) by dividing out the form factor (F(q), blue). Also plotted is the scaled q^{-4} envelope of the scattered intensities (grey). The insert shows the full two-dimensional I(q). Modified from [173].

If an experimental form factor cannot be measured, calculated form factors are often used based on the measured colloidal radius and polydispersity index. For spherical particles, the theoretical form factor is given by

$$P(q,R) = \left(\frac{3R^3\,sin(qR) - qR\,cos(qR)}{(qR)^3}\right)^2 \qquad (2.8)$$

This expression can be integrated over one or more particle distributions to give a calculated form factor for a particle suspension. It should be noted that when summing multiple particle distributions, the total intensity is given by

$$\Delta I(q) = I_0 \,.\, \sum_{i=1}^{N} (\Delta\rho)_i{}^2 \,.\, V_i{}^2 \,.\, P_i(q) \qquad (2.9)$$

where $\Delta\rho_i$ is the contrast of particle i and V_i is its volume. The squared dependence on volume means that larger particles dominate the form factor contribution in polymodal samples, while the contrast term means that denser materials can drown out less dense ones. This has interesting consequences in Chapter 5.3, which discusses, among other systems, a mixture of dense, low refractive index fluorinated latex (FL) particles and light, high refractive index polystyrene (PS) for photonic applications. The FL particles contribute more strongly to the SAXS, but the optical effects are dominated by the PS.

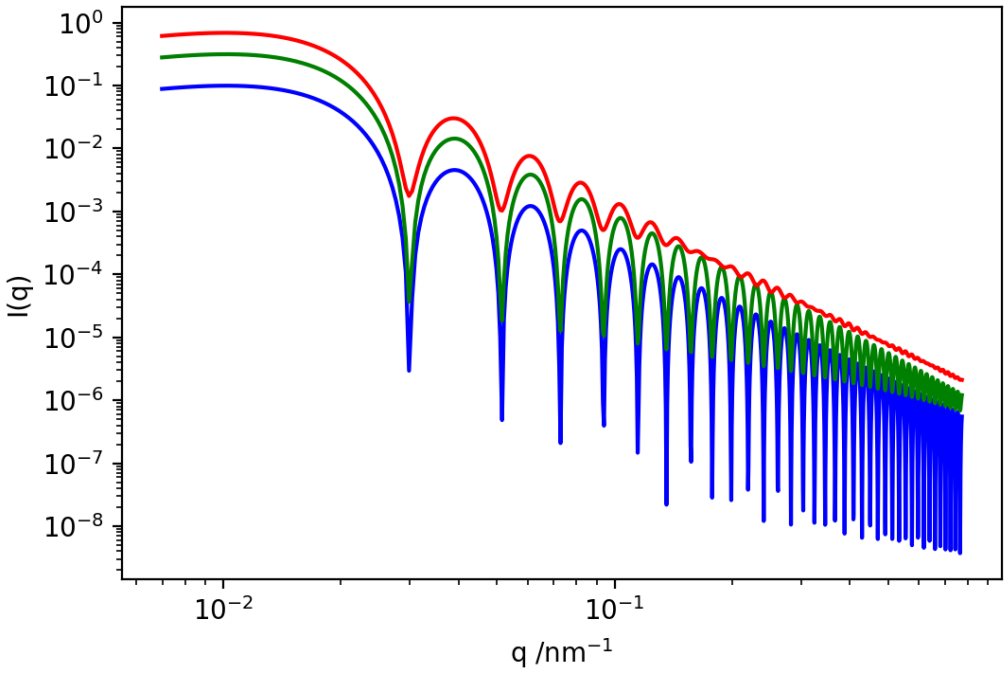

Figure 2.8: Form factors for a suspension of ideal 150 nm spherical particles with standard deviations of 0.1 (blue), 1 (green) and 10 (red).

Calculated form factors are shown in Figure 2.8 for a monomodal suspension of 150 nm colloids with standard deviations of 0.1 (blue), 1 (green) and 10 (red), showing the sharp wells in the form factor for monodisperse samples that become broader as polydispersity increases. In this work particle distributions were assumed to be narrow and Gaussian, which matches with results from DLS and SEM, and the Simpson integration method used to evaluate the integral when calculating form factors. Experimental form factors were also fitted to this function using a custom fitting algorithm to extract particle radii from SAXS data.

SAXS experiments in this thesis were performed at the ID02 beamline of the European Synchrotron Radiation Facility (ESRF) in Grenoble, France and the B21 beamline of the Diamond Light Source in Oxford, UK. X-rays used in both facilities had a wavelength of 1 Å. At the ESRF, the beam size was 50 x 50 µm, the sample-to-detector distance was either 1 m or 10 m depending on the experiment and the detector was a Rayonix MX170. At Diamond, the beam size was 1 x 1 mm, the sample-to-detector distance was 4 m and the detector was a Pilatus 300 K.

2.4 Image Analysis

2.4.1 Chord Analysis

Chord analysis is used to characterise the length-scales present in a phase-separated system and is particularly useful when considering gelled phases like those formed by DNACCs[124-126]. It involves the processing of images from optical or confocal microscopy to obtain a histogram of chord lengths, from which information can be derived about the structure of the phase and the process by which it is formed.

All image analysis in this work was performed using Python scripts written by the author. Confocal microscopy images were taken using a pixel size below the Abbe diffraction limit, and then an appropriate blur applied to remove oversampling artefacts. Blurring was accomplished by convoluting each pixel with those around it according to a Gaussian of fixed width. It was found that if too small a blur was used, artefacts were introduced at very short chord lengths, as was expected, while if too large a blur was used, all features were coarsened. The Gaussian blur radius was chosen to be sufficient to bring the information density to just above the diffraction limit but no further. The image was then binarised, to turn all pixels corresponding to the arrested phase to white and all pixels corresponding to the continuous phase to black. This was accomplished using Otsu's

algorithm, which assumes two classes of pixels and sets the binarisation threshold to minimise the intra-class variance[123]. Finally chords, continuous lines of white or black pixels, were reaped across all rows and columns and plotted in a histogram, as shown in Figure 2.9.

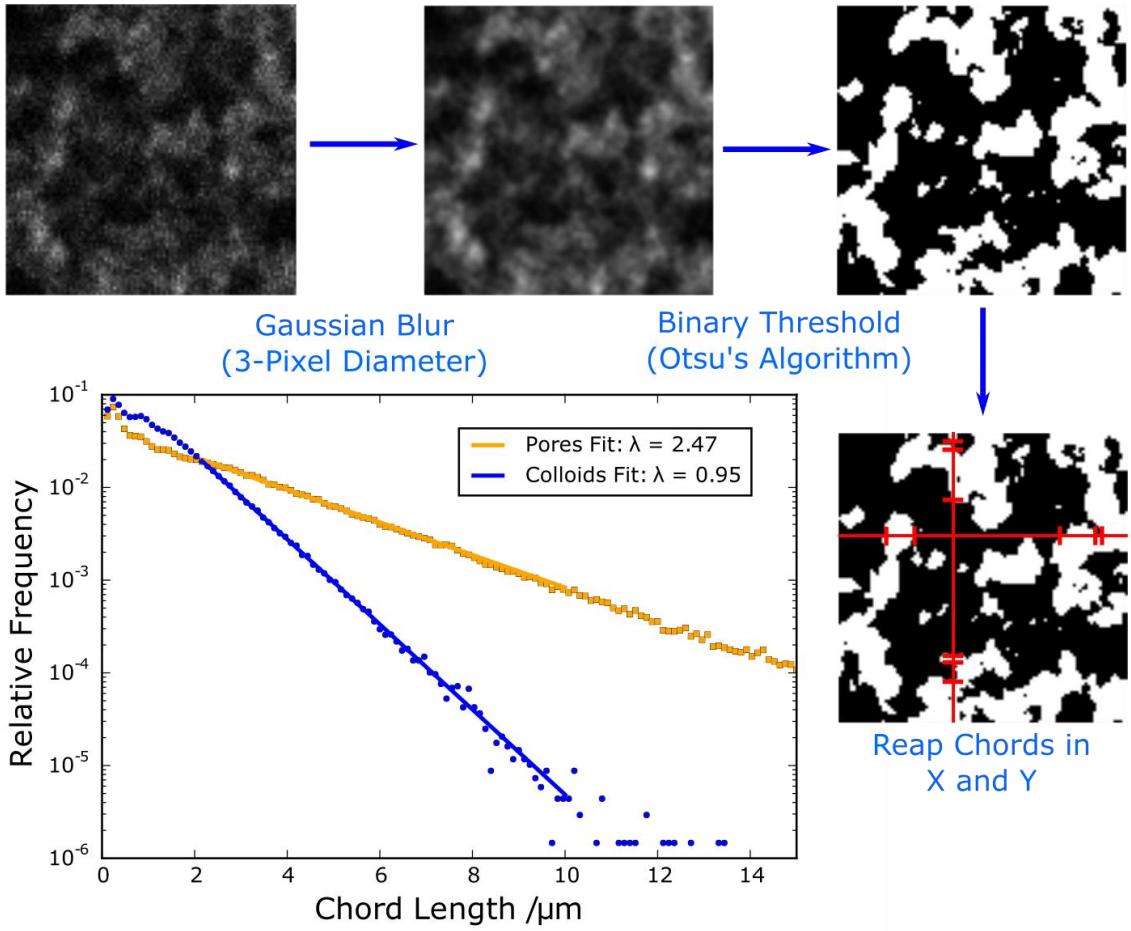

Figure 2.9: Confocal micrograph of a colloidal gel and the image at each stage of the processing. Clockwise: raw, blurred, binarised and an example of chord reaping. The plot shows a typical chord histogram for pores and branches on a semi-log plot.

The chord histogram is a polynomial for a fractal gel, but an exponential for a gel formed through arrested spinodal decomposition[126], of the form

$$f(r) \propto e^{-\lambda r} \tag{2.10}$$

The decay constant, λ, indicates the lengthscale over which the kinetic arrest occurs, and so is representative of the branch thickness in the colloidal gel[125,126]. It has been shown to be a useful metric for quantifying length-scales in porous systems[124]. In this thesis, the decay length was often used alongside the average chord length, obtained by integrating the chord histogram; it was found that the two are strongly correlated with one another.

2.4.2 Structure Factor

Optical and confocal micrographs can also be analysed to determine the structure factor of a two-phase material. In an exactly analogous way to that with x-rays and visible light, the structure factor is a representation of the structure of a material in reciprocal space. While for x-rays, the scattering pattern is used to generate the reciprocal space image of the material, $I(q)$, here the Fourier transformation of the real space image is taken and divided by the form factor, i.e. the Fourier transformed image of a single particle

$$S(q) = \frac{\langle \left| \hat{I}_{gel}(q_x, q_y) \right|^2 \rangle}{\langle \left| \hat{I}_{one}(q_x, q_y) \right|^2 \rangle} \tag{2.11}$$

The circumflex is used to denote the Fourier transform of a function and $\langle ... \rangle$ denotes the radial average of a 2D function. For this analysis to be valid, it has been assumed that the image intensity $I(x, y)$ is proportional to the material density $\rho(x, y)$.

3 COLLOIDAL SYNTHESIS AND FUNCTIONALISATION

The scope and variety of applications for colloids has exploded in recent decades, bringing with it a similar increase in the number of synthetic methods for their manufacture and functionalisation. Colloids are used in a wide range of industries, including paints, coatings, cosmetics and optoelectronics[127-131], and are proposed for an even wider range of future technologies, for example in biotechnology and self-assembly[132-134]. Polymer latex colloids are the most widespread in these regards, due to their relative ease of synthesis and extreme potential for customisation; almost any physical property of the colloids can be tuned across a wide range by selecting the right synthetic pathway. Conventional solution-phase polymerisation reactions exist in a variety of forms, including emulsion, dispersion and precipitation, alongside a number of more exotic versions, for example precipitation using supercritical fluids, but there is a strong drive in the literature for the development of more diverse or effective synthetic procedures.

This chapter details the development of the synthetic protocols and functionalisation techniques used to prepare DNA-coated colloids for the experiments done during this work, including those described in Chapters 4 and 5. Development of the surfactant-free emulsion polymerisation of polystyrene was done based on initial protocols developed by Dr Yang Lan. Experiments on the synthesis and functionalisation of fluorinated latex colloids were done in collaboration with Mykolas Zupkauskas.

3.1 Basic Principles

Polymer colloid synthesis is achieved, understandably, by very similar means to the synthesis of free polymers. A reactive group is created (initiation), which can then attack a monomer molecule, creating a growing chain able to attack further monomers (propagation). The reaction proceeds, adding monomers to the polymer backbone, until the reactive group is destroyed (termination). Polymerisation mechanisms can be cationic, anionic or free radical, of which free radical is the most common[135]. Many variants of these exist, for example reversible addition-fragmentation chain-transfer polymerisation (RAFT), which sets up an equilibrium between active and inactive chain forms to control relative propagation and termination kinetics[136]. This work focuses on free radical polymerisations.

The basic components of a polymerisation reaction are an initiator, monomer and solvent, and some reactions also involve co-monomers, seed particles or surfactants. The initiator produces free radicals, often through the pyrolysis or photolysis of a heteroatom-heteroatom bond, which catalyse the reaction between the growing chains and the monomers. Monomers may be soluble or insoluble in the solvent, or stabilised as an emulsion by the surfactant, depending on the desired particle morphology – generally, more stabilisation leads to smaller particles. Co-monomers are used to change the final particle properties or to impart a charge to the particles to prevent aggregation.

Figure 3.1 shows the broad classifications of polymer colloid syntheses dependent on the solubility of monomer and the presence or absence of a surfactant to stabilise the interface. *Suspension polymerisations* involve poorly soluble or insoluble monomers either stabilised by surfactants or suspended mechanically as a heterogenous suspension of droplets. The initiator dissolves in the monomer phase, and the droplets are the locus of polymerisation; monomer droplets are suspended through agitation, and polymerise completely, so particle size is determined predominantly by the stirring speed during the reaction[137]. Other polymerisation types typically use an initiator that is soluble in the continuous phase. In a *precipitation polymerisation*, monomers and small oligomers are soluble in the reaction medium, only precipitating out once they reach a certain molecular weight. Polymerisation occurs primarily in the continuous phase, with polymers eventually precipitating out into particles which can then grow by coalescing with one another. New particles will continue to form until all dissolved monomer is consumed[135]. Particle size is set by interfacial properties, polymer solubility and initiator concentration. *Dispersion polymerisation* is a sub-category of precipitation in which a surfactant is

added to stabilise the precipitating particles against coalescence. This means that precipitated particles are smaller and more numerous than in a precipitation polymerisation; this greater cumulative surface area of the heterogenous phase means that monomer can more easily diffuse to the dispersed particles. Hence the polymerisation locus becomes the particles instead of the bulk, with monomer slowly being added as the particles grow. Interfacial properties and hence particle size therefore also depend on surfactant concentration[135,137]. Finally, *emulsion polymerisations* use surfactants to stabilise an insoluble monomer; excess surfactant forms micelles in the bulk which swell with small amounts of monomer that diffuse through the medium[135,137,140]. Initiation occurs preferentially in these swollen micelles due to their much higher total surface area than the primary monomer droplets[138,139]. This mechanistic explanation was developed from experiments on polystyrene in water. Other systems can behave slightly differently[140].

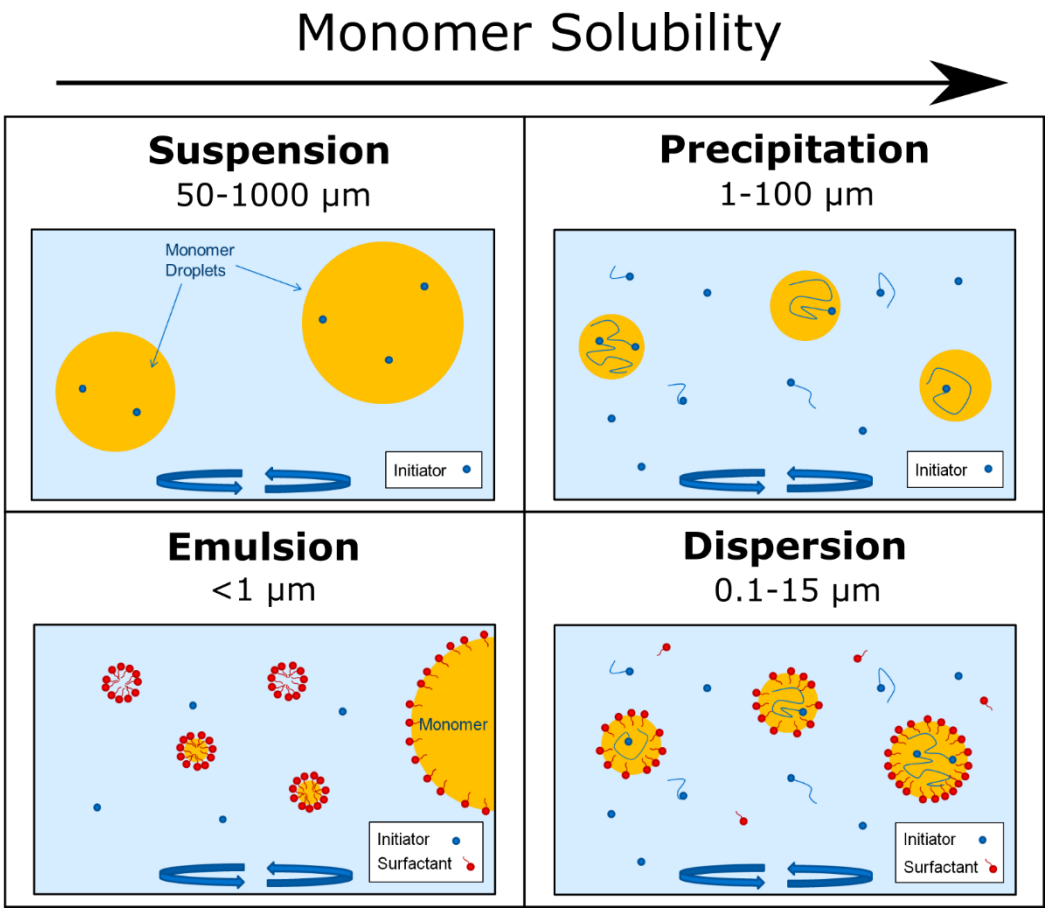

Figure 3.1: Diagrams of different polymerisation mechanisms depending on monomer solubility and presence/absence of surfactant showing typical particle sizes.

When synthesising free polymers, it is important to keep the growing chain well solvated throughout the reaction. In contrast, when synthesising polymer colloids it is ideal for the polymer to be poorly solvated after a certain molecular weight, in order to trigger phase separation into particles[135]. In addition, because a single particle will contain many individual polymer chains, particle properties are much more tolerant of chain properties, removing the need for very fine control over chain length and morphology.

Functionalisation can occur during synthesis through the choice of monomer, co-monomer or initiator or be achieved after polymerisation is complete. This is often accomplished for polymer colloids by either grafting polymers to the particle surface after synthesis, electrostatically adsorbing another species or using co-monomers that include a functional group with a preference for the interface that can then be modified by further chemistry[135].

3.2 Polystyrene Colloids

Initially during this work, polystyrene colloids were purchased pre-functionalised with streptavidin from Microparticles GmbH and used without further processing. However, it was found that the streptavidin surface density was too low for consistent behaviour and the particle size range was too restrictive, so the move was made to in-house synthesis and functionalisation of polystyrene colloids.

3.2.1 Surfactant-Free Emulsion Polymerisation

Polystyrene colloids with a size range of 80 – 500 nm were synthesised via a surfactant-free emulsion polymerisation (SFEP) using the protocol described in Chapter 2.1.1.1. Potassium persulfate (KPS) was used as an initiator in the copolymerisation of styrene with sodium vinylbenzenesulfonate (SVBS), a charged styrene derivative; during synthesis, the pendant sulfonate groups remain at the particle-water interface and ultimately lead to highly negatively charged colloids which are inherently stable against aggregation at low ionic strengths. SFEP is a variant of emulsion polymerisation which does not involve an added surfactant. Instead, growing oligomers act as surfactants to stabilise the monomer droplets and form micelles[135,138-140].

Size control was achieved in this synthesis primarily by varying the concentration of KPS, and secondarily by introducing ethanol to the reaction mixture, as shown in Table 3.1. Increasing the concentration of KPS increases the number of growing chains per particle and the rate at which monomer is consumed, leading to larger particles overall. All sizes

were found to have extremely low PDIs < 2%, indicating highly monodisperse suspensions. This was evidenced further by the formation of colloidal crystals on drying as observed in SEM, as shown in Figure 3.2, where a dry film of PS spheres are arranged in a typical hexagonal close packed plane. Crystallisation only occurs for suspensions with dispersities of less than 6%[141].

Batch	Diameter /nm	Dye	Water /ml	Ethanol /ml	Styrene /g	KPS /mg	SVBS /mg	Dye /mg
H11	200	-	300	0	15.6	405	61.8	-
H35	200	Rhod	300	0	15.6	405	61.8	6
H37	210	FITC	300	0	15.6	405	61.8	6
H40	80	Rhod	300	0	15.6	390	61.8	6
H41	420	FITC	120	180	15.6	405	60	6

Table 3.1: Representative synthesis batches of polystyrene colloids produced through surfactant-free emulsion polymerisation. "Rhod" is rhodamine B; "FITC" is fluorescein isothiocyanate.

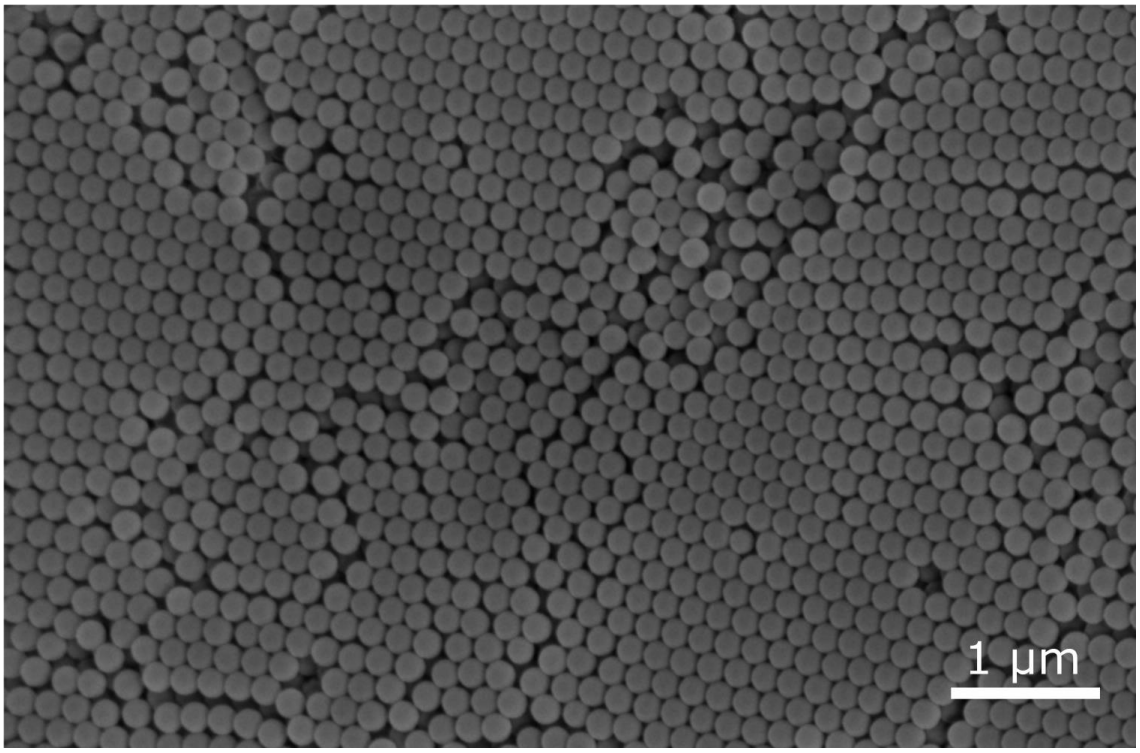

Figure 3.2: SEM micrograph of highly monodisperse 200 nm diameter polystyrene colloids (H11), showing assembly into crystalline close-packed layers on drying.

The extremely strong particle size dependence on KPS concentration can be attributed to the multiple roles the initiator plays in the system: growing chains both form and stabilise the particles, while the KPS sulfate group ultimately also stabilises growing particles against agglomeration through electrostatic repulsion. Replacing water with ethanol in the reaction medium makes the monomer and growing oligomers more soluble, as well as reducing the effective size of the sulfate "head group" on growing oligomers, meaning larger swollen micelles may form without becoming unstable.

The full reaction protocol is given in Chapter 2.1.1.1. One key finding from the development of this synthesis was the importance of injecting the monomer immediately on heating the initiator solution to 70 °C and stirring vigorously, as many processes occur simultaneously at the start of the reaction, including emulsification of the monomer, initiation of polymerisation, nucleation of the growing particles and the adsorption of species to the new interfaces.

3.2.2 Dispersion Polymerisation

For a number of projects, most notably the scaling laws discussed in Chapter 4, larger polystyrene colloids were required. It was found that the colloids produced by SFEP could not be made larger than 500 nm without either sacrificing monodispersity or requiring additional steps in the reaction, so a complementary synthesis was developed to make these particles, following a dispersion polymerisation archetype. Ideally, this new method would be effective at producing monodisperse spherical colloids between 500 nm and 5 μm in diameter and stable against aggregation even after the removal of any surfactant. While a number of polystyrene syntheses via dispersion polymerisations have been reported in the literature[142-144] and were tested for our purposes, they were found to either fall short on one or more of the above criteria or relied on multiple synthetic steps. Hence, we opted to develop our own procedure.

A requirement of a dispersion polymerisation is that the monomer and small oligomers are dissolved by the medium, so many dispersion polymerisations of PS have been reported using alcoholic solvents, most commonly methanol, ethanol and *n*-propanol[143,144]. Because we were aiming for particles that were stable against aggregation in the absence of surfactant, we wanted to incorporate charged functional groups in the particles for electrostatic stabilisation. However, KPS and SVBS are not soluble in alcoholic media, preventing their use in such systems. In order to circumvent this issue, we chose a water-ethanol mixture as the solvent for the reaction. Similar polymerisation

media have recently been shown to be effective for surfactant-free and semicontinuous micro-emulsion polymerisations of small, monodisperse polystyrene colloids[145,146]. By using this reaction medium, we were able to appropriately solvate the monomers and oligomers to obtain larger particles while also anchoring negatively charged sulfate groups to the surface of the growing particles through the use of persulfate initiators and SVBS. Finally, ammonium persulfate (APS) was used instead of KPS due to its greater solubility; azo-bisisobutyronitrile (AIBN) and benzoyl peroxide (BPO), two common initiators used in ethanolic solutions, were avoided as they have been reported to give more polydisperse particles[144]. Poly(vinylpyrrolidone) (PVP) was used as the surfactant. A full experimental method is detailed in Chapter 2.1.1.2, and a mechanistic study is given below, considering the effects of changing various parameters on the final particles' properties.

Particle size was primarily controlled by varying the concentration of initiator, as it proved to be the parameter that gave smooth, monodisperse particles across a broad size range. A plot of particle diameter against overall APS concentration is shown in Figure 3.3, from which it is evident that there is an approximately linear, positive correlation of particle size with initiator concentration. This is attributed to the greater number of growing oligomers when phase separation begins; while the surfactant is still moving to stabilise the new interface, more oligomers will be able to migrate to existing particles, resulting in more growing chains per particle and hence larger colloids. However, this effect is offset slightly by the decreased solubility of the growing particles due to their greater charge, giving the approximately linear dependence observed.

For APS concentrations over 30 mM, small secondary colloids were observed in addition to the primary distribution. As particles become larger for a constant initial monomer mass, their number density becomes correspondingly lower, so some new oligomers do not diffuse to existing particles as they phase separate, instead nucleating additional ones. At very high APS concentrations, these secondary particles have such a high surface area that they both deplete the PVP in solution and also introduce depletion forces between the larger colloids, resulting in polydispersity and aggregation, as shown in Figure 3.3d.

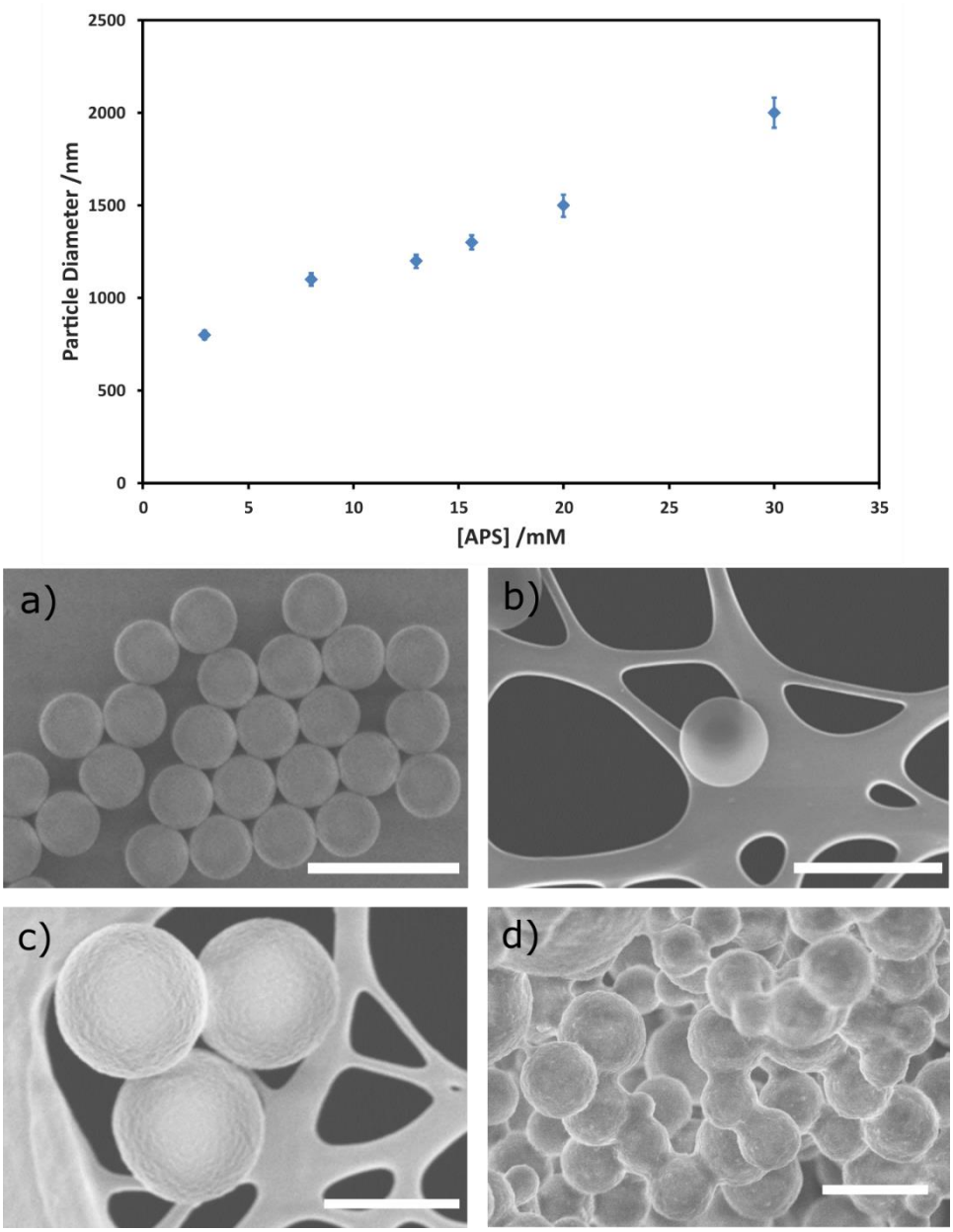

Figure 3.3: Plot of polystyrene colloid diameter dependence on APS concentration, and SEM micrographs of typical colloids obtained using 2.9 mM (a), 13 mM (b), 30 mM (c) and 40 mM (d) concentrations of APS. Ethanol, water, styrene and PVP quantities were kept constant at 25 ml, 3 ml, 2.2 ml (686 mM) and 11 mg (7 µM). Scale bars are 2 µm.

The effects of PVP concentration on particle size are plotted in Figure 3.4. Larger PVP concentrations gave progressively smaller particles, as additional surfactant was able to stabilise a larger total surface area of particles, leading to more, smaller, particles. However, the suspension surface area does not depend linearly on the PVP concentration used; moreover, for higher PVP concentrations the suspensions became increasingly polydisperse. We attribute this to the ability of surfactants to acts as nucleation sites for

polymerisation if an initiator molecule abstracts a hydrogen from the surfactant backbone[135]. As surfactant concentration increases, so does the rate of this secondary nucleation and the resulting polydispersity of the system. It was found that the particle size distribution was narrowest at 7.1 µM overall PVP concentration across a range of other parameters, and that lower concentrations gave extremely polydisperse samples of no practical use, corresponding to the limit of insufficient surfactant to stabilise the precipitating polymers.

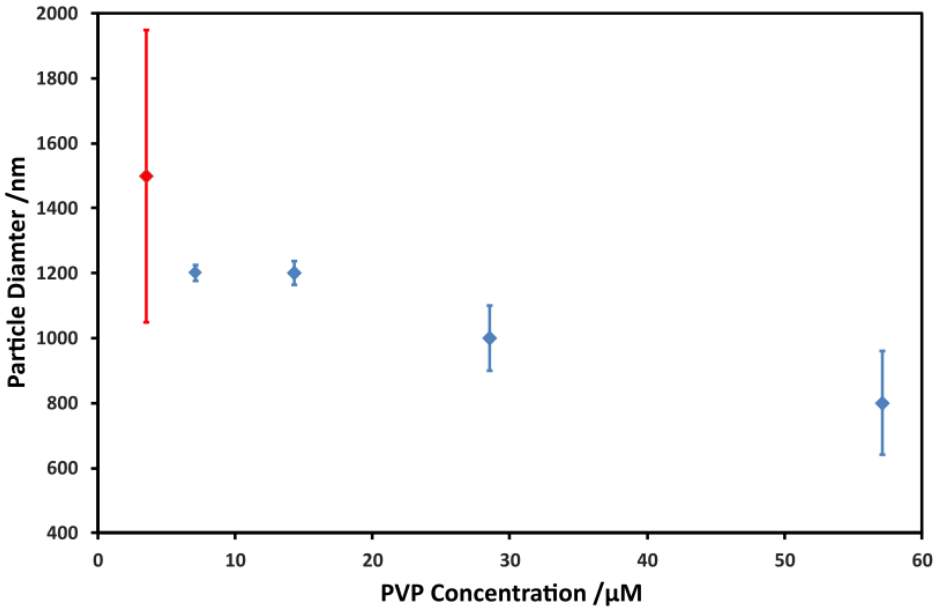

Figure 3.4: Plot showing the effects of PVP concentration on particle diameter. The red marker shows the size of the primary particles in a very polydisperse suspension. PVP concentration was varied between 3.5 - 56 µM while keeping ethanol, water, APS and styrene quantities constant at 25 ml, 3 ml, 13 mM and 2.2 ml (686 mM) respectively.

Previously, it has been reported that syntheses conducted in this type of mixed solvent are only viable over small solvent ratio ranges[147]. In contrast, we found that while the particle size showed a strong dependence on the solvent ratio, as shown in Figure 3.5, monodisperse particles were obtained using solvents with water fractions ranging from a few percent to up to a third.

Syntheses run in pure ethanol or with water fractions of more than a third gave very polydisperse samples from which a primary particle size could not be obtained. However, syntheses run in solvents with 3-20% water typically resulted in suspensions with PDIs of less than 5%. Variation in solvent character will change the solubility of all components: monomers, oligomers, PVP and APS. Monomers, oligomers and PVP all

became less soluble as water content was increased, while APS solubility increased. However, the particle size is dominated by the solubility of the monomers and oligomers: as they become less soluble, particles are less able to coarsen and combine, and more, smaller particles are formed.

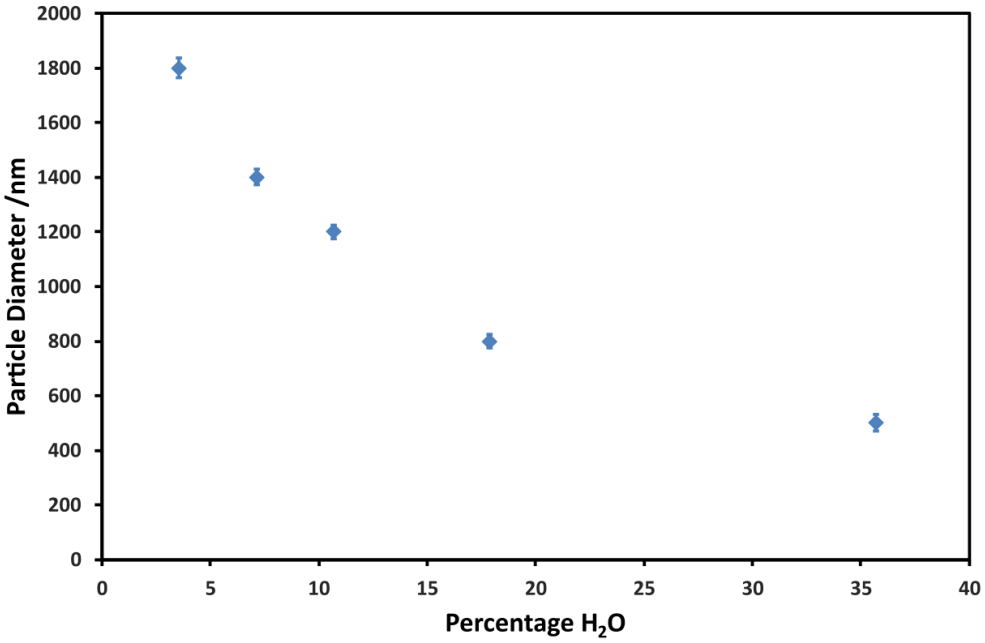

Figure 3.5: Variation in particle size with water:ethanol ratio in the reaction medium. Water volume was varied between 1 and 10 ml while keeping the total volume at 28 ml. APS, styrene and PVP were kept at 13 mM, 2.2 ml (686 mM) and 11 mg (7µM) respectively.

In light of this, the final dependence investigated gave unexpected results. Introduction of SVBS to the backbone was predicted to both decrease the solubility of the growing chains and increase the electrostatic repulsion between them, leading to smaller particles on both counts. Instead, the introduction of SVBS reproducibly led to larger particles, as shown in Figure 3.6. It should be noted, however, that the system could only tolerate very small proportions of SVBS. In contrast to the SFEP discussed above, for which SVBS represented up to 15% of the total monomer, this dispersion polymerisation became unstable above SVBS percentages of 1%, triggering the aggregation and fusion of all particles.

We are unable to conclusively assign this behaviour to the underlying chemistry of the system based on this work. We speculate that the decreased stability of the oligomers very early on in the reaction might cause phase separation into particles on a faster timescale than the surfactant can rearrange to stabilise it, allowing for the formation of larger

particles. This effect would not exist in the case of changing the solubility through changing of the reaction medium, as that necessarily also changes the solubility of the surfactant.

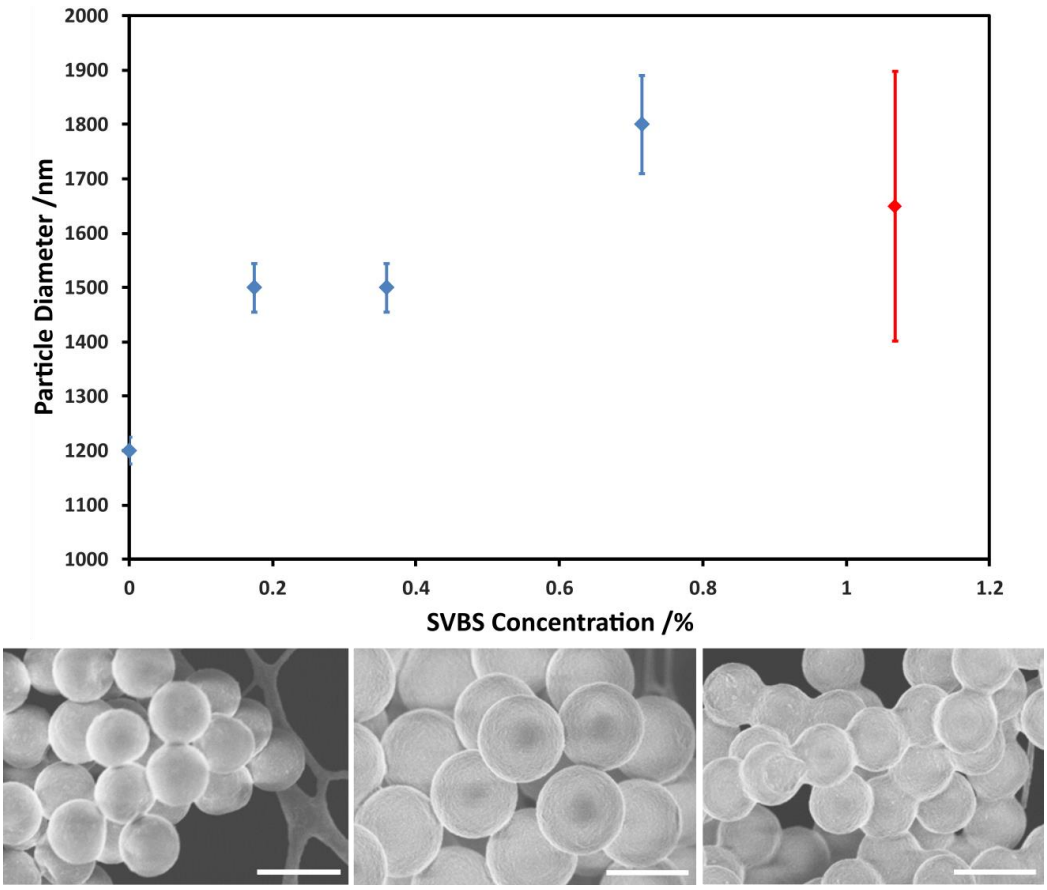

Figure 3.6: Plot showing the effects of SVBS concentration relative to styrene on particle diameter. The red marker shows the particle size of the system before aggregation and coagulation. SEM micrographs are shown below for colloids made with 0.18% (left), 0.72% (centre) and 1.07% (right) SVBS relative to styrene. Ethanol, water, APS, styrene and PVP quantities were kept constant at 25 ml, 3 ml, 13 mM, 2.2 ml (686 mM) and 11 mg (7 µM) respectively.

More generally, the development of these synthetic protocols emphasised the importance of careful control during synthesis to achieve high quality particles. If oxygen is not adequately removed from the reaction mixture, it will scavenge radicals and prevent good polymerisation kinetics, leading to polydispersity. If the stirring speed is not high enough, then particle size is no longer determined solely by the solubility of the components and the thermodynamic properties of the interfaces as the system is not well mixed.

A side result of this mechanistic study was the discovery of a robust synthetic path to "dimpled" particles. While investigating the behaviour of SVBS in the dispersion

polymerisation, monodisperse particles all exhibiting a single indentation were observed, as shown in Figure 3.7. Colloids were also visibly buckled in optical microscopy of the dispersion, implying that the buckling was not due to drying forces, but instead occurred during synthesis. Synthesis of non-spherical particles has proven to be of great interest in self-assembly and nanotechnology[25], so the development of a reliable, high-throughput, single-step synthesis would be particularly valuable.

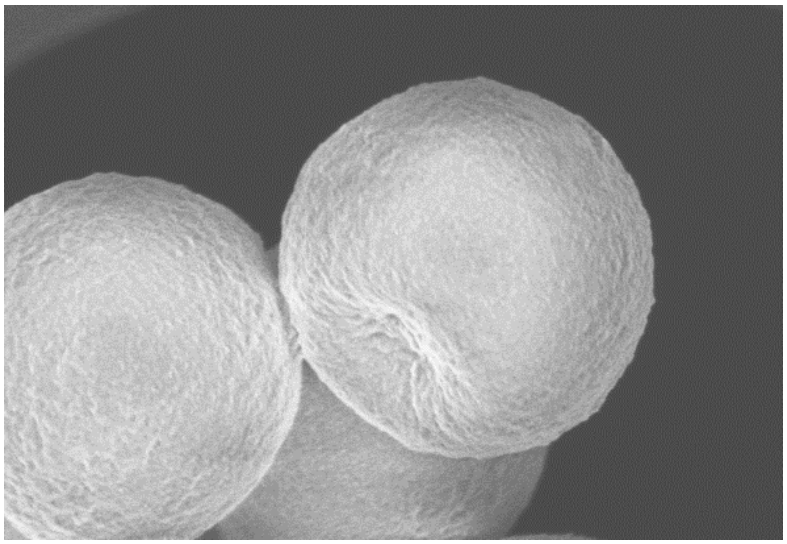

Figure 3.7: SEM micrograph of a "dimpled" polystyrene colloid approximately 1800 nm in diameter. Quantities used of ethanol, water, APS, styrene, PVP and SVBS were 25 ml, 3 ml, 35 mM, 2.2 ml (686 mM), 11 mg (7μM) and 21.6 mg (3.7 mM, 1.07%) respectively.

The origin of these indentations is attributed to the specific locus of polymerisation within a particle. The active end of a growing chain is tethered to the particle-solvent interface by the charged sulfate group from the initiator and the charged sulfonate groups on the polymer. As a result, monomer will diffuse from the centre of the particles to the surface, where it will be incorporated into the backbone, eventually forming a polymer shell and leaving the inside of the particle empty. If particles are large enough, this cavitation can cause significant stresses on the particle skin, ultimately leading to buckling of the shell at the thinnest point.

This buckling could also be explained by the removal of small amounts of water from the polymer matrix on drying, but this would less well explain the fact that the buckled particles could also be observed by optical microscopy of the aqueous (undried) suspension and the fact that the particles display exclusively a single dimple.

By increasing the initiator to monomer ratio sufficiently, we were also able to extend this behaviour to SVBS-free dispersion polymerisations using APS concentrations of 35 mM.

To counteract the effects of secondary nucleation, the solvent ratio used was 26:2 ethanol:water, to better solvate growing oligomers and encourage amalgamation into existing particles instead of the nucleation of new ones. The PVP concentration was also reduced to 4.5 μM, again to discourage the formation of smaller secondary colloids. While such changes led to polydispersity when synthesising smaller colloids using 13 mM APS, the suspension of larger particles was able to tolerate them, giving monodisperse buckled colloids 2200 nm in diameter.

3.2.3 Surface Functionalisation

Oh et al.[74] recently demonstrated a method of functionalising polystyrene colloids with DNA at extremely high coating densities of up to one strand per 14 nm^2. This was accomplished by grafting an amphiphilic diblock copolymer, polystyrene-*b*-poly(ethylene glycol) (PS-*b*-PEG), to the surface of particles with the hydrophobic polystyrene block enmeshed with the particle polymer matrix and the hydrophilic poly(ethylene glycol) block extending into the solution forming a sterically stabilising polymer brush. By pre-functionalising the ends of the polymer with specific functional groups before grafting, a wide range of functionality can be introduced to the polystyrene particle. In this work we attach either a fluorescent dye or an ssDNA oligomer to azide-terminated PEG brushes. This has the advantage over functionalisation on synthesis that no co-monomers are required, meaning particle size and functionality can be controlled independently.

Particles dispersed in water were swelled through the addition of tetrahydrofuran (THF), allowing the PS block of the copolymer to infiltrate the polymer matrix. The volume fraction of THF was then reduced by dilution and evaporation, causing the particles to deswell with the PS block trapped inside and the PEG block grafted to the surface. DNA was coupled to the azide-functionalised free end of the PEG block through the strain-promoted azide-alkyne cycloaddition reaction detailed in Chapter 2.2.3.

This protocol was adapted for the functionalisation of polystyrene colloids of a range of sizes. A number of different block copolymers were used in this thesis; PS_{13}-*b*-PEG_{127} (PS_{13}) was purchased from Polymer Source while Synperonic F108 (poly(ethylene glycol)-*b*-poly(propylene glycol)-*b*-poly(ethylene glycol), PEG_{133}-*b*-PPO_{50}-*b*-PEG_{133}) and Synperonic F127 (PEG_{100}-*b*-PPO_{65}-*b*-PEG_{100}) triblock copolymers were purchased from Sigma. In addition, PS_{30}-*b*-PEG_{79}-N_3 (PS_{30}) was synthesised by Dr Clément Mugemana and Professor Nico Bruns at the Adolphe Merkle Institute (see Appendix 1).

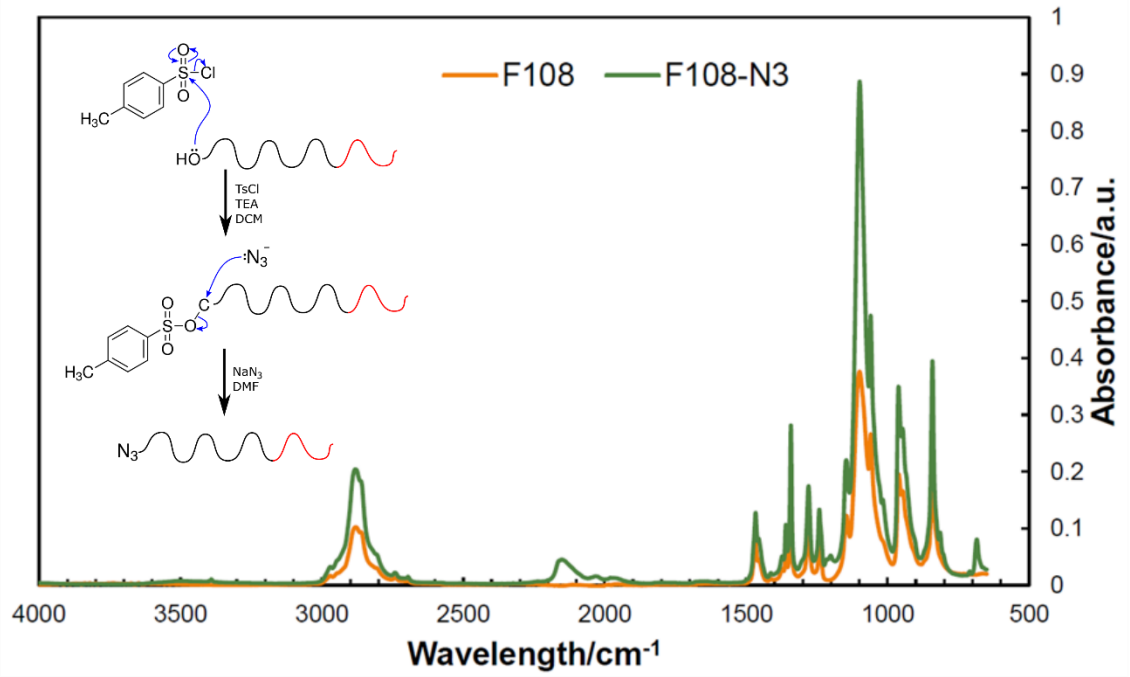

Figure 3.8: IR absorption spectrum of F108 before and after azide-functionalisation. The insert shows the reaction mechanism for the functional group conversion.

Purchased block copolymers were all hydroxyl-terminated and were azide-functionalised via the protocol described in Chapter 2.2.2.1. The successful reaction was confirmed via IR spectroscopy, as shown in Figure 3.8; azide groups have a characteristic absorption at 2150 cm^{-1}. The mechanism of the azide functionalisation is shown as an insert in Figure 3.8.

Particles were swelled with each diblock following the method detailed in Chapter 2.2.2.2. Aqueous suspensions of 200 nm and 400 nm particles were mixed with block copolymers dissolved in either water (PS_{13}, F108 and F127) or equal parts water and THF (PS_{30}). As the copolymers are all amphiphilic, they act as surfactants in colloidal suspensions, so the hydrophobic (PS or PPO) block adsorbed to the surface of the colloids upon mixing. THF was then added to bring the total THF volume fraction in the solvent to 50%. THF is less polar than water, and so preferentially solvates the polymer matrix of the particles, causing them to swell and allowing the adsorbed hydrophobic blocks to infiltrate the particles. When the THF volume fraction was reduced, first by dilution with additional water and then by evaporation under gentle heating, the particles deswelled, leaving the block copolymers permanently grafted to the particle surface. Excess surfactant was removed by washing with centrifugation.

Surface coating densities were measured by conducting fluorescence assays with DBCO-Cy5 dye, as detailed in full in Chapter 2.3.8; DBCO-Cy5 was reacted with the terminal azides on the grafted polymers and the residual fluorescence of the supernatant after centrifugation compared with that of a standard of known concentration. Figure 3.9 shows a plot of binding area per strand for each of the diblocks on 200 nm polystyrene particles (PS200). "F108 2x" refers to swelling the colloids with twice the normal concentration of F108 in the solution, to test whether increased block copolymer concentration gave significantly higher coverages. It can be seen that the effect is visible, but marginal, with the area per strand going from 14 nm^2 to 12 nm^2. F108 and F127 have been reported to give lower coverages on PS particles[148], however, while the F127 coating density was significantly lower than that of the others, F108 performed comparably to the diblocks, even at equivalent stoichiometries. The use of F108 had a distinct advantage over the use of PS_{13}, in that F108 is orders of magnitude cheaper, allowing larger concentrations to be used to achieve very dense coatings. However, both F108 and F127 exhibit chain-length polydispersity[149], while PS_{13} did not. It was also later shown by a DNA assay that the high azide-coverage of F108 does not transfer universally to a high DNA-coverage. We attribute this to the coiling of the longer hydrophilic PEG chain in F108 sterically hindering attack by the DNA when undergoing the alkyne-azide coupling reaction, as the reaction is slow. For these reasons, PS_{13} was used as the diblock of choice when performing experiments with DNA-coated colloids.

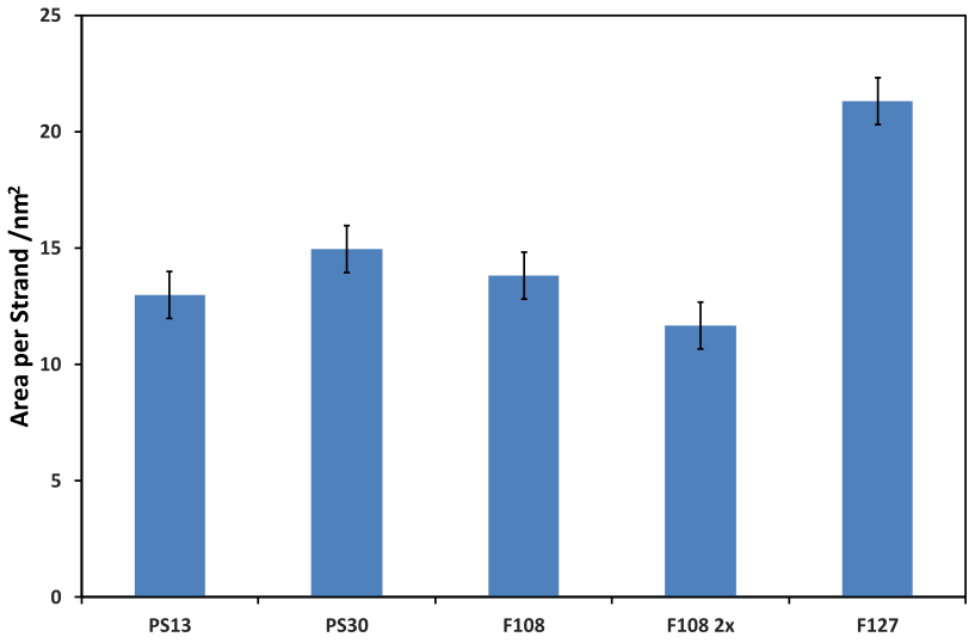

Figure 3.9: Coverages of different block copolymers grafted to 200 nm polystyrene particles via a swelling-deswelling mechanism.

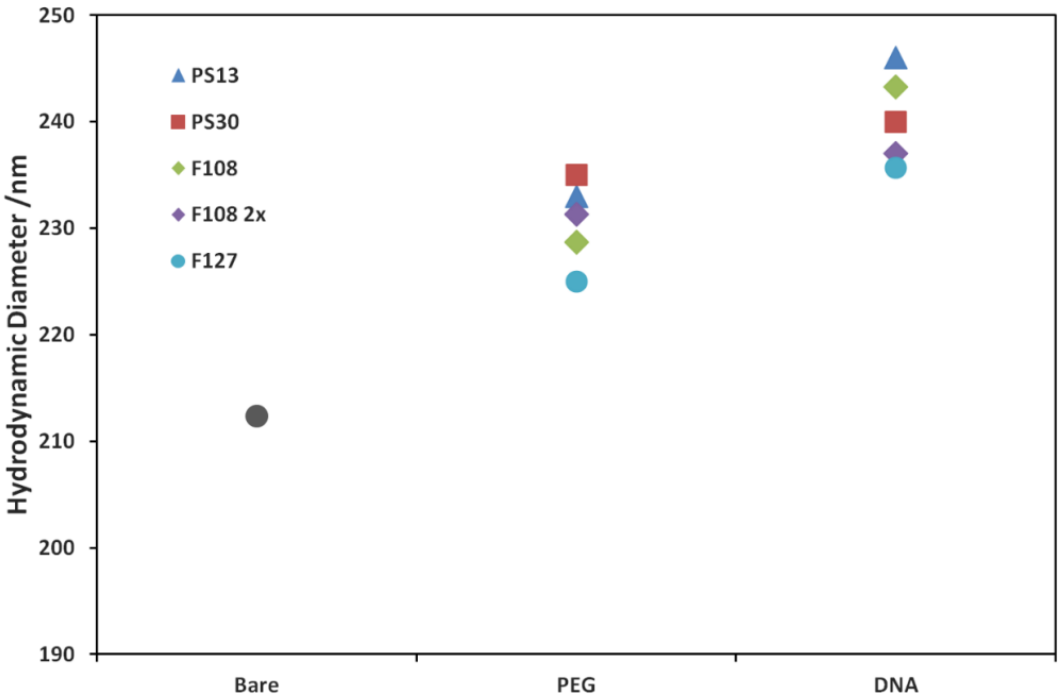

Figure 3.10: Plot showing the hydrodynamic diameters of 200 nm PS functionalised with different block copolymers and DNA. All measurements were made using DLS.

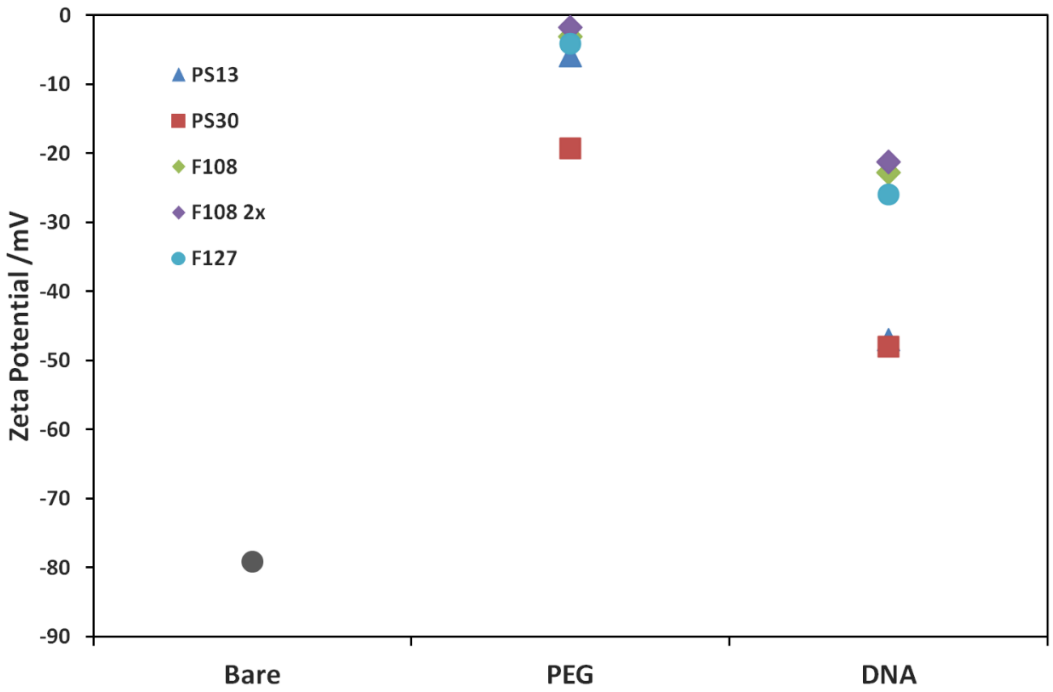

Figure 3.11: Plot of zeta potentials of bare, PEGylated and DNA-coated 200 nm polystyrene colloids after swelling with a range of block copolymers.

To complete the functionalisation, particles were reacted with complementary ssDNA oligomers α and α' using the protocol set out in Chapter 2.2.3. The hydrodynamic diameters and zeta potentials were measured for bare, PEGylated and DNA-coated

particles using each of the block copolymers. Results are plotted in Figure 3.10 and Figure 3.11 respectively. The size of the particles increased by around 20 nm upon PEGylation, which can be understood by consideration of the conformation and length of the PEG chains. As shown in Figure 1.5, grafted polymers can adopt a number of different configurations depending on their solvation by the medium and grafting density.

For an unconfined polymer, the radius of gyration is given by Flory theory, which combines the contribution from a polymer's behaviour as an entropic chain with an excluded volume for each repeat unit

$$R_F \approx aN^i \left(\frac{v}{a^3}\right)^{\frac{1}{5}} \tag{3.1}$$

where a is the Kuhn length of the polymer, N is the number of Kuhn segments and v is the excluded volume of a single segment. The exponent, i, depends on the solvation of the polymer by the medium. In a good solvent, like PEG in water[143], $i = \frac{3}{5}$. The Kuhn length of PEG is 0.76 nm and a single Kuhn segment is approximately two repeat units[150]. Hence the Flory radius of the polymers would be between 5 nm and 6.5 nm depending on the copolymer. For the densities observed, the distance between chains can be approximated by the square root of the area per chain, giving separations of 3.5 nm to 4.5 nm. As the chain-chain separation is consistently less than the Flory radius for the polymer, it can be assumed that all grafted polymers are in the brush regime. The height of such a brush is again given by Flory theory as

$$h \approx \left(\frac{1}{2}\sigma a^5\right)^{\frac{1}{3}} \tag{3.2}$$

where σ is the grafting density. This gives brush heights of just over 10 nm, explaining the observed ~20 nm increase in the hydrodynamic diameter of the particles.

ssDNA has a persistence length of ~1 nm, equivalent to around three base pairs. The sequences grafted during this experiment were 24 bases in length, corresponding to a height of around 5 nm in the brush regime, well matching what we observe in DLS. Two final points can be drawn from the DLS data; first, while the increased grafting density generally offsets the smaller size of the shorter polymers, the F127 grafting density is noticeably lower than the others, resulting in smaller diameter increases on PEGylation and DNA-binding. Second, while the coverage of PS_{30}-azide was high, the DNA coverage appears to be much lower.

Some explanation for this may be drawn from the zeta potential: while the bare particles are strongly negatively charged, grafting the inert PEG chains screens the surface charge from the solution and moves the slip plane further from the colloid surface[151], moving the zeta potential much closer to zero. This then aids with DNA binding, as the DNA backbone is negatively charged and would otherwise be electrostatically repelled by the colloid surface. Consequently, the zeta potential becomes negative again on DNA binding. Figure 3.11 shows the zeta potentials in each case, and also gives some insight into the poor DNA coverage of the PS_{30} coated particles. The zeta potential for the PS_{30}-azide particles is much less close to neutral than the other polymers, probably due to the much shorter PEG block. As a result, the increased electrostatic repulsion between the particles and the DNA backbone may have prevented high coverages. It can also be seen that the PS_{13} is the most negative, implying a high DNA coverage, matching results from assays.

3.3 Fluorinated Latex Colloids

While polystyrene particles were used predominantly in this thesis due to their robust syntheses, low density and ease of functionalisation, their high refractive index can hinder the effective production of structural colour due to multiple scattering. For example, crystalline dried films of PS particles of the type shown in Figure 3.2 exhibit intense colours at specific angles due to Bragg reflection but appear white at all other angles. Several methods were explored over the course of this work to reduce this effect, including the use of polypyrrole as a contrast agent to absorb multiply scattered light, in a similar manner to that discussed for natural materials in Chapter 1.4.2 and the increase of the refractive index of the medium by dissolving sucrose. However, polypyrrole is hydrophobic, and it proved difficult to achieve the desired contrast enhancement, while the dissolution of sucrose dramatically changes the physical properties of the medium, most notably increasing the viscosity. Greatest success was found through the synthesis and functionalisation of particles of a polymer with a lower refractive index, as is presented in Chapter 5.

3.3.1 Synthesis

The use of fluorinated monomers has been known for some time to produce polymers and particles that are nearly isorefractive with water; early examples included perfluorobutylacrylate[152] or tetrafluoroethylene copolymerised with perfluoroalkyl vinyl

ether (PFA)[153]. These works exploited the ability to image colloids deep inside aqueous samples to conduct studies on the effect of confinement on the translational and rotational diffusion of colloids[153], as well as explore the phase behaviour of charged colloids. Low refractive index colloids were assembled into glasses[154] and crystals[152], but no particular attention was given to the physical properties of such systems; instead the low refractive index of the particles was used as a vehicle for simpler imaging and characterisation. Unfortunately, the syntheses of these colloids also suffered from being extremely complicated, difficult to reproduce and giving poor size control over the particles produced[152-155]. 2,2,3,3,4,4,4-heptafluorobutyl methacrylate (HFBMA) colloids were first reported by Koenderink et al.[155], who synthesised particles with diameters across the wide range of 100 nm to 1.4 µm through simple one-pot or seeded emulsion polymerisation techniques. This protocol formed the basis for the synthesis of the fluorinated latex (FL) particles synthesised during this thesis and used in the experiments discussed in Chapter 5. As for the PS particle system discussed above, the parameter space of the method was explored both to gain an insight into the synthetic mechanism and to develop simple, robust syntheses. This development was led by Mykolas Zupkauskas.

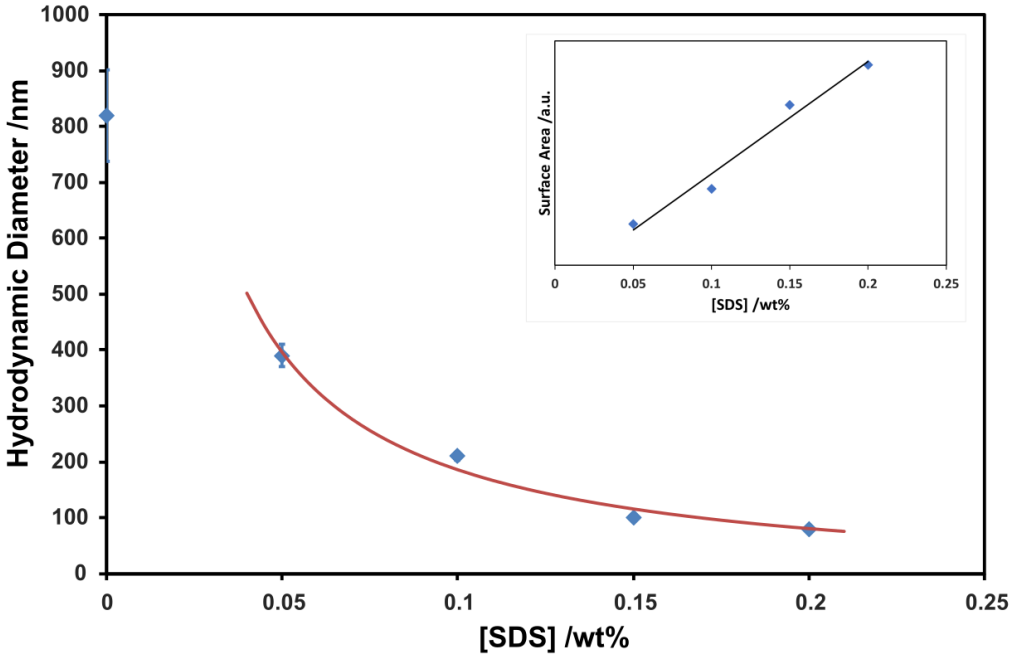

Figure 3.12: Plot of fluorinated latex colloid diameter dependence on SDS concentration. The red line is an isoline showing a constant surface area to SDS ratio. The insert shows the pseudo-linear relationship between total surface area and SDS concentration.

Optimisation of the protocol was done in smaller volumes than those described in Chapter 2.1.2, due to the cost of the fluorinated monomer. 1.3 g of HFBMA was emulsified at 70

°C in 50 ml of water with different concentrations of sodium dodecyl sulfate (SDS) varying between 0 and 0.2% w/w while stirring vigorously. The reaction was initiated by injecting 27.2 mg of KPS dissolved in 1 ml of deionised water and stopped after 12 hours by quenching on ice. Particles were washed by dialysis.

Figure 3.12 shows how the particle diameter depends on the SDS concentration in the reaction. The reaction follows the general trend established for emulsion polymerisations, where additional surfactant can stabilise particles earlier in their formation, leading to more, smaller colloids. The plot shows an approximately linear relationship between the total surface area of the colloids in the suspension and the concentration of SDS, as for a constant total particle volume, halving the average particle diameter will double the overall surface area.

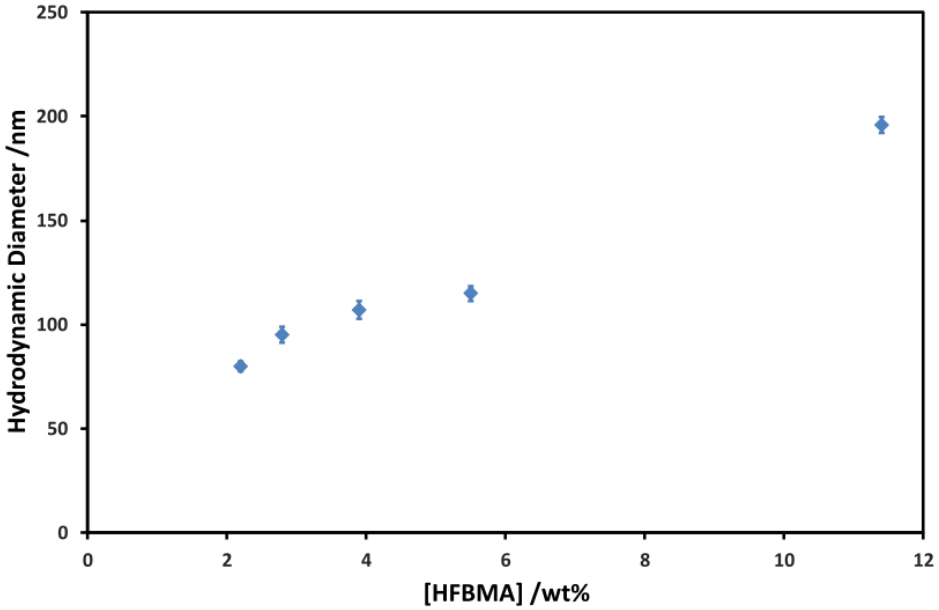

Figure 3.13: Plot of fluorinated latex colloid diameter dependence on monomer concentration.

Ultimately, more reliable control over the size of the particles was achieved by keeping the SDS concentration constant and varying the monomer concentration. Results are plotted in Figure 3.13. In a similar fashion to when varying SDS, increasing the monomer concentration increases the particle size as the system reacts to keep the surface area of growing particles constant. However, the dependence is no longer linear with surface area, as the monomer:initiator ratio is also changing.

The ability of the colloids to be index-matched to water was tested by dispersing 200 nm FL colloids at a concentration of 2% v/v in a series of sucrose solutions with concentrations varying between 0% and 26% w/v, as shown in Figure 3.14.

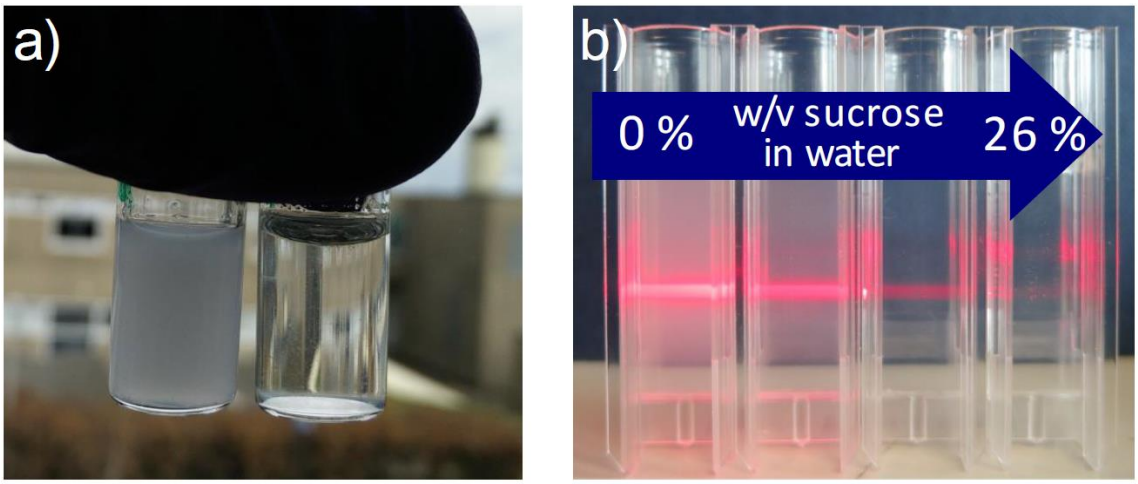

Figure 3.14: Refractive index matching of 200 nm FL particles in water with sucrose. a) Vials of 2% v/v FL200 colloids in deionised water and 26% w/v sucrose solution. b) The same suspension in a gradient series of sucrose concentrations, illuminated from the right. Taken from [83].

3.3.2 Surface Functionalisation

FL particles were functionalised by a similar swelling-deswelling method to the one developed for PS particles, due to its simplicity and high coverage. The same three commercially purchased block copolymers were used (PS_{30}, F108 and F127), but the PS_{30} synthesised by Mugemana and Bruns was replaced by poly(HFBMA)$_{14}$-*b*-PEG$_{79}$-N_3 (FL_{14}), under the expectation that the fluorinated polymer would have a higher affinity for the particle matrix than the polystyrene. One distinction was made from the PS functionalisation protocol, as it was found that a solvent of equal parts THF and water would dissolve the fluorinated latex particles. Instead, THF fractions of 33% and 20% were tested and the results measured by performing a fluorescence assay as before.

Coverages of different polymers at both 20% and 33% THF fractions are shown in Figure 3.15. It is immediately notable that coverages are better at 33% THF fractions, though the effect is more significant for some polymers than others. This is expected, as greater THF fractions will swell the particles more and improve the diffusion of the hydrophobic PS, FL or PPO blocks inside the particle matrix. FL_{14} displays good coverage at both 20% and 33% THF, perhaps not surprisingly, as the HFBMA block will have the strongest interactions with the particle matrix, while F127 shows poor coverage at both THF fractions. This is likely because F127 has by far the longest hydrophobic block and is a triblock instead of a diblock copolymer, hindering infiltration of the swollen particle.

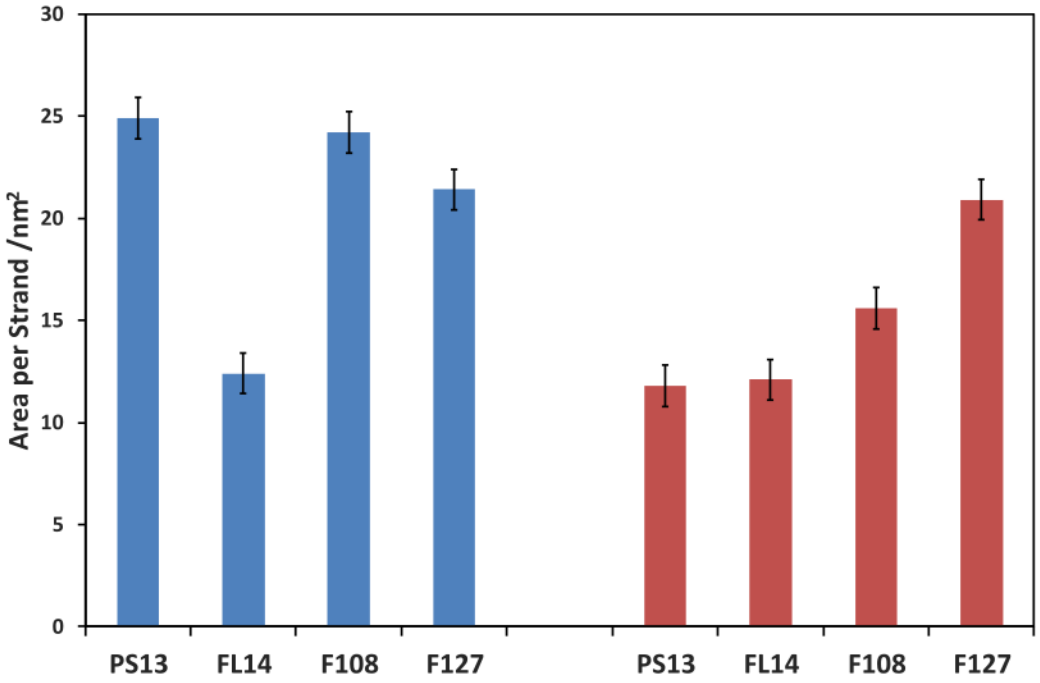

Figure 3.15: Coverages of different block copolymers grafted to 200 nm fluorinated latex particles via a swelling-deswelling mechanism. Blue bars represent those swelled at THF volume fractions of 20%, red those at 33%.

α DNA was bound to the azide-coated colloids via the SPAAC reaction, and the hydrodynamic diameters and zeta potentials measured for bare, PEGylated and DNA-coated colloids. These are plotted in Figure 3.16 and Figure 3.17 respectively.

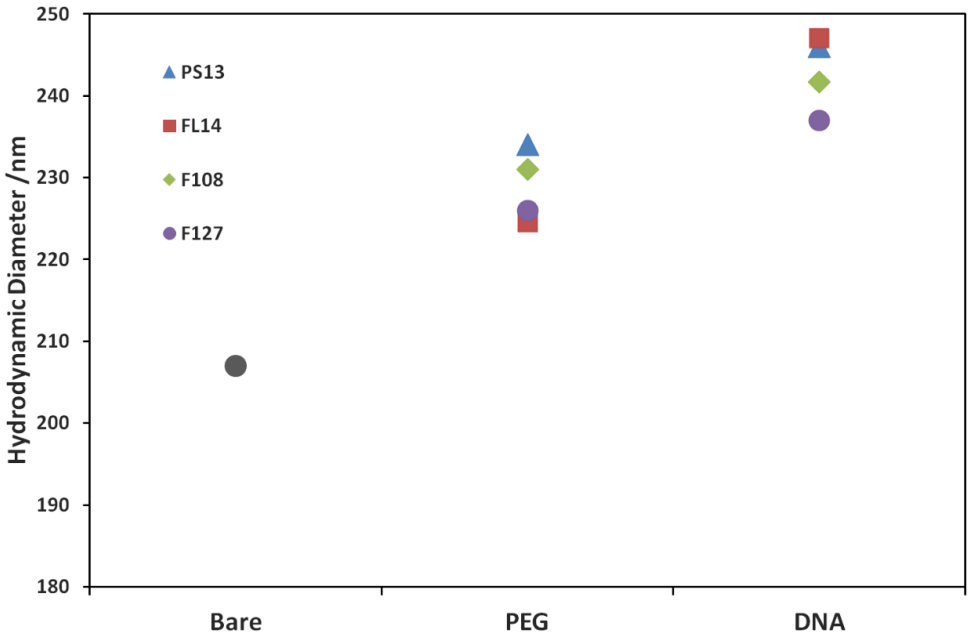

Figure 3.16: Hydrodynamic diameters of fluorinated latex colloids grafted with a range of block copolymers in the bare, PEGylated and DNA-coated states. Measured by DLS.

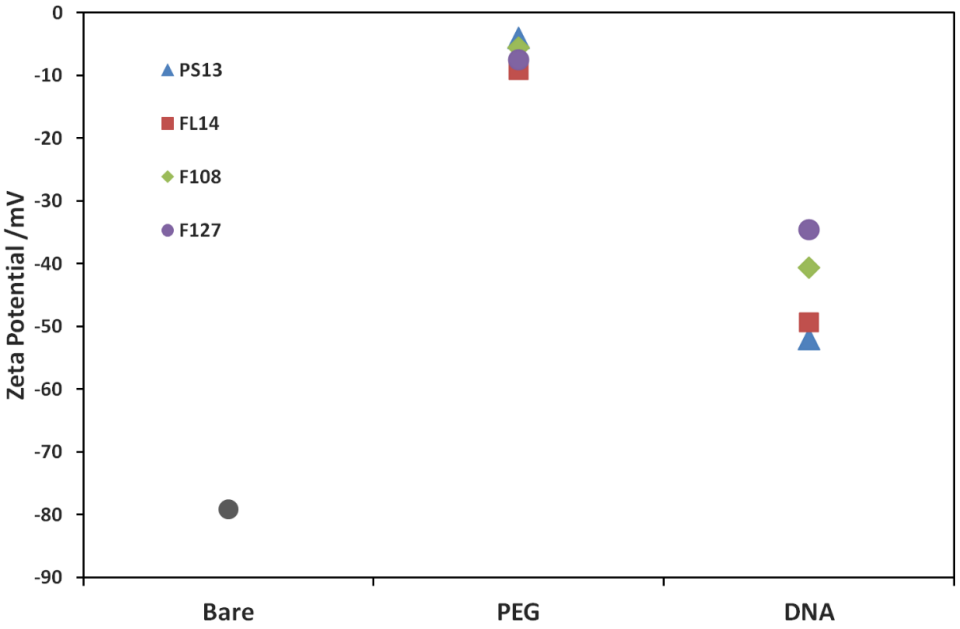

Figure 3.17: Zeta potentials of fluorinated latex colloids grafted with a range of block copolymers in the bare, PEGylated and DNA-coated states.

The diameters follow a predictable pattern based on the discussion of grafted polymer conformation from Chapter 3.2.3, with F127 showing the smallest size increase due to the low coverage. FL_{14} shows a small increase from bare to PEGylated due to the short length of the polymer, but a large increase from PEGylated to DNA-coated due to the high coverage. The zeta potentials follow a similar trend to those from PS, where the PEG chain screens the negative surface charge, before the negative backbone of the DNA makes the charge more negative again. As expected, the higher coverages achieved using the diblock copolymers compared to the triblocks leads to a lower zeta potential for the DNA-coated FL colloids grafted with FL_{14} and PS_{13}.

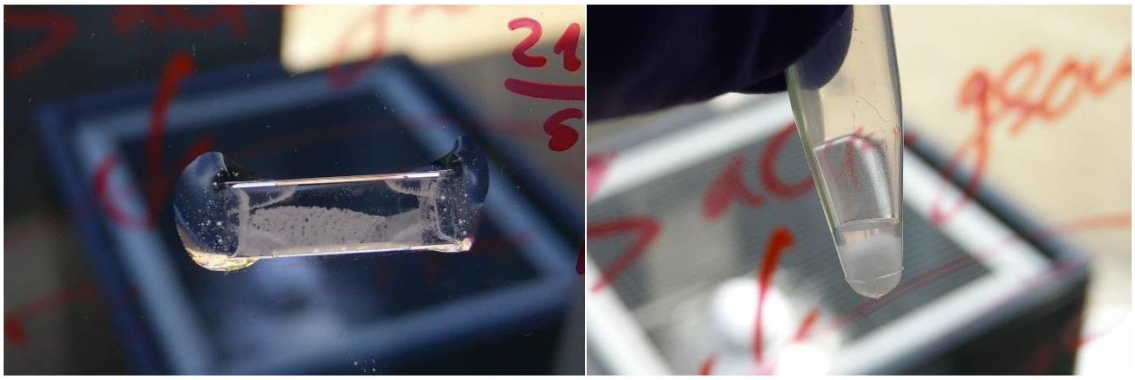

Figure 3.18: 1100 nm FL particles gelled through DNA-mediated attraction in a glass capillary 200 µm in thickness (left) and an Eppendorf tube (right). Image provided by Mykolas Zupkauskas.

Finally, 1.1 µm colloids coated with complementary α and α' DNA were mixed to check DNA coverage was high enough to mediate thermally reversible gelation. Complementary colloids were dispersed in 10 mM phosphate buffer (PB) with 50 mM NaCl to ensure good solvation of the DNA. Samples of 5% v/v 1.1 µm FL colloids coated with α and α' are shown in Figure 3.18 in a glass capillary and an Eppendorf tube. Gelation is clearly visible by eye. The gels formed do not percolate the full volume due to the high density of HFBMA, which causes the gels to partially collapse under their own weight immediately on formation.

3.4 Mixed Acrylate Colloids

Methacrylates and acrylates, most notably poly(methyl methacrylate) (PMMA) are perhaps the most widely studied of any polymers, particularly for their use as polymer colloids. PMMA and poly(butyl acrylate) (PBA) were investigated as part of this thesis as possible alternatives to PS and then later as candidates for low glass-transition temperature polymer colloids for fusion post self-assembly. Finally, colloids of PMMA, PBA and HFBMA were all synthesised using the same protocol and the results compared to give insight into the mechanism.

3.4.1 Synthesis

Methyl methacrylate (MMA) and butyl acrylate (BA) are both only partially soluble in water and so aqueous polymerisation reactions follow an emulsion or surfactant-free emulsion polymerisation archetype[156]. PMMA and BA below 100 nm were synthesised by polymerisation with SDS, while sizes between 100 nm and 500 nm were achieved without SDS.

For emulsion polymerisation, monomer(s) were added to an aqueous solution of SDS, purged with nitrogen for 30 minutes and then emulsified at 75 °C. A solution of KPS in water was injected and the reaction allowed to proceed with vigorous stirring (900 rpm) for 24 hours. Monodisperse colloids in the size range of 40 nm to 90 nm were collected by quenching on ice and washing by dialysis.

For surfactant-free emulsion polymerisation, KPS (160 mg, 12 mM) was dissolved in 50 ml deionised water and purged with nitrogen for 30 minutes before being sealed and heated to 75 °C. Monomer(s) (typically 1 g) were injected through the seal and the reaction allowed to proceed with vigorous stirring (900 rpm) for 24 hours, before being

quenched on ice. Colloids were washed either by dialysis or by centrifugation, depending on their size.

While monodisperse highly negatively charged colloids were obtained using both methods, both PMMA and PBA displayed greater charge polydispersity than PS particles. In addition, the lower density of PS means that colloids can be density matched with the medium by dispersion in moderate sucrose solutions, eliminating effective gravitational forces and therefore removing the barometric height distribution typically observed in colloidal suspensions. For these reasons, PS was used instead of PMMA and PBA for the experiments on DNA-coated and charge-stabilised colloids discussed in Chapters 4 and 5. However, the similar chemistry of MMA and BA makes them ideal candidates for the synthesis of copolymer colloids.

3.4.2 Random Copolymer Colloids

Copolymerisation can dramatically change the physical properties of a polymer or polymer colloid. Block copolymers frequently exhibit amphiphilic behaviour, as has already been exploited during this work. When block copolymers are self-assembled into particles or superstructures, a number of interesting materials are observed due to what is effectively intra-molecular phase separation[71,82,157]. In contrast, the synthesis of particles of random or statistical copolymers allows for the tuning of a wide range of physical properties between the extremes of the different components, including density, refractive index and glass transition temperature[158].

Despite their similar chemistry, PMMA and PBA have quite different physical properties. They have similar densities and refractive indices, but the glass transition temperature of PMMA is 105 °C, while for PBA it is -53 °C, allowing the tuning of the glass transition temperature through easily accessible experimental temperature ranges by varying the ratio of MMA:BA in a copolymerisation. In this work, PMMA-*r*-PBA particles with a glass transition temperature of 39 °C were synthesised, so that assembled structures could be fused at temperatures tolerant of DNA and other biomolecules. Due to the similar chemistry of MMA and BA, the monomers do not phase separate on polymer synthesis, instead forming a statistical copolymer instead of a block copolymer, as demonstrated by the single composition-dependent glass transition temperature measured by differential scanning calorimetry (DSC).

Particle size was found to be independent of initiator concentration over a wide range, analogously with the FL particles, but an approximately linear dependence was found

between monomer mass and particle volume, as shown in Figure 3.19. This is consistent with results reported in the literature for pure PMMA and PBA[159] and implies that particle size is determined early in the synthesis by the number of seed micelles formed. Once the reaction begins, oligomers are initiated and grow until the critical micelle concentration (CMC) is reached, at which point they form micelles. These micelles are then swollen by unreacted monomer diffusing from the droplet phase and act as the locus for all further polymerisation. The CMC depends only on the solubility and interfacial properties of the growing oligomers, so the number density of particles is set by the choice of monomer and solvent. By varying the monomer concentration, the final particle size can then be tuned across a wide range.

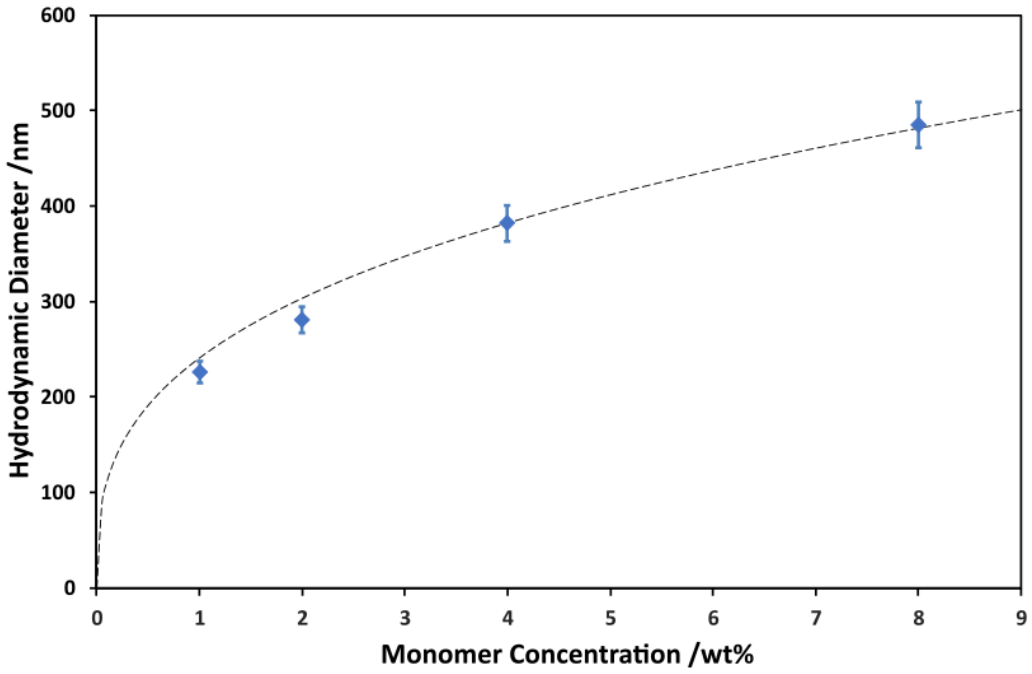

Figure 3.19: Effect of initial total monomer concentration during synthesis on the diameter of PMMA-r-PBA colloids. Monomer ratio, reaction volume and KPS concentration were fixed at 70:30, 50 ml and 160 mg (12 mM). The dashed line shows a cubic dependence.

It is unclear whether this is a true random copolymer, in which the probability of any unit in the backbone being a specific monomer is equal to that monomer's stoichiometry in the overall reaction[158], as it was also observed that the particle size is broadly independent of the ratio of different monomers, as shown in Figure 3.20, and more closely resembles the pure PMMA case, implying MMA polymerisation is more significant in the early stages of the reaction. This is due to the greater solubility of MMA in water[160]; as micelles form, MMA is better able to diffuse to them from the monomer droplets, giving the

particles greater MMA character during the initial stages of the reaction when the number of growing nuclei is determined[161].

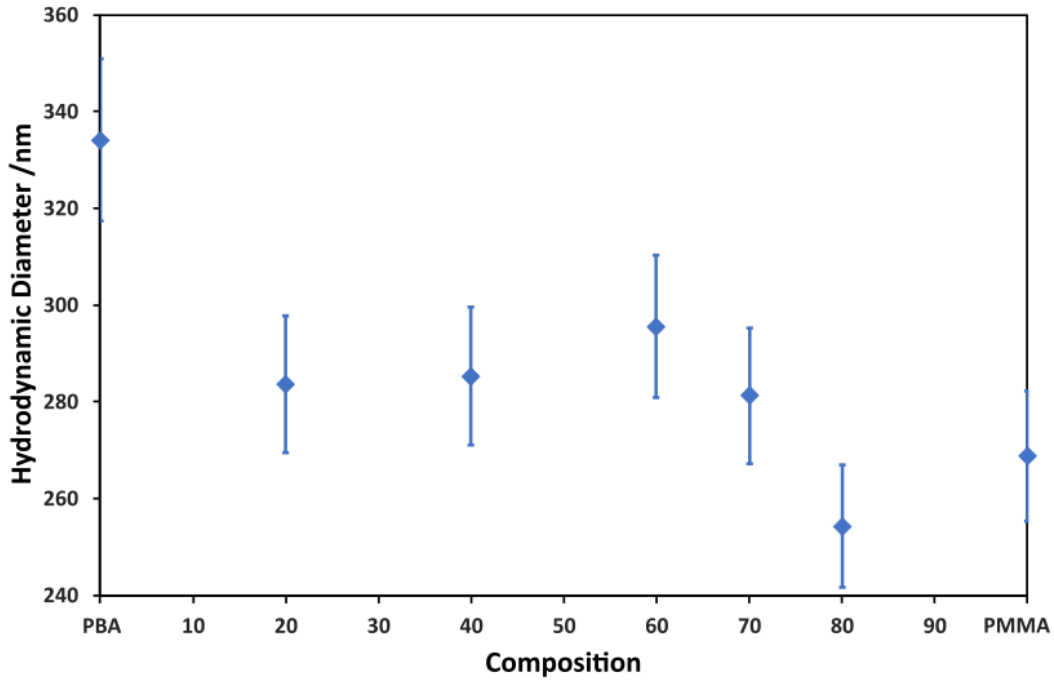

Figure 3.20: Effects of monomer ratio on particle size for PMMA-r-PBA colloids. Monomer, water and KPS quantities were fixed at 1 g, 50 ml and 160 mg (12 mM).

Finally, the effects of composition on the glass transition temperature of the colloids were investigated and are plotted in Figure 3.21. Glass transition temperatures were determined by differential scanning calorimetry. Samples of known mass were cycled between -60 °C and 120 °C at least three times and the glass transition observed as a peak overlaying a change in the heat flow gradient. The glass transition temperature was taken as the onset of this peak and averaged over both heating and cooling cycles.

The glass transition temperature varies smoothly between the pure cases and agrees well with the Kwei equation for the glass transition temperature of a polymer blend[162]

$$T_g(1,2) = \frac{w_1 T_{g,1} + k w_2 T_{g,2}}{w_1 + k w_2} + q w_1 w_2 \qquad (3.3)$$

where w_i and $T_{g,i}$ are the weight fraction and glass transition temperature of polymer i and k and q are fitting parameters. A value of $k = 1$ is common for similar polymers, and q can be interpreted as a measure of the change in stabilisation of the polymer backbone between the copolymer and the weighted average of the pure polymers[163]. In this case it implies that the backbones are less well stabilised in the random PMMA-*r*-

PBA polymer than in PMMA or PBA, which is expected, as efficient packing of the polymer backbones will be disrupted by copolymerisation, and no additional stabilising interactions (hydrogen bonding, dipole forces etc.) will be introduced due to the similar chemistry of MMA and BA.

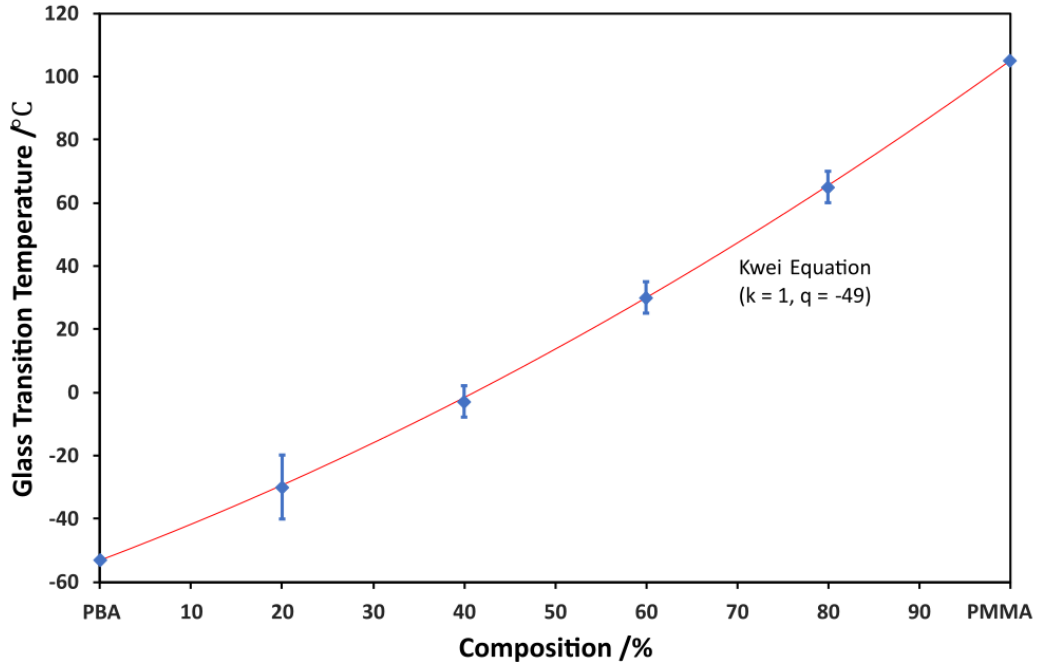

Figure 3.21: Dependence of the glass transition temperature of PMMA-r-PBA colloids on monomer ratio. The red curve shows the data fitted with the Kwei equation.

3.4.3 Comparison of Similar Monomers

PMMA, PBA and FL (PHFBMA) colloids were all prepared by the same surfactant-free emulsion polymerisation method. 1 g of monomer was injected into a flask containing 200 mg of KPS dissolved in 50 ml of water at 75 °C and reacted for 24 hours. The resulting sizes are shown in Figure 3.22. As the monomers become more hydrophobic and less soluble, the CMC of the growing oligomers becomes lower, leading to fewer micelles formed and therefore fewer, larger particles. The HFBMA monomer is so poorly soluble in water that the reaction no longer produces monodisperse particles, implying that micellisation is driven too quickly for the formation of well-defined particles.

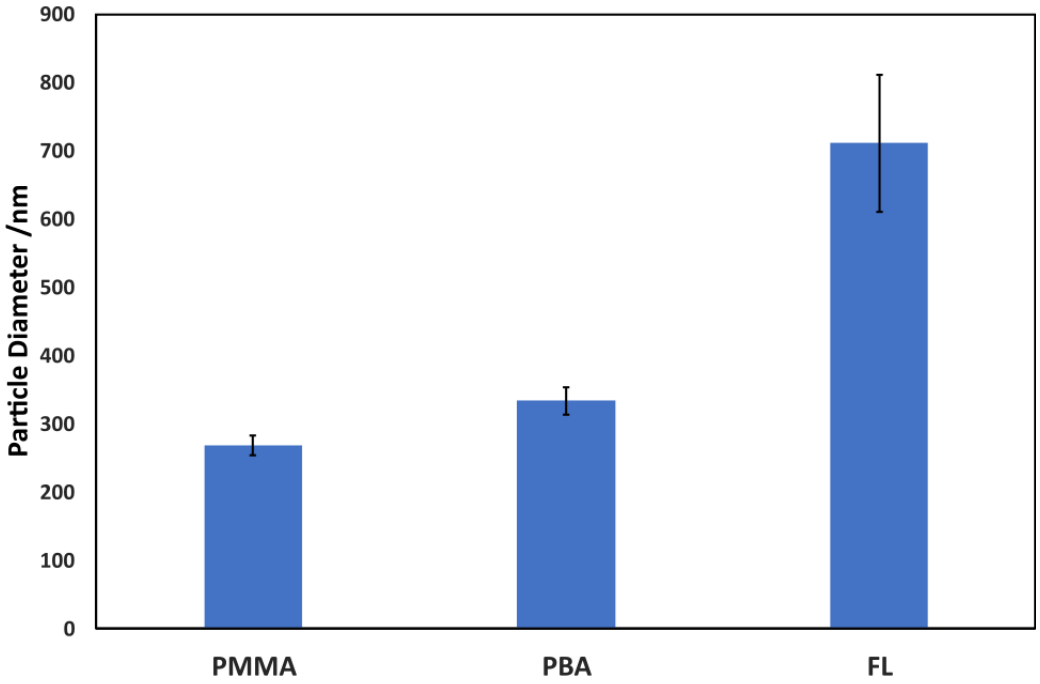

Figure 3.22: Sizes of different methacrylate and acrylate colloids produced using the same synthesis protocol.

3.5 Conclusions and Outlook

This chapter presented the colloidal synthesis and functionalisation methods developed as part of this thesis. Polystyrene, fluorinated latex and poly(methyl methacrylate)-*r*-poly(butyl acrylate) colloids were synthesised by a variety of surfactant-free emulsion, emulsion and dispersion polymerisations. Particle size was controlled by varying the initial concentrations of reactants; the specific effects of key reactants were reported, and the optimal control methods determined. Based on these results, coherent mechanisms were proposed for each type of synthesis.

Colloids were functionalised by densely grafting amphiphilic diblock and triblock copolymers to the particle surface via a swelling-deswelling mechanism with THF. Different conditions were trialled, and an optimal method developed. This surface grafting both stabilised the suspensions against non-specific aggregation and introduced surface functionality based on the terminal functional groups of the grafted polymers. DNA was bound to the colloids via a strain-promoted azide-alkyne cycloaddition between a DBCO group attached to the DNA and an azide group on the grafted PEG polymers.

These methods represent a substantial improvement on those reported in the literature, either in terms of simplicity, effectiveness or cost. Emphasis was placed on the development of one-pot, single-step colloidal syntheses that did not require additional processing steps as this vastly simplifies scale-up of such a method. Surface functionalisation and grafting densities were shown to be an order of magnitude higher than those of the commercial particles previously used and were equivalent or better than those reported by other research groups.

4 DNA-Coated Colloidal Gels

As discussed in Chapter 1, colloidal self-assembly has been demonstrated to be a viable route toward a large variety of long-range ordered, short-range ordered or amorphous materials. DNA-mediated self-assembly is one of the most widely used subcategories, due to the reliability, specificity, tuneability and thermal reversibility of the DNA hybridisation interaction. However, despite great interest in the use of DNA-coated colloids for the synthesis of new crystalline phases, success has been limited by their sharp melt curve and very long equilibration timescales.

Our group has demonstrated the assembly of DNA-coated colloids into percolating gels through kinetically arrested spinodal decomposition. These gels have been shown to have a range of interesting properties and potential applications, for example as high surface area scaffolds, bicontinuous media or low-density, high strength micromaterials. This thesis focuses on the application of colloidal gels as structural colour materials.

Keratin-air gels observed in nature have been shown to give rise to strong, non-iridescent, coherent structural colour[113-115]. These gels are formed via an arrested spinodal decomposition induced in a suspension of keratin fibres and are micro- and macroscopically very similar to the DNA-coated colloidal gels previously reported in the literature[73]. Hence, we propose DNA-coated colloidal gels as an excellent synthetic analogue for these unique natural materials.

This chapter discusses the gelation of polystyrene and silica DNA-coated colloids. Methods are presented for the production and characterisation of colloidal gels and the

dependence of gel structure on thermal history is investigated. In order to effectively synthesise materials with structural colour, fine control is needed over the length-scales present in the arrested phases. While the mechanism of colloidal gelation has at this point been well explored, no work has been done looking at how this mechanism varies with colloid size. Scaling laws are derived based on the behaviour of systems of DNACCs ranging in diameter from 80 nm to 800 nm. Finally, the optical activity of these synthetic gels is presented and compared with results from natural materials.

The results presented in this chapter comprise work published in reference [164] and another manuscript in preparation [165]. The experiments on silica gels were led by Zachary Ruff.

4.1 Preparation and Characterisation

Initially, the biotin-streptavidin functionalisation method was used to produce PS colloids for gelation experiments. However, it was found that DNA coverages were too low to give gels with consistent structures from experiment to experiment. Hence, PS colloids were synthesised and functionalised with PEG and DNA by the swelling-deswelling methods laid out in Chapter 2.2.2, due to their flexibility and resulting high grafting density. Particle preparation is shown schematically in Figure 4.1. Amine coated silica colloids were purchased from Micromod and functionalised via the carbodiimide chemistry protocol detailed in 2.2.4. Double-stranded DNA spacers were unnecessary, due to the presence of the long PEG polymer, and so α and α' DNA with a short thymine joint were used (sequences given in Chapter 2.2.3).

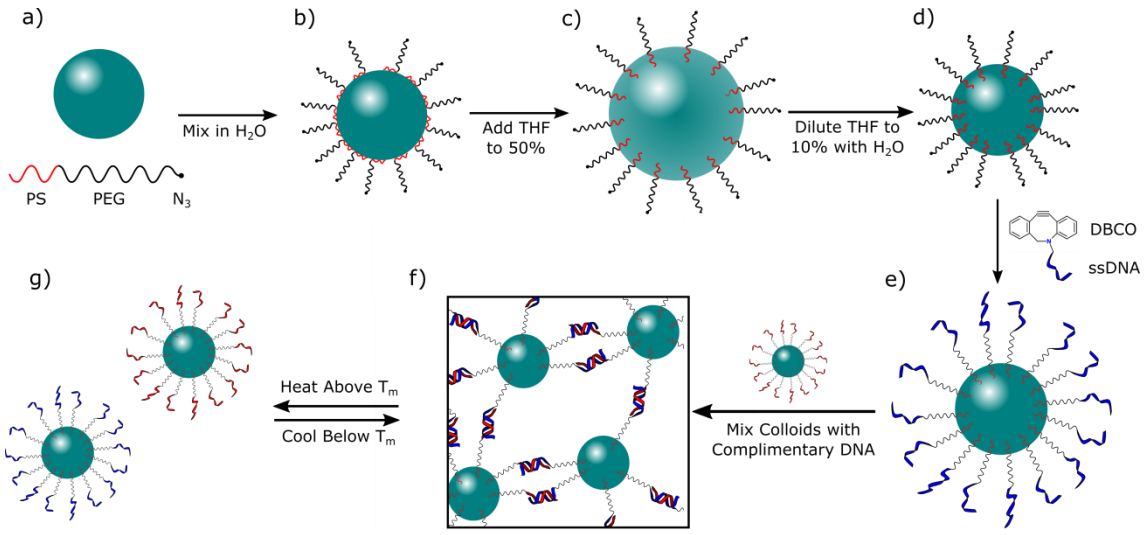

Figure 4.1: Particle functionalisation, showing amphiphilic polymer grafting via swelling-deswelling, DNA coupling and thermally reversible gelation.

Where necessary for imaging, colloids were also mixed with an excess of DBCO-Cy5 fluorescent dye after DNA binding, reacted overnight at 60°C and washed by centrifugation. The dye was found to bind to the ~10% of azide sites that remain unoccupied by DNA after initial functionalisation, allowing colloids to be imaged in fluorescence. This method was preferable to the earlier method of labelling particles with dye during synthesis, as it avoided the tendency of the hydrophobic dye to diffuse out and form droplets during heating.

Gels were prepared by mixing two suspensions of colloids functionalised with complementary strands of DNA in 10 mM PB with 62.5 mM NaCl, to provide an appropriate pH and ionic strength solution for DNA hybridisation. Where density matching was required, sucrose solution was added to 220 gL^{-1} to match the density of the solvent to that of the PS particles to < 10^{-3} g cm^{-3}. Gelation was immediately observed on mixing and could be coarsened by shearing through pipetting. Samples were injected into glass capillaries and sealed with epoxy. Before imaging, samples were heated on a Peltier stage to 75 °C, well above the melt temperature of the DNA sticky ends and held there for 90 minutes to homogenise the suspension. This removed any shear-dependent secondary structure and ensured the samples started as a homogenous colloidal gas. Samples were then quenched to room temperature at 20 $Kmin^{-1}$, deep into the two-phase region, triggering phase separation into a percolating gel. Figure 4.2 shows the same sample before and after homogenisation; before homogenisation the gel is far more globular and collapsed. Coarsening of the colloid-rich phase was clearly observable with the naked eye with sufficient pipetting.

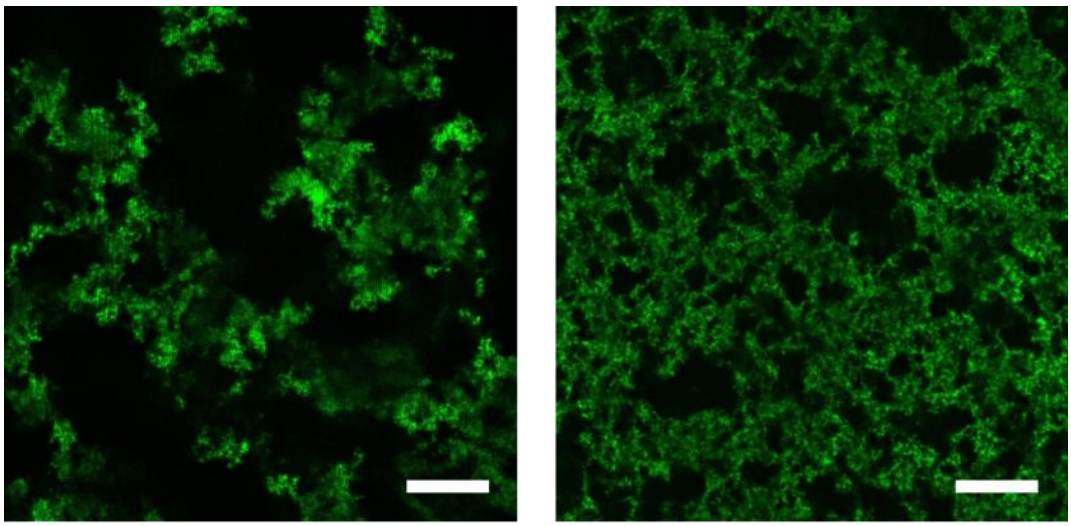

Figure 4.2: Confocal micrograph of the same 4% w/w gel of 210 nm polystyrene colloids immediately after pipetting and injection (left) and after homogenisation at 75 °C (right). Both images are taken at room temperature. Scale bars are 20 µm.

The effects of temperature variation on gel formation could not be imaged live using confocal microscopy as the melt temperature was above the safe working temperature of the oil immersion objective used. Hence, in situ temperature change experiments were imaged using a Peltier stage attached to an inverted optical microscope capable of imaging in bright field, reflectance or epifluorescence modes. Samples were again homogenised well above the melt temperature and then imaged during sequential cooling/heating cycles to observe the emerging structure on phase separation. Melt transitions were found to occur over a range of less than 1 °C, as shown in Figure 4.3, and displayed minimal hysteresis provided heating and cooling rates were slow. As discussed in Chapter 1.2.2, the melt temperature of the DNA-coated colloids (47°C) is much higher than the temperature of the free DNA strands (37.5°C) due to the presence of many hybridised DNA strands in the inter-particle volume[45]. It was shown that these gels had the same structure over many melt/quench cycles.

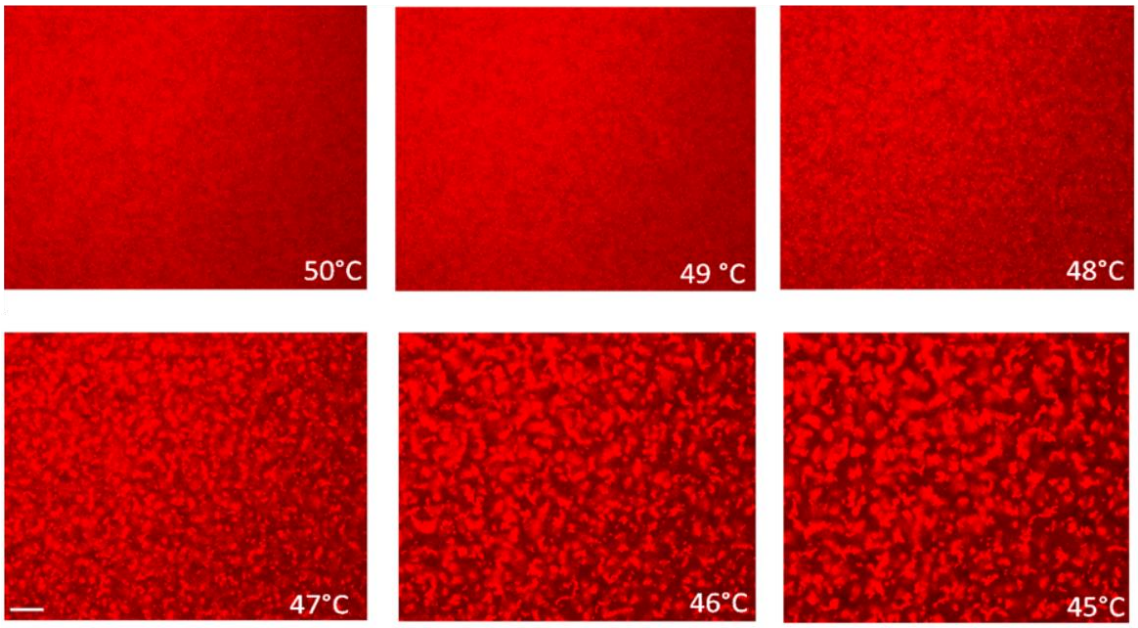

Figure 4.3: Optical microscopy of a 5% w/w suspension of 527 nm polystyrene colloids coated with A and A' DNA, showing the sharp melt transition at 47 °C. Scale bar is 10 µm.

Confocal microscopy was used to record high resolution *z*-stacks of gels - series of micrographs at different depths into the sample forming a complete three-dimensional record. Sedimentation in the system was minimised through density matching with sucrose, so the gels were isotropic, nominally allowing the use of any frame to obtain meaningful results. However, it was found that a small fraction of the colloids stuck to the glass walls of the capillary due to non-specific interactions. This "stuck layer" did

cause some distortions to the gel structure close to the edges, while contrast decreased deeper into the sample due to multiple scattering. To correct for this, *z*-stacks were processed to determine the height of the stuck layer and the "data frame" (the image on which further analysis was done and results extracted) was set at a specific height deeper into the sample, normally 10 µm. Examples of this analysis are shown in Figure 4.4. A reliable way to locate the stuck layer was to plot the average pixel intensity for each frame and take the second derivative with respect to height. The first zero in this function corresponded extremely well with the stuck layer, even for angled samples. This layer was then considered to be height 0 µm.

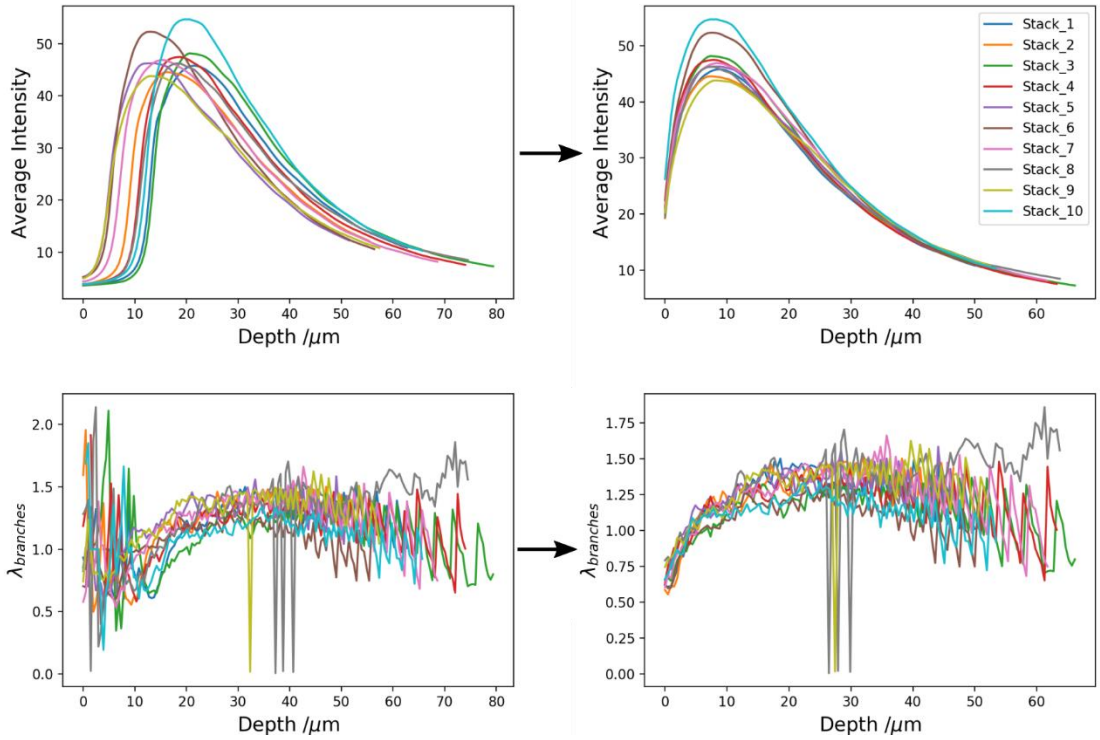

Figure 4.4: Analysis of multiple z-stacks from the same sample. Stacks were standardised by referencing all data to the capillary wall by finding the turning point in the gradient of the average frame pixel intensity. Raw (left) and corrected (right) data for the average frame pixel intensity (top) and the decay constant λ for the gel branches (bottom) are shown. Decay constants were calculated using the method described in Chapter 2.4.1.

To confirm the effects of frame height on the chord analysis results from the gel network, the decay length λ was calculated for each frame of a series of *z*-stacks taken from the same sample, following the method reported in Chapter 2.4.1. While the traces are quite noisy, due to the small sample size for each calculation, it is clear that after stuck layer correction, the values follow the same curve: smaller values are obtained close to the

capillary walls due to structural distortions from adsorbed colloids, before plateauing to a constant value.

Once this correction was applied, more accurate decay constants were calculated by combining data from multiple *z*-stacks. For each sample, at least ten *z*-stacks were measured, and the stuck layers and data frames determined. The chord histogram was then constructed by reaping chords from the data frames of all *z*-stacks before fitting the exponential, to determine a single value for $\lambda_{colloids}$ and λ_{pores} for each sample. Decay constants for different samples with the same suspension and quench conditions were found to have good agreement and were averaged to ensure a high level of accuracy.

4.2 SAXS of Colloidal Gels

Colloidal gels were also characterised using SAXS, as it gave information about finer features than those visible in optical microscopy. When using a sample-to-detector distance of 10 m and an x-ray wavelength of 1 Å, as described in Chapter 2.3.9, the measureable q range is between 0.0069 and 0.7727 nm^{-1}, corresponding to real-space length-scales between 8 and 901 nm in size. However, in practice, signal at very low q values is dominated by the form factor[122] and is obstructed by the beamstop, making features larger than 500 nm very difficult to distinguish in our samples, where the electronic contrast between the gel and the medium is low. Unfortunately, this means that for the 80 nm and 210 nm DNA-functionalised PS particles investigated with SAXS, it is impossible to extract quantitative information about features several colloid diameters in size, like the thickness of the gel branches. Nevertheless, SAXS does let us test a number of behaviours of colloidal gels that are otherwise difficult to measure.

Figure 4.5 shows SAXS data from gels of 80 nm PS colloids coated with α and α' DNA at overall concentrations of 2%, 4%, 8% and 16% w/w. Samples were all homogenised at 75 °C and quenched into the two-phase region at 20 $Kmin^{-1}$. The structure factor was extracted by dividing the scattered intensities by a form factor measured from a gas-phase suspension of 80 nm PS colloids at 2% w/w.

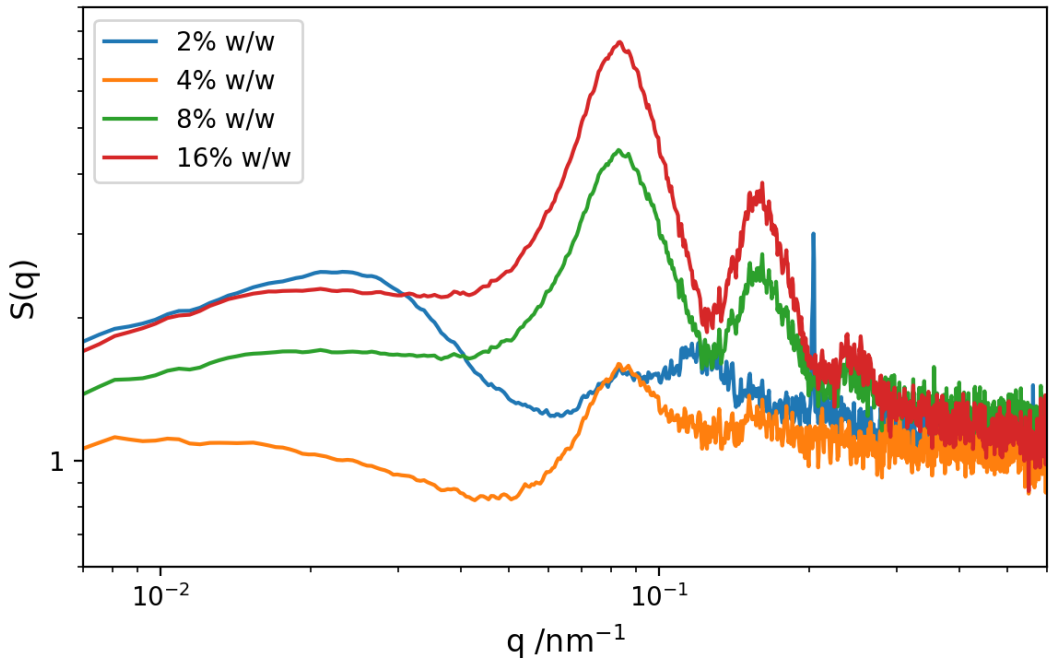

Figure 4.5: Structure factors obtained from SAXS for gels of 80 nm polystyrene colloids coated with α or α' DNA at concentrations of 2%, 4%, 8% and 16% w/w. Samples were all normalised against the background and divided by a form factor measured from a 2% w/w gas phase sample of the same colloids.

While the form factor division is not perfect, as evidenced by the "overtone" peaks at q values with integer fractions of the colloid diameter, some information can still be extracted. First, there is a clear signal at q values of 0.079 nm^{-1}, corresponding to real-space distances of 80 nm, or one colloid diameter. This peak grows quickly on gelation, as particles are bound in close contact by the DNA interaction. Second, there is a broader peak at q values of 0.02 nm^{-1}, corresponding to features ~300 nm across. This is in good agreement with previous works, which predicted that gels of DNACCs would have branches approximately four colloids thick[42,57,78]. Gels at all four concentrations show the same peak corresponding to the same branch width, which is consistent both with observations from optical microscopy, shown in Figure 4.15, and our model. As the concentration of a DNACC suspension increases, the characteristic thickness of the gel branches does not coarsen but instead the pores are subdivided by the formation of additional branches, as shown schematically in Figure 4.6.

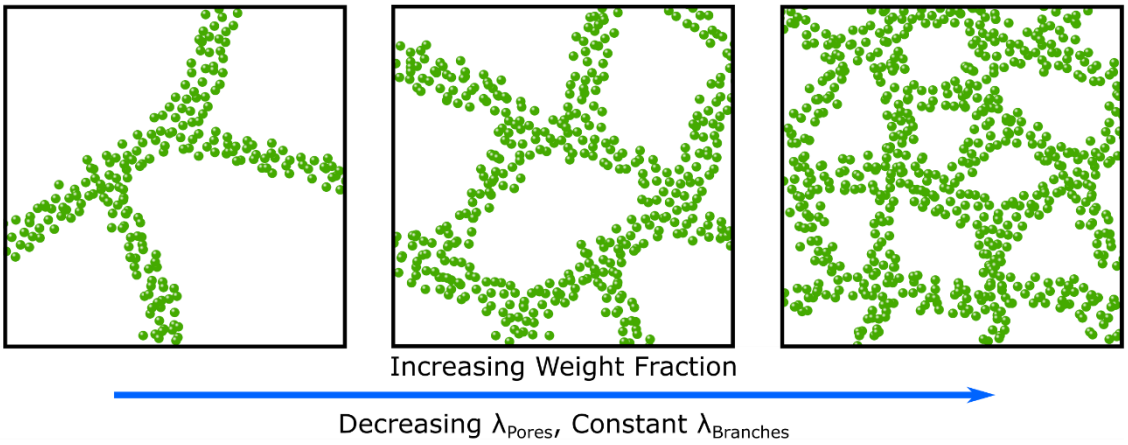

Figure 4.6: Schematic showing pore subdivision in a colloidal gel. Instead of coarsening existing arms, increasing the weight fraction of colloids instead forms new gel branches, making pores smaller.

SAXS traces were also recorded while samples were temperature cycled at a constant heating/cooling rate. An initially homogenised and subsequently rapidly quenched sample was loaded into a temperature controlled sample stage and held at 40 °C for 300 s before the temperature ramp was started. The sample was heated from 40 °C to 70 °C (or 75 °C) and held there for 300 s before cooling back down to 40 °C again, as shown in Figure 4.7b. Heating/cooling rates were fixed at 2 Kmin^{-1} and scattered intensities were measured every 10 s.

Figure 4.7a shows a series of structure factor $S(q)$ traces from a sample of 80 nm polystyrene DNACCs at an overall concentration of 4% w/w as the temperature ramp is carried out. It can be seen that the initial gel peaks observed in Figure 4.5 at 0.079 and 0.02 nm^{-1} quickly disappear once the sample reaches the melt tempeture of the DNACCs, here measured as 57 °C, leaving very little structural information in the melt phase as expected.

As the sample is cooled, a broad peak initially forms around 5 °C above the melt temperature at q values of around 0.055 nm^{-1}, corresponding to real-space distances of ~115 nm. This peak was observed across multiple quench depths and rates and colloidal volume fractions, binding strengths and sizes (although it does scale linearly with size), but appears exclusively during cooling. To our knowledge, the existence of a loose association phase has not been reported in any previous experimental literature and does not fit with the relatively mature theoretical understanding of this type of attractive colloids. As such, we attribute this peak to instrumentation error, most likely relating to temperature control. Temperature control was achieved using a sealed sample holder with

transparent windows equipped with a thermocouple and the imaged sample section suspended in an air gap. Heating was achieved using a heating element immediately adjacent to the sample, while cooling was done using air cooled with liquid nitrogen and is therefore likely to be non-uniform. We attribute this peak to the formation of transient clusters due to temperature inhomogeneities on cooling. Upon reaching the melt temperature, the suspension phase separates and these loose associations quickly decay as the colloids bind. Figure 4.7c displays a zoomed overlay of the $S(q)$ traces as gelation occurs upon cooling. It shows the broad association peak shifting to higher q values and sharpening into the characteristic nearest-neighbour peak while the broader "branch" peak also grows over the same narrow temperature window. This sudden behaviour supports the sharp melt transition for DNACCs reported extensively in the literature and observed previously in this work with optical microscopy.

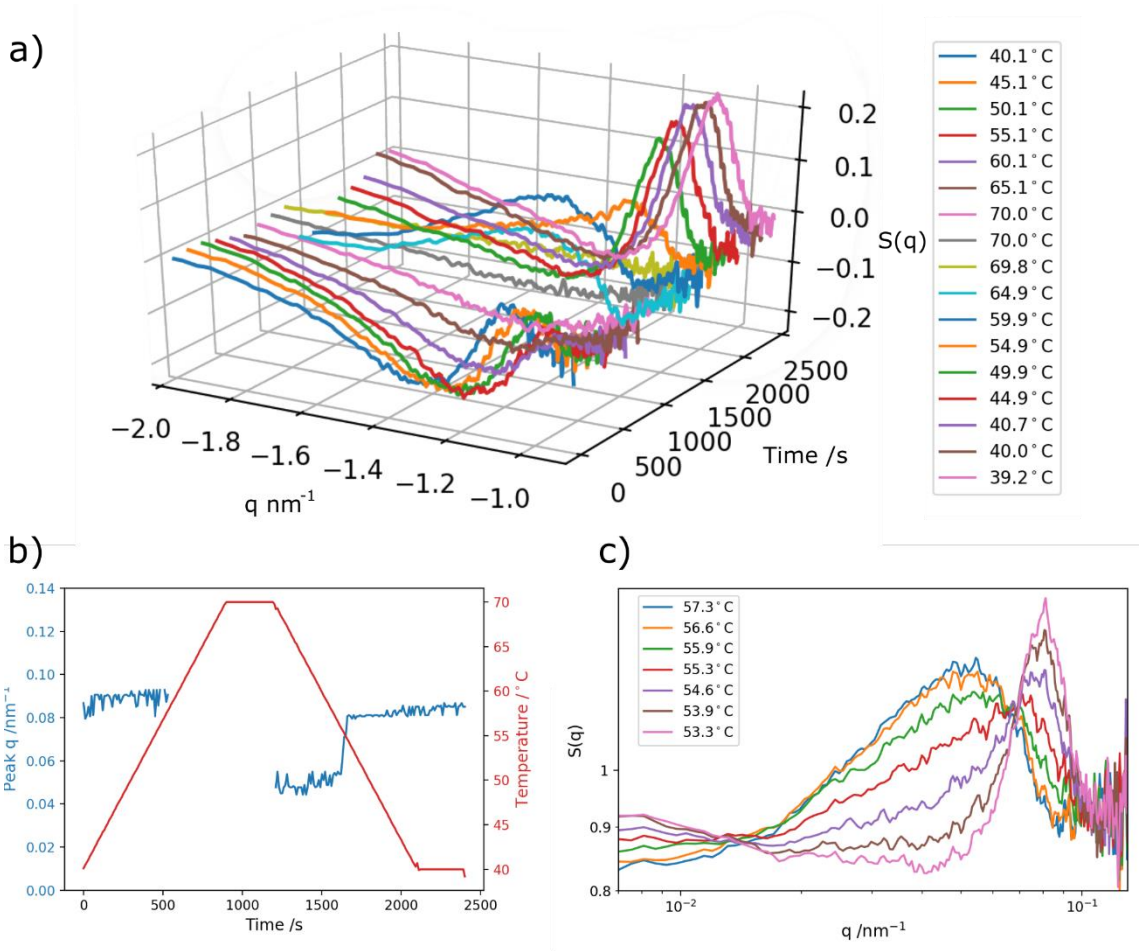

Figure 4.7: SAXS structure factors measured from a sample of 80 nm PS colloids at 4% w/w. a) S(q) traces as the temperature is ramped up and down. b) Temperature profile and the location of the peaks in S(q) against time. c) Zoomed overlay of S(q) traces as gelation occurs.

Figure 4.7 (left) shows the temperature profile used for the heating/cooling ramps and the location of the first peak in the $S(q)$ trace for each exposure. It should be noted that the broad "branch" peak was too shallow to be detected by this analysis; instead it highlights the hard-contact and loose-association peaks and the abrupt transition between the two regimes. No peak is detected between 500 and 1200 s, as the system is fully melted and hence has a structure factor $S(q) \approx 1$.

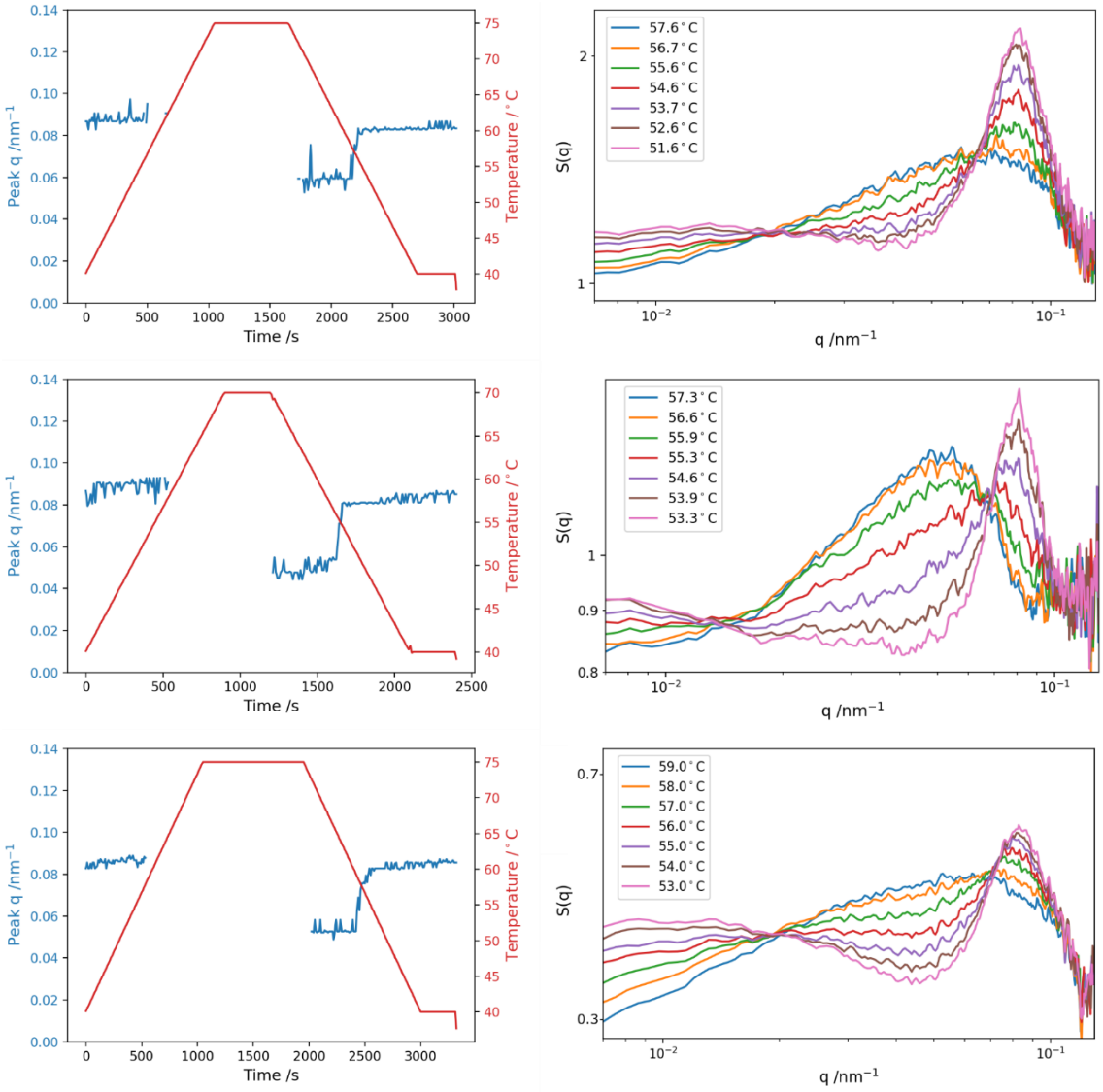

Figure 4.8: SAXS data from in situ heating and cooling of 80 nm PS DNACC gels at 2% w/w (top), 4% w/w (centre) and 16% w/w (bottom). Left: Temperature profile and the location of the first peak in S(q) against time. Right: Zoomed overlay of S(q) traces as gelation occurs.

Figure 4.8 shows similar SAXS data for samples at concentrations of 2%, 4% and 16% w/w during the same heating/cooling cycle. As expected, all concentrations display the

same colloidal melt temperature of 59 °C and position of the sharp $S(q)$ peak after gelation. They also all follow the same pattern of a broad association peak forming between 65 °C – 59 °C, which then sharpens on gelation. As concentration increases, this association peak becomes broader and moves to slightly lower q values, from around 0.06 nm^{-1} at 2% w/w to 0.05 nm^{-1} at 16% w/w, possibly due to a higher collision rate between particles.

In addition, as the concentration of the final gel increases, the ratio of the height of the "branch" peak to that of the nearest neighbour peak increases, while the position of the "branch" peak moves to slightly longer real-space distances, implying a very slight coarsening of the gel arms in addition to the pore subdivision already discussed. This effect is most visible in the structure factors of the fully quenched gels, as the S(q) continues to evolve in small ways even as much as 10 °C below the melt temperature, similar to the weak coarsening also seen in structure factors measured from optical microscopy. Figure 4.9 shows structure factors for PS80 gels at 2%, 4% and 16% w/w after quenching to 40 °C at 2 $Kmin^{-1}$, emphasising the "branch" peak at low q values shifting to even lower q's at higher weight fractions.

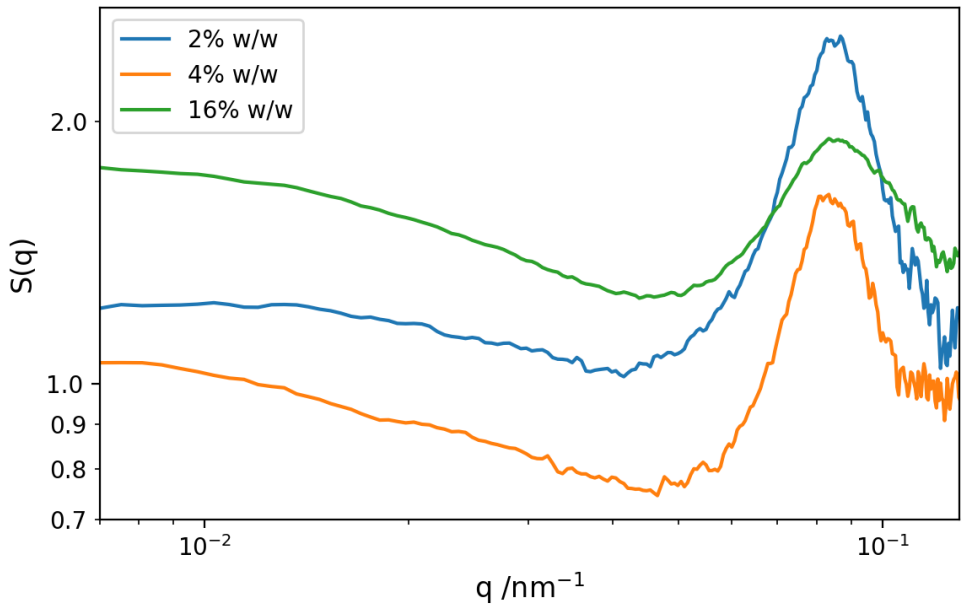

Figure 4.9: Final structure factors of gels of 80 nm PS colloids at 2%, 4% and 16% w/w after being cooled from 70 °C at 2 $Kmin^{-1}$.

In light of this, the effects of quench depth and quench rate on gel structure were also investigated. A sample of 80 nm PS colloids at 4% w/w was held at 70 °C for 300 s before being quenched to a series of temperatures between 55 °C and 35 °C, re-homogenising between each quench. Scattered intensities were measured immediately on reaching the

quench target temperature, after 60 s and after 300 s. No change was observed between 0 s and 300 s except for the 55 °C quench, likely due to its proximity to the melt temperature. Figure 4.10 shows the structure factors for each quench depth after 300 s. While the 55 °C quench has a very slightly different structure, all the curves are essentially identical in form.

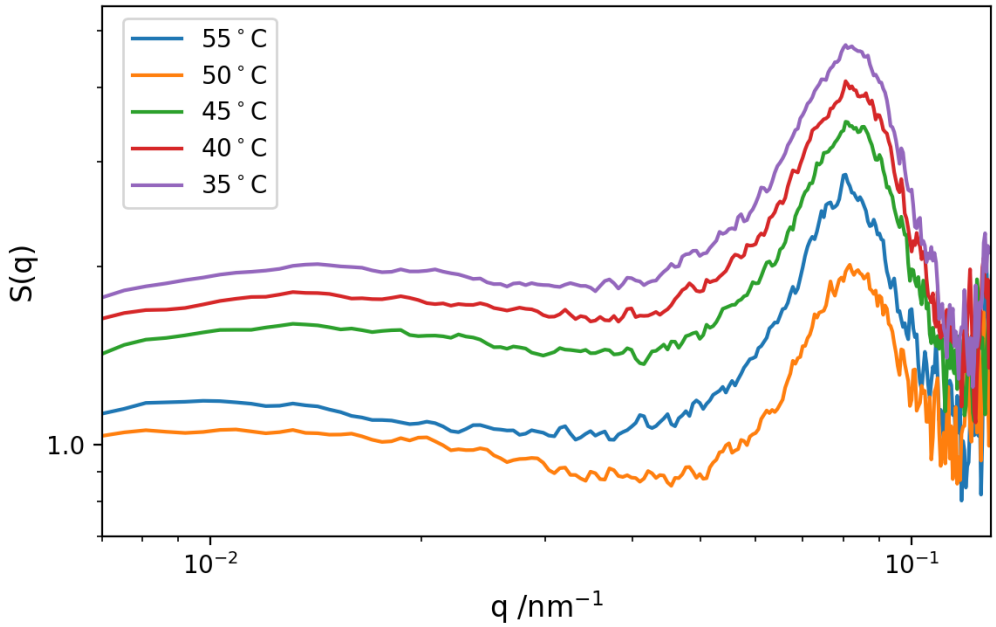

Figure 4.10: Structure factor curves for gels of 80 nm PS colloids at 4% w/w after quenching to different temperatures below the melt temperature at a rate of >10 Kmin^{-1}.

To test the effects of quench rate, the same 4% w/w sample was quenched from 70 °C to 40 °C at either 1 or 10 Kmin^{-1}. Structure factors for each case during cooling are plotted in Figure 4.11 both during the temperature ramp (top) and for the final gel (bottom). The model of "association" peak establishment, before a sharp change to the nearest-neighbour and "branch" peaks which subsequently develop slowly, is applicable for the 1 Kmin^{-1} case but distorted for the 10 Kmin^{-1} case. The more rapid quench causes a broadening of the "association" peak due to more pronounced temperature inhomogeneities and prevents any development in this or the "branch" peak as the structure does not have enough time to rearrange in either regime. This manifests in the final structure factor as a much broader "branch" peak at higher *q* values, corresponding to a more dendritic gel with narrower branches, again due to the inability of the colloids to rearrange before being kinetically trapped.

Commentary on the formation mechanism of these DNACC gels and their behaviour under different quench conditions was done primarily using SAXS data, as it was found

that the achievable resolution in optical microscopy was too large to distinguish subtler changes in the structure factor that indicate different behaviours. However, to look at how the gel structure scales with colloid size and concentration, information was needed about features on a micron scale, so confocal microscopy coupled with chord analysis was used.

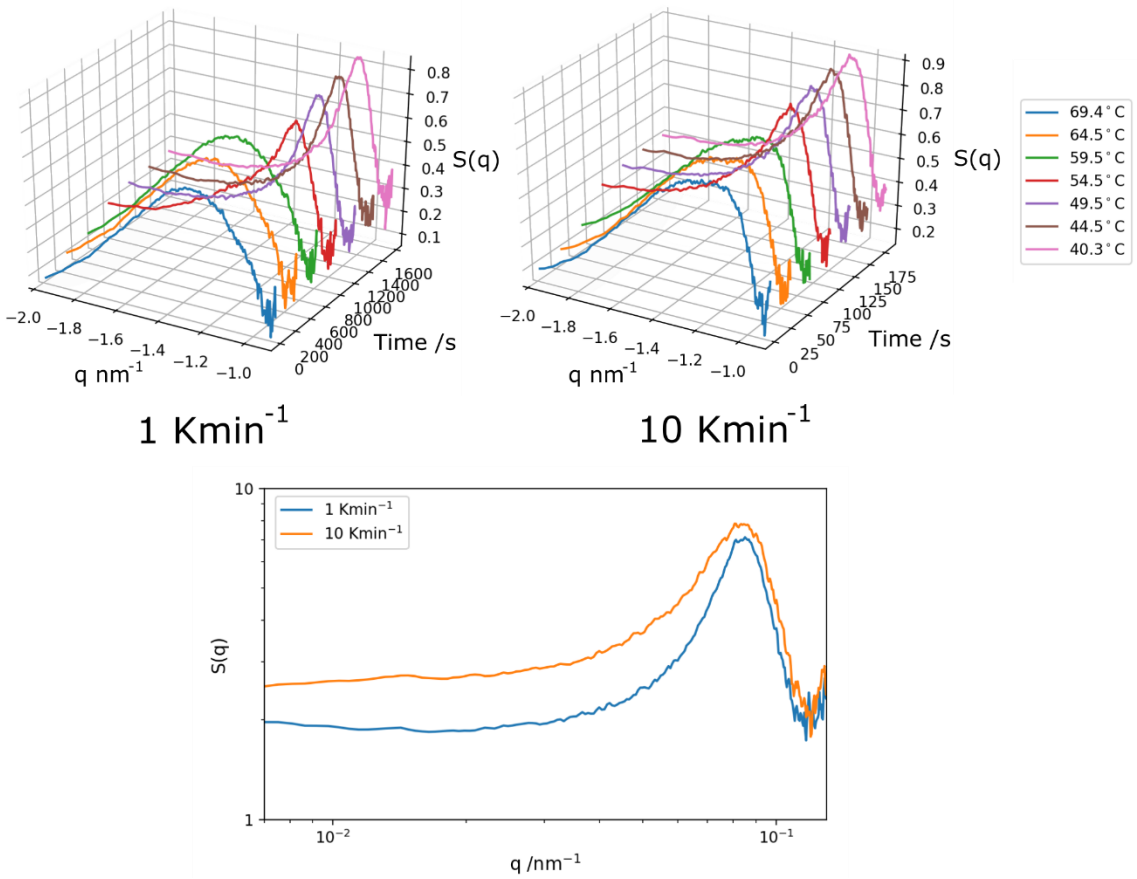

Figure 4.11: Structure factors of a PS80 gel at 4% w/w quenched at either 1 or 10 Kmin^{-1} during the quench (top) and for the final gel (bottom).

4.3 Structural Variation with Suspension Properties

In order to synthesise porous materials with emergent properties like structural colour, fine control is required over the length-scales in the microstructure. In the case of a colloidal gel, it is not sufficient to only control the colloid-colloid distance, as the relevant scatterers are not the individual colloids, but the pores and branches of the gel itself. Further, because the interaction potential between DNA-coated colloids is so strongly attractive, any synthesis that relies on an annealing step after the initial spinodal decomposition and subsequent kinetic arrest is likely to be unreliable because of the very sharp (~1°C) melting transition. The corollary to this is that once formed, the structure is effectively “locked in” by the colloids’ inability to rearrange.

Our SAXS measurements demonstrate that our systems show only a weak dependence of the gel structure on the quench depth or rate, again due to the sharp melt transition and strong hybridisation interaction between the DNACCs. This means that the two variables with the strongest effect on the length-scales in the final gel (and the most easily controlled) are the colloid diameter and the concentration of colloids in the initial suspension. Despite extensive work in the literature on the phase behaviour of attractive colloids, this parameter space is poorly explored computationally, particularly colloid size, as simulations tend to be run with periodic boundary conditions and scaled to the radius of the particles used. Here, we investigate how gel structure varies with colloid diameter and overall suspension volume fraction φ using an experimental system of DNACCs characterised by confocal microscopy and analysed using chord analysis, a standard characterisation tool for porous media[125].

While in the absence of sedimentation the gel structure might be expected to scale linearly with colloid radius, it has already been shown from work on DNA-coated colloidal crystals that the lower melt temperatures and higher diffusivities of smaller DNACCs can lead to dramatically different phase behaviour[66-68]. By quenching systems deep into the two-phase region, it was hoped that the effect of colloid size on melt temperature could be minimised by effectively making inter-particle attraction for all sizes so large as to be irreversible. Melt temperatures were measured by visually inspecting optical microscopy images during heating and cooling for DNACCs of 80, 210, 420, 800 and 1600 nm in diameter, and are plotted in Figure 4.12.

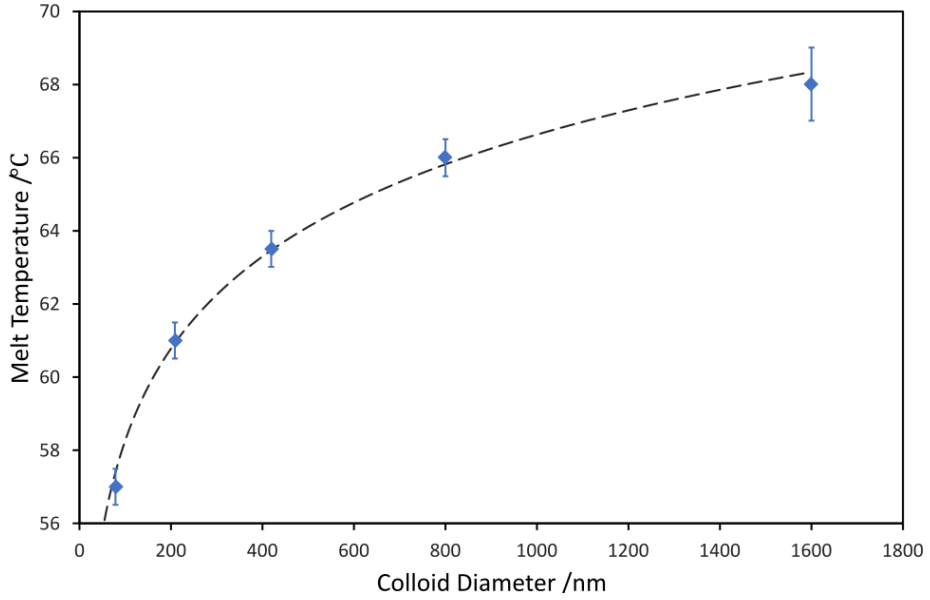

Figure 4.12: Melt temperatures of DNA-coated colloids with different diameters. The dashed line shows a logarithmic fit to the data.

The melt temperatures show a clear logarithmic dependence on colloid size. From equation 1.16 in Chapter 1.2.2, we expect a logarithmic dependence on the number of binding strands of DNA in the inter-colloidal volume. A simple geometrical argument[47] can be applied to give the number of DNA bonds between two colloids of radius R as

$$N_b = 2\pi\chi\rho R^2 \frac{L - \frac{h}{2}}{R + L} \tag{4.1}$$

where χ is the fraction of the bonds formed compared to the theoretical maximum, ρ is the grafting density (~0.05 nm^{-2}), L is the length of the DNA polymer (10 nm) and $h \approx L$ is the distance between the particle surfaces. From this we can see that the number of bonds formed, N_b, will be linearly proportional to the radius in the limit of $R \gg L$.

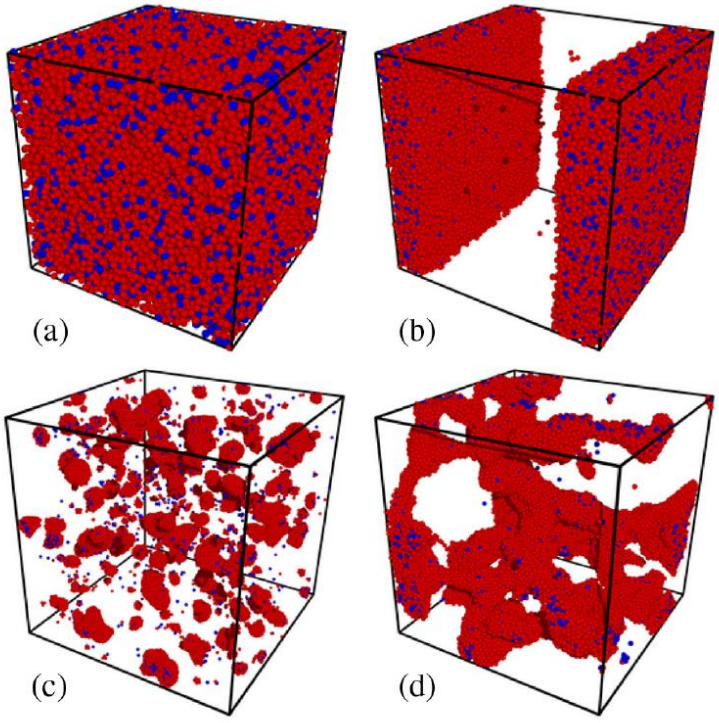

Figure 4.13: Simulation snapshots of a system of bimodal attractive colloids. a) A homogeneous gas phase exists above the melt temperature. b) Complete phase separation in the two-phase region but above T_g. c) Clusters formed in the two-phase region below T_g and below φ_p. d) A percolating gel formed below T_g but above φ_p. Taken from [166].

When a suspension of DNACCs is quenched into the two-phase region, several morphologies may be observed. As discussed in Chapter 1.3.1, the position of the dynamical arrest line determines the composition of the colloid-rich phase when the spinodal decomposition is arrested by the strong particle-particle interactions. Similarly,

the point at which the arrest line meets the spinodal line determines the temperature above which phase separation will go to completion and below which demixing becomes infinitely slow[57]. Theoretical results also predict a threshold in the total concentration of particles at which the gel becomes space-spanning in three dimensions and able to support stresses, known as the percolation threshold φ_p[57,79,166]. Above the percolation threshold, the final structure after phase separation and arrest will be a space-spanning colloidal gel. Below the percolation threshold, the colloidal volume fraction is too low to form a percolating gel, and instead discrete clusters of colloids are formed. This has been explored both experimentally[57] and computationally[166] for particles of a single size. Examples of these different behaviours are shown from simulations by Testard et al.[166] in Figure 4.13. The position of the percolation threshold has been discussed fairly extensively in the literature[57,166-169], with percolation reported in systems with volume fractions as low as 2%[164] and as high as 64%[167], corresponding to random close packing. The percolation threshold has been estimated to be 5-8% v/v for 500 nm DNACCs[57], in agreement with other systems of attractive spheres[161], but no information is available about the possible dependence of its position on colloid size.

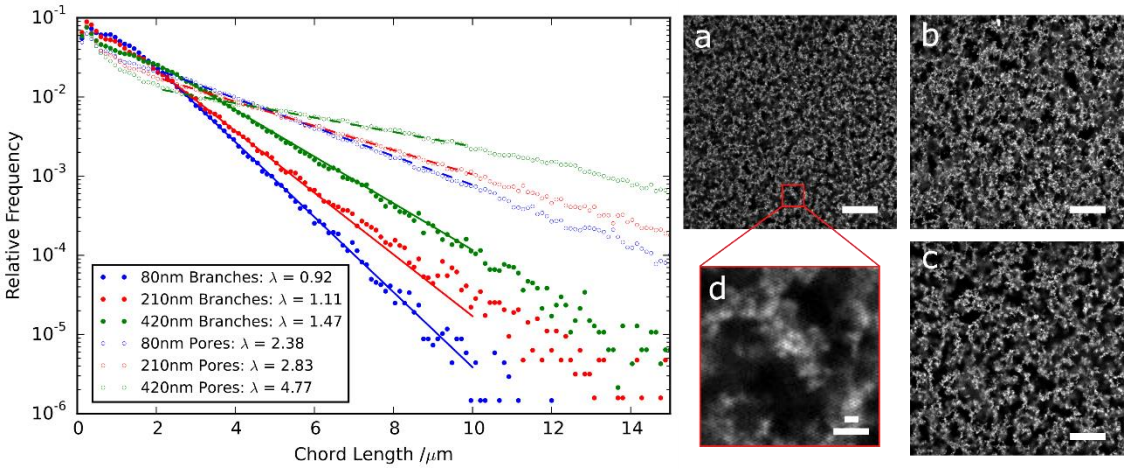

Figure 4.14: Chord histograms fitted with decay lengths for both branches and pores calculated from confocal micrographs of gels of 80, 210 and 420 nm polystyrene colloids, as shown in a), b) and c) respectively. Concentrations are 4% w/w and scale bars are 20 µm. d) shows a zoomed section of a) with scale bars of 0.92 and 2.38 µm, corresponding to the branch and pore decay lengths measured for that system.

Figure 4.14 shows chord histograms calculated from micrographs of gels and fitted with decay lengths for both gel branches and pores. The gels used were composed of 80, 210 and 420 nm polystyrene DNACCs respectively at 4% w/w, and typical confocal micrographs are shown in subplots a) - c). Subplot d) shows a zoomed section of a) with

scale bars equal to the decay length for the branches and pores, showing how the decay length corresponds to the typical length-scales of the colloid-rich and sparse phases.

The gels have very similar structures as the colloid diameter is increased, as visible in the micrographs and further evidenced by the same exponential behaviour of the chord histogram. However, length-scales and decay constants do not scale linearly with colloid size, implying that the higher mobility of smaller particles does indeed have an impact during phase separation. Smaller particles with correspondingly lower temperature and less sharp melt transitions would rearrange more readily, forming larger clusters before percolation is reached and the gel macrostructure finalised. This matches our observations above, where length-scales in the 210 nm gel are only ~20% larger than those in the 80 nm, instead of the ~170% we might predict from a purely geometrical argument, though some of this may be due to the finite resolution of the technique artificially coarsening some of the features of the 80 nm gel. This would not explain the full difference though: length-scales in the 420 nm gel are ~50% larger than those in the 210 nm, compared to 100% from a geometrical argument.

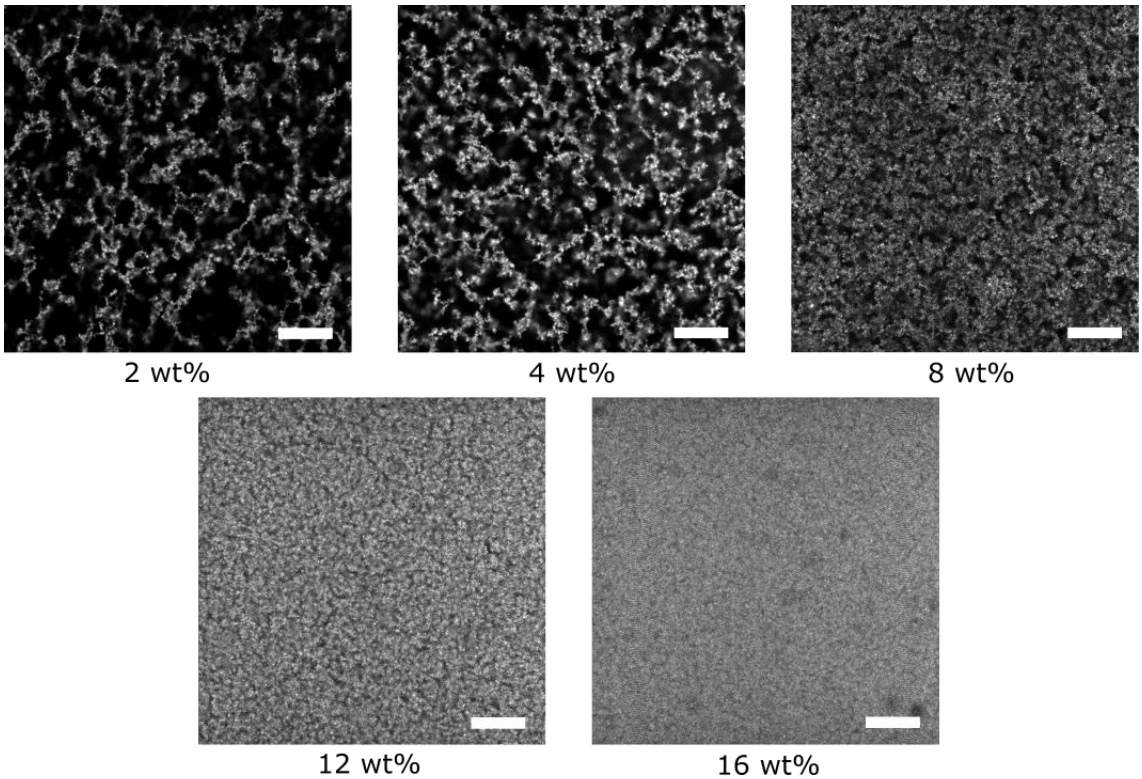

Figure 4.15: DNA-coated colloidal gels of the same 420 nm polystyrene colloids at different concentrations. Scale bars are 200 µm.

Figure 4.15 shows confocal images of gels of 420 nm colloids at weight fractions between 2 and 16% w/w. As the concentration of particles increases, two regimes are observed.

First, below the percolation threshold, the gel structure is broadly the same as the weight fraction increases, with coarsening of the gel branches and slight subdivision of the pores. In an ideal system with perfect density matching and no edge effects, this would more closely resemble isolated clusters of increasing size, as shown in Figure 4.13c. However, in a real system density matching to $< 10^{-3}$ g cm^{-3} may not be sufficient to completely remove sedimentation of growing clusters[170], and some colloids adsorb to the walls of the glass capillary, pinning some of the aggregated phase to the perimeter of the sample chamber. While the effects of the interface on structure were minimised by imaging deeper into the sample, the presence of adsorption serves to eventually deplete the solution of free colloid-rich clusters, as all clusters will eventually bind to the aggregated phase locked in place at the walls.

The second regime, above the percolation threshold, corresponds to the pore subdivision model proposed above and shown schematically in Figure 4.6. Enough material is present to percolate the entire volume and gel branches have a similar structure as weight fraction increases but are arranged in increasingly branched gels with more subdivided pores. The percolation threshold, defined in terms of the colloidal volume fraction φ_p, which corresponds to the boundary between these two regimes, appears to be between 6 – 8% w/w for 420 nm colloids from inspection of optical and confocal micrographs of the gels.

To obtain a complete overview of the behaviour of our system, characteristic length-scales for both gel branches and pores were determined by chord analysis for a series of colloidal gels of density matched 80, 210, 420 and 800 nm colloids at overall concentrations of 2%, 4%, 8%, 12% and 16% w/w. The decay lengths λ, characteristic of the length-scales in the branches and pores, are plotted in Figure 4.16. Typical confocal micrographs of all gels are shown in Appendix 2.

Some care needs to be taken when interpreting this data. First, laser light with a wavelength of 633 nm was used to image the sample through a 1.2 numerical aperture lens, making the Abbe diffraction resolution limit of the imaging technique ~260 nm. In reality, the resolution will be slightly poorer than this due to the finite size of the pinhole and scattering by colloids above and below the focal plane, as discussed in Chapter 2.3.4. Hence, we might reasonably expect features on the order of a few hundred nanometres, notably the branch thickness of the 80 nm particle gels and to a lesser extent the 210 nm particle gels, to be artificially coarsened. Second, as the gel becomes highly branched at high weight fractions, the image contrast between the branches and pores goes down. As a result, the image processing method used sometimes fails to detect the branch-pore

interface correctly, again resulting in artificial broadening of characteristic features. This is most significant for the 80 nm gels at 12% and 16% w/w and is clearly visible in the data as a sharp uptick from the expected values.

It is also necessary at this point to briefly discuss the units of suspension concentration. Concentrations were measured experimentally by drying an aliquot and comparing the wet and dry masses, thus allowing the accurate and exact calculation of the weight fraction. However, concentrations in the literature are often quoted as volume fractions, as it allows for easy comparison between materials of different densities. Strictly, the relationship between the two is non-linear, but it can be approximated for low concentrations as

$$weight\ fraction = \frac{\rho_{colloids}}{\rho_{solvent}} \times volume\ fraction \qquad (4.2)$$

where ρ is density. For our system, where the density ratio is 1.05, the errors between this approximation and the exact values of the volume fraction were found to be less than 0.5% and so weight and volume fractions are treated as directly proportional.

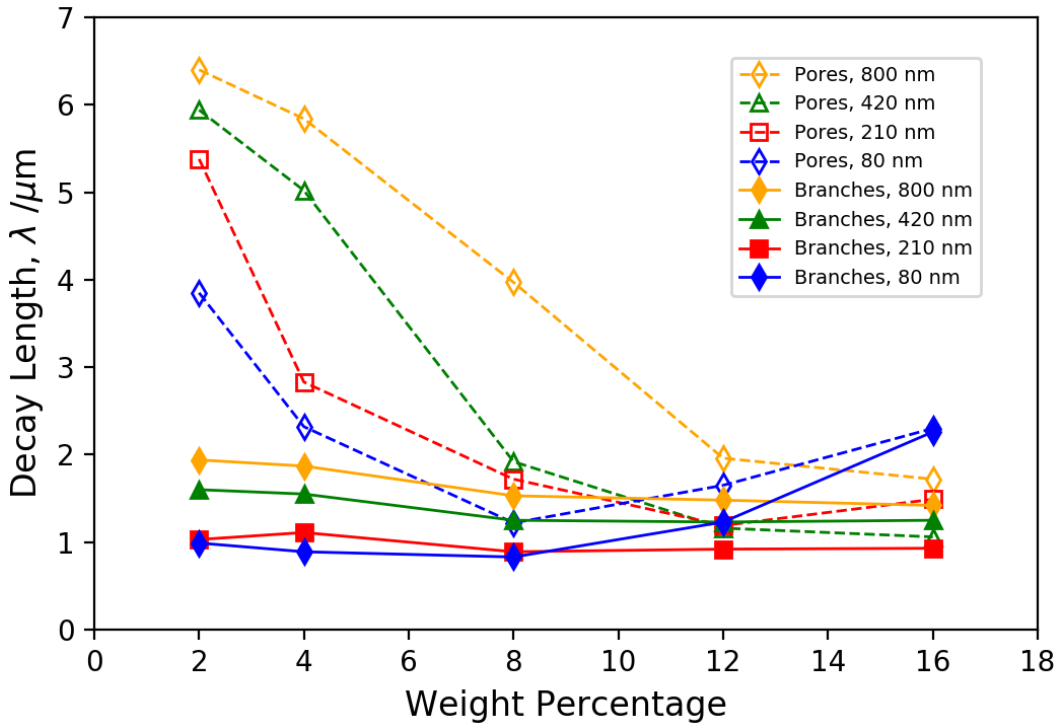

Figure 4.16: Decay lengths λ for colloid-rich branches (solid) and colloid-sparse gel pores (dashed) for DNA-coated colloidal gels of 80, 210, 420 and 800 nm colloids at 2%, 4%, 8%, 12% and 16% w/w. All samples were measured at room temperature after cooling from 75 ℃ at 10 Kmin^{-1}.

Taking these limitations into account, several trends are visible in the decay lengths. As the concentration increases, λ_{pores} drops slowly at first and then more quickly as the system moves between the cluster growth and gel subdivision regimes. This is accompanied by a subtler change in $\lambda_{branches}$, which transitions between two approximately constant regimes: coarser branches above the percolation threshold and finer branches below it. All four sizes of colloids show similar behaviour but the apparent percolation threshold trends downward with decreasing colloid radius. 800 nm colloids show the regime change at 7 – 9.5% v/v, 420 nm at 6 – 7.5% v/v, 210 nm at 5 – 7% v/v and 80 nm at 4 – 6% v/v, estimated qualitatively by looking at the steepest part of the curve for λ_{pores} and the shift in $\lambda_{branches}$. This implies that the more mobile, less strongly binding colloids percolate at lower volume fractions. This fits with experimental results from other systems: Ruff et al.[164] reported percolation of 25 nm silica DNACCs at 2% v/v and Di Michele et al.[79] report the percolation threshold of 1 µm polystyrene DNACCs as 7 – 10% v/v. This behaviour has also been observed tangentially in computer simulations: Safran et al. reported that as the ratio of the volume of the binding shell to the volume of the hard colloid increases, percolation occurs at lower concentrations[167]. In our system, the binding shell volume is set by the length of the grafted polymer and DNA oligomer and is constant across all colloid radii, making the binding shell:colloid volume ratio higher for smaller colloids.

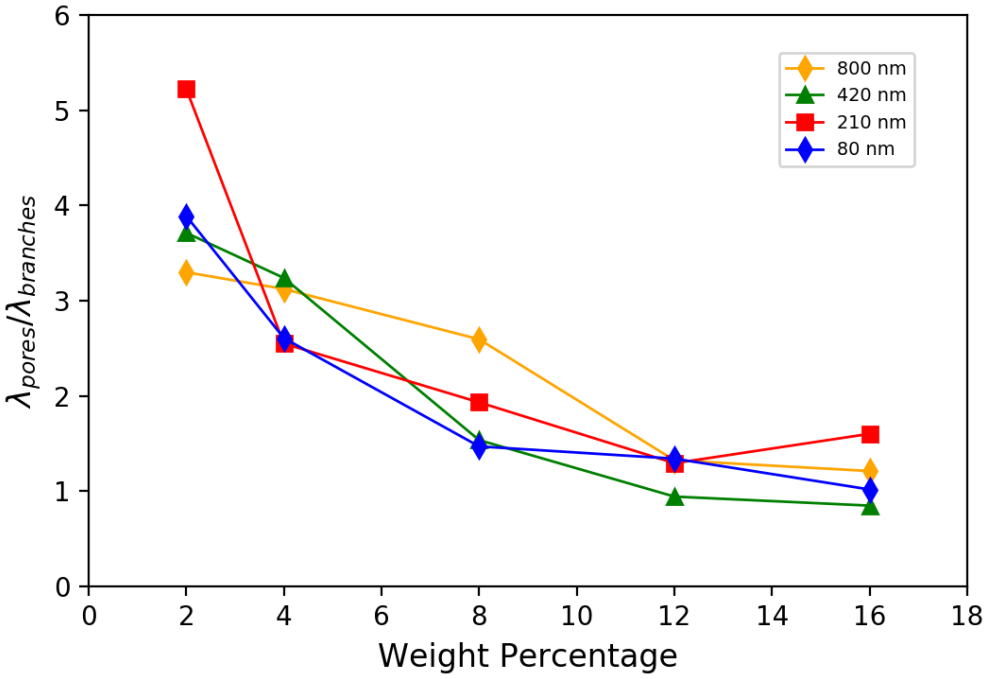

Figure 4.17: Ratio of λ_{pores} to $\lambda_{branches}$ for gels of 80, 210, 420 and 800 nm colloids at 2%, 4%, 8%, 12% and 16% w/w.

Finally, the transition can be followed by calculating the ratio of $\lambda_{pores}/\lambda_{branches}$. Unfortunately, this method propagates the errors in $\lambda_{branches}$ for the 80 nm and 210 nm colloid gels and so detailed interpretation was done using the full data plotted in Figure 4.16. Nonetheless, a plot of $\lambda_{pores}/\lambda_{branches}$ clearly highlights the percolation threshold and the difference between the two regimes for the 420 nm and 800 nm colloid gels. This is plotted in Figure 4.17.

4.4 Optical Activity of Colloidal Gels

Percolating gels formed through an arrested spinodal decomposition mechanism have been shown to act as non-iridescent coherent light scatterers in nature and are particularly abundant in the feather barbs of many bird species. In this section we investigate the propensity for colloidal gels produced via a similar mechanism to interact with light in the same way.

4.4.1 Polystyrene

Even in a best-case scenario with well-defined branches no more than four colloids thick, we would not expect to see coherent scattering of visible light from 80 nm colloidal gels. A gel can be expected to scatter visible light when the dimensions of either phase of the gel a_r become similar to the wavelength of light[164]

$$a_r = \frac{\lambda_r}{2n_{eff}} \tag{4.3}$$

where λ_r is the scattered wavelength and n_{eff} is the effective refractive index of the phase. The effective refractive index for the colloid-rich phase at volume fraction φ can be calculated using the Maxwell-Garnett equation[171]

$$n_{eff} = n_{solvent}\frac{\sqrt{2n_{solvent}^2 + n_{colloid}^2 + 2\varphi(n_{colloid}^2 - n_{solvent}^2)}}{\sqrt{2n_{solvent}^2 + n_{colloid}^2 - \varphi(n_{colloid}^2 - n_{solvent}^2)}} \tag{4.4}$$

While it is difficult to measure the volume fraction in the colloid-rich phase, it is expected to be close to the upper bound of 64% at random close packing[166]. Using $n_{PS} \approx 1.6$ and $n_{water} = 1.33$ gives an effective refractive index of 1.499, placing limits on the sizes of feature that will scatter visible light between 133 nm for blue light (λ_r = 700 nm) and 233 nm for red light (λ_r = 400 nm). Gels with lower volume fractions in the gel arms than

64% or composed of a lower refractive index material will meet these scattering conditions for slightly larger feature sizes.

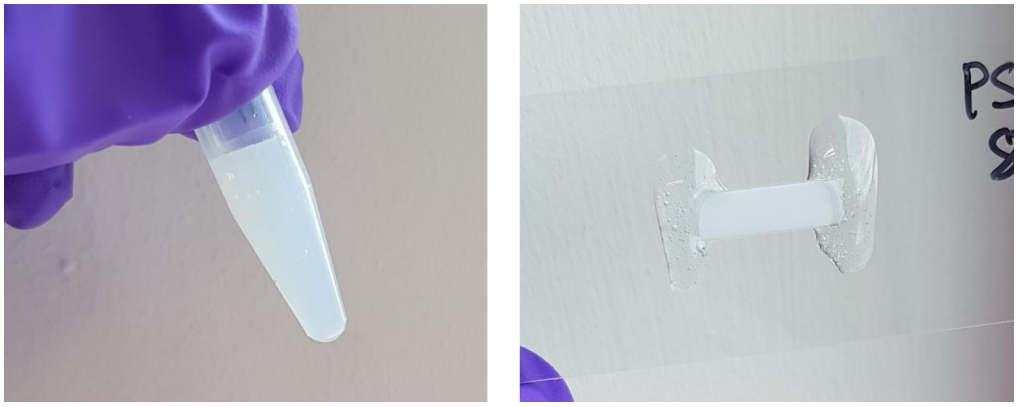

Figure 4.18: Images of 80 nm polystyrene colloids well dispersed in water (left) and quenched into an arrested colloidal gel (right). Blue colour is observed when dispersed but not when gelled.

Gels of 80 nm particles are expected to have a minimum gel branch thickness of 320 nm, above the cut off for visible light scattering. Hence, while 80 nm polystyrene particles appear blue to the naked eye when dispersed, due to incoherent scattering, they display only a white reflection over all angles once gelled, as shown in Figure 4.18. However, analysis of these coarser gels can still give insight into the similarities or differences with the microstructures of natural materials.

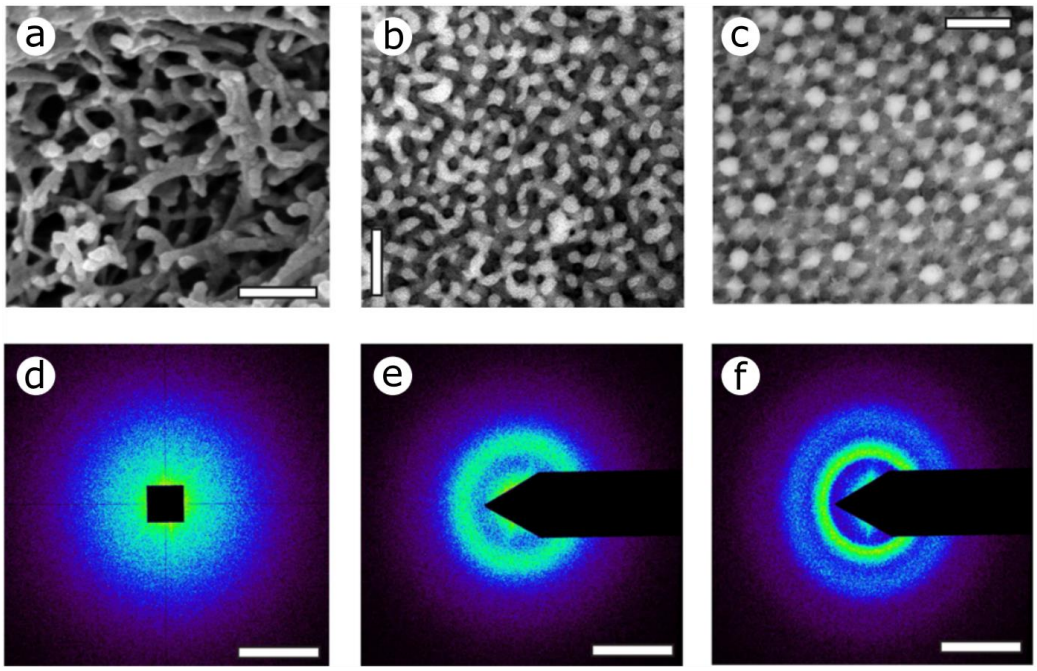

Figure 4.19: Images and power spectra for three naturally occurring keratin-air gels which coherently scatter light with little-to-no intensity and hue dependence on viewing angle. Scale bars: a) 250 nm, b), c) 500 nm, d) – f) 0.05 nm^{-1}. Taken from [114].

Two-dimensional power spectra are often used to gain insight into how and why a material interacts with light in a particular way as they give information about the length-scales present in a system and can be measured directly by scattering experiments such as SAXS or calculated by taking the Fourier transform of electron or optical microscopy images. Figure 4.19 shows SAXS diffraction patterns from the three keratin-air gels discussed in Chapter 1.4.2 and Figure 1.15. A broad ring or circle in the power spectrum has been shown to be characteristic of this type of angle-independent coherent scattering arising from structures without long-range order[164] and was used to falsify the previous hypothesis that these materials scattered light incoherently via Rayleigh or Mie scattering[108,112,114].

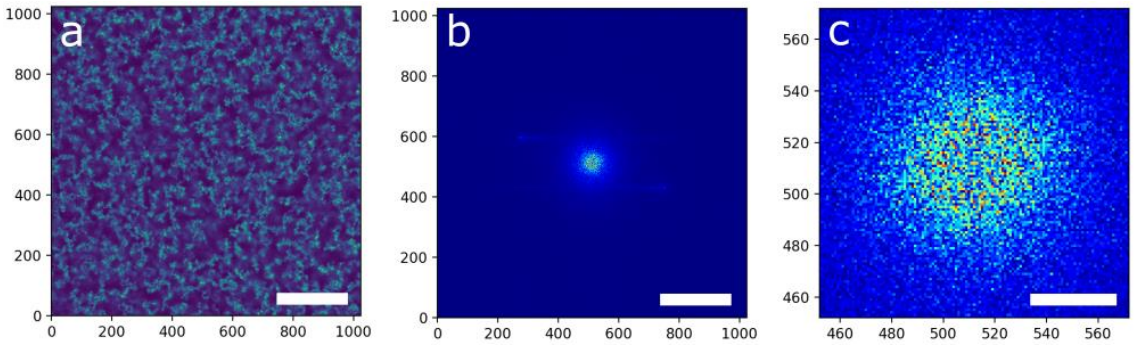

Figure 4.20: Two-dimensional power spectra and micrograph of a 2% w/w gel of 80 nm DNACCs. a) Confocal micrograph of the gel. Scale bar = 30 µm. b) Two-dimensional power spectrum of a). Scale bar = 1 µm^{-1}. c) Zoomed section of b) Scale bar = 0.1 µm^{-1}.

To compare synthetic and natural gels, experimental power spectra from DNACC gel samples were compared with those of natural gels from the literature. A confocal micrograph of a 2% w/w 80 nm colloidal gel is shown alongside its two-dimensional power spectrum in Figure 4.20 . The power spectrum was calculated by taking the two-dimensional Fourier transform of the image and plotting the square amplitudes. The horizontal streaking is due to periodic noise caused by the microscope during image capture and could not be completely removed by changing microscope settings or post-processing. However, it was shown that the presence of this noise did not affect image analysis and so it was ignored. The zoomed section showed a ring in the power spectrum similar to those measured in natural materials but at much smaller wavevectors. Blue coherent scatterers in nature typically have a peak in the power spectrum corresponding to real-space distances of ~140 nm[112,114], in good agreement with the optimal feature size range derived above, while the peak measured for the colloidal gel equates to real-space distances of ~3 µm, due to the much coarser structure.

Despite the confidence these results gave us that DNA-coated colloidal gels would make good synthetic analogues for naturally occurring keratin-air scatterers, we were unable to reduce the size of the system sufficiently to observe coherent visible light scattering from polystyrene colloidal gels. While PS colloids as small as 30 nm were synthesised with low polydispersities, they proved difficult to functionalise to the same high coating densities as larger colloids. This lower grafting density, coupled with higher curvature of the particle surface, reduced the binding strength and consequently made the melt transition wider. These factors prevented the system from exhibiting reproduceable gelation behaviour similar to that observed for larger particles.

4.4.2 Silica

Silica nanoparticles have several advantages and disadvantages when compared to polystyrene for the synthesis of functional colloidal gels. Robust functionalisation methods were developed for each, but silica nanoparticles as small as 27 nm could be reliably functionalised and assembled into a gel, compared to 80 nm for polystyrene. However, due to the much higher density of silica, it was not possible to remove the effects of sedimentation through density matching. Experiments on silica were led by Zachary Ruff.

Silica colloids with a diameter of 27 nm were functionalised with PEG-azide chains using the carbodiimide protocol described in Chapter 2.2.4 and coupled with DNA via an azide-alkyne cycloaddition as for polystyrene. The grafting density was measured by fluorescent assay as 104 ± 5 nm^2 per oligomer, substantially lower than those achieved on polystyrene particles; these coating densities correspond to inter-chain spacings of around 10 nm. When compared with the radius of gyration of the PEG-DNA complex of ~2.5 nm, it is clear the grafted polymer will be in the “mushroom” regime, with bare silica exposed between grafted chains. As the coiling of the polymer backbone can hinder access to the terminal azide group for DNA binding, a Cu(I)-catalysed azide-alkyne cycloaddition was used to couple DNA to the covalently grafted polymers. The Cu(I)-catalysed variant has much faster kinetics than the strain-promoted reaction used on polystyrene colloids. While Cu(I) ions have been shown to damage DNA[120], any damage occurred in this work was not significant enough to be measureable. In addition, assays showed a complete conversion of terminal azide groups to DNA, in contrast to literature suggesting additional ligands are often necessary to achieve full conversion[172].

Suspensions of silica nanoparticles were much less viscous than polystyrene DNACCs. Well dispersed polystyrene suspensions became too viscous to pipette above φ = 25%, while 30 nm silica could still be injected into capillaries at φ = 35%. Confocal microscopy was used to characterise the pores and branches of silica gels at φ = 1%, 2% and 5%. It is important to note that as discussed previously the minimum resolvable volume using this microscope configuration is approximately 250 x 250 x 500 nm, which is larger than the expected features in a gel of 30 nm nanoparticles. Nevertheless, it is interesting to compare the decay parameters for a silica gel as a function of the particle volume fraction with those obtained for polystyrene gels.

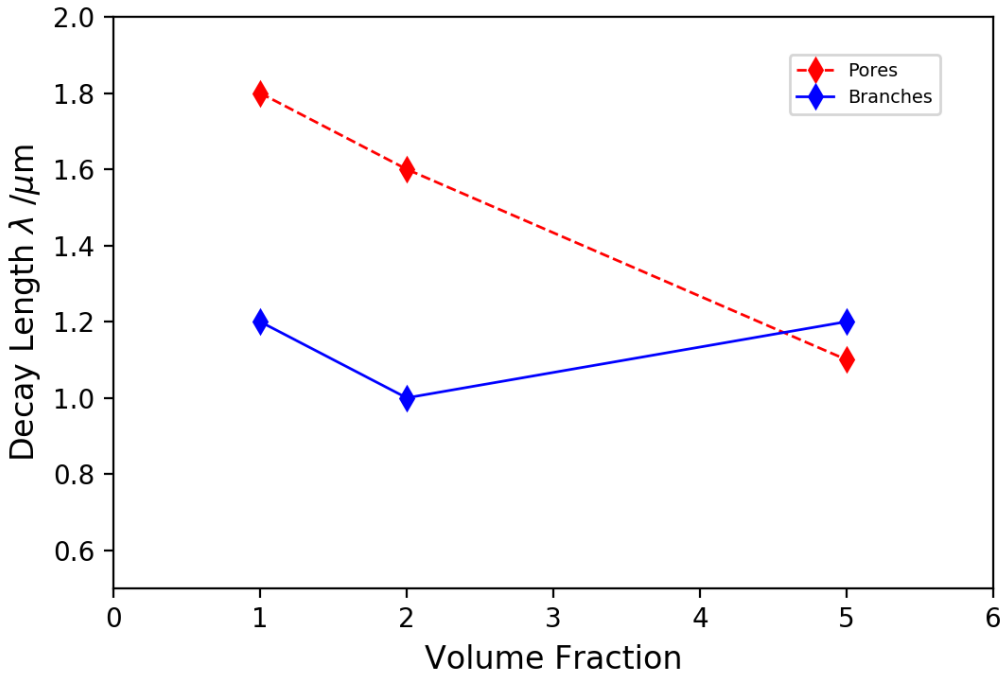

Figure 4.21: Decay lengths for the pores and branches of a gel of 27 nm silica colloids imaged with confocal microscopy.

Figure 4.21 shows the decay lengths calculated by chord analysis of gels of 27 nm silica colloids. Despite the limitations of the resolution, the broad trends mimic those observed for polystyrene: an approximately constant $\lambda_{branches}$ and a decreasing λ_{pores} as the pores become increasingly subdivided at higher volume fractions.

To characterise the branch thickness in the silica gels, X-ray nanotomography was performed at the nano-imaging beamline at the European Synchrotron Radiation Facility (ESRF, beamline ID16A-NI). A 35% DNA-NP gel was loaded into a Mark-style borosilicate capillary (0.3 mm inner diameter) and sealed with epoxy. Magnified phase contrast images of the sample were collected over 1800 angles at four detector distances

and an X-ray energy of 17 keV. A phase retrieval algorithm, in conjunction with a tomographic reconstruction algorithm, were used to generate a three-dimensional image of the colloidal gel in the aqueous state. The full tomographic volume sampled was 71.7 x 71.7 x 71.7 µm (2048 pixels x 2048 pixels x 2048 pixels) with a pixel size of 35 nm. Figure 4.22 shows a two-dimensional cross-section extracted from the volume.

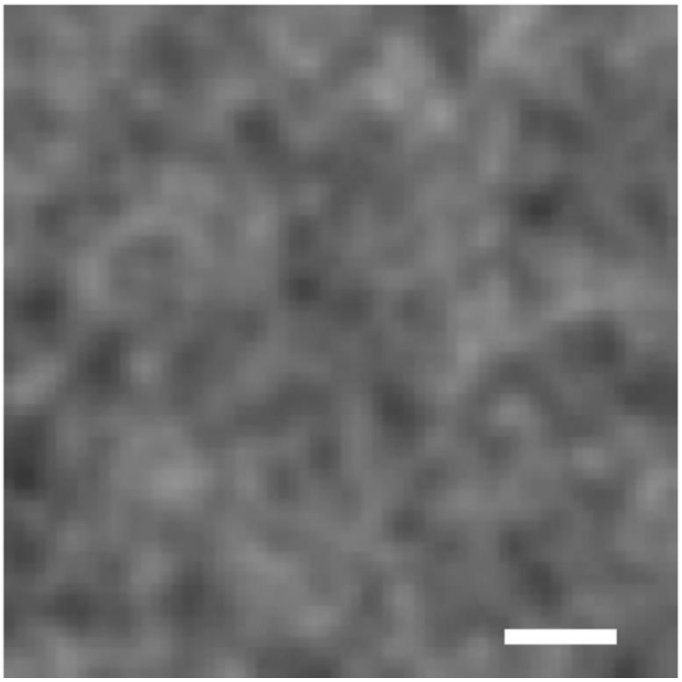

Figure 4.22: Tomographic reconstruction image of a 35% v/v DNA-NP gel of 30 nm silica colloids. The colloid-rich phase is dark and the colloid-sparse phase is light. This image is 64 x 64 pixels and the scale bar is 280 nm.

The 35% v/v gel was homogenous throughout the full tomographic volume. It should be noted that the denser phase in tomography appears darker, so the colloid-rich branches appear dark and the colloid-sparse pores appear light. The pixel size of 35 nm allows us to probe the feature sizes of the gel but is too coarse to be able to accurately locate individual colloids. The tomography shows clear phase-separation of colloid-rich and colloid-sparse phases on the scale of a few pixels. Branches are approximately four pixels thick, corresponding to widths of ~120 nm, in keeping with previous models. This tomography experiment was the first of its kind for imaging aqueous samples with such a high spatial resolution and the only one with a resolution of < 100 nm. Tomography experiments were also attempted on polystyrene colloids with a larger diameter, to compliment the SAXS and confocal microscopy results, but it was found that the contrast between the particles and medium was too low to reliably reconstruct the image and resolve features.

The predicted and measured branch thickness for a 27 nm silica gel of ~120 nm corresponds well to our predictions of a visible light scatterer in the blue region, as silica has a lower refractive index than polystyrene. To test the optical properties of silica gels, more concentrated samples were prepared in glass capillaries and characterised by optical spectroscopy. Silica colloids coated with complementary DNA with a melt temperature between 55°C and 65°C were mixed in phosphate buffer with no added salt to volume fractions of 15%, 25% and 35% v/v. At these low ionic strengths, the electrostatic repulsion between colloids due to the highly charged DNA backbone is too great for gelation to occur, and so the colloids remained well dispersed. The suspension was injected into glass sample capillaries and a small volume of concentrated salt solution added to one end of the capillary, before it was sealed with epoxy. Gelation occurred instantly in the vicinity of the salt solution and spread throughout the sample as the salt diffused through the volume. Samples were equilibrated overnight, giving a final salt concentration of 150 mM. While the initial suspension was largely transparent even at φ = 35% due to the small diameter of the particles ($\lambda >> R$) and the low absorption of silica, the gel displayed a distinct blue colour immediately upon formation.

The reflectivities of gels made up at 15%, 25% and 35% v/v were measured after homogenising above the melt temperature for an hour and quenching to room temperature. Reflection spectra were measured normal to the sample and standardised against a capillary filled with phosphate buffer. Recorded spectra were found to be invariant with position (x,y) and depth (z). Results are plotted in Figure 4.23, showing a peak at 385 nm.

The drop-off at low wavelengths can be explained by the absorption edge of silica and glass in the near-UV, while the tail at longer wavelengths has good agreement with the $1/\lambda^4$ dependence predicted by Rayleigh-Gans theory, which describes the scattering by objects similar in size to the incident wavelength and with low refractive index contrasts[85]. As volume fraction increases, the shape of the reflectance spectrum remains the same, but the magnitude increases as the scattered intensity is proportional to the square of the volume of the scattering objects. This fits with our model of pore subdivision, as increasing the volume fraction results in more gel branches of the same average structure. If raising the concentration caused coarsening of the gel arms, we would expect the peak to shift to higher wavelengths.

The absence of any structural colour from the uncoated suspension allows us to confidently assign the source of the structural colour peak to the nanoscale structure of the gel. This system, in an analogous way to the natural materials discussed in Chapter 1.4.2, allows for the decoupling of the particles' form factor from the assembly's structure factor, making it an excellent candidate for full-spectrum non-iridescent structural colour.

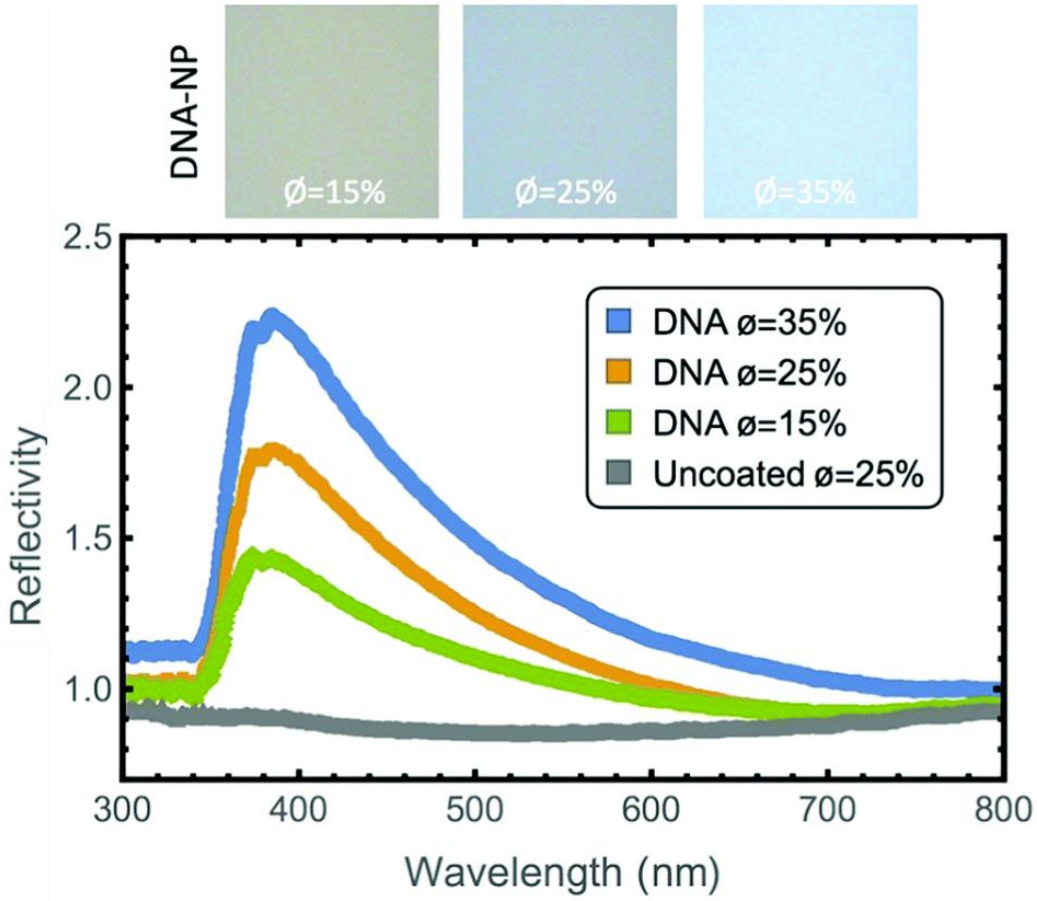

Figure 4.23: Reflectivity measurements of silica nanoparticle gels. Top) Images of the samples. Scale is 43.9 μm square. Bottom) Normalised reflectivity spectra of nanoparticle gels at 15%, 25% and 35% v/v and a suspension of uncoated colloids at 25% v/v relative to a capillary filled with buffer. Modified from [164].

4.5 Conclusions and Outlook

This chapter presented the synthesis and characterisation of DNA-mediated colloidal gels. By coupling SAXS measurements with in situ heating and confocal microscopy of gel structures, we have proposed a coherent mechanism for the formation of colloidal gels via an arrested spinodal decomposition that is consistent with the experimental and computational results from the literature. We have described the scaling behaviour of such a system with both colloid radius and suspension concentration and shown that substantial control can be achieved over the gel microstructure by varying these parameters without the need for thermal processing.

We showed that polystyrene gels had an appropriate microstructure for the coherent scattering of light very similar to those found in nature, but that currently achievable length-scales were too large to realise structural colour in the visible range. Silica gels demonstrated identical behaviour to polystyrene but were able to be scaled down sufficiently to exhibit non-iridescent coherent structural colour. The hue of this colour was linked to the nanoscale structure of the gel formed and shown to be invariant with suspension concentration. In particular, the features responsible for the scattering of visible light were shown not to be the individual colloids, allowing for the decoupling of the form and structure factors.

Promising future work in this area would include the development of synthesis and functionalisation techniques for polymer nanoparticles with diameters in the 30 – 50 nm range. These could assemble into optically active gels without sedimentation effects and with higher refractive index contrast for stronger overall reflectance, tuneable for wavelengths across the visible spectrum. The accessible wavelength range of the reflectance should also be investigated by repeating these experiments with larger silica nanoparticles. Finally, the effects of temperature cycling and external fields on gel structure and optical response should be examined with the idea of designing chromo-responsive metamaterials.

5 Fluorinated Latex Photonic Crystals

As discussed in Chapter 1, the realisation of full-spectrum structural colour requires the decoupling of the form factor from the structure factor to prevent scattering being dominated by the incoherent component, which is always blue[89,91]. In Chapter 4, we presented colloidal gels as biomimetic materials that achieved this through the assembly of colloids into nano- and micro-structures with distinct features larger than the colloids themselves. Partial success has also been reported by Manoharan et al.[101], who assembled photonic glasses of core-shell colloids where the cores have higher refractive indices than the shells and hence dominate the scattering. However, such a system still requires spheres in hard contact and the low refractive index shells still scatter noticeably as scattering intensities depend on the square of the scatterer volume, so these assemblies still displayed a blue edge in the reflectivity spectrum due to incoherent scattering.

In this chapter we describe the synthesis and characterisation of ultra-soft photonic crystals and glasses of colloids stabilised by electrostatic repulsion through a Wigner-type mechanism[173] and not in hard contact. By doing so, the particle-particle separation, the parameter that primarily determines the structure factor of a crystal or glass, is decoupled from the colloid radius, the parameter that primarily determines the form factor. When such systems were constructed from highly charged polystyrene spheres, glassy and crystalline phases where the spheres were not in hard contact could be measured by SAXS, but the optical reflectivity was dominated by a white background due to multiple scattering overlaid with a few strong Bragg reflections. To address this,

we also synthesised Wigner glasses of fluorinated latex colloids with a refractive index of 1.37, very similar to that of water. These systems displayed high transparency due to the reduction in multiple scattering, alongside strong non-iridescent structural colour tuneable throughout the visible spectrum.

The work discussed in this chapter is also presented in a manuscript accepted for publication by *RSC Materials Horizons* and is available on arXiv:1808.06260 (2018)[174]. Portions of the text in this chapter are modified from the text of the manuscript. Simulations were done by Talha Erdem and form factor fitting was done using code written by Alessio Caciagli.

5.1 Preparation and Characterisation

Fluorinated latex (FL200) particles were synthesised using the emulsion polymerisation methods detailed in Chapters 2.1.2 and 3.3.1 and washed thoroughly after synthesis to remove any surfactant. Particle diameter was measured as 193 nm by DLS with a PDI of 1.6%. SEM measurements of dried samples of the same colloids estimated the diameter as 160 ± 25 nm. As DLS measures the hydrodynamic size not the true size, we would expect the DLS diameter to be larger than the SEM, particularly for such highly charged colloids, but not by such a large amount. This implies that the particles undergo significant shrinkage upon drying and imaging in a vacuum; deformation and aggregation on drying and in vacuo imaging has been reported previously by Koenderink et al.[155]. This effect can be seen in the raw SEM micrograph, Figure 5.1.

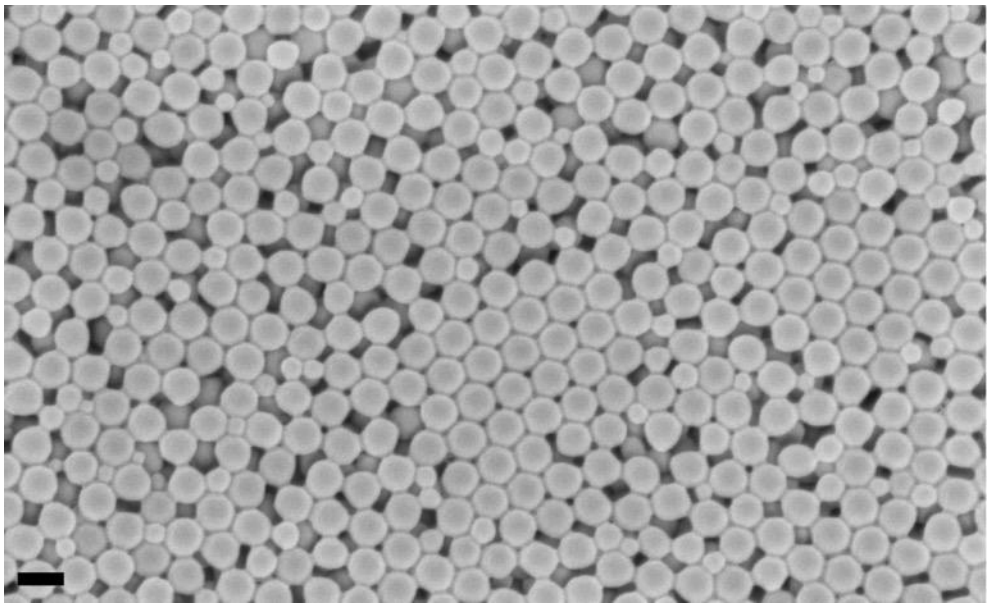

Figure 5.1: SEM image of 193 nm fluorinated latex colloids. Scale bar = 200 nm. Taken from [174].

Polystyrene (PS200) colloids were synthesised by the surfactant-free emulsion polymerisation methods detailed in Chapters 2.1.1.1 and 3.2.1 and were found to have a diameter of 220 nm with a PDI of 1.4% by DLS and a diameter of 190 ± 5 nm by TEM. Hence both the PS and FL colloids are similar in size but were not expected to crystallise with one another as the size difference between them is larger than 5%, which is the limiting size polydispersity for hard-sphere crystallisation[141].

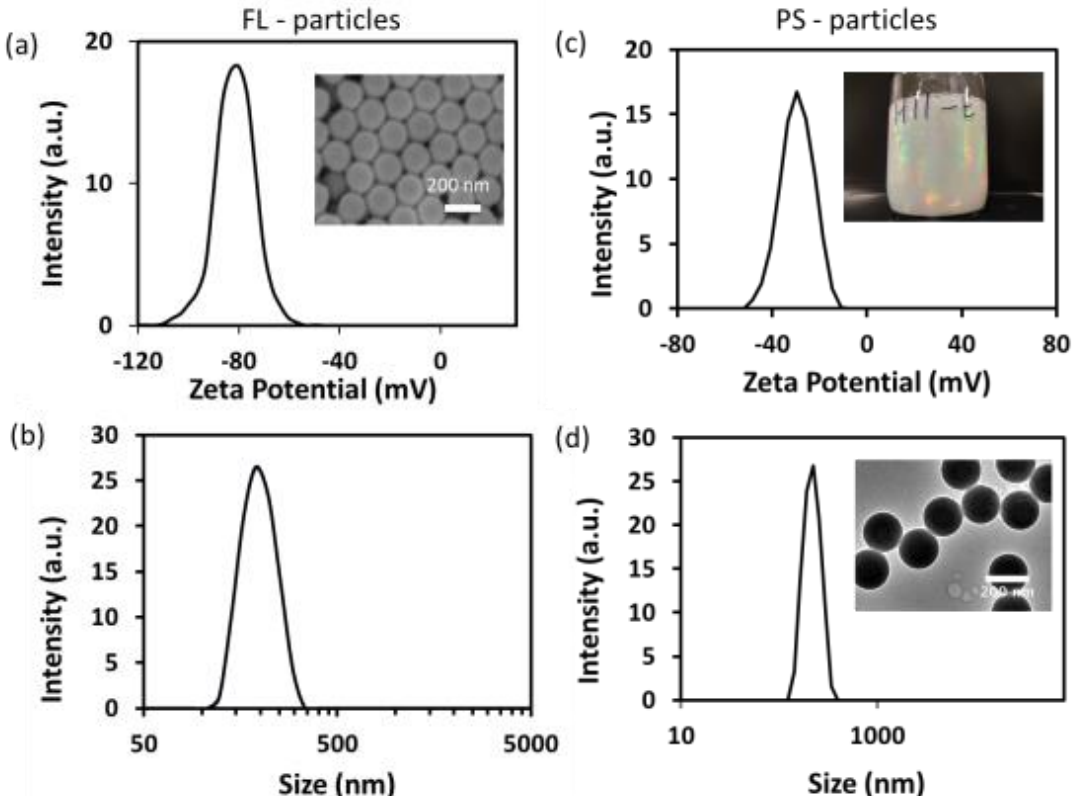

Figure 5.2: Zeta potential (top) and size (bottom) measurements for fluorinated latex (left) and polystyrene (right) colloids measured by DLS and zeta potential measurements. Inserts in a) and d) show SEM and TEM images of the colloids, while the insert in c) shows a macroscopic image of the suspension. Taken from [174].

Zeta potentials were also measured for both types of colloid and were found to be -82 ± 4 mV for the FL and -30 ± 4 mV for the PS particles. Size distributions and zeta potentials as measured by light scattering are shown in Figure 5.2. Inserts show SEM and TEM images of the FL and PS colloids respectively, along with a macroscopic image of the PS particles in a glass vial at 2% v/v. Strong, iridescent colours are visible to the naked eye in the PS suspension due to Bragg scattering from Wigner crystal formation close to the glass. These colours disappeared on agitation of the suspension. If the suspension was left undisturbed the colours also eventually disappeared, implying some ageing mechanism

occurred in the colloid layers close to the glass walls of the vial. If the suspension was agitated or poured into a fresh vial and allowed to stand briefly, the colours would return.

Dried films were prepared by immersing a glass slide in a dilute (2% v/v) suspension of colloids at a 30° angle and evaporating the solvent in an oven at 50 °C. Films of FL colloids were completely opaque and white at all angles, except over a very narrow angular range where a strong violet Bragg reflection was observed. Films of PS colloids had an even stronger white appearance overlaid with sharp blue Bragg reflections at well-defined angles, as shown in Figure 5.3. These Bragg reflections are due to ordering of the colloids into hexagonally close-packed layers at the air water interface during drying.

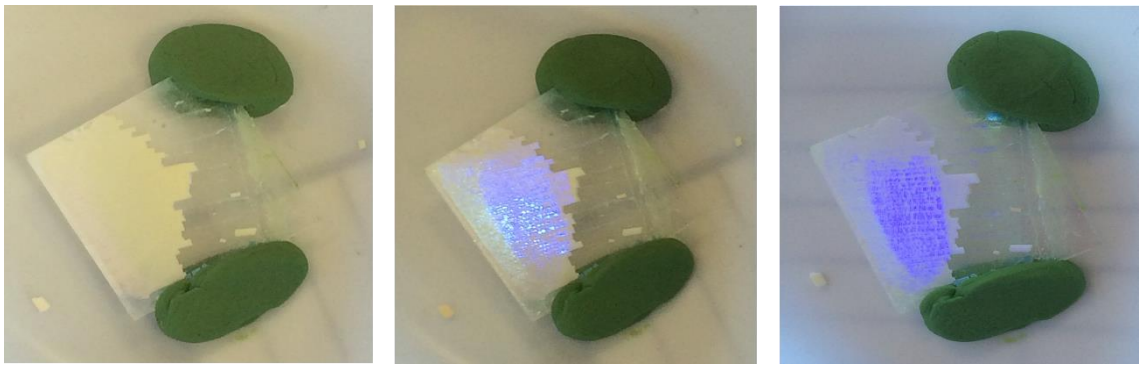

Figure 5.3: Images of a dried film of 200 nm polystyrene particles, showing the white background and sharp Bragg peaks. Images are taken over a very narrow angle range. Taken from [174].

Dilute (2% v/v) dispersions of both species of colloids appeared white and opaque. However, concentrating the FL suspensions by centrifugation to volume fractions above 15% led to significantly increased transparency coupled with a strong peak in the reflectance at a specific wavelength that was tuneable throughout the visible spectrum by varying the suspension concentration, as shown in Figure 5.4.

These observed colours were completely isotropic and did not vary noticeably in hue or intensity with different viewing angles, implying a lack of long-range order in the samples. They persisted, unchanged, whether the suspension was in an Eppendorf tube, a pipette tip or a glass capillary. This could be indicative of either a photonic glass or many small polycrystalline domains. However, polycrystallinity is normally characterised by a reduction in transparency due to the presence of grain boundaries and defects, which significantly add to diffuse scattering and crystallisation would not be expected in a colloidal system with such a broad size distribution. Hence we attribute this behaviour to the formation of macroscopic photonic Wigner glasses.

In contrast, suspensions of polystyrene colloids of similar size and charge remained predominantly white and opaque all the way up to 40% v/v, as expected due to the much higher refractive index contrast between polystyrene and water ($\Delta n \approx 0.23$). However, at concentrations above 20% v/v strongly angle-dependent colour was observed due to Bragg peaks. Unlike the transient colours observed in bulk 2% suspensions, these reflections were far more persistent with agitation.

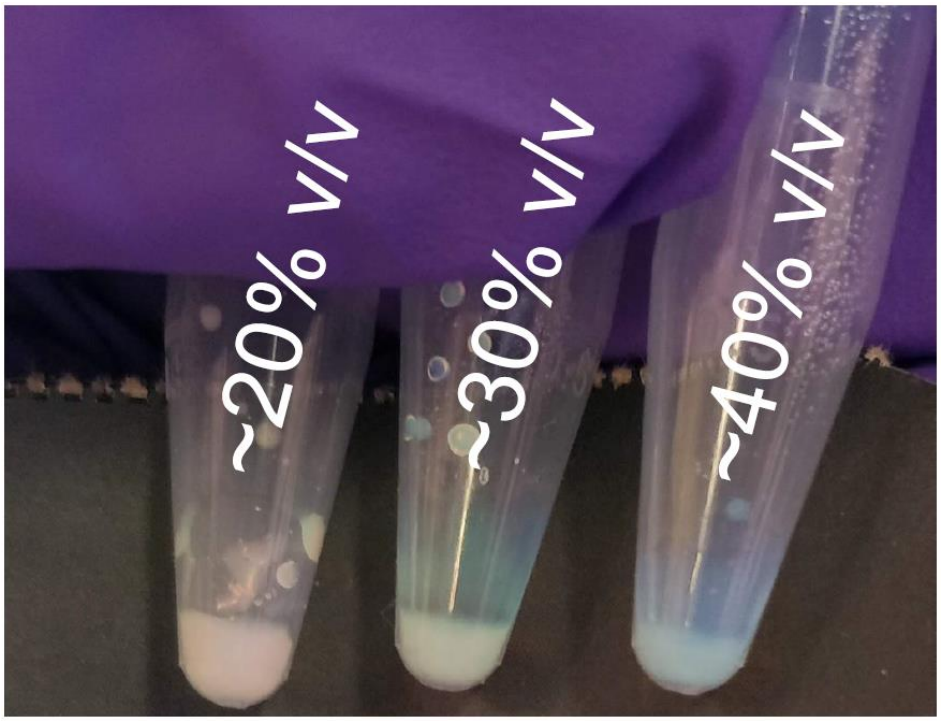

Figure 5.4: Images of suspensions of ~200 nm fluorinated latex particles at volume fractions of 20%, 30% and 40% under ambient lighting conditions. Image provided by Mykolas Zupkauskas.

To characterise these samples further by SAXS and optical reflectivity, suspensions at 20%, 30% and 40% v/v were loaded into rectangular cross-section glass capillaries 0.2 x 4 x 25 mm in dimensions and sealed with epoxy, as shown in Figure 5.5. Interestingly, if these samples were left for a few hours or days, they began to slowly develop additional strong Bragg peaks on top of the isotropic background and visible crystallinity. This behaviour was only observed for volume fractions of less than 30%. This is not unexpected: if the colloids are not in hard contact, but instead in a softer electrostatic potential, they will be able to rearrange slowly to form crystal domains. This is faintly visible in the lowest volume fraction (red) sample in Figure 5.5.

FL samples displayed a strong blue reflection at ~40%, green at volume fractions of around 26-33% and red at 20-23%. This strong colour dependence on concentration

implies that the distance between colloidal particles is not fixed by their size, i.e. they are not in hard contact. Instead, the particles are stabilised by a strong electrostatic repulsion, due to their high surface charge, similar to a Wigner crystal[173]. Red and green colours are visible over broad concentration ranges, while orange, yellow and teal are very narrow, due to the non-linear response of the human eye to pure colours. We expect the wavelength of scattered light to vary linearly with particle separation, but the human eye sees reds, greens and to a lesser extent blues more vividly than other colours[175].

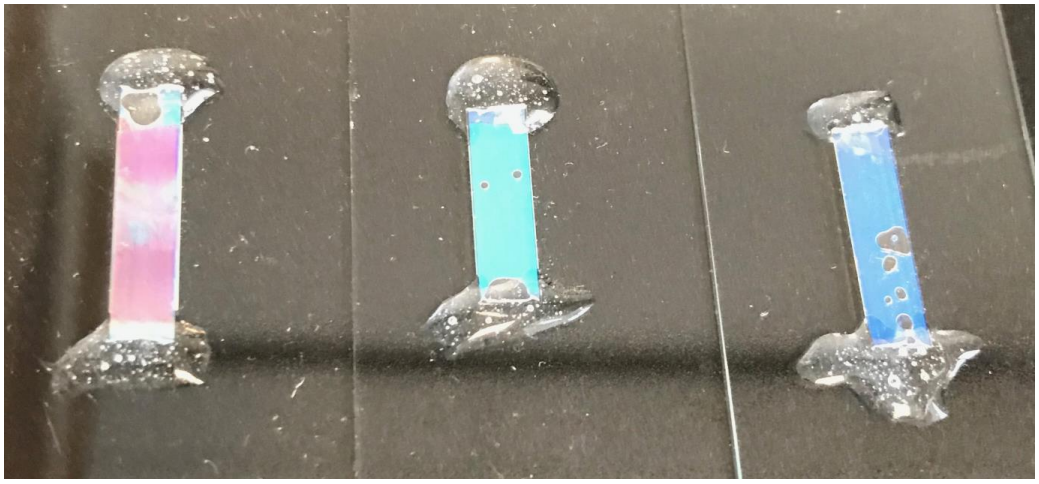

Figure 5.5: Fluorinated latex colloids at 20%, 30% and 40% v/v respectively from left to right.

5.2 Reflectivity and Transmissivity

Hard, spherically symmetric colloids that are larger than 100 nm can form crystals with photonic activity in the visible range with either face-centred cubic (FCC), hexagonal close-packed (HCP), or random hexagonal closed-packed (RHCP) lattices[176,177]. In contrast, softer spheres with long-range repulsive Coulomb interactions can form body-centred cubic (BCC) and other lattice structures, depending on the strength of the interaction[178-180]. Use of long polymers grafted to nanoparticles[181] is another means to introduce ‘soft’ interactions.

The type of lattice formed, as well as the size and refractive index of the colloids, govern the optical features of these photonic systems. For example, close-packed FCC lattices made of a single type of colloid cannot exhibit a full bandgap regardless of the refractive index difference between the medium and the colloids[95]. However, strong Bragg reflections can be observed at certain angles[96]. The refractive index contrast Δn between the colloid and the surrounding medium is an essential parameter for designing materials with structural colour. Finlayson et al.[182] demonstrated that while the strength of the

reflection in photonic crystals is expected to have a $(\Delta n)^2$ dependence due to Fresnel reflections, the distortions in the lattice structure and the size distribution of the colloids change this dependence to a linear variation in Δn[181]. It was also showed that when $\Delta n = 0.05$, the reflectance from the solid colloidal photonic crystals is <10% and strongly angle dependent[183]. In contrast, photonic crystals with strong structural colour tend to have very low transmission. In other words, it is challenging to make photonic crystals that have strong structural colours yet are not opaque.

5.2.1 Fluorinated Latex Photonic Systems

Compared to previous works on colloidal crystals, which typically report a white background with sharp Bragg reflections, our fluorinated latex suspensions display three interesting properties. First, they exhibit substantial transparency for volume fractions ranging between 15% and 40%. Second, they display angle-independent colour in reflection at a well-defined wavelength tuneable anywhere in the visible spectrum. This is also shown when particles are filled into conic pipette tips, demonstrating structural colour over a full angular distribution. Third, some but not all samples showed additional strong Bragg reflections within a very narrow angular range, typical for photonic crystals of spherical particles. Those that did not show such Bragg reflection still displayed enhanced transparency and isotropic structural colour.

The transmissivity of these samples was measured by UV-Vis spectrometry over a path length of 1 cm. Fluorinated latex colloids are compared with polystyrene and 1:1 volume ratio mixtures of both colloids at volume fractions between 13% and 40%. Results are plotted in Figure 5.6. Solid lines correspond to pure FL suspensions and are coloured to match their physical appearance. Dashed black lines correspond to pure PS suspensions and dashed purple correspond to the 1:1 FL+PS mixtures. While the pure PS and mixed FL+PS samples display the expected trend of lower transmittance as concentration increases, pure FL samples counterintuitively show a dramatic increase in transparency going from 13% to 40%. We attribute this change to a transition from a more liquid disordered state to an ordered state, coupled with the low refractive index contrast. Higher volume fraction samples could not be investigated, as they became too viscous to pipette.

Samples with a mixture of FL and PS particles were included as we were interested if the lower average refractive index contrast would lead to partial transparency while retaining strong structural colour. While these mixtures were still opaque and white with negatively

correlated transmissivity and concentration, they did show some strong Bragg peaks as discussed in Section 5.3.

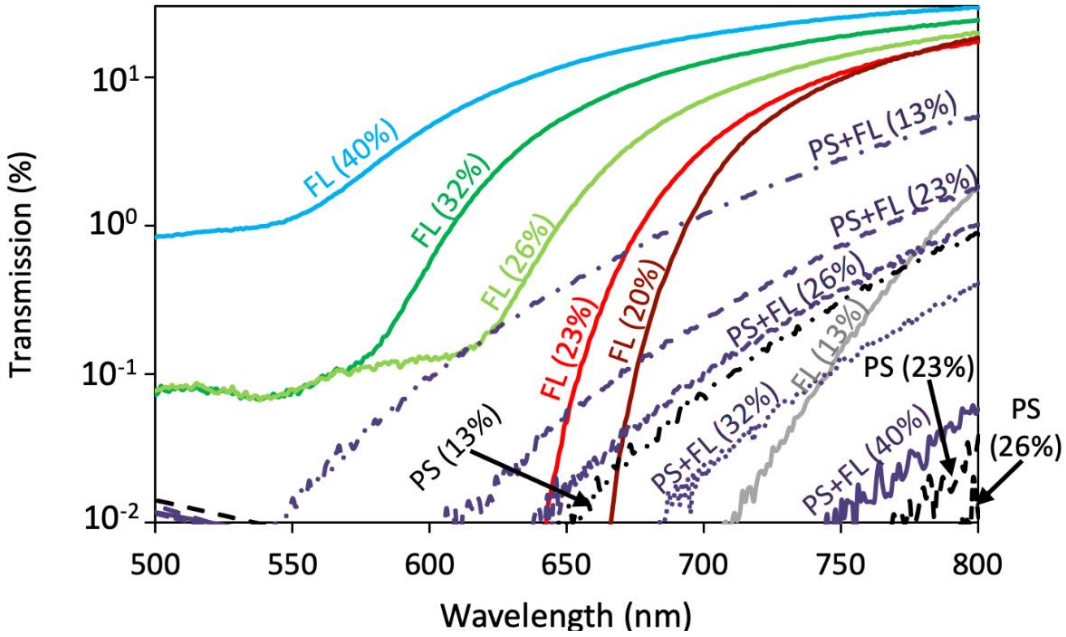

Figure 5.6: Transmission spectra for suspensions of fluorinated latex, polystyrene and 1:1 volume mixtures of both colloids at different volume fractions. Modified from [174].

Reflectivity measurements were taken using a reflection-probe bundle equipped with different LED light sources and a spectrometer. Illumination and collection were done at normal angle. The green and red samples were illuminated with a fibre-coupled white LED (Thorlabs MCWHF2) and the blue sample was illuminated with a cyan LED emitting at 490 nm (Thorlabs M490F3). The spectra were measured using a Thorlabs CCS 100 spectrometer. Reference measurements were taken using a Thorlabs BB1-E02 dielectric mirror.

Reflectance spectra were taken for samples of FL colloids at 20% (red), 30% (green) and 40% (blue) at multiple different positions in the sample and are shown in Figure 5.7. All samples showed sharp peaks at well-defined wavelengths, consistent with the macroscopically observed colour. Peaks were Gaussian and narrow, with a full width at half maximum of 15 – 20 nm. Measurements at different positions on the sample gave slightly shifted peaks in the reflectance spectrum. This weak variability suggests the existence of multiple domains having similar but slightly different average inter-particle distances. This could arise due to either charge or size fractionation of colloids in the suspension. Suspensions were uniform and isotropic immediately after mixing, but as discussed above slowly developed macroscopic inhomogeneities on the timescale of hours due to microscopic rearrangement of the particles.

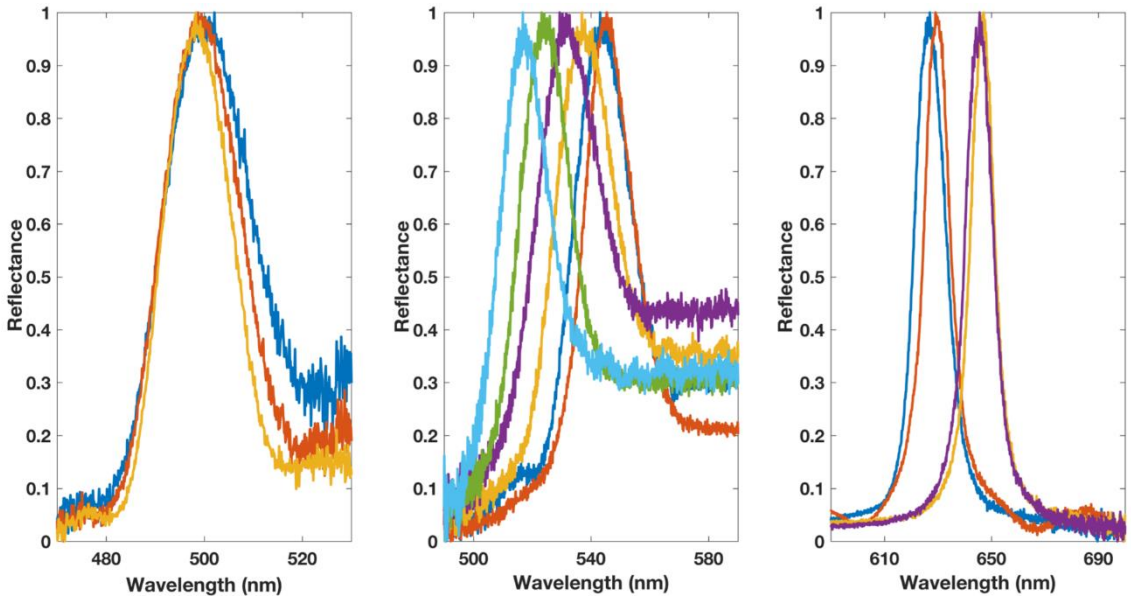

Figure 5.7: Normalised reflectance spectra for samples of fluorinated colloids at 40% (left, blue), 30%, (centre, green) and 20% (right, red). Modified from [174].

Suspensions of smaller (150 nm) and larger (250 nm) FL colloids were also prepared at the same volume fractions and both found to exhibit non-iridescent colours. These colours were blue- or red-shifted respectively compared to the ~200 nm case, but scattered light was most intense for the 200 nm case.

5.2.2 Inverse Opals

We were also able to prepare "inverse opal" structures by raising the refractive index of the continuous phase to 1.4, above that of FL, by dissolving sucrose. The refractive index of a 50% w/v sucrose solution in water was measured as 1.406, giving a contrast of $\Delta n \approx 0.036$ between FL and sucrose solution, compared to $\Delta n \approx 0.04$ between FL and pure water. A new batch of FL colloids was used for this experiment, with a DLS diameter of 190 nm, slightly smaller than those used above (FL190).

Figure 5.8 shows images of inverse opal suspensions at 20%, 30% and 40% v/v next to suspensions in pure water. It should first be noted that the colours in the pure water dispersions are blue-shifted from the classic R/G/B behaviour observed for 200 nm FL particles, due to the smaller colloid diameter. The inverse opals are strongly red-shifted even at the same nominal concentration. It is unclear whether this is a genuine effect of the opposite crystal, loss of material on concentration and resuspension due to the high viscosity and density of the sucrose solution or due to the higher average refractive index

of the suspension. The white inverse opals are also substantially more transparent than the pure water dispersions, despite the similar refractive index contrast.

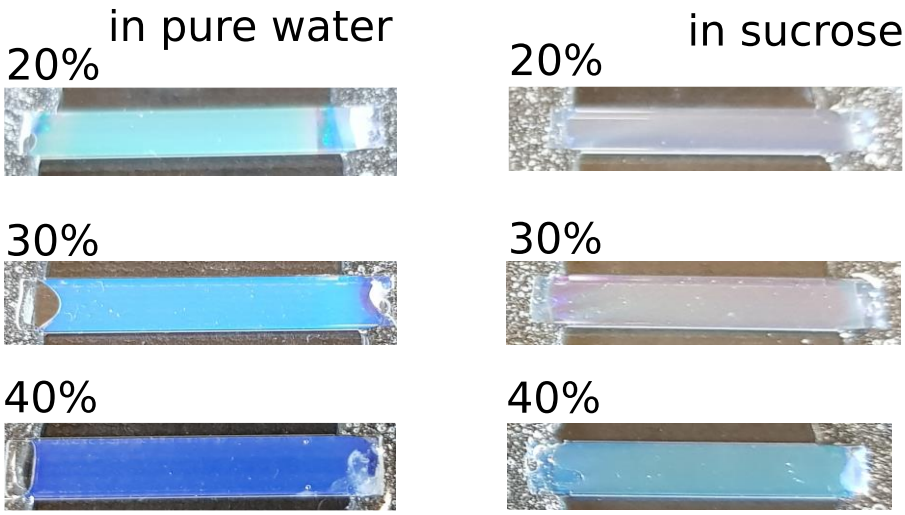

Figure 5.8: Suspensions of 190 nm fluorinated latex at 20%, 30% and 40% v/v dispersed in deionised water (left) and 50% w/v sucrose solution (right). Taken from [174].

The inverse opals displayed the same enhanced transparency and isotropic structural colour as the pure water system but were also more likely to show additional Bragg peaks and visible crystallinity. Small crystalline domains are visible in the images in Figure 5.8, which were taken very soon after injection into the capillaries. Despite this, SAXS measurements show predominantly liquid-like structure, as shown in Section 5.3. We attribute this to the reduction of the zeta potential in the high-sucrose solution, leading to softer repulsion and more thermally-induced disorder. Coupled with the increased viscosity of the system, this lack of strong repulsion leads to bulk disorder with no strongly correlated particle-particle distances and the ability to rearrange into small crystallites at the flat capillary walls.

5.3 Small-Angle X-ray Scattering

Following the reflectivity measurements that indicated that the charge-stabilised FL colloids form short-range ordered structures that coherently scatter non-iridescent light, we performed SAXS measurements to characterise these ordered phases. SAXS was done at the ID02 beamline of the ESRF in Grenoble. As discussed in Chapter 4.2 for polystyrene gels, two-dimensional scattered intensities were collected and azimuthally integrated to extract a one-dimensional profile of scattered intensities $I(q)$ against the scattering vector q. The contribution of the sample chamber was subtracted, and the form factor $F(q)$ divided out to give the structure factor $S(q)$ for each sample. Raw two-

dimensional scattered intensities are also presented here for many samples, as the presence of crystallinity can be seen through the existence of azimuthal anisotropy in $I(q)$.

5.3.1 Particle Sizing

An SEM image of FL200 particles shown in Figure 5.1 indicates a degree of polydispersity in the particle size distribution as a number of smaller particles are clearly visible. However, a proper analysis is limited due to the small statistics one obtains from such images. Hence, we performed SAXS measurements on a dilute 0.1% suspension of FL200, allowing us to obtain the form factor of the particles. The scattered intensity of a dilute dispersion containing multiple sizes of particle is

$$I(q) = c \int_0^\infty N(R)\, P(q,R) dR \qquad (5.1)$$

where c is a scaling factor and $\mathrm{P(q,R)}$ is the form factor. For spherical colloids, as is the case here, the form factor has the form given in Equation 2.8. The size distribution $\mathrm{N(R)}$ was extracted from the azimuthally integrated scattered intensities by fitting them to a kernel of the form factor via a constrained regularization method (CONTIN). The fitting was done using a MATLAB routine developed in-house by Alessio Caciagli. In Figure 5.9 we show the intensity and its fit (limited to the first two minima for accuracy) and the calculated size distribution $N(R)$. We find that a bimodal Gaussian distribution fits $N(R)$ best. The first peak (68% amplitude) corresponds to a FL-particle mean radius of 93 nm with standard deviation σ = 2.3 ± 0.1, while the second peak (32% amplitude) is at R = 67nm with σ = 2.1 ± 0.2. The data were measured at the B21 station of the Diamond light source.

This analysis predicts a bimodal distribution of colloids with 70% having a diameter of 186 nm and the remaining 30% having a diameter of 134 nm. However, it is unusual that this bimodality was not picked up by DLS, as peak separations of this magnitude are within resolution for both the standard cumulant and more accurate CONTIN methods. In addition, this behaviour persisted over multiple different batches of colloids, and is challenging to explain from a synthetic mechanistic perspective. It is more likely that the distribution is monomodal but broad and non-Gaussian. As the fitting algorithm was limited to the sum of Gaussian distributions, it erroneously approximates this asymmetric distribution as a bimodal one. Both DLS and SAXS scattering from the proposed bimodal

suspension would be dominated by the larger colloids. An R^6 term appears in the scattered intensities for both, leading to the 134 nm particles only contributing 1% of the total scattering power of the suspension.

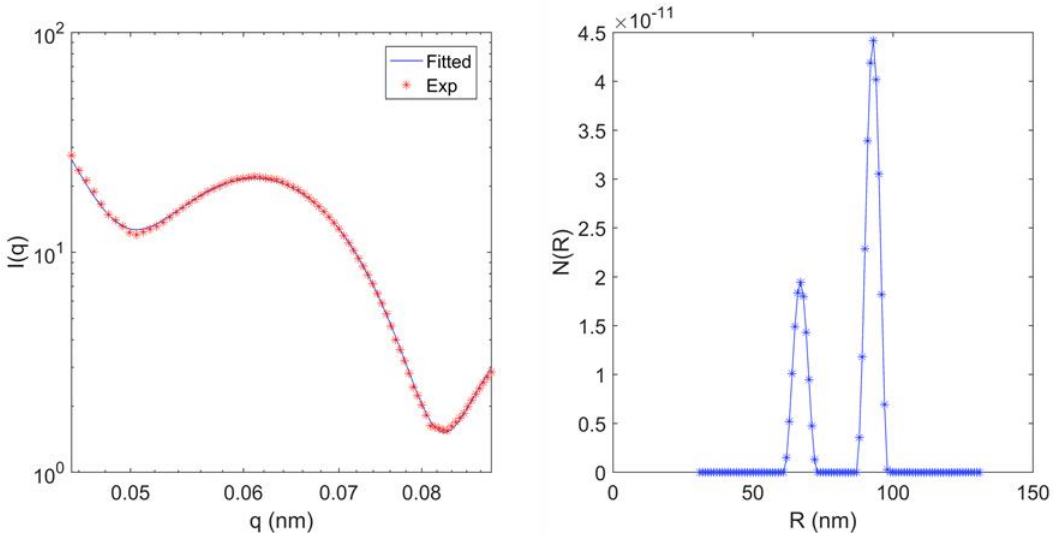

Figure 5.9: Measurement of particle size by fitting a theoretical form factor to SAXS data measured from a dilute solution of fluorinated latex colloids. Left) Experimentally measured SAXS intensity $I(q)$ of a 0.1% particle dispersion in deionized water. Right) The distribution of the number of particles as a function of particle radius used to fit the $I(q)$ data. Taken from [174].

This polydispersity does help to explain the observed scattering: while the size polydispersity is less important for this system because the colloids are not in hard contact, the accompanying charge polydispersity could lead to fractionation of particle sizes over longer timeframes. This would explain the origin of the strong angle-dependent Bragg peaks. It also explains the origin of the isotropic structural colour and suggests that the suspended colloids form a Wigner glass, as opposed to polycrystallinity on the nanoscale. Photonic glass formation in hard sphere systems has been shown to be dramatically promoted through the incorporation of between 10% and 50% secondary colloids with a diameter approximately 70% of the primary particles[184,185], very similar to the distribution predicted here.

5.3.2 Wigner Glasses and Photonic Crystals

SAXS was initially done on older samples of FL200 and equal-volume mixtures of FL200 and PS200 at 30% v/v. Both samples had plenty of time to undergo the slow ageing described above and displayed visible crystallinity and strong angle-dependent Bragg peaks. Two-dimensional scattered intensities and one-dimensional structure factors are

shown for each sample in Figure 5.10. $S(q)$ curves have been analysed and fitted to a crystal lattice and the peaks assigned to specific Miller indices.

As expected, the pure FL suspension displayed numerous Bragg peaks, arising from the scattering planes of an FCC lattice: the azimuthally integrated 2D-SAXS spectrum in Figure 5.10b reveals a first peak at q_0 = 0.0403 nm^{-1}. From this, we compute the lattice parameter to be 270 nm and the nearest-neighbour separation to be 195 nm. This correlates with our hypothesis that the suspension forms a Wigner crystal, as the particle hydrodynamic diameter is only 186 nm. The strong hexagonal symmetry of the peaks stems from the alignment of the close-packed (111) planes to the flat top wall of the capillary.

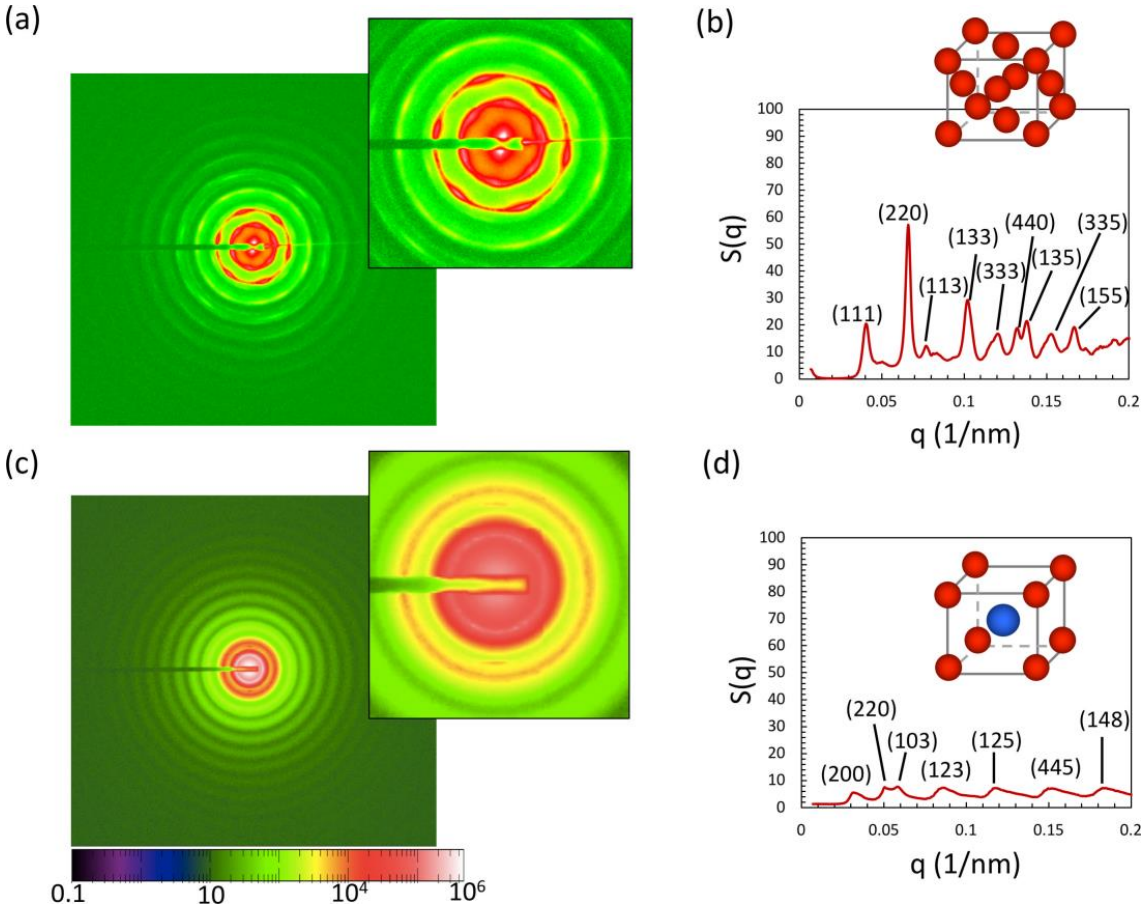

Figure 5.10: SAXS spectra of 30% v/v suspensions of ~200 nm fluorinated latex particles (a,b) and 1:1 mixtures of fluorinated latex and polystyrene particles (c,d), showing two-dimensional scattered intensities (a,c) and one-dimensional structure factors (b,d). Taken from [174].

While well-defined Bragg peaks normally imply the presence of a single crystal, closer inspection of the 2D spectrum and its radially integrated scattering intensity reveals three

additional characteristics. First, the Bragg peaks are slightly blurred radially, which indicates a slight spread of the rotational orientation of the (111) planes with respect to the confining walls. It would be surprising to have a single crystal in the sample considering the sample thickness is 200 µm and the beam size is 150 x 150 µm. Similar scattering patterns were obtained taking measurements at different positions along the same sample capillary. Second, there are also faint hexagonal scattering patterns like rotated shadows of the strong peaks but at slightly higher q values. This may be due to the formation of secondary crystalline domains with slightly smaller lattice spacing. The difference in lattice spacing can be understood in terms of the broad size distribution across all FL colloids, leading to local charge or size fractionation. Although it is known that FCC crystals of hard spheres never form in suspensions with a size distribution larger than 6%, it will have minimal effect on the formation of a Wigner crystal[141]. Since the colloids in a Wigner crystal are not in hard contact, the suspensions are able to rearrange, allowing for the coarsening of individual crystalline domains and both size and charge fractionation of colloids.

Interestingly, the integrated spectra show many weaker peaks which could not be assigned to an FCC lattice, but did fit a BCC lattice with Bragg peak positions at q = 0.049, 0.083, and 0.117 nm^{-1} corresponding to the (200), (222), and (224) planes, respectively, and a lattice constant of 260 nm. This is very similar to the situation observed by Sirota et al.[180] who measured a coexistence between FCC and BCC crystals. They performed systematic SAXS measurements of charged PS-particle suspensions, establishing a phase diagram by plotting the measured structure as a function of the ionic strength in the sample[180]. At very low ionic strengths, they observe a first transition from a liquid, disordered phase to a BCC crystal followed by a coexistence region between BCC and FCC structure as the colloid volume fraction is increased from <5% to 6-15% and 16-22%, respectively. At even higher volume fractions the dispersions became glassy, characterized by the broadening of the FCC-crystal peaks.

With a zeta potential of around -80 mV our FL particles show a very similar behaviour in dialysed aqueous suspensions, although at shifted volume fractions. Like Sirota et al.[180], we observe the loss of crystallinity coinciding with the loss of transparency and the appearance of diffuse scattering when the samples' volume fraction became smaller than ~13%. Upon increasing particle concentration to 40%, angle-independent structural colour in reflection and transparency are retained, but iridescence disappears, which is

most likely due to the increasingly glassy structure. SAXS images of these very concentrated samples show more liquid-like scattering with up to 20 diffraction rings.

The integrated SAXS intensities measured for the 30% FL+PS suspensions also show many scattering orders but appear initially to indicate a predominantly liquid structure. Macroscopically, these AB-type colloidal mixtures appear white, but on closer inspection we observe iridescence under certain angles in reflection, which can only arise from local order. When zooming into the 2D-SAXS spectrum, we observe small but clear Bragg peaks, as shown in Figure 5.10c. After dividing out the form factor (here using only the $F(q)$ measured for the FL particles) we assigned the Miller indices (*hkl*) to the peaks in the resulting $S(q)$. In the case of our 1:1 mixture we see peaks at all combinations of (*hkl*), implying a primitive cubic lattice. This would represent a CsCl lattice of FL and PS particles driven by the similar size but distinct surface charge of the two particle species. The large width of the scattering peaks reflects the polydispersity and thus a small crystallite size in our system. Nevertheless, it is interesting that these seemingly different particles do not segregate from each other. This can be rationalized by the Hume-Rothery rules stating that if the difference in particle size is no more than 15%, then AB crystals will form[186].

To investigate the ordering in fresher samples that had not been allowed to completely crystallise and where the scattering was primarily isotropic instead of dominated by Bragg peaks, FL190 colloids were prepared at 20%, 30% and 40% along with PS200 at 20% and 30%. SAXS spectra for these samples are plotted in Figure 5.11. All samples still show some crystallinity, as SAXS could not be performed immediately after injection; crystal peaks in the 2D-SAXS spectra can all be matched to an FCC lattice. The PS samples show many more diffraction rings than the FL, likely due to the more monodisperse suspension.

FL samples at all volume fractions show predominantly glassy or liquid-like disorder with weak Bragg scattering superimposed. The strong first peak in $S(q)$ again implies a photonic Wigner glass. The *q*-value of the first peak was converted to a real-space feature size, and that size used to calculate approximate wavelengths for scattering using Equation 4.3. This predicts a peak of 490 nm for the 40% sample and 570 nm for the 30%, in excellent agreement with the reflectivity measurements.

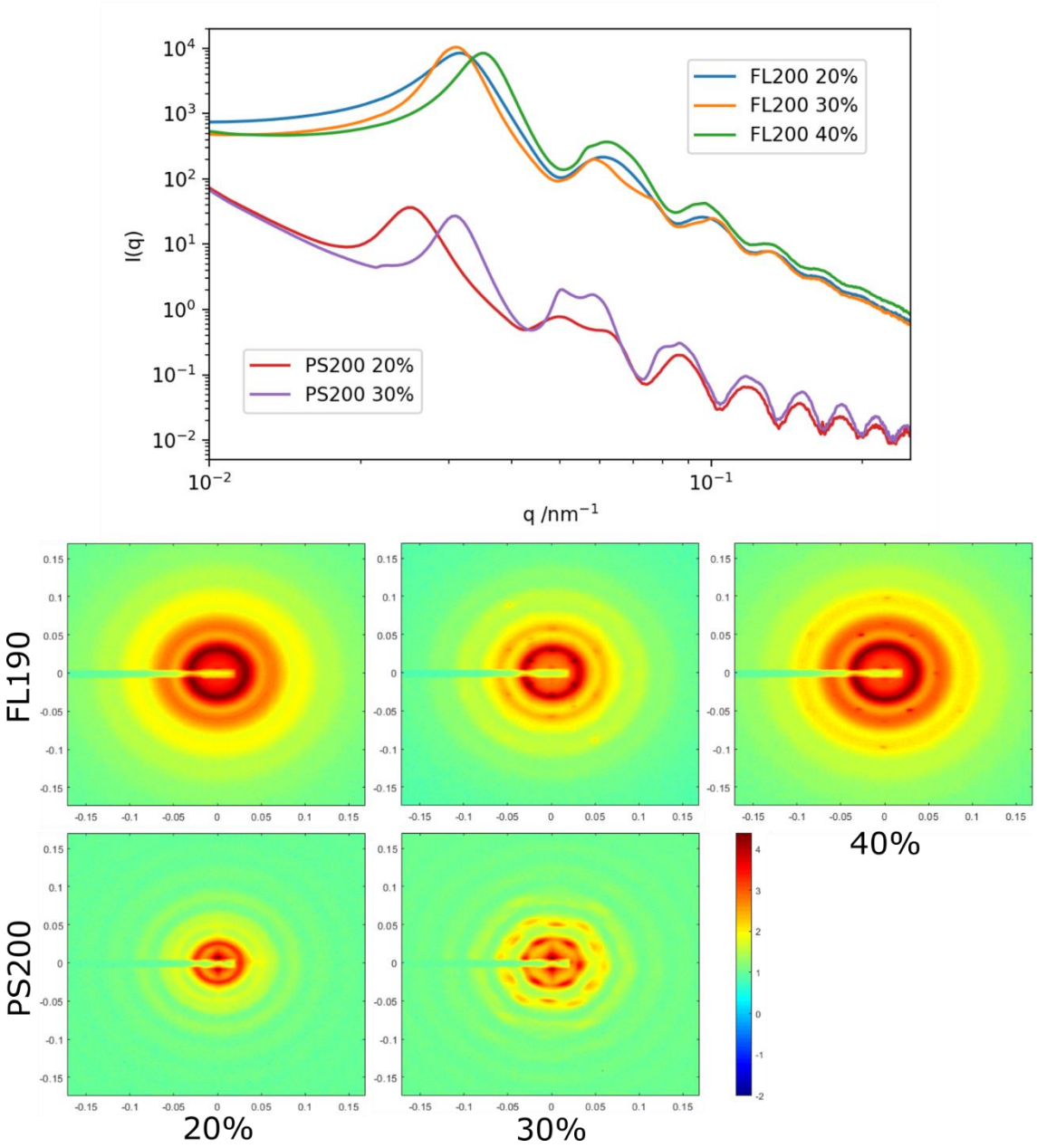

Figure 5.11: SAXS spectra of FL190 and PS200 colloids at 20%, 30% and 40% v/v, showing both two-dimensional scattered intensities and azimuthally integrated curves. In this case, the form factor has not been divided out. Scales are q /nm^{-1}.

SAXS experiments were also performed on FL samples which were prepared immediately before measurement, to avoid ageing and crystallisation. These experiments were performed at the B21 beamline of the Diamond Light Source and showed exclusively glassy behaviour with no long-range order or crystallinity at any volume fraction. However, unfortunately the q-range at the B21 beamline was not sufficient to resolve the first peak in $S(q)$.

5.3.3 Inverse Opals

"Inverse opal" FL Wigner glasses discussed in Section 5.2.2 were also characterised using SAXS. 2D-SAXS spectra and azimuthally integrated traces are plotted in Figure 5.12. In contrast to the crystalline flecks visible by eye in these samples, as shown in Figure 5.8, SAXS results reveal exclusively liquid-like order and show no superimposed Bragg peaks in the two-dimensional scattered intensities. This is attributed to the screening of the Coulombic repulsion by the sucrose in the solution. As the electrostatic interaction is screened by ions in solution, it becomes less long-range and effectively "harder", as the gradient of the interaction potential is higher. The colloids are therefore less constrained by interparticle interactions and more disorder is introduced by thermal motion.

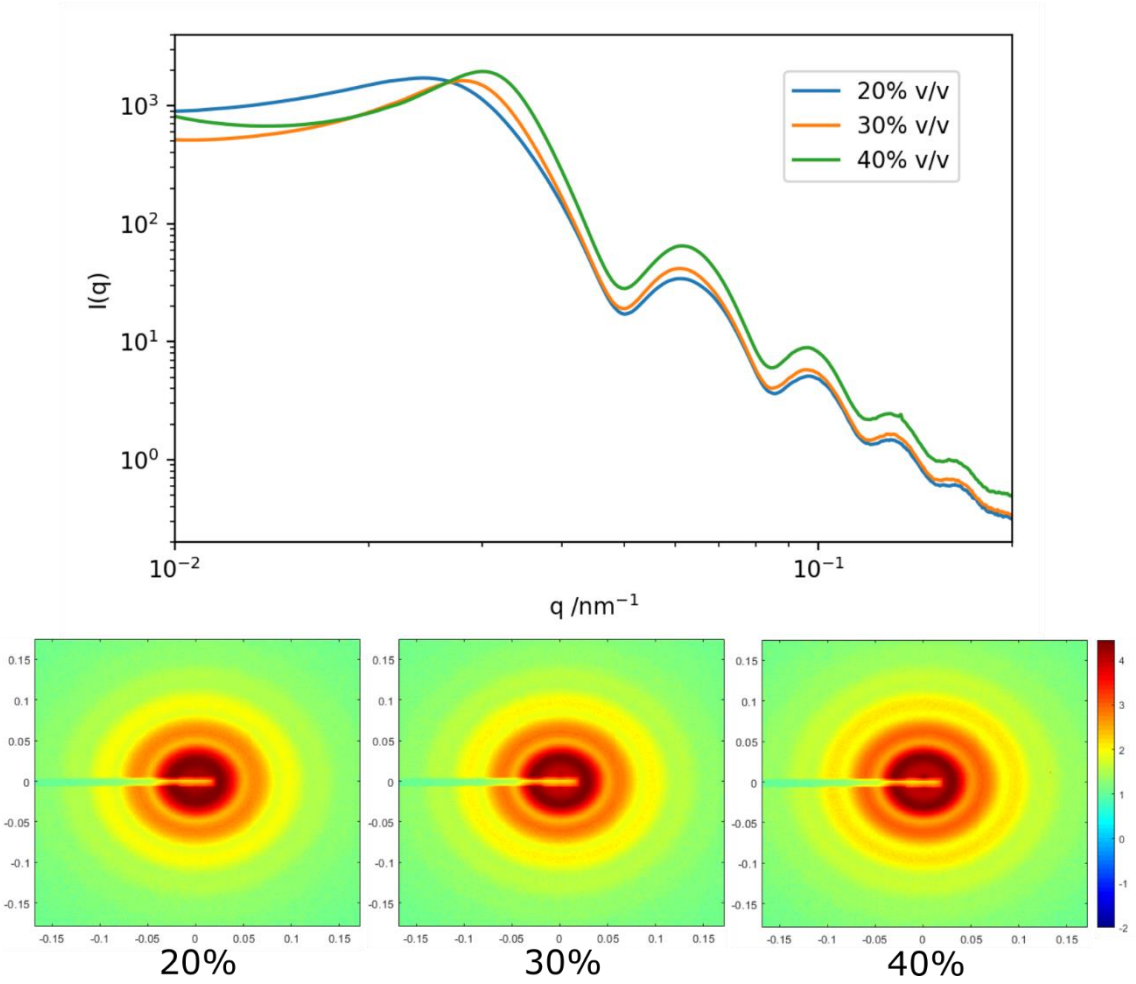

Figure 5.12: SAXS spectra of "inverse opals" of 190 nm fluorinated latex colloids dispersed in 50% w/v sucrose solution. Both two-dimensional scattered intensities and azimuthally integrated curves are shown. The form factor has not been divided out. Scales of 2D plots are q /nm^{-1}.

The presence of isotropic structural colour even in the absence of Bragg peaks implies that there is still a degree of short-range order in the system. A concentration-dependent

peak in the structure factor was observed. Conversion of these peaks to expected wavelengths using the method from above gives 40%: ~590 nm, 30%: ~675 nm and 20%: ~750 nm, which correspond closely to the observed colours from macroscopic samples. It also explains the increased transparency of the 20% sample: unlike FL190 particles at 20% v/v in pure water, which lose their glassy character and become disordered and milky, 20% inverse opals are still a Wigner glass, but reflect in the near-IR.

5.3.4 Mixed Colloidal Systems

Finally, due to the mixed Wigner crystals observed in AB mixtures of FL and PS particles, we also prepared 30% v/v solutions of AB_2, A_2B, AB_{13} and $A_{13}B$ ratios of the same particles, as they all have analogues as binary metal crystals[187]. 2D-SAXS spectra and azimuthally averaged traces are plotted in Figure 5.13. While all samples appeared white, they did display some Bragg reflections at specific angles, again due to ordering at the walls. The FL-rich phases appear to be more crystalline than the PS-rich phases, though this may be an artefact of the higher density and therefore higher SAXS contrast of fluorinated latex. The A_2B sample shows a very large number of peaks, implying multiple crystal domains of different lattice parameter due to fractionation of the two colloidal species. We were unable to assign the peaks to one or more crystal lattices.

Conversely, the $A_{13}B$ sample appears very similar in structure to the pure FL sample at 30%, implying that in this case the crystal is able to tolerate a low volume fraction of secondary colloids without changing the lattice structure, akin to a solid solution in metallurgy.

Interestingly, while the FL-rich mixed systems displayed the most order in SAXS, the PS-rich systems displayed stronger Bragg reflections to the naked eye. This is due to the higher refractive index but lower density of PS, meaning it scatters visible light more strongly than FL but X-rays less strongly.

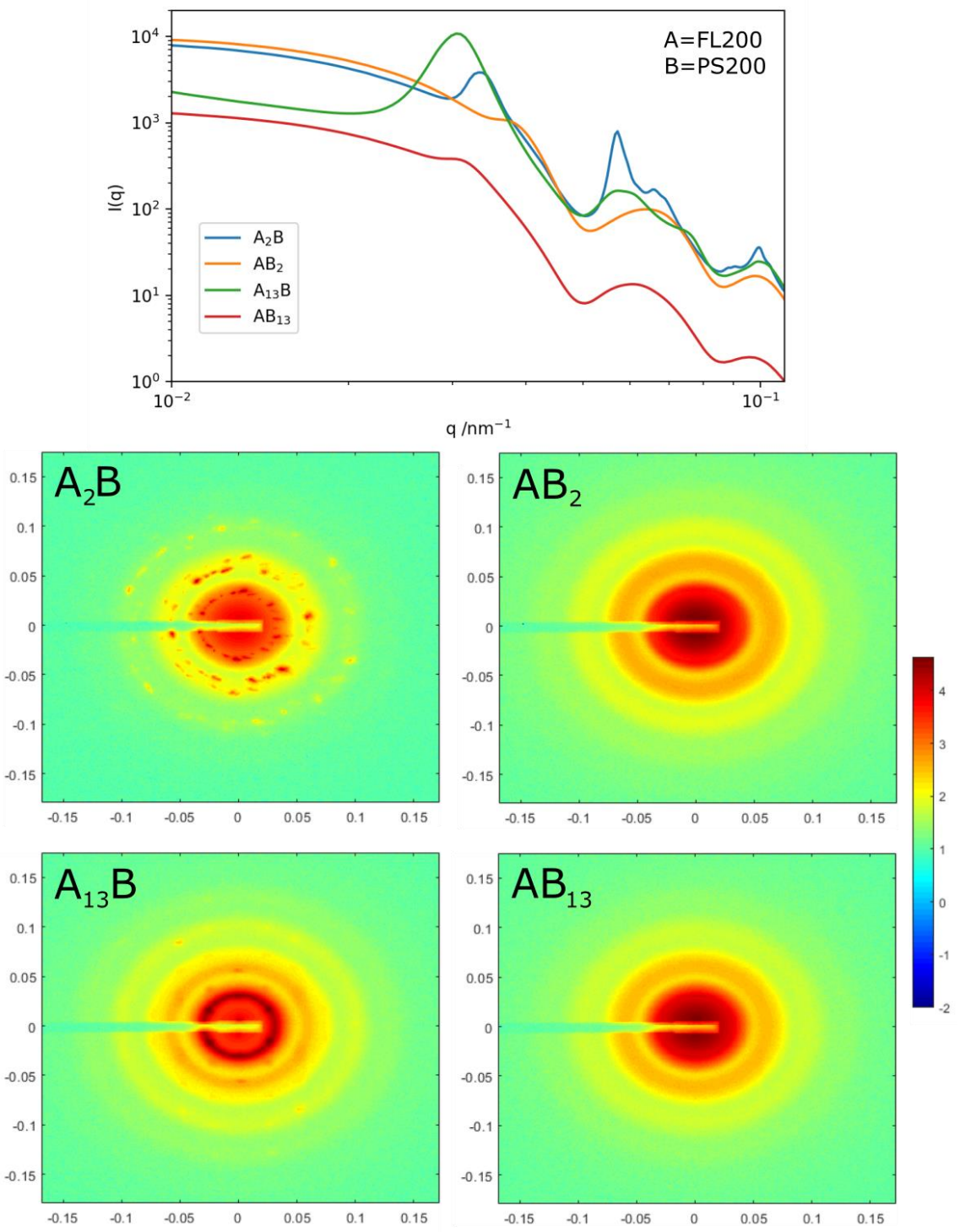

Figure 5.13: SAXS spectra of mixed suspensions of FL200 (A) and PS200 (B). Both two-dimensional scattered intensities and azimuthally integrated curves are shown. The form factor has not been divided out. Scales of 2D plots are q /nm^{-1}.

5.4 Electromagnetic Simulations

Based on the SAXS measurement results, we carried out electromagnetic simulations to model how changing the lattice parameter of the FCC crystal sets the reflection colour. Electromagnetic simulations were carried out using a commercially available finite-difference time-domain simulator in three dimensions (Lumerical Inc., FDTD). Here, latex particles were modelled as dielectric spheres with a refractive index of 1.37 while the background index was set to 1.33 to mimic water. The colloidal lattice constant was varied between 300 and 500 nm. The structure was illuminated at normal angle by a broadband plane-wave source. Bloch-boundary conditions were applied at the x- and y-boundaries of the simulation region while the *z*-boundary was set as a perfectly matched layer. Modelled reflectance, plotted in Figure 5.14, shows that despite the low refractive index contrast between the medium and the colloids, this system can still reflect the incident radiation over a well-defined peak of wavelengths determined by the lattice constant. We also show that full spectrum structural colour is accessible using this system, further proving the feasibility of using our materials in colour filters, reflectors, and optical coatings. Simulations were carried out by Dr Talha Erdem.

Reflectance peaked at different wavelengths and volume fractions for different colloid diameters but ~200 nm colloids gave the most intense reflections across the visible spectrum, consistent with our experimental observations.

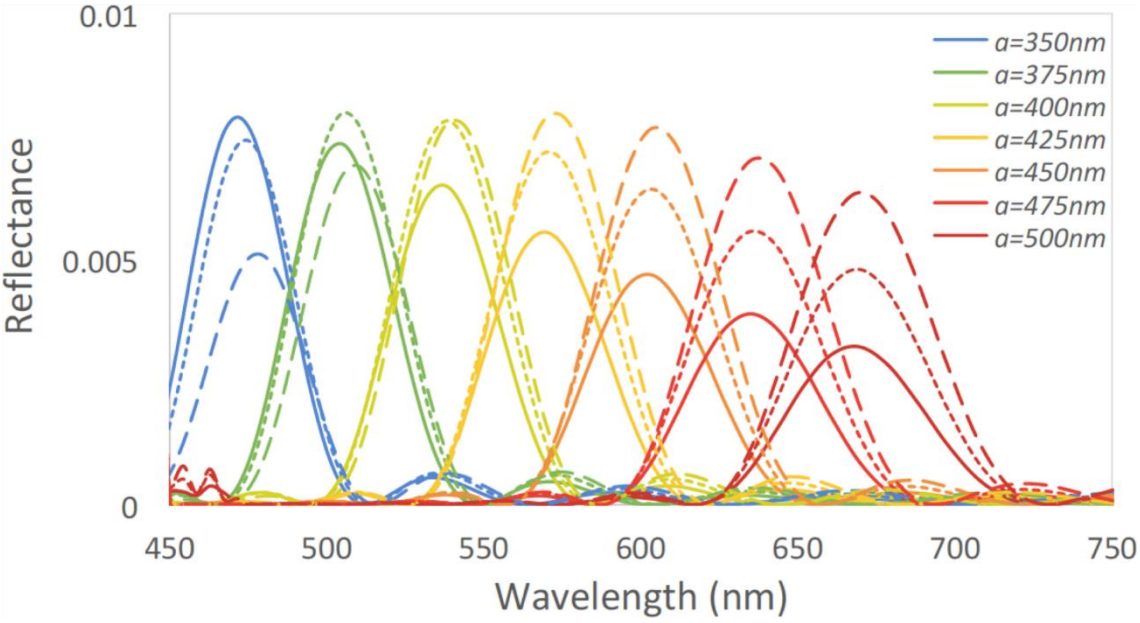

Figure 5.14: Simulated reflectance spectra of modelled FCC crystals of 170 (solid), 190 (short dashed) and 210 nm (long dashed) colloids with a lattice parameter, a, varying between 350 and 500 nm. Taken from [174].

5.5 Conclusions and Outlook

This chapter presented the use of low refractive index fluorinated latex particles in solution-phase assemblies that exhibit structural colour and high transparency. SAXS, reflectivity measurements and electromagnetic simulations were used to characterise the structure of these liquid-phase assemblies and showed that the particles were not in hard contact but were instead held in position by strong electrostatic repulsion between the colloids. Particles were primarily arranged in a Wigner glass with no long-range order and short-range correlations between the particles, which gave rise to isotropic coherent scattering of light with a narrow wavelength range. Because the particles are not in hard contact, the position of this peak could be tuned throughout the visible spectrum independently of the particle size by varying the volume fraction of the suspension, making it an ideal candidate for non-iridescent coherent scattering.

With ageing, these systems began to develop Bragg peaks in addition to the isotropic structural colour. These Bragg peaks were shown to be caused by the size and charge fractionation of colloids and the subsequent growth of Wigner crystals of predominantly FCC character. This ultimately led to the formation of transparent photonic crystals with high transparency but strong reflectance at specific wavelengths. Being transparent but also possessing a tuneable reflection band, these colloidal photonic crystals hold great promise for low cost optical coatings, filters, and displays. We also showed that suspensions with inverted contrast behaved in the same way, albeit with red-shifted reflectance peaks and lower tendency to form crystals.

Finally, we showed that while even the presence of just 7% polystyrene colloids in the system was enough to remove the enhanced transparency and isotropic structural colour, well defined mixtures of particles could assemble into a variety of phases otherwise seen for alloys and mixed metal oxides, including mixed Wigner crystals and solid solutions, implying the characteristics of such systems could be tuned easily be mixing particles with various properties.

Promising future work could focus on maximising the intensity of the scattered light without sacrificing transparency. In particular, the use of a cross-linkable medium to arrest particles immediately after dispersion is currently being investigated by the author. This would allow the retardation of ageing processes and crystal formation, ensuring systems retained full photonic Wigner glass character over long timescales.

6 OTHER PROJECTS

6.1 DNA-Coated Oil Droplets

Oil-in-water (O/W) emulsions play a key role in many domestic and industrial soft materials[188] and are also used as templates for advanced materials fabrication[189,190]. Oil droplets can effectively act as soft colloids with reconfigurable surfaces, due to the mobility of the surfactants at the interface. Just as with hard colloids, DNA has been used to functionalise these soft interfacial materials and to mediate hierarchical self-assembly[191]. However, until this point, DNA-functionalised emulsion droplets have only been achieved with relatively low coating densities and at low yields, making their scale-up impractical. Here we introduce the synthesis and assembly of densely-coated DNA functionalised O/W emulsion droplets via a number of methods using the functionalised surfactants discussed in Chapter 3.2.3.

This section reports work published in [192] and from another manuscript under preparation [200]. Synthesis of DNA-coated emulsion droplets was done by Alessio Caciagli and Mykolas Zupkauskas using the functionalised diblocks developed by this author in collaboration with Mykolas Zupkauskas. Experiments on colloids on oil droplets were done by this author in collaboration with Alessio Caciagli.

6.1.1 Preparation

Various methods, including ultrasonication, microfluidics and membrane emulsification were used to create oil droplets of either silicone (50 cSt) or hexadecane (2 cSt) oil. The interface was stabilised with either the PS_{30} diblock synthesised by C. Mugemana and N. Bruns or commercially available Pluronic F108, both with azide-functionalised PEG ends

using the protocol described in Chapter 2.2.2.1. The range of droplet sizes used was highly dependent on the emulsification method used: ultrasonication, microfluidics and membrane emulsification gave droplets 20 – 1000 nm, ~20 – 100 µm and >50 µm in size, respectively. The method, oil and surfactant used were interchangeable, and could be chosen to determine the size, stability against coalescence and coating density of the droplets, but were irrelevant to the success of the protocol.

Figure 6.1 shows the protocol for the synthesis of DNA-coated O/W emulsion droplets. Azide-functionalised di- or tri-block copolymers were dissolved in deionised water and mixed with the desired oil. The system was emulsified by one of the three methods stated above and detailed below to give emulsion droplets of a well-defined size stabilised by the presence of the surfactant at the interface. DNA or dye functionalisation was then achieved by reacting the terminal azide groups on the hydrophilic PEG chains with either DBCO-Cy5 fluorescent dye or DBCO-DNA via a strain-promoted azide-alkyne cycloaddition[118,119]. Fluorescence assays of silicone oil droplets emulsified by microfluidics and stabilised with PS_{30} showed coverages of ~70,000 azides per μm^2, a sevenfold increase over previously reported coating densities[193].

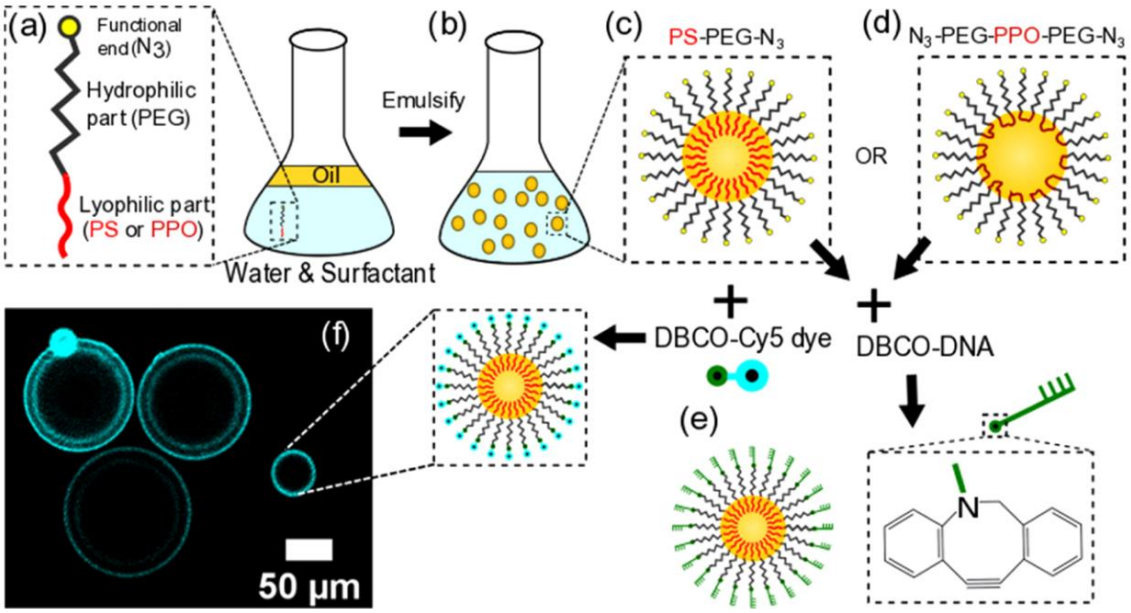

Figure 6.1: Schematic protocol of DNA-functionalized oil droplet synthesis. (a) An aqueous solution containing the block-copolymer is mixed with immiscible silicone or hexadecane oil. (b) Emulsification via microfluidics, membrane, or sonication gives oil-in-water droplets stabilized by a densely packed PEG-corona (c or d). Terminal azide groups on the PEG chains are reacted either with DBCO-Cy5 dye and imaged in confocal microscopy (f) or with DBCO-DNA (e). The second inner ring visible in the confocal image is due to lensing and is not a signature of a double emulsion. Taken from [192].

6.1.1.1 Membrane Emulsification

The emulsions were obtained by a membrane technique using an LDC-1 Dispersion Cell (Micropore Technologies Ltd.). 5 ml of the dispersed phase (hexadecane or silicone oil) was injected through the membrane (20 μm pore size, 80 μm intrapore distance) into 50 mL of deionised water containing 2% w/v surfactant (PS_{30}-*b*-PEG_{79}-N3 or F108-N3) by means of a syringe pump (Aladdin 1000, WPI) with a flow rate of 0.5 mL min^{-1}. The agitator was driven by a 24 V direct current motor, and the paddle rotation speed was set to 19.066 Hz (1144 rpm), corresponding to an applied voltage of 10 V.

6.1.1.2 Ultrasonic Emulsification

Surfactant (1600 μL) at 2% w/v in deionised water was mixed with oil (200 μL) and water (200 μL) in a glass vial. The mixture was vortexed and then ultrasonicated with a probe sonicator (Bandelin Sonopuls HD 2200) at 20% amplitude for 10 min in pulsed mode at 1 Hz. The resulting droplets were kept at room temperature.

6.1.1.3 Microfluidics

A single junction co-flow microdroplet device was designed with AutoCad (Autodesk) in collaboration with A. Levin. Microfluidic channels with a height of 25 μm were fabricated in polydimethylsiloxane (PDMS; Dow Corning), using SU8 on silicon masters and standard soft lithography techniques and then plasma bonded to glass slides to create sealed devices. Formed PDMS devices were plasma treated for 500 s (Diener Femto) forming a hydrophilic surface coating. The channels were immediately filled with water to ensure they remained hydrophilic for the duration of the experimental procedure. The oil phase (hexadecane or silicone oil) was flowed at 50 $\mu L h^{-1}$ and the water phase containing 2% w/w surfactant was flowed at 250 $\mu L h^{-1}$ through this T-junction microfluidic device. The droplets were stored at room temperature.

6.1.2 Characterisation

For each method, two combinations of oil and surfactant were chosen: hexadecane with a custom PS−PEG diblock copolymer and silicone oil with a commercial triblock copolymer (Synperonic F108). Droplets were sized by either image analysis for microfluidic and membrane emulsification methods and DLS for ultrasonication. Images of obtained droplets and representative size distributions are shown below in Figure 6.2.

The membrane emulsification strategy produced a slightly polydisperse emulsion according to the method's typical yield. A lower polydispersity was achieved using the

triblock copolymer/silicone oil combination. Rather than an effect of the surfactant, this improved monodispersity was due to the higher viscosity ratio between the dispersed and continuous phases, which decreased the supply of the dispersed phase during droplet formation, resulting in smaller droplets[194]. The droplets have been shown to be stable against coalescence for months, with a slight broadening of the size distribution over time due to Ostwald ripening.

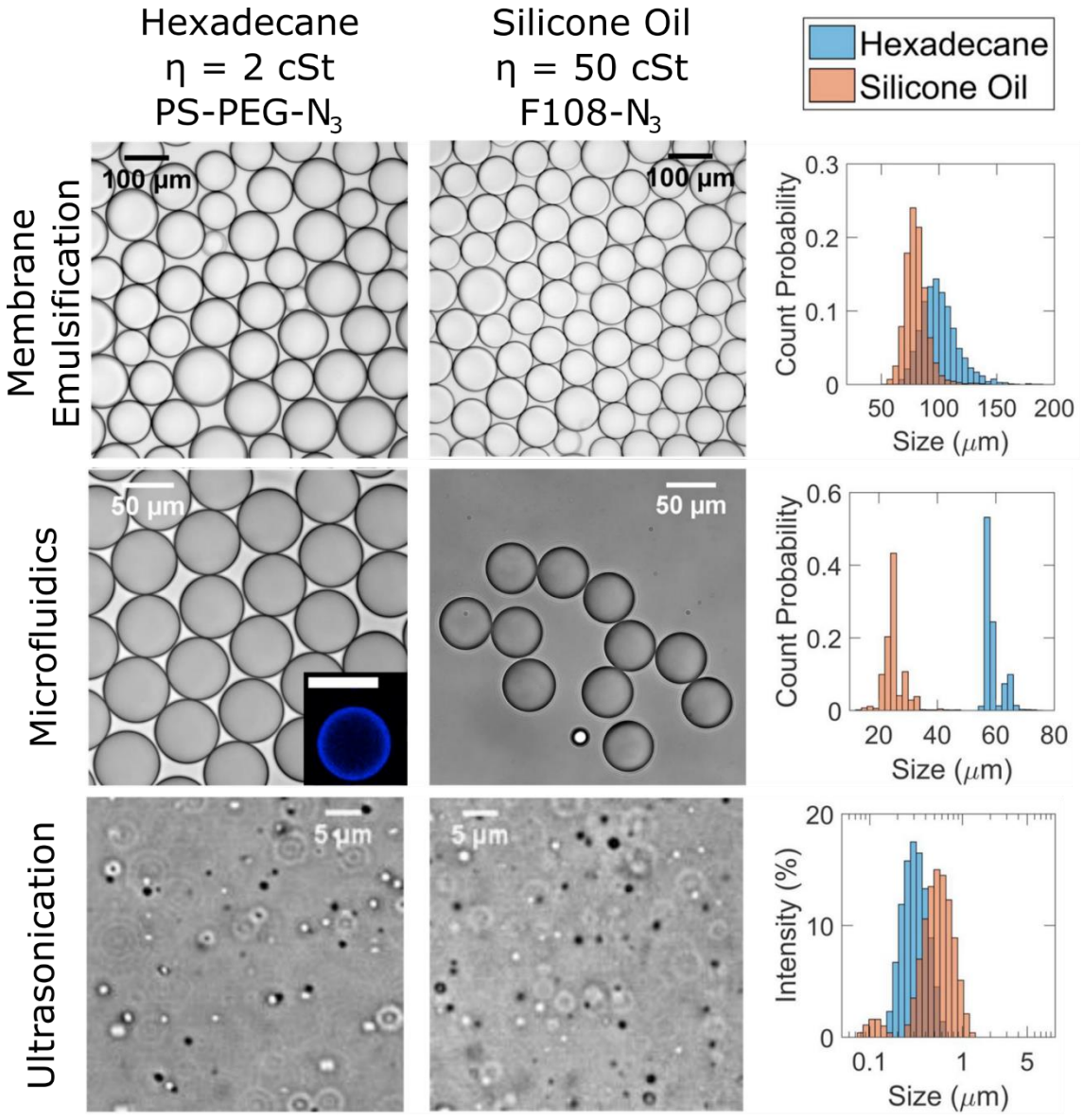

Figure 6.2: Comparison of droplets made with different emulsification methods. Brightfield optical microscopy images and droplet size distributions are shown for hexadecane and silicone oil droplets produced through membrane emulsification, microfluidics and ultrasonication. Modified from [192].

Droplets produced by microfluidics were very monodisperse, with a polydispersity index of less than ~10%. The diblock copolymer/hexadecane combination produces larger droplets, probably as a result of the lower viscosity ratio between the dispersed and continuous phases, that are of slightly better quality, due to faster kinetics of surfactant adsorption at the interface. We ascribe this fast kinetics to two effects. First, the adsorption is faster for lower viscosity ratios between the dispersed and continuous phase. Second, although triblock copolymers have a greater interfacial anchoring strength than diblock copolymers of the same geometry, their diffusion is slower due to their larger size[195]. Both effects favour the hexadecane system.

Finally, the ultrasonication emulsification strategy produced a more polydisperse nanoemulsion, which is typical for the method[196]. The diblock copolymer/hexadecane combination again gave superior quality droplets (smaller and more monodisperse), which can be explained using the same viscosity and surfactant mobility arguments given in the microfluidics case.

Caciagli et al. went on to show that such DNA-coated oil droplets can be both self-assembled into gels and supraparticles and attached to DNA-coated surfaces for controlled release[192]. All of these systems showed the specific, thermally-reversible melt transition characteristic of DNA-coated colloids.

6.1.3 Colloids on Oil Droplets

DNA-coated oil droplets provide a unique platform for the study of colloid behaviour on a two-dimensional plane. If DNA-coated colloids are bound to the surface of an emulsion droplet through DNA hybridisation, they remain mobile across the surface due to the inherent mobility of the surfactant along the oil-water interface. Binding colloids to the surfactants stabilising an interface instead of directly to the interface in a Pickering emulsion has several advantages. First, binding strength can be tuned by the choice of DNA and is typically ~10 k_BT, compared to >100 k_BT via a Pickering mechanism[197]. This allows colloids to be attached and detached to/from the interface at will. Second, particles stabilising a Pickering emulsion experience strong capillary forces due to the curvature of the interface. These forces are both strong and long-range, typically causing non-specific aggregation of colloids in the 2D plane[198]. In contrast, colloids tethered to an emulsion droplet behave far more like a 2D colloidal gas[193].

Systems of DNA-coated colloids tethered to O/W emulsion droplets through hybridisation interactions were first reported by Joshi et al.[193] in the Eiser group. They

used a trilayer structure to attach DNA to the droplets. SDS was used to stabilise the interface of a silicone oil/water emulsion, resulting in droplets with a negative surface charge. A graft copolymer, poly(L-lysine)-*g*-poly(ethylene oxide) (PLL-*g*-PEG), comprising a positively charged PLL backbone with pendant PEG chains end-functionalised with streptavidin, was bound electrostatically to the negatively charged interface. Finally, biotinylated DNA was bound to the free streptavidin sites[57]. The end result is a droplet electrostatically coated with a number of mobile PLL-*g*-PEG-DNA "rafts" capable of binding with appropriately functionalised DNA-coated colloids, as shown in Figure 6.3.

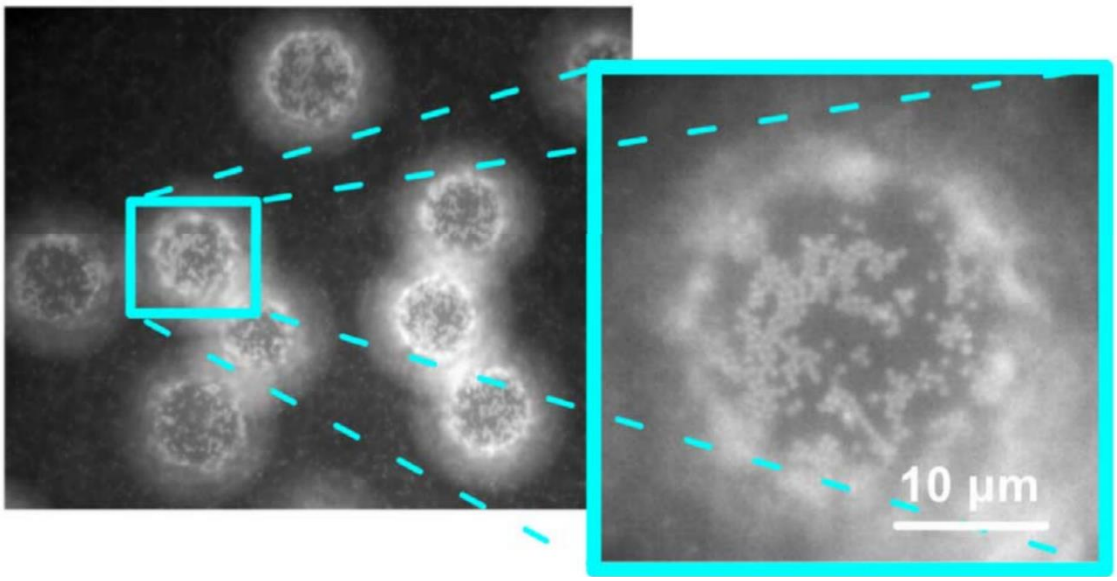

Figure 6.3: 527 nm polystyrene colloids bound to 20 µm silicone oil droplets via DNA-hybridisation to an electrostatically adsorbed PLL-g-PEG-DNA layer. Taken from [193].

Joshi et al.[193] showed that colloids could be reversibly bound to the oil droplets using this method, though they noted that melt temperatures were much higher than those for comparable colloid-colloid binding mediated by the same DNA strands, due to the flexibility of the interface and the much larger binding volumes that allowed.

However, the melt transition of these systems was no longer sharp, instead occurring over windows of up to 20 °C. This was attributed to inequality in the number of PLL-*g*-PEG rafts per colloid; colloids which attached to the droplet sooner could scavenge many PLL-*g*-PEG rafts, while those that bound later would bind with only a few. At a certain binding concentration, all rafts would be scavenged, and no further binding would be possible. In addition, rafts could bridge between two colloids and colloidal diffusion on the surface was slowed by the bulky graft copolymer.

This system was used alongside simulations by Joshi et al. to study the phase behaviour of colloids mobile in a 2D-plane in the presence of a depletant, as shown in Figure 6.4. Concentrations of SDS were raised above what was necessary to stabilise the droplets until excess surfactant formed micelles at the CMC. SDS micelles are less than 2 nm in size[199], making them effective depletants for DNA-coated colloids of a range of sizes.

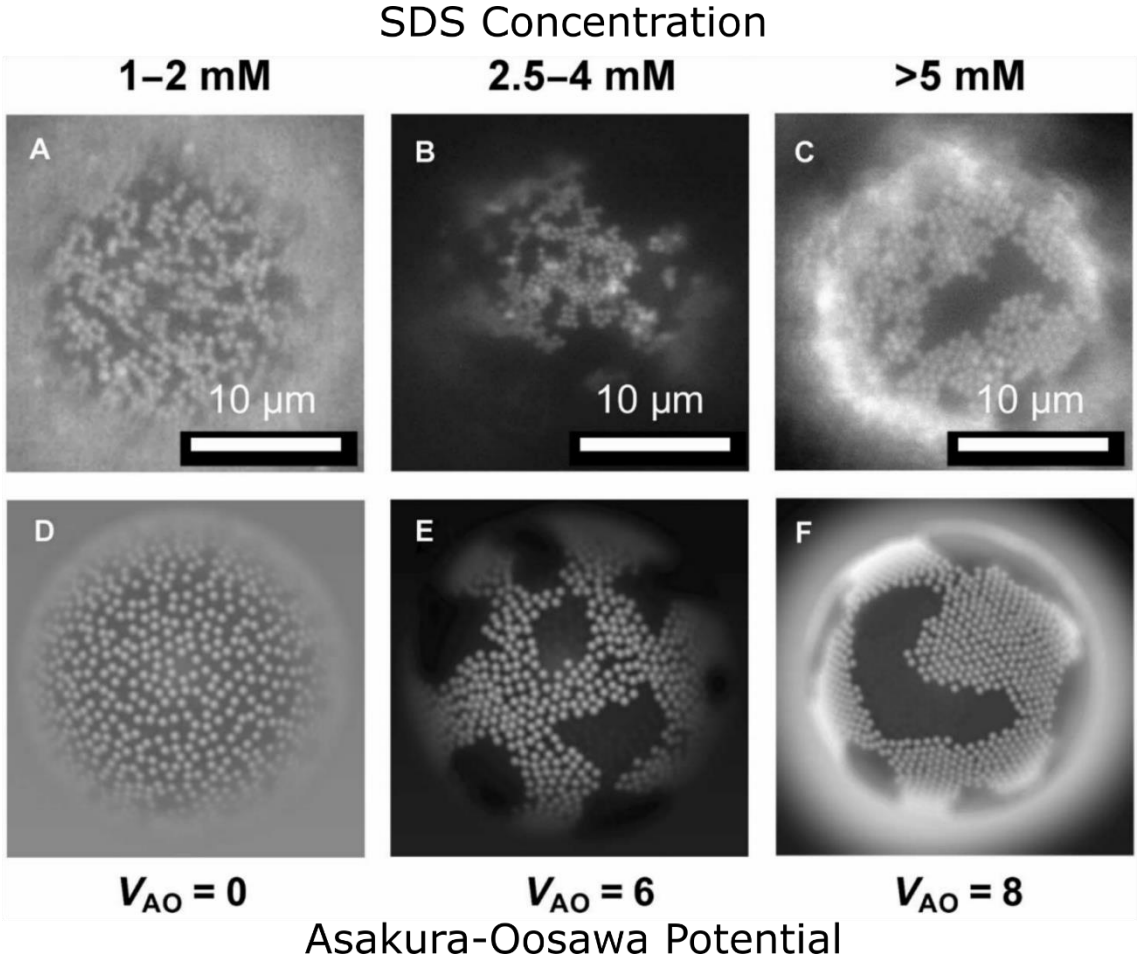

Figure 6.4: Packing of colloids tethered to a two-dimensional interface at different interaction strengths. Top) Fluorescence micrographs of 527 nm polystyrene DNACCs as a function of bulk SDS concentration. Bottom) Simulations snapshots for different strengths of the Asakura-Oosawa potential. Modified from [193].

However, when we attempted to extend this system to mixtures of colloids, it was found that the unequal distribution of PLL-g-PEG rafts and reduced colloidal mobility prevented us from getting reliable results. For these reasons, we used the DNA-coated emulsion droplets produced by membrane emulsification instead to conduct experiments on colloids tethered to a two-dimensional interface. Because the DNA on the oil droplet is attached directly to the stabilising surfactant, this system avoids many of the issues of the PLL-*g*-PEG system while also being substantially simpler to synthesise.

To create samples for microscopy, 24 µl of a suspension of colloids at 1% w/w was mixed with 100 µl of creamed DNA-coated droplets and the volume made up to 250 µl with phosphate buffer containing 100 mM NaCl and 0.5% functionalised surfactant. Samples were loaded into rectangular glass capillaries for imaging with bright-field and fluorescence microscopy. Colloidal binding was immediately observed and very high grafting densities achieved, as shown in Figure 6.5.

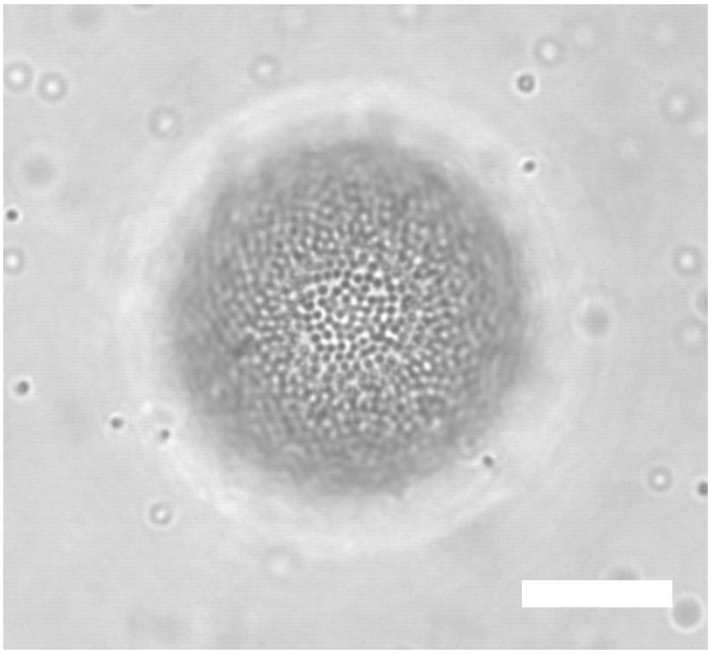

Figure 6.5: 420 nm polystyrene DNACCs on the surface of a hexadecane droplet produced by membrane emulsification and stabilised with PS-b-PEG-DNA. Scale bar is 5 µm. Taken from [200].

Figure 6.6 shows optical micrographs taken in fluorescence showing the successful binding of 800 nm and 200 nm polystyrene DNACCs to 100 µm hexadecane droplets produced via membrane emulsification and stabilised with F108-DNA. 200 nm colloids are very close to the resolution limit of the microscope and objective used, so appear as single pixels, while 800 nm colloids appear very bright due to their larger volume. The droplets are so large that only a portion of them is in the focal plane of the microscope at any particular time. Large areas at the top or bottom of the droplet can be imaged simultaneously, but imaging in the middle of the droplet appears instead as a ring of attached colloids. The 200 nm colloids are small enough to fit in the interstices of a close-packed layer of 800 nm particles at the interface. Further experiments are ongoing on this system now to characterise the behaviour of the 200:800 nm binary mixture.

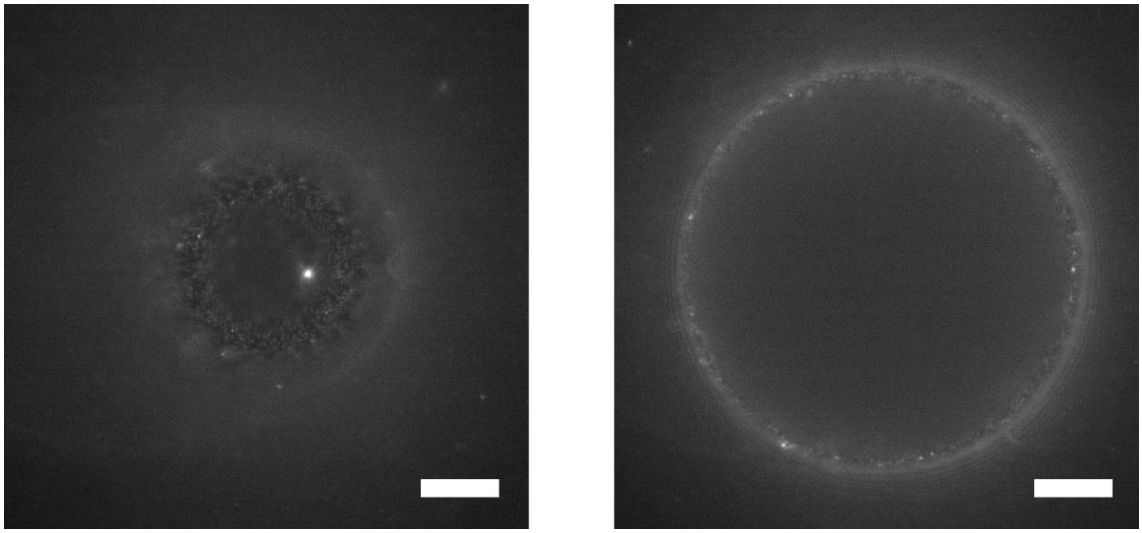

Figure 6.6: Fluorescence images of 200 nm and 800 nm polystyrene DNACCs attached to the surface of a ~100 µm hexadecane droplet produced by membrane emulsification with the focal plane at the top (left) and middle (right) of the droplet. Scale bar is 20 µm. Taken from [200].

6.1.4 Conclusions

We have demonstrated a facile synthetic method for the production of DNA-coated emulsion droplets that is tolerant of the choice of oil, surfactant and emulsification method. DNA-coated colloids were shown to bind to these oil droplets up to very high coating densities and had improved properties compared to those reported in the literature. Further experiments on the phase behaviour of binary mixtures of colloids on this type of two-dimensional interface are currently being carried out by this author for publication in a future manuscript.

6.2 Silica-PEG Gels

While conducting the experiments on DNA-coated silica nanoparticles detailed in Chapter 4.4, we observed that PEGylated silica colloids also exhibited a thermally reversible melt transition, despite not being coated with DNA. These systems behaved very similarly to DNA-coated silica, undergoing spinodal decay when cooled below a certain temperature and phase separating into an arrested colloidal gel that exhibited isotropic structural colour. Synthesis and development of these Silica-PEG systems was done by Zachary Ruff during his PhD. Characterisation by SAXS and X-ray tomography was done by Zachary Ruff in collaboration with this author.

6.2.1 Preparation and Characterisation

PEGylated silica nanoparticles (Si-PEG) were prepared using the carbodiimide chemistry described in Chapter 2.2.4. Instead of binding DBCO-DNA to the terminal azide groups on the PEG chains, the colloids were purified and used without further functionalisation. Si-PEG particles were still strongly negatively charged, with a zeta potential of -31 mV, compared to -36 mV for Si-DNA particles. This strong negative charge prevented gelation when dispersed in buffer with no added salt. As for the SI-DNA system discussed in Chapter 4.4, particles were loaded into rectangular glass capillaries, before concentrated salt solution was added to the end to bring the total salt concentration to 150 mM. Particles gelled immediately on the addition of salt, visible to the naked eye by the appearance of a strong non-iridescent blue colour.

The surface coating density of PEG was measured by fluorescence assay to be 10^{12} cm^{-2}, corresponding to an inter-chain distance of ~10 nm. This is much larger than the radius of gyration of the PEG chain, here estimated to be 2.5 nm, leaving bare regions of silica exposed between strands, as shown in Figure 6.7.

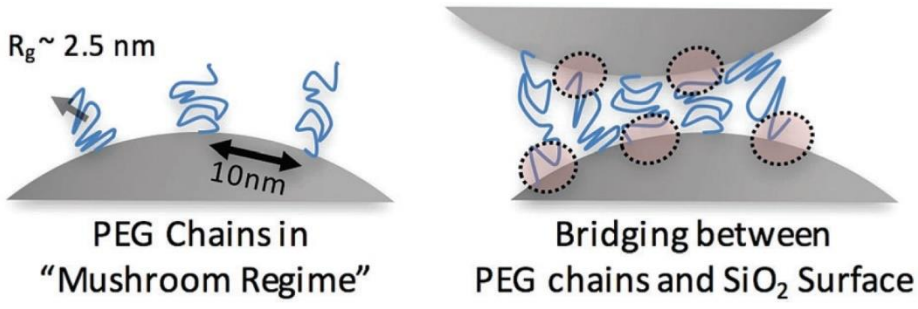

Figure 6.7: Cartoon of PEG chain morphology at the surface of a silica colloid in a good solvent. Left) Chains are in the mushroom regime as R_g > d. Right) Bridging interactions between PEG chains and bare silica may lead to aggregation. Taken from [164].

As a result, PEG chains are able to bridge to uncoated portions of other silica colloids in close proximity at low temperatures. These weak van der Waals interactions are expected to be on the order of a few k_BT[201], giving rise to the thermally reversible aggregation observed. This hypothesis was supported by the reduced melt transition temperature observed for Si-PEG gels, shown by optical microscopy in Figure 6.8 to be 45 – 55 °C, compared to that of Si-DNA gels of 55 – 65 °C.

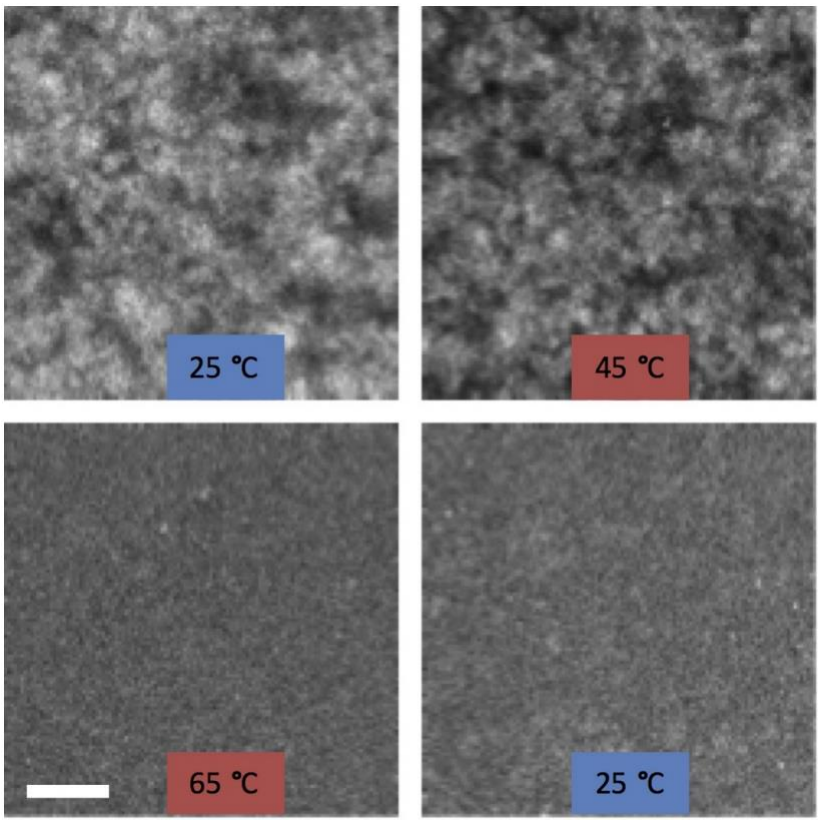

Figure 6.8: Confocal micrographs of a 2% v/v Si-PEG suspension at different temperatures starting at 25 °C immediately after injection into the capillary (top left). Scale bar is 20 µm. Taken from [164].

6.2.2 Comparison with Silica-DNA Gels

Optical micrographs and structure factors calculated as described in Chapter 2.4.2 showed that Si-PEG and Si-DNA gels were very similar, as shown in Figure 6.9. Structure factor peaks were at the same value of q but were slightly broader for Si-PEG gels than for Si-DNA, supporting the idea that both gels formed via the same mechanism and in agreement with previous findings that strongly attractive colloids undergo kinetic arrest more rapidly than weakly attractive ones[201].

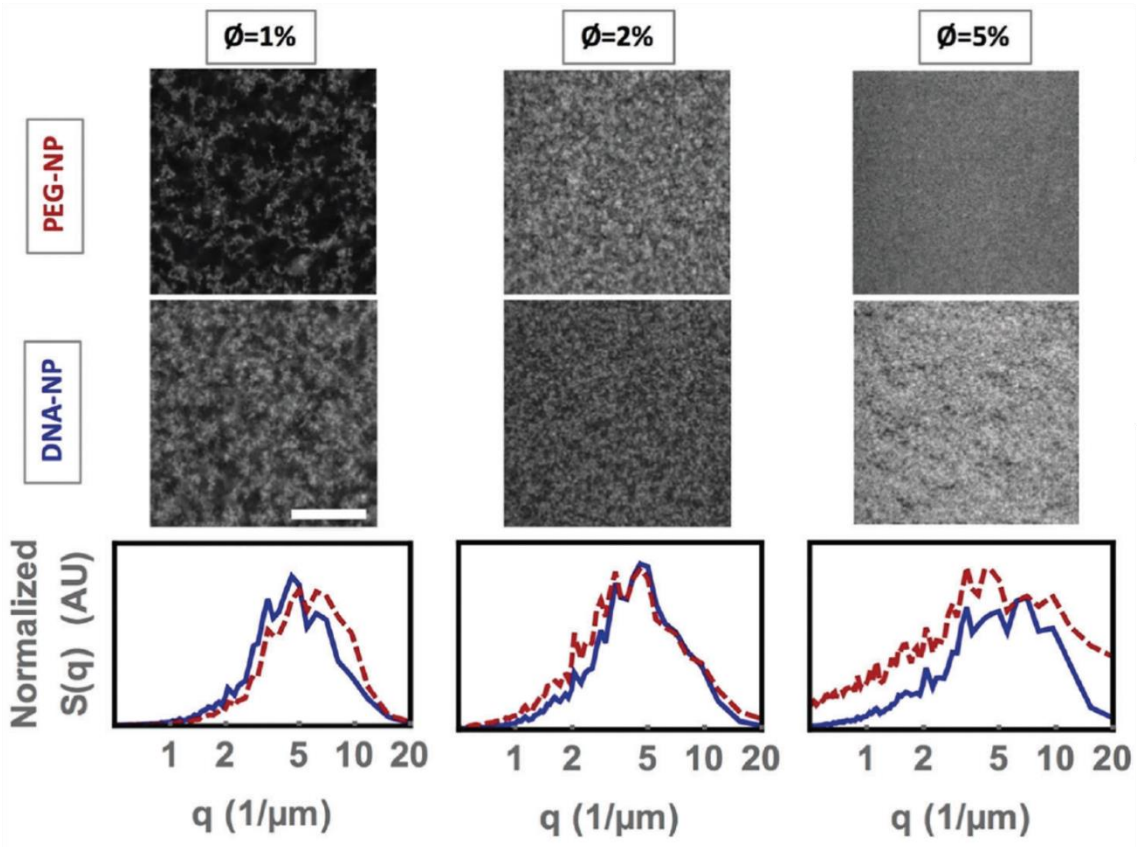

Figure 6.9: Confocal microscope images of Si-PEG and Si-DNA gels at 1%, 2% and 5% v/v and their respective structure factors, measured at room temperature. Scale bar is 20 μm. Taken from [164].

The most significant difference between the Si-PEG and Si-DNA gels is the behaviour at 1% v/v. Si-PEG gels at 1% v/v exhibited much larger pores and slightly coarser branches than the same Si-DNA gels. This was very reminiscent of the behaviour observed for polystyrene gels below the percolation threshold in Chapter 4. The role of the size ratio between the binding shell and the particle was discussed in the context of those experiments and theoretical predictions[167] and the percolation threshold φ_P was shown to increase with a smaller binding shell for a given particle size. As the binding volume is ~2.5 nm from the surface for Si-PEG colloids but ~6 nm for Si-DNA colloids, we attribute the difference in morphology between the two species to be due to Si-PEG being below their percolation threshold at 1% v/v while Si-DNA are above. Due to the similar structures of the 2% v/v gels, we expect both systems to be above the percolation threshold at 2% v/v. This is supported by the decay lengths measured by chord analysis, plotted in Figure 6.10. Si-PEG gels show the characteristic percolation transition discussed in Chapter 4.3 between 1% – 2% v/v, while Si-DNA gels are above the percolation threshold for all volume fractions discussed here.

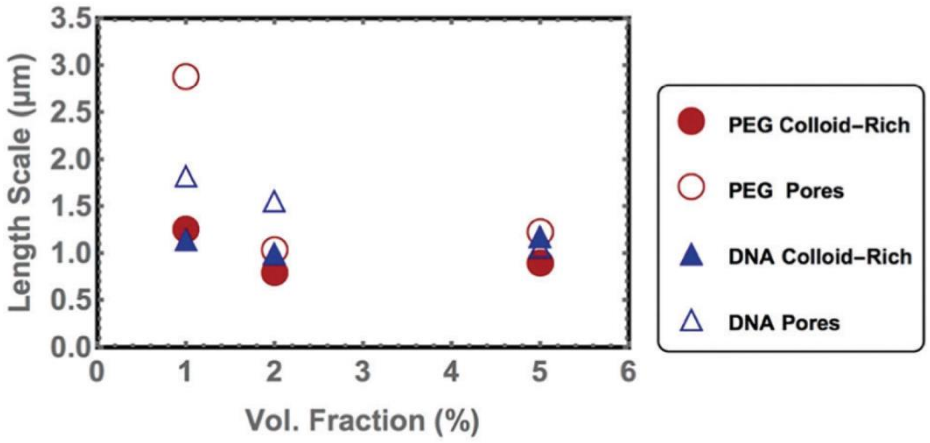

Figure 6.10: Decay lengths for the branches and pores of the gels shown in Figure 6.9, calculated by chord analysis. Taken from [164].

6.2.3 Conclusions

We have demonstrated that PEG-coated silica nanoparticles undergo a thermally reversible gelation transition of the kind more normally observed in systems of DNA-coated particles. It was shown that these PEGylated silica gels shared many similarities with a DNA-mediated gel of the same particles, supporting the hypothesis that they form by an analogous mechanism based on short-range attractive interactions. Subtle differences were rationalised due to the weaker and shorter-range interactions of Si-PEG compared to Si-DNA systems. As these gels also displayed non-iridescent structural colour, they could provide a powerful, cheap method to synthesise full-spectrum isotropic coherent scatterers as they do not rely on expensive DNA oligomers to mediate gelation.

6.3 Low T_g Colloids for Encapsulation

Encapsulation is a common industrial method to increase the commercial value of products through the implementation of new properties, for example specific texture, lasting fragrance, targeted delivery or controlled release of active ingredients. Many encapsulation methods have been developed, including solvent evaporation, thermal gelation, polymerization and layer by layer polyelectrolyte deposition[202]. However, most of those methods exhibit limits for the encapsulation of biological compounds. A new self-assembly method has recently emerged employing colloidosomes, emulsion droplets stabilised by the presence of colloids at the interface, as the encapsulating species. This type of particle-stabilised interface is referred to as a Pickering emulsion[197]. These new systems appear promising for medical applications due to their ease of preparation, tuneable properties and ability to encapsulate a vast range of biological compounds (small molecules, enzymes, cells or bacteria)[203-205]. Preparation of colloidosomes of PMMA-*r*-PBA copolymer nanoparticles was done by David Brossault using particles synthesised by this author.

6.3.1 Background

Despite the advantages of colloidosomes for encapsulation in terms of ease of preparation and tuneability, limitations have been reported during the last few years, particularly for drug delivery applications. To efficiently circulate in the bloodstream without being targeted by the immune system and to diffuse through endothelium and tissues, colloidosomes need to be submicron in size[206]. However, most colloidosomes presented in the literature are larger than 2 µm. Additionally, payload is able to diffuse out through the pores between colloids in the shell. This requires the formation of an additional shell to seal the capsules against leakage, and has been previously reported using calcium carbonate[205], silver[207] or gold[208].

The goal of this project was to fabricate submicron colloidosomes, which imposes two main restrictions[206,209,210] on the synthetic protocol. First, to sufficiently reduce droplet size, large amounts of energy must be supplied, for example by using ultrasonication. This was confirmed by different experiments carried out using manual shaking or vortex mixing to produce colloidosomes. Second, the particles forming the shell must be small enough to stabilise an interface with high curvature. The synthesis of colloidosomes small enough to be viable *in vivo* also inherently solves the porosity issue, as the use of smaller particles reduces the size of the pores in the shell, as shown in Figure 6.11.

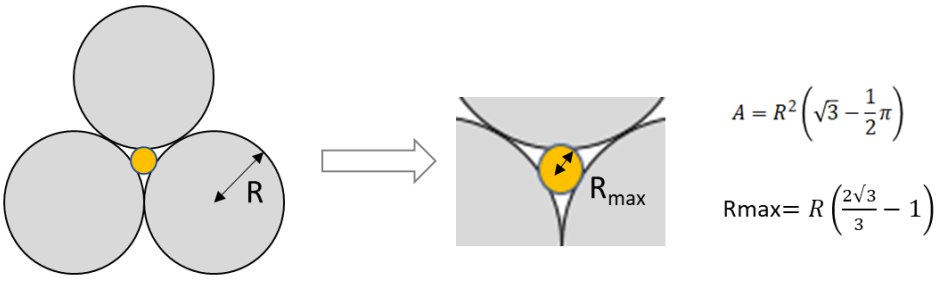

Particle radius R (nm)	Pore area A (nm²)	Maximal radius of the particle crossing the pore Rmax (nm)
20	64	3
50	400	8
150	3600	23
500	40000	78

Figure 6.11: Pore size variation with particle radius for a colloidosome. Top) Schematic of pore size geometry. Bottom) Table of typical pore areas and maximum transmitted particle size for different radius colloids. Image provided by David Brossault.

6.3.2 Preparation and Characterisation

The production of colloidosomes is well described in the literature[203-205] and is composed of three steps, as shown in Figure 6.12: (1) Emulsification to obtain droplets stabilised by nanoparticles, (2) Locking, during which the shell particles are linked together to obtain a solid capsule and (3) Transfer into an appropriate medium.

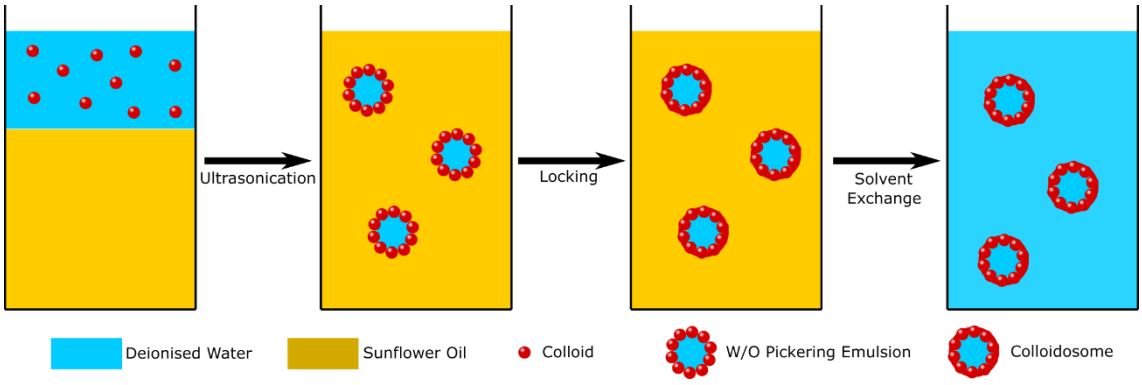

Figure 6.12: Colloidosome preparation method. Locking of the Pickering emulsion was accomplished by heating the system above the glass transition temperature of the polymer colloids, causing them to fuse.

An aqueous payload can be encapsulated by dissolving it in the aqueous phase before ultrasonication. It then remains dissolved in the aqueous core of the water-in-oil (W/O) emulsion droplets and is locked in upon fusion of the shell.

Colloidosomes were fused in this work by heating the system above the glass transition temperature of the polymer colloids, causing them to fuse into a homogenous shell. This had the advantage over the coating methods discussed previously[205,207,208] that no additional chemical step was required, it avoided issues with poor adhesion of the coating layer to the colloidosomes and it could be done at very tolerant conditions for a biological payload with the correct choice of nanoparticles.

Latex colloidosomes were produced using an ultrasonic homogenizer from a water in oil emulsion stabilized with PMMA-*r*-PBA latex nanoparticles. PMMA-*r*-PBA nanoparticles with a diameter of ~50 nm were synthesised using the methods described in Chapter 3.4.1. A monomer ratio of 70:30 MMA:BA was chosen to give nanoparticles with a glass transition temperature of $T_g \approx 35\,°C$. Colloidosomes were fused after synthesis by thermal annealing in a 50 °C water bath for one hour.

During different experiments, both the sample composition and preparation method have been investigated. Studies carried out on sonication parameters showed local heating and fusion of the colloids with extended sonication. By cooling the system in an ice bath during sonication and sonicating for reduced times, agglomeration of particles was minimized. If sonication times were too short, insufficient energy was imparted to form the new interface, leading to larger droplets. Similarly, for very long sonication times, an overshearing phenomenon was observed that led to agglomeration of capsules.

The experiments highlighted that the combination of a high energy emulsification method and use of small 50 nm particles enabled the production of colloidosomes smaller than 500 nm. Zeta potential measurements of these colloidosomes gave zeta potentials of -50 mV, suggesting high stability of the capsules obtained. SEM images of both the single colloids and the colloidosomes are presented in Figure 6.13.

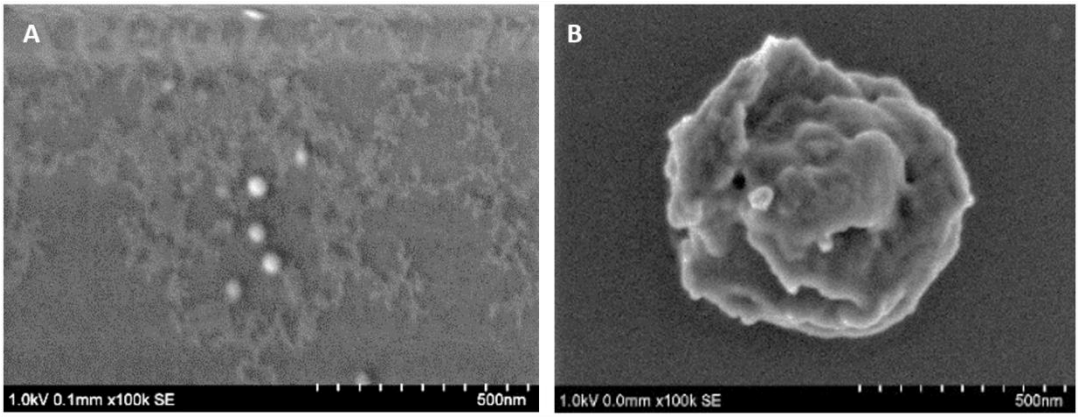

Figure 6.13: SEM images of single PMMA-r-PBA nanoparticles and colloidosomes.

However, despite the success of the synthesis, particle recovery after redispersion in water was low. Experiments on latex colloidosomes showed that the addition of Span 80 and SDS surfactants improved the redispersion of the capsules into water, but additional progress is needed for the protocol to be viable for scale-up. This is being addressed in ongoing experiments.

6.3.3 Conclusions

We have successfully demonstrated the synthesis of biocompatible 500 nm colloidosomes with fused shells through the ultrasonication of water-oil mixtures stabilised by polymer nanoparticles. These colloidosomes are fuseable without the use of high temperatures or additional synthetic steps, and as such could make excellent candidates for the targeted delivery of sensitive biological therapies. Experiments are currently being done to improve the yield of the solvent exchange step and to test the encapsulation of biological molecules and enzymes.

7 Closing Remarks

Colloidal self-assembly has enormous potential for the synthesis of novel micro- and macromaterials with properties governed by their structure on the nanoscale. This dissertation has explored the synthesis, functionalisation and assembly of DNA-coated and bare submicron colloids for photonic applications. Through careful design of colloidal assemblies, it has been shown that a wide range of different phases are accessible without external manipulation.

Syntheses of polymer and inorganic colloids were presented in Chapter 3. Polystyrene, fluorinated latex and silica colloids were synthesised by a variety of methods depending on the desired particle size, charge and physical properties. Focus was given to the development of one-pot syntheses to maximise the simplicity, scalability and broad applicability of the methods, without sacrificing monodispersity. It was shown that polymer colloids could be densely grafted with inert polymers and coupled with DNA to give stable suspensions that exhibited a specific, tuneable attractive interaction with complementary DNA-coated colloids.

Colloidal gels are an accessible yet versatile phase that can be tuned in a variety of ways by the choice and concentration of colloids used. This phase space was explored in Chapter 4. Such systems exhibit tuneable porosity and have potential as low density, high strength materials or scaffolds for bicontinuous systems such as semiconductor junctions. As the assembly process is governed by the surface properties of the colloids, the colloids themselves can be substituted for those of a different material as required.

A specific class of natural materials show the atypical combination of vivid structural colour produced through coherent scattering without iridescence. Such systems are

impossible to recreate using traditional top-down manufacturing techniques, due to the small length-scales involved over three dimensions, but are ideal candidates for colloidal self-assembly. In this work we showed that DNA-coated colloidal gels exhibit structural colour with the same characteristics, making them excellent candidates for a wide range of colour applications including next generation non-backlit displays. Colour production in this way has been essentially unrealised previously with synthetic systems due to the requirement to deconvolve the particle and structural contributions to the scattering.

This concept was explored further using a system of fluorinated latex colloids with a low refractive index. Chapter 5 described how systems of highly charged colloids could be assembled into Wigner glasses that exhibit enhanced transparency and isotropic, full-spectrum structural colour of a similar kind to the natural materials and colloidal gels discussed in Chapter 4. Due to the high viscosity of these systems, crystallisation was slowed, with very concentrated suspensions retaining isotropic structural colour for over a year. Further work to stabilise the photonic glass and prevent crystallisation is now ongoing.

Chapter 6 presented an aside to the main work of this dissertation and detailed the synthesis of DNA-coated emulsion droplets to which DNA-colloids could be reversibly bound. These colloids remained mobile in a quasi-2D environment and could be used to study colloidal diffusion and aggregation in pure and binary systems. Also presented was the unexpected finding that PEG-coated silica nanoparticles undergo a thermally reversible gelation transition. The structure of these gels was compared with that of analogous DNA-coated silica gels. Finally, the low glass transition temperature copolymer colloids synthesised in Chapter 3 were used to create fuseable colloidosomes for encapsulation and slow release of a payload.

The findings in this thesis represent several novel breakthroughs in the field of colloidal self-assembly and have the potential to underpin a number of new functional materials that exhibit structural colour.

8 REFERENCES

[1] T. Graham, "On the Properties of Silicic Acid and other Analogous Colloidal Substances", *J. Chem Soc.*, 1864, 17, 318-327

[2] J. N. Israelachvili, *Intermolecular and Surface Forces*, Academic Press, 2011

[3] D. F. Evans and H. Wennerström, *The Colloidal Domain: Where Physics, Chemistry, Biology and Technology Meet*, Wiley-VCH, 1999

[4] E. Busseron, Y. Ruff, E. Moulin and N. Giuseppone, "Supramolecular Self Assemblies as Functional Materials", *Nanoscale*, 2013, 5 (16), 7098-140

[5] L. S. Hirst, *Fundamentals of Soft Matter Science*, CRC press, 2013

[6] A. Einstein, "On the Motion of Small Particles Suspended in Liquids at Rest Required by the Molecular-Kinetic Theory of Heat", *Ann. Phys.*, 1905, 17, 549–560

[7] A. Einstein, "Zur Theorie der Brownschen Bewegung", *Ann. Phys.*, 1906, 324, 371–381

[8] T. G. Mason and D. A. Weitz, "Optical Measurements of Frequency Dependent Linear Viscoelastic Moduli of Complex Fluids", *Phys. Rev. Lett.*, 1995, 74 (7), 1250

[9] S. Fujime, "Quasi-Elastic Scattering of Laser Light: A New Tool for the Dynamic Study of Biological Macromolecules", *Adv. Biophys.*, 1972, 3, 1–43

[10] A. J. Levine and T. C. Lubensky, "One- and Two-Particle Microrheology", *Phys. Rev. Lett.*, 2000, 85 (8), 1774–1777

[11] P. N. Pusey and A. Van Megen, “Phase Behaviour of Concentrated Suspensions of Nearly Hard Colloidal Spheres”, *Nature*, 1986, 320, 340-342

[12] H. C. Hamaker, “The London - Van der Waals Attraction Between Spherical Particles”, *Physica*, 1937, 4 (10), 1058-1072

[13] Y. Min, M. Akbulut and K. Kristiansen, “The Role of Interparticle and External Forces in Nanoparticle Assembly”, *Nat. Mater.*, 2008, 7, 527-538

[14] P. Van Rysselberghe, “Remarks Concerning the Clausius-Mossotti Law”, *J. Phys. Chem.*, 1931, 36 (4), 1152–1155

[15] W. B. Russel, D. A. Saville, and W. R. Schowalter, *Colloidal Dispersions*, Cambridge University Press, 1989

[16] B. Derjaguin and L. Landau, “Theory of the Stability of Strongly Charged Lyophobic Sols and of the Adhesion of Strongly Charged Particles in Solutions of Electrolytes”, *Acta. Phys. Chem.*, 1941, 14, 633-662

[17] D. Fairhurst and R. W. Lee, “The Zeta Potential & Its Uses in Pharmaceutical Applications - Part 1: Charged Interfaces in Polar & Non-Polar Media & The Concept of the Zeta Potential”, *Drug Development & Delivery*, 2011, 11 (6), 60-64

[18] E. J. W. Verwey and J. T. G. Overbeek, “Theory of the Stability of Lyophobic Colloids”, *Elsevier*, 1948

[19] D. Guo, G. Xie and L. Jianbin, “Mechanical Properties of Nanoparticles: Basics and Applications”, J. *Phys. D Appl. Phys.*, 2014, 47 (1), 013001

[20] Y. Min, M. Akbulut, K. Kristiansen, Y. Golan, and J. Israelachvili, “The Role of Interparticle and External Forces in Nanoparticle Assembly”, *Nat. Mater.*, 2008, 7 (7), 527–538

[21] P. G. de Gennes, “Polymers at an interface; a simplified view”, *Adv. Colloid Interface Sci.*, 1987, 27 (3–4), 189–209

[22] S. Asakura and F. Oosawa, “Interaction Between Particles Suspended in Solutions of Macromolecules”, *J. Polym. Sci.*, 1958, 33 (126), 183–192

[23] D. J. Kraft et al., “Surface Roughness Directed Self-Assembly of Patchy Particles into Colloidal Micelles”, *Proc. Natl. Acad. Sci.*, 2012, 109 (27), 10787–10792

[24] J. R. Wolters et al., “Self-Assembly of ‘Mickey Mouse’ Shaped Colloids into Tubelike Structures: Experiments and Simulations”, *Soft Matter*, 2015, 11 (6), 1067– 1077

[25] S. Sacanna, W. T. M. Irvine, P. M. Chaikin, and D. J. Pine, “Lock and Key Colloids”, *Nature*, 2018, 464 (7288), 575–578

[26] S. Sacanna et al., “Shaping Colloids for Self-Assembly”, *Nat. Commun.*, 2013, 4, 2–7

[27] A. C. Balazs, T. Emrick, and T. P. Russell, “Nanoparticle Polymer Composites: Meet Two Small Worlds”, *Science*, 2013, 314 (5802), 1107–1110

[28] B. Meets, “Biotechnology Meets Materials Science”, *Mater. Sci.*, 2001, 40 (22), 4128–4158

[29] Y. Lan, Y. Wu, A. Karas, and O. A. Scherman, “Photoresponsive Hybrid Raspberrylike Colloids Based on Cucurbit[8]uril Host-Guest Interactions”, *Angew. Chem. Int. Ed.*, 2014, 53 (8), 2166–2169

[30] Y. Lan, X. J. Loh, J. Geng, Z. Walsh, and O. A. Scherman, “A Supramolecular Route Towards Core–Shell Polymeric Microspheres in Water via Cucurbit[8]urilC”, *Chem. Commun.*, 2012, 48 (70), 8757

[31] C. A. Mirkin, R. L. Letsinger, R. C. Mucic, and J. J. Storhoff, “A DNA-Based Method for Rationally Assembling Nanoparticles into Macroscopic Materials”, *Nature*, 1996, 382 (6592), 607–609

[32] A. P. Alivisatos et al., “Organization of ‘Nanocrystal Molecules’ Using DNA”, *Nature*, 1996, 382 (6592), 609–11

[33] J. D. Watson and F. H. Crick, “Molecular Structure of Nucleic Acids; A Structure for Deoxyribose Nucleic Acid”, *Nature*, 1953, 171, 737

[34] G. Karthikeyan, M. D. Wagle and B. J. Rao, “Non-Watson-Crick Base Pairs Modulate Homologous Alignments in RecA Pairing Reactions”, *FEBS Letters*, 1998, 425 (1), 45–51

[35] S. Brinkers, H. R. C. Dietrich and F. H. de Groote, “The Persistence Length of Double Stranded DNA Determined Using Dark Field Tethered Particle Motion”, *J. Phys. Chem.*, 2009, 130, 215205

[36] H. H. Kazazian, *Mobile DNA: Finding Treasure in Junk*, FT Press, 2011

[37] "DNA", *Wikipedia*, 2019

[38] B. Tinland, A. Pluen, J. Sturm and G. Weill, "Persistence Length of Single-Stranded DNA", *Macromolecules*, 1997, 30 (19), 5763-5765

[39] J. SantaLucia and D. Hicks, "The Thermodynamics of DNA Structural Motifs", *Annu. Rev. Biophys. Biomol. Struct.*, 2004, 33 (1), 415–440

[40] J. SantaLucia, "A Unified View of Polymer, Dumbbell, and Oligonucleotide DNA Nearest-Neighbor Thermodynamics", *Proc. Natl. Acad. Sci.*, 1998, 95 (4), 1460–1465

[41] C. Schildkraut and S. Lifson, "Dependence of the Melting Temperature of DNA on Salt Concentration", *Biopolymers*, 1965, 3, 195

[42] N. Geerts, *DNA-Driven Assembly of Micron-Sized Colloids*, Universiteit van Amsterdam, 2009

[43] C. Calladine, H. Drew, B. Luisi and A. Travers, *Understanding DNA*, Academic Press (3rd Edition), 2004

[44] M. H. Caruthers, "Gene Synthesis Machines: DNA Chemistry and Its Uses", *Science*, 1985, 230, 281

[45] N. Geerts and E. Eiser, "DNA-Functionalized Colloids: Physical Properties and Applications", *Soft Matter*, 2010, 6, 4647-4660

[46] I. Tinoco, "Hypochromism in Polynucleotides", *J. Am, Chem. Soc.*, 1960, 82 (18), 4785-4790

[47] R. Dreyfuss et al., "Simple Quantitative Model for the Reversible Association of DNA Coated Colloids", *Phys. Rev. Lett.*, 2009, 102, 048301

[48] L. Di Michele and E. Eiser, "Developments in Understanding and Controlling Self Assembly of DNA-Functionalized Colloids", *Phys. Chem. Chem. Phys.*, 2013, 15, 3115-3129

[49] R. J. Macfarlane et al., "Nanoparticle Superlattice Engineering with DNA", *Science*, 2011, 334 (6053), 204-208

[50] R. S. Hoy, J. Harwayne-Gidansky and C. S. O'Hern, "Structure of Finite Sphere Packings Via Exact Enumeration: Implications for Colloidal Crystal Nucleation", *Phys. Rev. E*, 2012, 85 (5), 051403

[51] S. Hormoz and M. P. Brenner, "Design Principles for Self-Assembly with Short-Range Interactions", *PNAS*, 2011, 108 (13), 5193-5198

[52] Z. Zeravcic, V. N. Manoharan and M. P. Brenner, "Size Limits of Self-Assembled Colloidal Structures Made Using Specific Interactions", *PNAS*, 2014, 111 (45), 15918-15923

[53] D. Yang and K. Okamoto, "Structural Insights into G-Quadruplexes: Towards New Anticancer Drugs", *Future Med. Chem.*, 2010, 2 (4), 619-646

[54] J. Lindsey, "Self-Assembly in Synthetic Routes to Molecular Devices. Biological Principles and Chemical Perspectives: A Review", *New J. Chem.*, 1991, 15, 153-180

[55] S. Zhang, "Fabrication of Novel Biomaterials Through Molecular Self-Assembly", *Nat. Biotechnol.*, 2003, 21 (10), 1171-1178

[56] E. V. Shevchenko, D. V. Talapin, N. A. Kotov, S. O'Brien and C. B. Murray, "Structural Diversity in Binary Nanoparticle Superlattices", *Nature*, 2006, 439, 55-59

[57] F. Varrato et al., "Arrested Demixing Opens Route to Bigels", *PNAS*, 2012, 109, 19155–19160

[58] G. M. Whitesides and M. Boncheva, "Beyond Molecules: Self-Assembly of Mesoscopic and Macroscopic Components", PNAS, 2002, 99 (8), 4769-4774.

[59] J. Y. Cheng, A. M. Mayes and C. A. Ross, "Nanostructure Engineering by Templated Self Assembly of Block Copolymers", *Nat. Mater.*, 2004, 3 (11), 823-828

[60] P. J. Lu et al., "Gelation of Particles with Short-Range Attraction", *Nature*, 2008, 453 (7194), 499-503

[61] N. C. Seeman, "Nucleic Acid Junctions and Lattices", *J. Theor. Biol.*, 1982, 99 (2), 237-247

[62] F. Hong, F. Zhang, Y. Liu and H. Yan, "DNA Origami: Scaffolds for Creating Higher Ordered Structures", *Chem. Rev.*, 2017, 117 (20), 12584-12640

[63] M. Caruthers, "Gene Synthesis Machines: DNA Chemistry and its Uses", *Science*, 230 (4723), 281–285

[64] R. Jin, G. Wu, Z. Li, C. A. Mirkin and G. C. Schatz, "What Controls the Melting Properties of DNA-Linked Gold Nanoparticle Assemblies?", *J. Am. Chem. Soc.*, 2003, 125, 1643-1654

[65] S. J. Hurst, A. K. R. Lytton-Jean and C. A. Mirkin, "Maximizing DNA Loading on a Range of Gold Nanoparticle Sizes", *Analytical Chemistry*, 2006, 78 (24), 8313-8318

[66] S. Y. Park et al., "DNA-Programmable Nanoparticle Crystallization", *Nature*, 2008, 451 (7178), 553-556

[67] M. M. Maye, D. Nykypanchuk, D. van der Lelie and O. Gang, "A Simple Method for Kinetic Control of DNA-Induced Nanoparticle Assembly", *J. Am. Chem. Soc*, 2006, 128 (43), 14020-14021

[68] M. M. Maye, D. Nykypanchuk, D. van der Lelie and O. Gang, "DNA-Regulated Micro- and Nanoparticle Assembly", *Small*, 2007, 3 (10), 1678-82

[69] D. Nykypanchuk, M. M. Maye, D. van der Lelie and O. Gang, "DNA-Guided Crystallisation of Colloidal Nanoparticles", *Nature*, 2008, 451 (7178), 549-552

[70] C. Zhang et al., "A General Approach to DNA-Programmable Atom Equivalents", *Nat. Mater.*, 2013, 12 (8), 741–746

[71] A. V. Tkachenko, "Morphological Diversity of DNA-Colloidal Self-Assembly", *Phys. Rev. Lett.*, 2002, 89, 148303

[72] Y. Wang et al., "Crystallization of DNA-Coated Colloids", *Nat. Commun.*, 2015, 6, 7253

[73] P. L. Biancaniello, A. J. Kim and J. C. Crocker, "Colloidal Interactions and Self-Assembly Using DNA Hybridization", *Phys. Rev. Lett.*, 2005, 94, 058302

[74] J. S. Oh, Y. Wang, D. J. Pine, and G. R. Yi, "High-Density PEO-*b*-DNA Brushes on Polymer Particles for Colloidal Superstructures", *Chem. Mater.*, 2015, 27 (24), 8337–8344

[75] E. Zaccarelli, "Colloidal Gels: Equilibrium and Non-Equilibrium Routes", J. *Phys. Condens. Matt.*, 2007, 19, 323101

[76] N. Geerts, T. Schmatko and E. Eiser, "Clustering Versus Percolation in the Assembly of Colloids Coated with Long DNA", *Langmuir*, 2008, 24 (9), 5118-5123

[77] L. Di Michele et al., "Multistep Kinetic Self-Assembly of DNA-Coated Colloids", *Nat. Commun.*, 2013, 4, 2007

[78] L. Di Michele, *Multicomponent Amorphous Phases of DNA-Functionalized Colloids*, University of Cambridge, 2013

[79] L. Di Michele et al., "Aggregation Dynamics, Structure, and Mechanical Properties of Bigels", *Soft Matter*, 2014, 10 (20), 3633- 3648

[80] M. F. Hagan, O. M. Elrad, and R. L. Jack, “Mechanisms of Kinetic Trapping in Self-Assembly and Phase Transformation”, *J. Chem. Phys.*, 2011, 135 (10), 104115

[81] E. J. W. Crossland et al., “A Bicontinuous Double Gyroid Hybrid Solar Cell”, *Nano Letters*, 2009, 9 (8), 2807-2812

[82] A. M. Urbas, M. Maldovan and E. L. Thomas, “Bicontinuous Cubic Block Copolymer Photonic Crystals”, *Adv. Mat.*, 2002, 14 (24), 1850-1853

[83] M. Zupkauskas, Y. Lan, D. Joshi, Z. Ruff and E. Eiser, “Optically Transparent Dense Colloidal Gels”, *Chem. Sci.*, 2017, 8, 5559-5566

[84] Q. Chen, S. C. Bae and S. Granick, “Directed Self-Assembly of a Colloidal Kagome Lattice”, *Nature*, 2011, 469, 381-384

[85] A. B. Pawar and I. Kretzschmar, “Fabrication, Assembly and Application of Patchy Particles”, *Macromol. Rapid Commun.*, 2010, 31, 150-168

[86] G. R. Yi, D. J. Pine and S. Sacanna, “Recent Progress on Patchy Colloids and Their Self-Assembly”, *J. Phys. Condens. Matter*, 2013, 25, 193101

[87] Sacanna et al., “Shaping Colloids for Self-Assembly”, *Nat. Comm.*, 2013, 4 (1688), 1-6

[88] M. Grünwald and P. L. Geissler, “Patterns Without Patches: Hierarchical Self-Assembly of Complex Structures from Simple Building Blocks”, *ACS Nano*, 2014, 8 (6), 5891-5897

[89] H. C. van de Hulst, *Light Scattering by Small Particles*, Dover Publications, 1981

[90] C. F. Bohren and D. R. Huffman, *Absorption and Scattering of Light by Small Particles*, John Wiley and Sons, 1983

[91] S. Magkiriadou, J. Park, Y. Kim and V. N. Manoharan, “Absence of Red Structural Color in Photonic Glasses, Bird Feathers, and Certain Beetles”, *Phys. Rev. E,* 2014, 90, 062302

[92] Y. Takeoka, “Angle-Independent Structural Coloured Amorphous Arrays”, *J. Mat. Chem.,* 2012, 22 (44), 23299

[93] P. D. Garcia, R. Sapienza, A. Blanco and C. López, “Photonic Glass: A Novel Random Material for Light”, *Adv. Mater.,* 2007, 19 (18), 2597-2602

[94] D. S. Wiersma, “Disordered Photonics”, *Nat. Photonics,* 2013, 7, 188-196

[95] T. T. Ngo, C. M. Liddell, M. Ghebrebrhan and J. D. Joannopoulos, “Tetrastack: Colloidal Diamond-Inspired Structure with Omnidirectional Photonic Band Gap for Low Refractive Index Contrast”, *Appl. Phys. Lett.,* 2006, 88, 1–4

[96] I. Tarhan and G. Watson, “Photonic Band Structure of FCC Colloidal Crystals”, *Phys. Rev. Lett.,* 1996, 76, 315–318

[97] V. L. Colvin, “From Opals to Optics: Colloidal Photonic Crystals”, *MRS Bull.,* 2001, 26, 637–641

[98] H. Wang and K. Q. Zhang, “Photonic Crystal Structures with Tuneable Structure Color as Colorimetric Sensors”, *Sensors,* 2013, 13, 4192–4213

[99] F. S. Diana et al., “Photonic Crystal-Assisted Light Extraction from a Colloidal Quantum Dot/GaN Hybrid Structure”, *Nano Lett.,* 2006, 6, 1116–1120

[100] S. Furumi, H. Fudouzi and T. Sawada, “Self-Organized Colloidal Crystals for Photonics and Laser Applications”, *Laser Photonics Rev.,* 2010, 4, 205–220

[101] J. Park et al., “Full Spectrum Photonic Pigments with Non-iridescent Structural Colors through Colloidal Assembly”, *Angew. Chem. Int. Ed.,* 2014, 53 (11), 2899-2903

[102] M. Teshima et al., “Preparation of Structurally Colored, Monodisperse Spherical Assemblies Composed of Black and White Colloidal Particles Using a Micro-Flow-Focusing Device”, *J. Mat. Chem. C*, 2015, 3 (4), 769-777

[103] J. Zi et al., “Coloration Strategies in Peacock Feathers”, *PNAS*, 2003, 100 (22), 12576-8

[104] J. A. Peteya, J. A. Clarke, Q. Li, K. Gao and M. D. Shawkey, “The Plumage and Colouration of an Enantiornithine Bird from the Early Cretaceous of China”, *Palaeontology*, 2017, 60 (1), 55-71

[105] Q. Li et al., “Plumage Color Patterns of an Extinct Dinosaur”, *Science*, 2010, 327 (5971), 1369-1372

[106] S. Vignolini, E. Moyroud, B. J. Glover and U. Steiner, “Analysing Photonic Structures in Plants”, *J. R. Soc. Interface*, 2013, 10, 20130394

[107] R. O. Prum, R. L. Morrison and G. R. Ten Eyck, “Structural Color Production by Constructive Reflection from Ordered Collagen Arrays in a Bird (Philepitta Castanea: Eurylaimidae)”, *J. Morph.*, 1994, 222 (1), 61-72

[108] R. O. Prum, R. H. Torres, S. Williamson and J. Dyck, “Coherent Light Scattering by Blue Feather Barbs”, *Nature*, 1998, 396, 28-29

[109] R. O Prum, “Development and Evolutionary Origin of Feathers”, *J. Exp. Zool.*, 2002, 285 (4), 291-306

[110] R. O. Prum and R. H. Torres, “Structural Colouration of Avian Skin: Convergent Evolution of Coherently Scattering Dermal Collagen Arrays”, *J. Exp. Biol.*, 2003, 206, 2409-2429

[111] R. O. Prum and R. H. Torres, “Structural Colouration of Mammalian Skin: Convergent Evolution of Coherently Scattering Dermal Arrays”, *J. Exp. Biol.*, 2004, 207, 2157-2172

[112] R. O. Prum and R. H. Torres, “A Fourier Tool for the Analysis of Coherent Light Scattering by Bio-Optical Nanostructures”, *Integr. Comp. Biol.*, 2003, 43, 591-602

[113] E. R. Dufresne et al., “Self-Assembly of Amorphous Biophotonic Nanostructures by Phase Separation”, *Soft Matter*, 2009, 5 (9), 1792-1795

[114] V. Saranathan et al., “Structure and Optical Function of Amorphous Photonic Nanostructures from Avian Feather Barbs: a Comparative Small Angle X-ray Scattering (SAXS) Analysis of 230 Bird Species”, *J. R. Soc. Interface*, 2012, 9 (75), 2563-2580

[115] R. O. Prum, E. R. Dufresne, T. Quinn and K. Waters, “Development of Colour-Producing β-keratin Nanostructures in Avian Feather Barbs”, *J. R. Soc. Interface*, 2009, 6 (S2), 253–265

[116] Y. Takeoka, M. Honda, T. Seki, M. Ishii and H. Nakamura, “Structural Colored Liquid Membrane without Angle Dependence”, *ACS Appl. Mater. Interfaces*, 2009, 1 (5), 982- 986.

[117] W. Stöber, A. Fink and E. Bohn, “Controlled Growth of Monodisperse Silica Spheres in the Micron Size Range”, *J. Colloid Interface Sci.*, 1968, 26 (1), 62-69

[118] H. C. Kolb, M. G. Finn and K. B. Sharpless, “Click Chemistry: Diverse Chemical Function from a Few Good Reactions”, *Angew. Chem. Int. Ed.*, 2001, 40 (11), 2004-2021

[119] C. Spiteri and J. E. Moses, "Copper-Catalyzed Azide-Alkyne Cycloaddition: Regioselective Synthesis of 1,4,5-Trisubstituted 1,2,3-Triazoles", *Angew. Chem. Int. Ed.*, 2009, 49 (1), 31-33

[120] M. P. Cervantes-Cervantes, J. V. Calderón-Salinas, A. Albores and J. L. Muñoz-Sánchez, "Copper Increases the Damage to DNA and Proteins Caused by Reactive Oxygen Species", *Biol. Trace Elem. Res.*, 2005, 103 (3), 229-248

[121] R. A. L. Jones, *Soft Condensed Matter*, Oxford university Press, 2002

[122] H. Schnablegger, *The SAXS Guide: Getting Acquainted with the Principles*, Anton Paar GmbH, 2013

[123] N. Otsu, "A Threshold Selection Method from Gray-Level Histograms", *IEEE Trans. Sys. Man. Cyber.*, 1979, 9 (1), 62-66

[124] J. Méring and D. Tchoubar, "Interprétation de la Diffusion Centrale des Rayons X par les Systèmes Poreux", *J. Appl. Crystallogr.*, 1968, 1 (3), 153–165

[125] P. Levitz and D. Tchoubar, "Disordered Porous Solids : From Chord Distributions to Small Angle Scattering", *Journal de Physique I*, 1992, 2 (6), 771-790

[126] P. Levitz, "Toolbox for 3D Imaging and Modelling of Porous Media: Relationship with Transport Properties", *Cem. Concr. Res.*, 2007, 37 (3), 351–35

[127] H. Fudouzi and Y. Xia, "Photonic Papers and Inks: Color Writing with Colorless Materials", *Adv. Mater.*, 2003, 15 (11), 892–896

[128] D. V. Talapin, J. Lee, M. V. Kovalenko, and E. V. Shevchenko, "Prospects of Colloidal Nanocrystals for Electronic and Optoelectronic Applications", *Chem. Rev.*, 2010, 110 (1), 389–458

[129] S. Brahim, D. Narinesingh, and A. Guiseppi-Elie, "Amperometric Determination of Cholesterol in Serum Using a Biosensor of Cholesterol Oxidase Contained

Within a Polypyrrole-Hydrogel Membrane", *Anal. Chim. Acta*, 2001, 448 (1–2), 27– 36

[130] S. H. Im, Y. T. Lim, D. J. Suh and O. O. Park, "Three-Dimensional Self-Assembly of Colloids at a Water–Air Interface: A Novel Technique for the Fabrication of Photonic Bandgap Crystals", *Adv. Mat.*, 2002, 14 (19), 1367-1369

[131] X. Xu, S. A. Majetich and S. A. Asher, "Mesoscopic Monodisperse Ferromagnetic Colloids Enable Magnetically Controlled Photonic Crystals", *J. Am. Chem. Soc.*, 2002, 124 (46), 13864-13868

[132] M. H. Kim, S. H. Im and O. O. Park, "Rapid Fabrication of Two- and Three-Dimensional Colloidal Crystal Films via Confined Convective Assembly", *Adv. Func. Mat.*, 2005, 15 (18), 1329-1335

[133] S. Margel and M. Offarim, "Novel Effective Immunoadsorbents Based on Agarose-Polyaldehyde Microsphere Beads: Synthesis and Affinity Chromatography", *Anal. Biochem.*, 1983, 128 (2), 342-350

[134] L. Lunelli, L. Pasquardini, C. Pederzolli, L. Vanzetti and M. Anderle, "Covalently Anchored Lipid Structures on Amine-Enriched Polystyrene", *Langmuir*, 2005, 21 (18), 8338-8343

[135] G. Odian, *Principles of Polymerization*, Wiley Interscience, 2004

[136] G. Moad, E. Rizzardo and S. H. Thang, "Radical Addition Fragmentation Chemistry in Polymer Synthesis", *Polymer*, 2008, 49 (5), 1079-1131

[137] R. Arshady, "Suspension, Emulsion and Dispersion Polymerization: A Methodological Survey", *Colloid. Polym. Sci.*, 1992, 270, 717-732

[138] W. V. Smith and R. H. Ewart, "Kinetics of Emulsion Polymerisation", *J. Chem. Phys.*, 1948, 16 (6), 592-599

[139] W. D. Harkins, "A General Theory of the Mechanism of Emulsion Polymerization", *J. Am. Chem. Soc.*, 1947, 69 (6), 1428-1444

[140] R. G. Gilbert, *Emulsion Polymerization: A Mechanistic Approach*, Academic Press, 1996

[141] N. Geerts, S. Jahn and E. Eiser, "Direct Observation of Size Fractionation During Colloidal Crystallization", *J. Phys. Condens. Matter*, 2010, 22, 104111

[142] Y. Almog, S. Reich and M. Levy, "Monodisperse Polymeric Spheres in the Micron Size Range by a Single Step Process", *Polym. Int.*, 1982, 14 (4), 131-136

[143] C. K. Ober, K. P. Lok and M. L. Hair, "Monodispersed, Micron-Sized Polystyrene Particles by Dispersion Polymerization", *J. Polym. Sci.*, 1985, 2(2), 103-108

[144] C. M. Tseng, Y. Y. Lu, M. S. El-Aasser and J. W. Vanderhoff, "Uniform Polymer Particles by Dispersion Polymerization in Alcohol", *J. Polym. Sci.*, 1986, 24, 2995-3007

[145] X. Kong, Q. Wu, W. Hu and Z. Wang, "Monodisperse Ultrafine Polystyrene Nanoparticles Prepared by a Semicontinuous Microemulsion Polymerization", *J. Polym. Sci.*, 2008, 46 (13), 4522-4528

[146] A. Olsen, H. Lee, M. Hatzopoulos, J. Van Duijneveldt and B. Vincent, "Synthesis of Amphoteric Polystyrene Particles Using Mixed Initiators", *Langmuir*, 2008, 24, 3801-3806

[147] J. Zhang, Z. Chen, Z. Wang, W. Zhang and N. Ming, "Preparation of Monodisperse Polystyrene Spheres in Aqueous Alcohol System", *Mat. Lett.*, 2003, 57 (28), 4466-4470

[148] A. J. Kim, P. L. Biancaniello, and J. C. Crocker, "Engineering DNA-Mediated Colloidal Crystallization", *Langmuir*, 2006, 22 (5), 1991–2001

[149] P. G. de Gennes, “Conformations of Polymers Attached to an Interface,” *Macromolecules*, 1980, 13 (5), 1069–1075

[150] F. Kienberger et al., “Static and Dynamical Properties of Single Poly(Ethylene Glycol) Molecules Investigated by Force Spectroscopy,” *Single Mol.*, 2000, 1 (2), 123–128

[151] A. M’Pandou and B. Siffert, “Polyethyleneglycol Adsorption at the TiO_2-H_2O Interface: Distortion of Ionic Structure and Shear Plane Position”, *Colloid. Surface.*, 1987, 24 (2-3), 159-172

[152] W. Härtl, H. Versmold and X. Zhang-Heider, “Tracer Particle Diffusion in Crystal- and Fluid-like Ordered Colloidal Suspensions”, *Ber. Bunsenges. Phys. Chem.*, 1995, 95 (9), 1105-1111

[153] V. Degiorgio, R. Piazza and R. B. Jones, “Rotational Diffusion in Concentrated Colloidal Dispersions of Hard Spheres”, *Phys. Rev. E*, 1995, 52, 2707

[154] W. Härtl, H. Versmold and X. Zhang-Heider, “The Glass Transition of Charged Polymer Colloids”, *J. Chem. Phys.*, 1995, 102, 6613

[155] G. H. Koenderink, S. Sacanna, C. Pathmamanoharan, M. Raşa and A. P. Philipse, “Preparation and Properties of Optically Transparent Aqueous Dispersions of Monodisperse Fluorinated Colloids”, *Langmuir*, 2001, 17, 6086-6093

[156] J. W. Goodwin, J. Hearn, C. C. Ho and R. H. Ottewill, “Studies on the Preparation and Characterisation of Monodisperse Polystyrene Lattices”, *Colloid Polym. Sci.*, 1974, 252 (6), 464-471

[157] Song et al., “Hierarchical Photonic Pigments via the Confined Self-Assembly of Bottlebrush Block Copolymers”, *ACS Nano*, 2019, 13 (2), 1764-1771

[158] P. C. Painter and M. M. Coleman, *Fundamentals of Polymer Science*, CRC Press, 1997

[159] M. Egen and R. Zentel, "Surfactant-Free Emulsion Polymerization of Various Methacrylates: Towards Monodisperse Colloids for Polymer Opals", *Macromol. Chem. Phys.*, 2004, 205, 1479-1488

[160] P. Daswani and A. van Herk, "Solubility Data of Comonomer Pairs Relevant to Aqueous Phase Study in Emulsion Copolymerization", *Dataset Papers in Materials Science*, 201s, 2013, 610329

[161] Y. Yurekli, S. A. Altinkaya and J. M. Zielinski, "Solubility and Diffusivity of Methylmethacrylate and Butylacrylate Monomers in an MMA-BA Copolymer", *J. Polym. Sci. B*, 2007, 45, 1996-2006

[162] T. K. Kwei, "The Effect of Hydrogen Bonding on the Glass Transition Temperatures of Polymer Mixtures", *J. Polym. Sci. C*, 1984, 22 (6), 307-313

[163] A. A. Lin, T. K. Kwei and A. Reiser, "On the Physical Meaning of the Kwei Equation for the Glass Transition Temperature of Polymer Blends", *Macromol.*, 1989, 22, 4112-4119

[164] Z. Ruff, P. Cloetens, T. O'Neill, C. P. Grey and E. Eiser, "Thermally Reversible Nanoparticle Gels with Tuneable Porosity Showing Structural Colour", *Phys. Chem. Chem. Phys.*, 2018, 20, 467-477

[165] T. O'Neill, Z. Ruff, M. Zupkauskas, Y. Lan and E. Eiser, "Scaling Laws in the Structure of DNA-Mediated Mesoporous Colloidal Gels", *In Preparation.*

[166] V. Testard, L. Berthier and W. Kob, "Influence of the Glass Transition on the Liquid-Gas Spinodal Decomposition", *Phys. Rev. Lett.*, 2011, 106, 125702

[167] S. A. Safran, I. Webman and G. S. Grest, “Percolation in Interacting Colloids”, *Phys. Rev. A*, 1984, 32 (1), 506-511

[168] M. Laguës, “Electrical Conductivity of Microemulsions: A Case of Stirred Percolation”, *J. Physics Lett.*, 1979, 40, 331-333

[169] D. W. Heermann and D. Stauffer, “Phase Diagram for Three-Dimensional Correlated Site-Bond Percolation”, *Z. Phys. B*, 1981, 44, 339-344

[170] P. N. Segrè, V. Prasad, A. B. Schofield and D. A. Weitz, “Glasslike Kinetic Arrest at the Colloidal-Gelation Transition”, *Phys. Rev. Lett.*, 2001, 86 (26), 6042-6045

[171] J. C. Maxwell Garnett, “Colours in Metal Glasses and in Metallic Films”, *Philos. T. Roy. Soc. A*, 1904, 203 (359-371), 385-420

[172] Q. Wang et al., “Bioconjugation by Copper(I)-Catalysed Azide-Alkyne [3 + 2] Cycloaddition”, *J. Am. Chem. Soc.*, 2003, 125 (11), 3192-3193

[173] E. Wigner, “On the Interactions of Electrons in Metals”, *Phys. Rev.*, 1934, 46 (11), 1002-1011

[174] T. Erdem, T. O’Neill et al., “Tuneable Colloidal Photonic Crystals”, *arXiv:1808.06260*, 2018

[175] T. Young, “Bakerian Lecture: On the Theory of Light and Colours”, *Phil. Trans. R. Soc. Lond.*, 1802, 92, 12-48

[176] V. N. Manoharan, “Colloidal Matter: Packing, Geometry and Entropy”, *Science*, 2015, 349, 1253751

[177] B. J. Alder and T. E Wainwright, “Phase Transition for a Hard Sphere System”, *J. Chem. Phys.*, 1957, 27, 1208-1209

[178] D. Gottwald, C. N. Likos, G. Kahl and H. Löwen, “Phase Behaviour of Ionic Microgels”, *Phys. Rev. Lett.*, 2004, 92, 068301

[179] A. Yethiraj and A. Van Blaaderen, "A Colloidal Model System with an Interaction Tunable from Hard Sphere to Soft and Dipolar", *Nature*, 2003, 421, 513–517

[180] E. B. Sirota et al., "Complete Phase Diagram of a Charged Colloidal System: A Synchrotron X-ray Scattering Study", *Phys. Rev. Lett.*, 1989, 62, 1524–1527

[181] D. M. Heyes and A. C. Brańka, "Interactions Between Microgel Particles", *Soft Matter*, 2009, 5, 2681

[182] C. E. Finlayson et al., "Interplay of Index Contrast with Periodicity in Polymer Photonic Crystals", *Appl. Phys. Lett.*, 2011, 99, 1-4

[183] C. F. Lai, C. L. Hsieh and C. J. Wu, "Light-Spectrum Modification of Warm White-Light-Emitting Diodes with 3D Colloidal Photonic Crystals to Approximate Candlelight", *Opt. Lett.*, 2013, 38, 3612–3615

[184] M. Harun-Ur-Rashid et al., "Angle-Independent Structural Colour in Colloidal Amorphous Arrays", *Chem. Phys. Chem.*, 2010, 11 (3), 579-583

[185] J. D. Forster et al., "Biomimetic Isotropic Nanostructures for Structural Colouration", *Adv. Mat.*, 2010, 22 (26-27), 2939-2944

[186] W. Hume-Rothery and H. N. Powell, "On the Theory of Super-Lattice Structures in Alloys", *Z. Krist.*, 1935, 91 (1-6), 23-47

[187] L. Fillion and M. Dijkstra, "Prediction of Binary Hard-Sphere Crystal Structures", *Phys. Rev. E*, 2009, 79, 046714

[188] T. F. Tadros, *Emulsion Formation and Stability*, John Wiley and Sons, 2013

[189] B. P. Binks and R. Murakami, "Phase Inversion of Particle-Stabilised Materials from Foams to Dry Water", *Nat. Mater.*, 2006, 5, 865-869

[190] V. N. Manoharan, M. T. Elsesser and D. J. Pine, "Dense packing and Symmetry in Small Clusters of Microspheres", *Science*, 2003, 301, 483-487

[191] Y. Zhang et al., "Sequential Self-Assembly of DNA Functionalised Droplets", *Nat. Commun.*, 2017, 8, 21

[192] A. Caciagli et al., "DNA-Coated Functional Oil Droplets", *Langmuir*, 2018, 34, 10073-10080

[193] D. Joshi et al., "Kinetic Control of the Coverage of Oil Droplets by DNA-Functionalised Colloids", *Sci. Adv.*, 2016, 2 (8), 1600881

[194] M. Kukizaki, "Shirasu Porous Glass (SPG) Membrane Emulsification in the Absence of Shear Flow at the Membrane Surface:…", *J. Membr. Sci.*, 2009, 327 (1-2), 234-243

[195] C. Holtze et al., "Biocompatible Surfactants for Water-in-Fluorocarbon Emulsions", *Lab Chip*, 2008, 8, 1632-1639

[196] C. Solans, P. Izquierdo, J. Nolla, N. Azemar and M. J. Garcia-Celma, "Nano-Emulsions", *Curr. Opin. Colloid Interface Sci.*, 2005, 10 (3-4), 102-110

[197] S. U. Pickering, "Emulsions", *J. Chem. Soc. Trans.*, 1907, 91, 2001-2021

[198] M. Cavallaro, L. Botto, E. P. Lewandowski, M. Wang and K. J. Stebe, "Curvature-Driven Capillary Migration and Assembly of Rod-like Particles", *PNAS*, 2011, 108, 20923-20928

[199] G. Duplâtre, "Size of Sodium Dodecyl Sulfate Micelles in Aqueous Solutions as Studied by Positron Annihilation Lifetime Spectroscopy", *J. Phys. Chem.*, 1996, 100 (41), 16608-16612

[200] T. O'Neill, A. Caciagli, M. Zupkauskas, D. E. P. Pinto, D. Joshi and E. Eiser, "Crystallisation and Phase Separation of Colloids at a Two-Dimensional Interface", *In Preparation*.

[201] F. Xei, C. E. Woodward and J. Forsman, "Theoretical Predictions of Temperature-Induced Gelation in Aqueous Dispersions Containing PEO-Grafted Particles", *J. Phys. Chem. B,* 2016, 120 (16), 3969-3977

[202] H. N. Yow and A. F. Routh, "Formation of Liquid Core-Polymer Shell Microcapsules", *Soft Matter,* 2006, 2 (11), 940-949

[203] P. Keen, N. Slater and A. F. Routh, "Encapsulation of Yeast Cells in Colloidosomes", *Langmuir,* 2012, 28 (2), 1169-1174

[204] P. Keen, N. Slater and A. F. Routh, "Encapsulation of Lactic Acid Bacteria in Colloidosomes", *Langmuir,* 2012, 28 (46), 16007-16014

[205] P. Keen, N. Slater and A. F. Routh, "Encapsulation of Amylase in Colloidosomes", *Langmuir,* 2014, 30 (8), 1939-1948

[206] G. Sobczak, T. Wojciechowski and V. Sashuk, "Submicron Colloidosomes of Tuneable Size and Wall Thickness", *Langmuir,* 2017, 33 (7), 1725-1731

[207] Q. Sun, H. Gao, G. B. Sukhorukov and A. F. Routh, "Silver-Coated Colloidosomes as Carriers for an Anticancer Drug", *Appl. Mater. Interfaces,* 2017, 9 (38), 32599-32606

[208] Q. Sun et al., "A Fabrication Method of Gold Coated Colloidosomes and their Application as Targeted Drug Carriers", *Soft Matter,* 2018, 14, 2594-2603

[209] T. Bollhorst et al., "Bifunctional Submicron Colloidosomes Coassembled from Fluorescent and Superparamagnetic Nanoparticles", *Angew. Chem.*, 2014, 127 (1), 120-125

[210] T. Bollhorst et al., "Synthesis Route for the Self-Assembly of Submicrometer-Sized Colloidosomes with Tailorable Nanopores", *Chem. Mater.*, 2013, 25 (17), 3464-3471

9 APPENDICES

APPENDIX 1: DIBLOCK COPOLYMER SYNTHESIS

Synthesis of the PS_{30}-PEG_{79}-N_3 diblock copolymer was done by Dr Clément Mugemana and Prof Nico Bruns at the Adolphe Merkle Institute.

All chemicals and solvents (purity > 95%) were bought from Sigma-Aldrich. $CDCl_3$ was bought from Cambridge Isotope Laboratories Inc. Azide end-functionalized polyethylene glycol (Mn= 3300 g mol^{-1}, degree of polymerization = 75, Đ= 1.07) was purchased from RAPP Polymere. Styrene was purified by passing it over a neutral aluminium oxide column to remove the inhibitor before polymerisation.

^{1}H NMR spectroscopy was measured on a Bruker 300 MHz Avance III spectrometer using $CDCl_3$ as solvent. Size-exclusion chromatography (SEC) experiments were performed on an Agilent 1200 series HPLC system equipped with an Agilent PLgel mixed guard column (particle size = 5 µm) and two Agilent PLgel mixed-D columns (ID = 7.5 mm, L = 300 mm, particle size = 5 µm). Signals were recorded by a UV detector (Agilent 1200 series), an Optilab REX interferometric refractometer, and a mini Dawn TREOS light scattering detector (Wyatt Technology Corp.). Samples were run using THF as the eluent at 30 °C and a flow rate of 1.0 mL min^{-1}. Data analysis was performed on Astra software (Wyatt Technology Corp.) and molecular weights were determined based on narrow-molecular-weight polystyrene calibration (from 2340 to 364000 g mol^{-1}). FT-IR spectra were recorded on PerkinElmer Spectrum 65 equipped with an attenuated total reflection (ATR) measuring device.

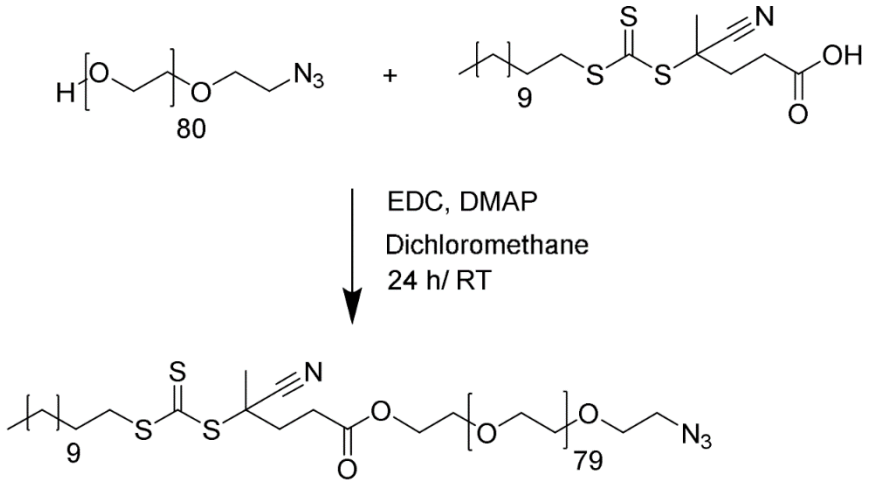

Figure 9.1: Synthesis of azide-PEG-chain transfer agent (N_3-PEG-CTA).

The synthesis of the CTA-functionalized PEG was adapted from literature.1 Azide-functionalized polyethylene glycol (0.4 g, 0.13 mmol, 1 eq.) and 4-cyano-4-

[(dodecylsulfanylthiocarbonyl)sulfanyl]pentanoic acid (0.08 g, 0.2 mmol, 1.5 eq.) were introduced in a 50 mL round-bottom flask under nitrogen atmosphere and dissolved in 7 mL of dry dichloromethane (DCM). The flask was then placed in an ice bath. 1-Ethyl-3-(3-dimethylaminopropyl)carbodiimide (38 mg, 0.2 mmol, 1.5 eq.) was dissolved in 3 mL of dry DCM and added dropwise to the reaction mixture under gentle stirring. 4-(Dimethylamino)pyridine (density: 0.884 g cm^{-3} and purity of 99%) (2.7 mL, 16 μmol, 0.12 eq.) was added in the same manner. The round-bottom flask was then removed from the ice bath, and the reaction mixture was stirred for 24 h at room temperature under nitrogen atmosphere. After the reaction, the solution mixture was concentrated (to yield a viscous solution) under reduced pressure using a rotary evaporator. The polymer was then precipitated into diethyl ether and dried under vacuum. The yield of the reaction was 75% (0.3 g). ^{1}H NMR (400 MHz, $CDCl_3$): δH 4.24 ppm (t, 2.0H, h); 3.89 ppm (t, 1.7H, i); 3.64 ppm (s, 320H, j+k); 3.38 ppm (t, 3.1H, l); 3.32 ppm (t, 2.1 H, g); 2.66 ppm (t, 2.0H, f); 2.49 ppm +2.37 ppm (m, 2.5H, d); 1.87 ppm (s, 3.0H, e); 1.83 ppm (s, water); 1.69 ppm (t, 2.6H, c), 1.25 ppm (s, 18.6H, b), 0.87 ppm (t, 3.3H, a); degree of polymerization (PEG) = 80; Mn= 3920 g mol^{-1}. GPC (calibration against PS): S3 N3-PEG-CTA: Mn= 5212 g mol^{-1}, Mw= 5733 g mol^{-1}; Đ= 1.1; FT-IR: ν = 2970-2680, 2095, 2035, 1736, 1465, 1340, 1275, 1241, 1150, 1108, 1065, 954, 840 cm^{-1} .

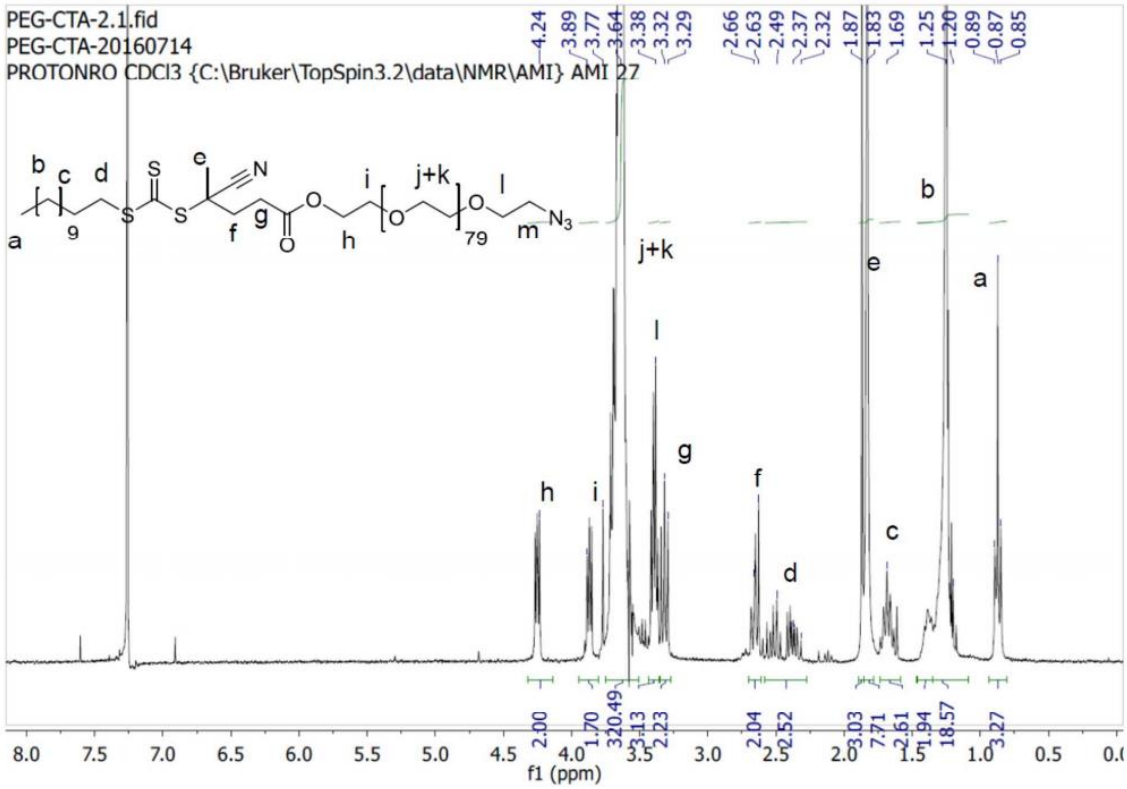

Figure 9.2: ^{1}H NMR spectrum of N_3-PEG-CTA.

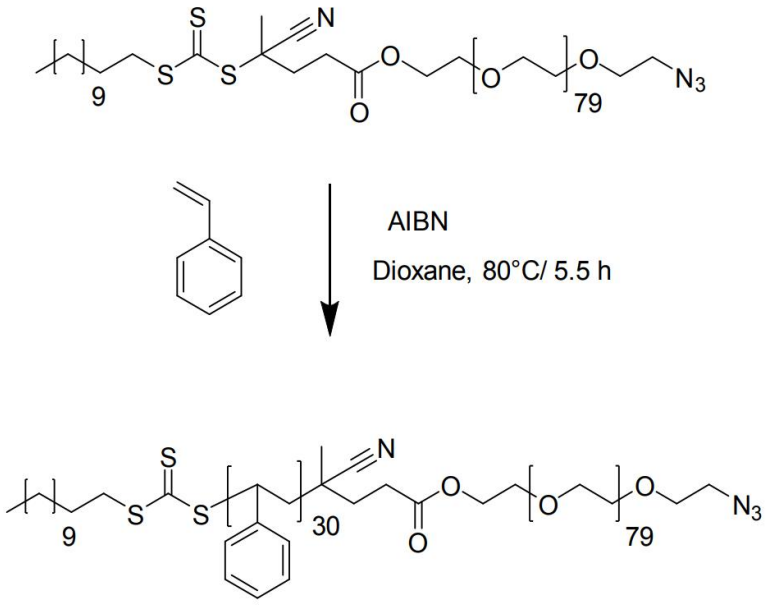

Figure 9.3: Synthesis of polystyrene-block-*PEG-azide (PS-b-PEG-N_3).*

N3-PEG-CTA (0.2 g, 59 μmol, 1 eq.) was introduced in a dry Schlenk tube containing a magnetic stirring bar. Styrene (0.676 mL, 0.612 g, 5.882 mmol, 100 eq.) and AIBN (2.4 mg; 14.7 μmol; 0.25 eq.) were added and the mixture was dissolved in 0.9 mL dry dioxane. The solution underwent 3 cycles of freeze-pump-thaw cycles to remove oxygen. The flask was then filled S4 with argon and immersed in an oil bath heated at 80°C for 5 ½ hours. After the reaction, the Schlenk tube was transferred to a cold water bath to quench the polymerization, and the solution was concentrated using a rotary evaporator. The block copolymer was precipitated into diethyl ether and dried under vacuum. The yield of the reaction was 65% (0.25 g). ^{1}H NMR (400 MHz, $CDCl_3$): δH 7.25-6.25 ppm (broad, 153.9H, a); 5.78-5.72 and 5.26-5.23 ppm (residual vinylic protons of styrene); 4.17 ppm (broad, 1.5H, d); 3.86 ppm (t, 2.0H, e) 3.52 ppm (s, 320H, c); 2.10-1.25 ppm (broad, 142, b + f); degree of polymerization (PEG) = 80; degree of polymerization (PS) = 30; Mn= 6923 g mol^{-1}. GPC (calibration against PS): N3-PEG-CTA: Mn= 5212 g mol^{-1}, Mw= 5733 g mol^{-1}; Đ= 1.1; PS-*b*-PEG-N3: Mn = 10490 g mol^{-1}, Mw = 12380 g mol^{-1}, Đ = 1.18. FT-IR: ν = 2700-3120, 1960, 1745, 1605 1454, 1340, 1280, 1240, 1110, 965, 843, 760, 700, 540 cm^{-1}.

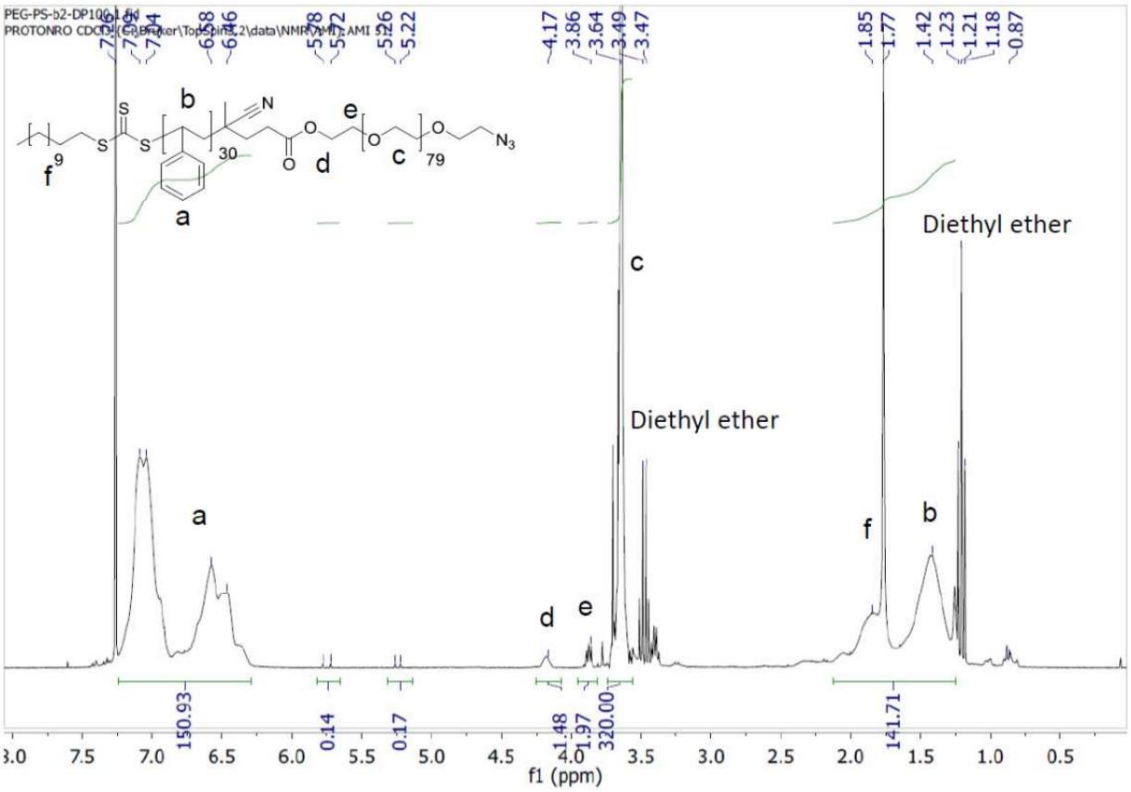

Figure 9.4: ^{1}H NMR spectrum of PS-b-PEG-N_3.

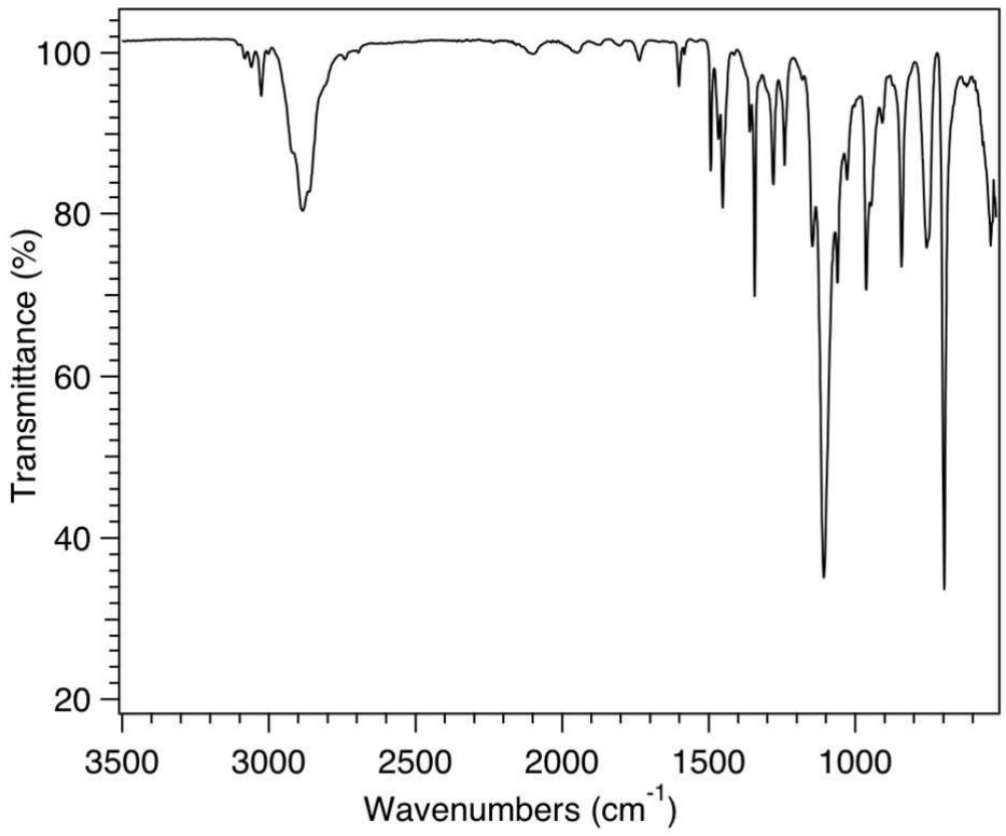

Figure 9.5: FT-IR spectra of PS_{30}-b-PEG-N_3.

APPENDIX 2: GEL IMAGES OF ALL SAMPLES

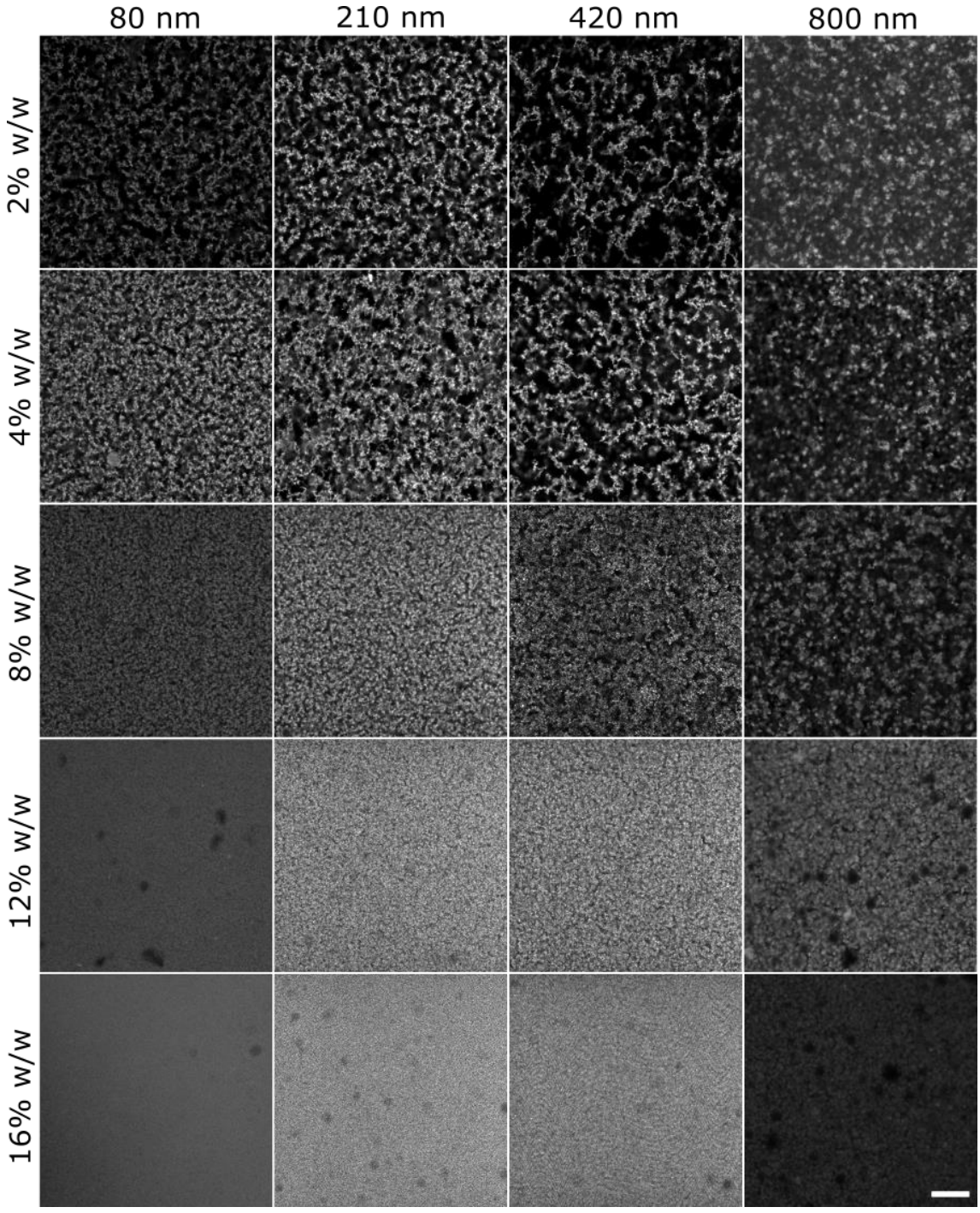

Figure 9.6:Typical confocal micrographs used for chord analysis of gels of 80, 210, 420 and 800 nm colloids at concentrations of 2%, 4%, 8%, 12% and 16% w/w at a depth of 10 µm. Scale bar is 20 µm.